

REACTION KINETICS OF DIRECT GAS-PHASE
PROPYLENE EPOXIDATION ON AU/TS-1 CATALYSTS

by

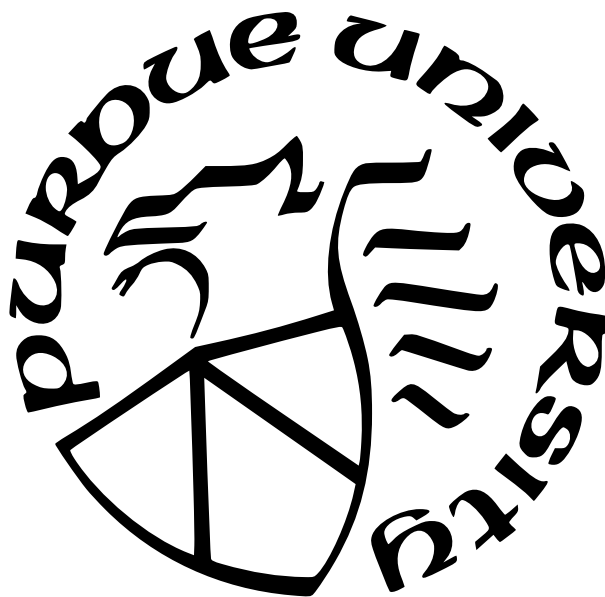
Jeremy W. Arvay

A Dissertation

Submitted to the Faculty of Purdue University

In Partial Fulfillment of the Requirements for the degree of

Doctor of Philosophy



Davidson School of Chemical Engineering

West Lafayette, Indiana

May 2022

**THE PURDUE UNIVERSITY GRADUATE SCHOOL
STATEMENT OF COMMITTEE APPROVAL**

Dr. Fabio Ribeiro, Chair

Davidson School of Chemical Engineering

Dr. Rajamani Gounder

Davidson School of Chemical Engineering

Dr. Jeffrey Greeley

Davidson School of Chemical Engineering

Dr. Christina Li

School of Chemistry

Approved by:

Dr. John Morgan

ACKNOWLEDGMENTS

My Ph.D. experience has pushed me to grow personally and professionally as I've faced greater challenges than I ever have before, and the people along the way who've supported and encouraged me have been the keys to any of the successes I've had.

First, I'd like to thank my parents and grandparents for always encouraging me to pursue an education in whatever interested me and for providing a stable environment in which I could focus on learning.

I will forever be indebted to Prof. Nick Delgass for providing an example of what to strive for as a researcher and a person. Always friendly and supportive, always willing to help and dive into the work itself, and forever excited by the possibility of new scientific understanding, Prof. Delgass lead by example and enabled not only the growth of his students but the flourishing of the communities to which he devoted himself. I will always remember our research discussions and how frequently the time limits set on the meeting weren't enough to cover everything that had come up. If it weren't for his support, patience, and contagious enthusiasm, especially during the 2020 quarantine, my Ph.D. experience would have been far different, and I don't think I would have grown to become the person I am today. I'm lucky to have known him and to have been his student, and will always cherish the memories I have of him.

Prof. Fabio Ribeiro has always pushed me to do my best, mentored me in how to work efficiently, and allowed me to grow as a professional. From his enthusiasm for fostering collaboration to address one this generation's grand challenges to his love for puns, I will always be thankful to Prof. Ribeiro for allowing me to see a star in action.

Next, I'd like to thank Prof. James Harris at the University of Alabama, who I know as Jamie from his days serving as my mentor at Purdue while he was finishing his time here and I was just beginning mine. I'll always be thankful to him for teaching me the basics of lab work in the time before he graduated so that I could hit the ground running with my project. I'm also thankful for being able to rely on him for feedback as I was finishing up my work at Purdue after Prof. Delgass' unfortunate passing. Jamie is always one for discussing research ideas, and I'm sure he will continue to lead a very successful career in academia.

I'd like to thank Professors Raj Gounder, Jeff Greeley, and Christina Li for serving on my committee and for asking insightful questions about my work. I'd also like to thank Prof. Gounder for the opportunity to work with his students as we started several new projects over the last few years, as well as for purchasing an espresso machine for his students' office.

I want to thank Dr. Abhijit Talpade, Dr. Richard Caulkins, and Evan Sowinski for always being ready to help in the lab, for their discussions, and for always striving to put their best foot forward. Working with you all has been a highlight of my time at Purdue, and I wish nothing but the best for you.

I want to thank the Purdue Catalysis Center (PCC) for providing an incredible environment to learn more about catalysis, what other students are doing, and for fostering ongoing discussions among the students. I'm thankful to the RHEACT team (Prof. Fabio Ribeiro, Dr. Jay Devaraj, Prof. Ray Mentzer, Sopuru Ezenwa, Vikrant Gajria, Dr. Abhijit Talpade, and Dr. Pushkar Ghanekar) for using their personal time to collaborate in the construction of a tool with the aim of lowering the barriers to safe laboratory practices. Being involved in this effort has been an engaging and rewarding experience.

I'd also like to thank Dr. Yury Zvinevich for all of his help and advice over the years. Yury's expertise and willingness to help students make him a pleasure to work with and an indispensable resource for every student who passes through chemical engineering research groups at Purdue. I want to thank Dr. Gabriela Nagy for her commitment to safety and willingness to work with students on issues found in the labs. I also want to thank the graduate office and business office staff, as well as Nick Humphrey, Jeff Valley, Jason Davenport, and everyone else who works to keep the department running.

Last but not least, I'd like to thank everyone I've had the chance to make friends with during my time at Purdue. Grad school has been an arduous, transformative journey, and having like-minded people to blow off steam and explore interests with has rounded out the experience.

TABLE OF CONTENTS

LIST OF TABLES	9
LIST OF FIGURES	11
ABSTRACT	26
1 INTRODUCTION	28
References	30
2 CONSEQUENCES OF PRODUCT INHIBITION IN THE QUANTIFICATION OF KINETIC PARAMETERS	33
2.1 Introduction	33
2.2 Experimental Methods	35
2.2.1 Catalyst preparation	35
2.2.2 Catalyst characterization	35
2.2.3 Catalytic testing	37
2.3 Results	38
2.3.1 Kinetic experiments in presence of NO ₂ in the feed stream	38
2.3.2 Kinetic experiments in absence of NO ₂ in the feed stream	40
2.4 Discussion	43
2.4.1 Quantitative analysis of the NO ₂ inhibition effect	43
2.4.2 Product inhibition is more likely than expected	45
2.4.3 Generalization of the analysis	49
2.4.4 A simple test for product inhibition	51
2.5 Conclusions	52
2.6 Supplementary Information	53
2.6.1 Elemental Analysis	53
2.6.2 X-ray Diffraction (XRD) Patterns	54
2.6.3 Sample Argon Adsorption Isotherms	55
2.6.4 Diffuse Reflectance UV-Visible-NIR	56

2.6.5	Cu K-edge X-ray Absorption Spectroscopy (XAS)	57
2.6.6	Dry NO oxidation kinetics on Cu-SSZ-13 catalysts	58
2.6.7	Relaxation of differential assumption for PFR	63
2.6.8	Derivation of equation 2.10	66
2.6.9	Range of parameter space where errors from neglecting product inhibition are significant	67
2.6.10	Derivations for Section 2.4.2	70
	References	74
3	PROPYLENE OXIDE INHIBITS PROPYLENE EPOXIDATION OVER AU/TS-1	78
3.1	Introduction	78
3.2	Experimental methods	81
3.2.1	Catalyst synthesis	81
	TS-1 synthesis	81
	Gold deposition	82
	Catalyst characterization	83
	Kinetic studies of propylene epoxidation	84
3.3	Results and discussion	87
3.3.1	Structural characterization of titanosilicates	87
3.3.2	Measurement of reaction kinetics of over Au/TS-1 catalysts	88
	Propylene epoxidation	88
	Measurement of reaction orders and activation energies for hydrogen oxidation over Au/TS-1	99
3.4	Conclusions	102
3.5	Supplementary Information	103
3.5.1	Reactor Apparatus	103
3.5.2	XRD Patterns	105
3.5.3	Nitrogen Isotherms	106
3.5.4	Diffuse Reflectance UV-Visible Spectroscopy	107
3.5.5	Additional Kinetic Data and Derivations	109

3.5.6	Example Log Derivative Derivation	121
3.5.7	Sequential Mechanism, Rate Law, and Log Derivatives	122
	References	124
4	KINETICS OF PROPYLENE EPOXIDATION OVER EXTRA-CRYSTALLINE GOLD ACTIVE SITES ON AU/TS-1 CATALYSTS	130
4.1	Introduction	130
4.2	Experimental methods	132
4.2.1	Catalyst synthesis	132
	TS-1 and S-1 synthesis	132
	Preparation of Au-PVP/TS-1 and Au-PVP/S-1 samples	133
4.2.2	Catalyst characterization	134
4.2.3	Kinetic testing	136
4.3	Results and discussion	138
4.3.1	Characterization of titanosilicate-1 and silicate-1	138
4.3.2	In-situ removal of PVP ligands	140
4.3.3	Measurement of reaction kinetics on Au-PVP/TS-1 and Au-PVP/S-1	144
	Propylene epoxidation	144
	Hydrogen oxidation kinetics	146
	Active site models and rate normalization for Au-DP/TS-1 and Au- PVP/TS-1	149
4.4	Conclusions	155
4.5	Supplementary Information	157
4.5.1	Reactor schematic	157
4.5.2	XRD patterns	158
4.5.3	Nitrogen physisorption isotherms	159
4.5.4	Diffuse reflectance UV-Visible spectroscopy	160
4.5.5	Estimation of internal and external mass transfer limitations	163
4.5.6	CO ₂ Generation during H ₂ /O ₂ /N ₂ co-feed after propylene epoxidation	167
4.5.7	Initial TGA experiment, stepped temperature program, Au-PVP/TS-1	168

4.5.8	Consumption of PO during PO reaction order experiment on 0.082Au-PVP/S-1	169
4.5.9	Truncated cubo-octahedron crystal model and related active site models	170
4.5.10	Gold nanoparticle size distributions	174
4.5.11	Proximal Ti active site model	178
4.5.12	Model fits of propylene epoxidation rate data	186
4.5.13	Model fits of hydrogen oxidation rate data	206
	References	226

LIST OF TABLES

2.1	Literature examples of the quantitative effects of inhibition of products.	52
2.2	Bulk elemental analysis of Si, Al, and Cu content in Cu-SSZ-13 catalysts measured using atomic absorption spectroscopy (AAS). Data for all samples except that with Cu wt% 7.40 were originally reported in Verma et al. [10]	53
2.3	Values for pre-exponential factors and activation energies reported by Metkar et al. [11].	72
3.1	Characterization data for all catalyst samples used in this study.	88
3.2	Measured reaction orders compared to those reported in literature.	90
3.3	Relation between the true reaction order and the coverages of the most abundant surface species, according to the mechanism shown in Figure 3.4 and the mechanistic assumptions resulting in Eq. 3.15.	98
3.4	Apparent and PO-inhibition-corrected reaction orders and activation energies for propylene oxide formation and H ₂ oxidation determined by averaging the measured kinetic parameters for eight separate Au/TS-1 samples (0.092Au/TS-1(75), 0.019Au/TS-1(143), 0.040Au/TS-1(81), 0.030Au/TS-1(81), 0.044Au/TS-1(81), 0.033Au/TS-1(143), 0.069Au/TS-1(143), and 0.064Au/TS-1(143)).	100
3.5	Parameters used to calculate the Mears criterion for Au/TS-1 catalysts used in this study.	110
3.6	Parameters used to calculate the Mears criterion for Au/TS-1 catalysts used in this study.	111
3.7	Apparent reaction orders and activation energies for PO formation measured over all catalysts in this study. Activation energies were measured in the temperature range 443-483 K with a feed composition of 10% H ₂ / 10% O ₂ / 10% C ₃ H ₆ / 70% N ₂ and a space velocity of 26,000 cm ³ g _{cat} ⁻¹ h ⁻¹ in a gas-phase CSTR. Reaction orders were measured at 473 K with a feed composition of 2.5-10% H ₂ / 2.5-10% O ₂ / 2.5-10% C ₃ H ₆ / 0-0.3% PO/ balance N ₂ and a space velocity of 26,000 cm ³ g _{cat} ⁻¹ h ⁻¹ in a gas-phase CSTR.	119
3.8	Apparent reaction orders and activation energies for PO formation measured over all catalysts in this study. Activation energies were measured in the temperature range 443-483 K with a feed composition of 10% H ₂ / 10% O ₂ / 10% C ₃ H ₆ / 70% N ₂ and a space velocity of 26,000 cm ³ g _{cat} ⁻¹ h ⁻¹ in a gas-phase CSTR. Reaction orders were measured at 473 K with a feed composition of 2.5-10% H ₂ / 2.5-10% O ₂ / 2.5-10% C ₃ H ₆ / 0-0.3% PO/ balance N ₂ and a space velocity of 26,000 cm ³ g _{cat} ⁻¹ h ⁻¹ in a gas-phase CSTR.	120

4.1	Gold nanoparticle number average diameters and standard deviations calculated from TEM-derived particle size distributions for all samples used in this study. Particle size distributions were measured after air treatment, H ₂ /O ₂ /N ₂ treatment, and the conclusion of all kinetic experiments for all samples.	140
4.2	Apparent and PO-inhibition-corrected reaction orders and activation energies for propylene oxide formation and H ₂ oxidation determined by averaging the measured kinetic parameters for eight separate Au/TS-1 samples (0.092Au/TS-1(75), 0.019Au/TS-1(143), 0.040Au/TS-1(81), 0.030Au/TS-1(81), 0.044Au/TS-1(81), 0.033Au/TS-1(143), 0.069Au/TS-1(143), and 0.064Au/TS-1(143)).	144
4.3	Comparisons of catalytic site-time yield (STY) of propylene epoxidation, unselective hydrogen oxidation (Eq. 4.4), and total C1-C3 byproduct generation on 0.11Au-PVP/TS-1(73), 0.083Au-PVP/TS-1(126) (averaged over two sets of experiments), and 0.082Au-PVP/S-1. Reaction conditions: 10/10/10/70 mol% C ₃ H ₆ /H ₂ /O ₂ /N ₂ , SV = 14,000 cm ³ h ⁻¹ g _{cat} ⁻¹ , T = 473 K, P = 101.3 kPa.	145
4.4	Apparent and PO-inhibition-corrected reaction orders and activation energies for propylene oxide formation and H ₂ oxidation determined by averaging the measured kinetic parameters for eight separate Au/TS-1 samples (0.092Au/TS-1(75), 0.019Au/TS-1(143), 0.040Au/TS-1(81), 0.030Au/TS-1(81), 0.044Au/TS-1(81), 0.033Au/TS-1(143), 0.069Au/TS-1(143), and 0.064Au/TS-1(143)).	148
4.5	UV-Vis peak centers and edge energies for TS-1 samples dehydrated using flowing dry He at 573 K.	162
4.6	Parameters used in the calculation of the Mears criterion.	165
4.7	Parameters used in the calculation of the Thiele modulus.	166
4.8	Equations relating the edge length (m) of a given truncated cubo-octahedron with (100) top facet (Fig. 4.17) to the numbers of each type of surface atom, all surface atoms, and all atoms in the nanoparticle.	171
4.9	Equations relating the edge length (m) of a given truncated cubo-octahedron with (111) top facet (Fig. 4.18) to the numbers of each type of surface atom, all surface atoms, and all atoms in the nanoparticle.	173

LIST OF FIGURES

2.1	Arrhenius plot for NO oxidation with NO ₂ in the feed (0.304 kPa NO, 0.015 kPa NO ₂ , 10.13 kPa O ₂ , 90.876 kPa N ₂ , 500 to 585 K). Differential conversion in the PFR makes the measured performance equivalent to that of a CSTR. Space velocities were maintained at 1300 s ⁻¹	40
2.2	Natural log of the NO oxidation rate at 543 K as a function of NO ₂ pressure (red circles), O ₂ pressure (black diamonds), and NO pressure (green triangles). All kinetic data points included in this plot were obtained with NO ₂ co-feeding. NO ₂ pressures between 0.004 and 0.022 kPa were used for NO ₂ orders. NO pressure between 0.02 and 0.05 kPa were used for NO orders, O ₂ pressures between 8 and 20 kPa were used for O ₂ orders. Space velocities were maintained at 1300 s ⁻¹ . .	41
2.3	Variation of the rate of NO oxidation per mole Cu with temperature, in the absence of NO ₂ co-feeding, evaluated with a CSTR model and ignoring product inhibition. Feed conditions: 0.304 kPa NO, 10.13 kPa O ₂ , 90.891 kPa N ₂ , at 380–580 K. Space velocities were maintained at 1300 s ⁻¹	42
2.4	Variation of the ln of the rate of NO oxidation per mole Cu, with the ln of the NO and O ₂ concentrations during dry NO oxidation conditions (0.304 kPa NO, 10.13 kPa O ₂ , 90.891 kPa N ₂ , 543 K). O ₂ concentrations were varied between 80 and 270 kPa while holding NO and NO ₂ gas pressures constant. NO concentrations were varied between 0.024 and 0.05 kPa while holding O ₂ and NO ₂ gas pressure constant. NO ₂ was not co-fed in the feed stream.	43
2.5	Series of elementary steps consistent with the data collected in this manuscript and the data reported previously by Verma et al. [10].	48
2.6	Ambient XRD patterns from 10°to 60°2θon Cu-SSZ-13 Si:Al = 4.5 with Cu wt% of 3.6, 7.4, and 18.9, and H-SSZ-13. All Cu-SSZ-13 materials were Si:Al = 4.5 and were calcined after Cu-exchange then cooled and exposed to ambient air prior to collecting ambient XRD spectra.	54
2.7	Argon adsorption isotherms (87 K) of H-SSZ-13 (diamonds) and Cu-SSZ-13 (Cu wt% = 3.75, triangles)). Both samples are Si:Al = 4.5.	55
2.8	Diffuse reflectance UV-visible spectra of Cu-SSZ-13 samples with Cu wt% ranging from 1.74-18.93 and of CuO, collected under ambient conditions (298 K, ambient air).	56
2.9	Ambient Cu K-edge X-ray absorption spectra collected on bulk Cu(II)O (red), aqueous Cu(NO ₃) ₂ (blue), and five Cu-SSZ-13 samples with Cu wt% from 0.82-18.93. All Cu-SSZ-13 materials were Si:Al = 4.5 and were calcined after Cu-exchange then cooled and exposed to ambient air prior to collecting ambient XAS spectra. These data were originally reported in Verma et al. [10].	57

2.10	The dry NO oxidation reaction rate normalized per gram of catalyst plotted versus the Cu wt%. Dry NO oxidation conditions (300 ppm NO, 150 ppm NO ₂ , 10% O ₂ , in balance N ₂ , 543 K). Cu-SSZ-13 catalysts with a Si:Al molar ratio of 4.5 and Cu wt% from 0-19 were synthesized and used for this study. The yellow shaded area between 0 and 4 wt% represents samples with all Cu as ionic Cu ²⁺ /Cu ¹⁺ species. The grey shaded area between 4 to 19 wt% represents samples that contain bulk Cu _x O _y species. Data for all samples except that with Cu wt% 7.40 were originally reported in Verma et al. [10].	58
2.11	The dry NO oxidation apparent activation energy plotted versus the Cu wt%. Dry NO oxidation conditions (300 ppm NO, 150 ppm NO ₂ , 10% O ₂ , in balance N ₂ , 543 K). Cu-SSZ-13 catalysts with a Si:Al molar ratio of 4.5 and Cu wt% from 0-19 were synthesized and used for this study. The yellow shaded area between 0 and 4 wt% represents samples with all Cu as ionic Cu ²⁺ /Cu ¹⁺ species. The grey shaded area between 4 to 19 wt% represents samples that contain bulk Cu _x O _y species. Data for all samples except that with Cu wt% 7.40 were originally reported in Verma et al. [10].	59
2.12	NO reaction orders plotted versus the Cu wt% under dry NO oxidation conditions (300 ppm NO, 150 ppm NO ₂ , 10% O ₂ , in balance N ₂ , 543 K). Cu-SSZ-13 catalysts with a Si:Al molar ratio of 4.5 and Cu wt% from 0-19 were synthesized and used for this study. The yellow shaded area between 0 and 4 wt% represents samples with all Cu as ionic Cu ²⁺ /Cu ¹⁺ species. The grey shaded area between 4 to 19 wt% represents samples that contain bulk Cu _x O _y species. Data for all samples except that with Cu wt% 7.40 were originally reported in Verma et al. [10]. . .	60
2.13	O ₂ reaction orders plotted versus the Cu wt% under dry NO oxidation conditions (300 ppm NO, 150 ppm NO ₂ , 10% O ₂ , in balance N ₂ , 543 K). Cu-SSZ-13 catalysts with a Si:Al molar ratio of 4.5 and Cu wt% from 0-19 were synthesized and used for this study. The yellow shaded area between 0 and 4 wt% represents samples with all Cu as ionic Cu ²⁺ /Cu ¹⁺ species. The grey shaded area between 4 to 19 wt% represents samples that contain bulk Cu _x O _y species. Data for all samples except that with Cu wt% 7.40 were originally reported in Verma et al. [10]. . .	61
2.14	NO ₂ reaction orders plotted versus the Cu wt% under dry NO oxidation conditions (300 ppm NO, 150 ppm NO ₂ , 10% O ₂ , in balance N ₂ , 543 K). Cu-SSZ-13 catalysts with a Si:Al molar ratio of 4.5 and Cu wt% from 0-19 were synthesized and used for this study. The yellow shaded area between 0 and 4 wt% represents samples with all Cu as ionic Cu ²⁺ /Cu ¹⁺ species. The grey shaded area between 4 to 19 wt% represents samples that contain bulk Cu _x O _y species. Data for all samples except that with Cu wt% 7.40 were originally reported in Verma et al. [10].	62
2.15	Conversion as a function of τ as determined by numerical integration of Eq. 2.23 using trapezoid rule with 200 mesh points.	64
2.16	Conversion at a fixed value of τ as a function of k_{eff}	65

2.17	Percent difference in the rate of reaction when product inhibition is not included in the rate expression, as a function of the pressure of the inhibiting product (B) and the enthalpy of adsorption of species B. Plots (a)-(c) use the upper bound for entropy of adsorption as reported by Vannice et al. [36] (see Section 2.4.2 of the main text,), plots (d)-(f) use the average of the upper bound and lower bound adsorption entropy, and plots (g)-(i) use the lower bound for adsorption entropy ($-41.8 \text{ J (mol K)}^{-1}$) at 400 K (a,d,e), 500 K (b,e,h), and 600 K (c, f, i).	69
2.18	Series of elementary steps reported by Metkar et al. [11].	71
3.1	Time on stream (TOS) profile for 0.092Au/TS-1(75). Initial rate increase occurs during temperature ramp (0.0083 K s^{-1}) until reaction temperature (473 K) is reached. Returns to 10% H_2 /10% O_2 /10% C_3H_6 /70% N_2 (by volume) are represented by white boxes after the initial activation under these conditions. Reaction orders are measured by non-monotonically varying the reactant (or product) flow rate of interest while keeping the total flow rate constant ($\text{SV} = 14,000 \text{ cm}^3 \text{ g}_{\text{cat}}^{-1} \text{ h}^{-1}$ up to 25 h, then 26,000 for $\text{TOS} > 25 \text{ h}$) and varying the balance N_2 flow rate to compensate. N_2 flow at reaction temperature maintained between each experiment to maintain O_2 - and moisture-free atmosphere.	89
3.2	Natural log of the net PO rate ($\text{mol g}_{\text{cat}}^{-1} \text{ s}^{-1}$ total minus $\text{mol g}_{\text{cat}}^{-1} \text{ s}^{-1}$ fed) (diamonds) and natural log of the H_2 oxidation rate ($\text{mol g}_{\text{cat}}^{-1} \text{ s}^{-1}$ H_2 consumed minus net $\text{mol g}_{\text{cat}}^{-1} \text{ s}^{-1}$ PO formed) (squares) as a function of the natural log of the total gas phase PO mol fraction over 0.030Au/TS-1(81) at 473 K with gas composition 10% H_2 /10% O_2 /10% C_3H_6 , balance N_2 and PO (PO mol fraction in feed 0–0.003) at a SV of $26,000 \text{ cm}^3 \text{ g}_{\text{cat}}^{-1} \text{ h}^{-1}$. The dashed lines show the linear regressions to the data resulting in the reported reaction orders. Error bars represent one standard deviation.	91
3.3	(a) PO production rate (circles) and H_2 oxidation rate (squares) in a gas-phase CSTR as a function of space time (b) natural log of C_3H_6 conversion (circles), natural log of H_2 conversion (filled squares), and natural log of H_2 oxidation computed from the H_2 conversion by subtracting PO formation (open squares) as functions of the natural log of space time (c) natural log of PO production rate (circles) and natural log of H_2 oxidation rate (squares) as functions of the natural log of the total gas phase PO mol%. Dotted lines in (b) and (c) are linear trendlines fit to the data resulting in the reported equations, while the thick dotted line in (c) is the average of the natural log of the H_2 oxidation rates included to guide the eye. Mass of catalyst ranged from 0.080 to 0.400 g 0.10Au/TS-1(143), 473 K, 10% H_2 /10% O_2 /10% C_3H_6 / 70% N_2 (vol%) and the total flow rate was varied from 0.6 to $1.4 \text{ cm}^3 \text{ s}^{-1}$, resulting in a range of space times from 1.6 to $19 \times 10^5 \text{ h g}_{\text{cat}} \text{ cm}^{-3}$	93
3.4	Proposed reaction mechanism for propylene oxide synthesis over Au/TS-1 catalysts. S_1 is a Au site, S_2 is an Au-Ti interfacial site, and that they are neighboring sites.	95

3.5	Single-site reaction mechanism proposed by Barton and Podkolzin for hydrogen oxidation over Au/TS-1 catalysts [42].	101
3.6	Photograph of gas-phase CSTR system with heat-traced recirculation loop (left). P&ID diagram for gas-phase PFR/CSTR system (right).	103
3.7	Diagram of Pyrex reactor (left). Photograph of pyrex reactor (right).	104
3.8	XRD patterns for calcined (a) TS-1(75) and (b) TS-1(81) and (c) TS-1(143). Patterns are normalized to their maximum intensity and offset vertically for clarity.	105
3.9	N ₂ adsorption isotherms for TS-1(75) (circles) and TS-1(81) (squares) TS-1(143) (triangles). Isotherms are offset by 120 cm ³ _(STP) g ⁻¹ for clarity. Micropore volumes are reported in Table 3.1.	106
3.10	DRUV-Vis spectra in Kubelka-Munk units (normalized to the maximum F(R) intensity) for (a) TS-1(75) (b) TS-1(81) and (c) TS-1(143), collected (i) under ambient conditions (solid line), (ii) after dehydration at 523 K (dashed line). . .	107
3.11	Tauc plots for (a) TS-1(75) and (b) TS-1(81) and (c) TS-1(143) measured under dehydrated conditions (He flow, 523 K).	108
3.12	Determination of the deactivation rate constants in the initial deactivation (large dashed line, circles) and the steady-state deactivation (small dashed lines, squares) regimes for 0.092Au/TS-1(75). Note that after 24 h time on stream, the space velocity was changed from 14,000 to 26,000 cm ³ g _{cat} ⁻¹ h ⁻¹ and the reactor operating mode changed from PFR to CSTR, resulting in an increased reaction rate at 25 h time on stream. (T = 473 K, feed was 10% H ₂ / 10% O ₂ / 10% C ₃ H ₆ / 70% N ₂ by volume).	112
3.13	Example determination of the first-order exponential decay constant for correction of steady-state reaction rates during PO order measurement on 0.063Au/TS-1(75). Data collected in CSTR mode, SV= 26,000 cm ³ g _{cat} ⁻¹ h ⁻¹ , T = 473 K, feed = 10% H ₂ /10% O ₂ /10% C ₃ H ₆ /0-0.012% PO/Balance N ₂ over 0.063Au/TS-1(75) and represent returns to the standard condition with 0% PO co-feed. Over the time scale studied, the deactivation is approximately linear.	113
3.14	Apparent (a) H ₂ , (b) O ₂ , and (c) C ₃ H ₆ reaction orders measured over 0.092Au/TS-1(75) at 473 K and a space velocity of 26,000 cm ³ g _{cat} ⁻¹ h ⁻¹ in a gas-phase CSTR.	114
3.15	Apparent activation energies (deactivation corrected, not PO corrected) for PO formation measured over (a) 0.019Au/TS-1(143), (b) 0.040Au/TS-1(81), and (c) 0.022Au/TS-1(143) from 443-483 K with a feed composition of 10% H ₂ / 10% O ₂ / 10% C ₃ H ₆ / 70% N ₂ and a space velocity of 26,000 cm ³ g _{cat} ⁻¹ h ⁻¹ in a gas-phase CSTR.	115

3.16	Example PO order measurement (a) before and (b) after correction for deactivation over time on stream. Numbers near each data point represent the non-monotonic order in which the data were collected (data points 1 and 6 represent no PO co-feed). Data collected in CSTR mode, $SV = 26,000 \text{ cm}^3 \text{ g}_{cat}^{-1} \text{ h}^{-1}$, $T = 473 \text{ K}$, feed = 10% H_2 /10% O_2 /10% C_3H_6 /0-0.024% PO/Balance N_2 over 0.069Au/TS-1(143).	116
3.17	Propylene oxide formation rate as a function of time on stream (filled circles) and CO_2 inlet pressure (open squares) over 0.11Au/TS-1(81) with 10% H_2 , 10% O_2 , 10% propylene, and balance N_2 flow ($SV = 14,000 \text{ cm}^3 \text{ g}_{cat}^{-1} \text{ h}^{-1}$, $T = 473 \text{ K}$). . .	117
3.18	Apparent water order measured over 0.069Au/TS-1(143) at 473 K, $SV = 26,000 \text{ cm}^3 \text{ g}_{cat}^{-1} \text{ h}^{-1}$, 10% H_2 , 10% O_2 , 10% C_3H_6 , 0-0.86% H_2O , and balance N_2 in a gas phase CSTR.	118
3.19	One variation of the sequential mechanism. In this mechanism, S_1 refers to a Au site, and S_2 refers to a Ti site.	122
4.1	TEM micrograph of gold nanoparticles on 0.082Au-PVP/S-1, after kinetic experiments. The scale bar represents 10 nm.	139
4.2	Gold nanoparticle size distribution, measured from TEM micrographs taken on 0.083Au-PVP/TS-1(126) after kinetic experiments. The number average gold nanoparticle diameter is $6.5 \pm 2.9 \text{ nm}$ and the distribution is based on a count of 498 gold nanoparticles.	140
4.3	Sample mass (a) and heat flow (b) over the course of a TGA experiment. Calcined TS-1(126) (solid line), as-made 0.083Au-PVP/TS-1(126) (dash dot), post-air treatment (long dashes), and air and $\text{H}_2/\text{O}_2/\text{N}_2$ -treated 0.083Au-PVP/TS-1(126) (dots) catalysts were held at ambient temperature with $1.67 \text{ cm}^3 \text{ s}^{-1}$ of dry air flowing for 900 s before ramping to 1073 K (10 K min^{-1}) and holding for 1800 s. The strong negative trend in the heat flow at high temperature is an artifact of the instrument.	141
4.4	HRTEM micrographs of typical gold nanoparticles on (a) 0.08 Au-PVP/TS-1(126) after treatment in air and $\text{H}_2/\text{O}_2/\text{N}_2$, (b) 0.11Au-PVP/TS-1(73) after treatment in air and $\text{H}_2/\text{O}_2/\text{N}_2$ as well as an activation period in $\text{C}_3\text{H}_6/\text{H}_2/\text{O}_2/\text{N}_2$ (Fig. 5, below) , and (c) 0.08Au-PVP/TS-1(126) after all three treatments (air, $\text{H}_2/\text{O}_2/\text{N}_2$, and an activation period in $\text{C}_3\text{H}_6/\text{H}_2/\text{O}_2/\text{N}_2$) and the conclusion of all kinetic experiments. The scale bars represent 10 nm.	142
4.5	The rate of propylene epoxidation for 0.11Au-PVP/TS-1(73) during the first six hours of reaction time after treatment in air at 573 K and 3/3/94 mol% $\text{H}_2/\text{O}_2/\text{N}_2$ at 473 K. Reaction conditions: 10/10/10/70 mol% $\text{C}_3\text{H}_6/\text{H}_2/\text{O}_2/\text{N}_2$, $T = 473 \text{ K}$, $SV = 14,000 \text{ cm}^3 \text{ h}^{-1} \text{ g}_{cat}^{-1}$, $P = 101.3 \text{ kPa}$	143

4.6	Proposed series of elementary steps for propylene epoxidation on Au/TS-1 catalysts known as the ‘simultaneous’ mechanism. Stars are Au sites and empty squares are Ti sites and they are assumed to be in proximity, such that a gold-adsorbed HOOH and titanium-adsorbed propylene can react to form propylene oxide.	146
4.7	Dual-site reaction mechanism for hydrogen oxidation on gold nanoparticles, proposed by Barton and Podkolzin [16]. Stars represent Au sites accessible to all species, and squares represent Au sites accessible only to hydrogen.	147
4.8	PO rate normalized to total gold mass vs. corner Au fraction (a) and proximal Ti per Au (b) for Au-PVP/TS-1 (Si/Ti = 126) (black triangles), Au-PVP/TS-1 (Si/Ti = 73) (Orange diamonds), and Au-DP/TS-1 ([17], red circles) catalysts. For the proximal Ti model, a Au-Ti interaction distance of 0.44 nm was used. The slope of the plotted line corresponds to the best-fit turnover frequency for the entire data set, which is shown in the upper right-hand corner of each plot. Reaction conditions: 10/10/10/70 mol% C ₃ H ₆ /H ₂ /O ₂ /N ₂ , SV = 14,000 cm ³ h ⁻¹ g _{cat} ⁻¹ , T = 473 K, P = 101.3 kPa.	152
4.9	(a) Model fit of experimental data for the hydrogen oxidation rate data set consisting of 0.083Au-PVP/TS-1(126) catalysts (black triangles), 0.11Au-PVP/TS-1(73) (orange diamonds) and Au-DP/TS-1(100) catalysts (red circles) reported in [39] for the surface atom model (prediction shown by dashed line). (b) Residual plot for the model regression in (a). Reaction conditions: 10/10/10/70 mol% C ₃ H ₆ /H ₂ /O ₂ /N ₂ , SV = 14,000 cm ³ h ⁻¹ g _{cat} ⁻¹ , T = 473 K, P = 101.3 kPa.	154
4.10	P&ID of gas-phase recycle reactor system, operated with a recycle ratio 30 so that the reactor behaves as a CSTR. The recirculation loop is heated to 323 K to prevent condensation of gas-phase products. Red arrows show the default positions of automated valves in the event of a power failure or alarm state. Temperatures from temperature controllers 2 and 3 are read out to a PC with Labview software, which is used to automatically carry out kinetic experiments according to user-written instructions. A mass balance across the system is closed by reading signals from MFC control boxes 1, 2 and the mass flow meter (left of recirculation loop) to detect leaks or malfunctioning mass flow controllers. A separate flammables gas detector is positioned over the glass recirculation loop and will put the system in an emergency shutdown state if triggered.	157
4.11	(a) XRD patterns for calcined (top) S-1, (middle) TS-1(73), and (bottom) TS-1(126). (b) Inset shows the peak at 2θ = 24.6° for calcined (top) S-1, (middle) TS-1(73), and (bottom) TS-1(126), the lack of splitting in which indicates the presence of an orthorhombic unit cell [27]. Patterns are normalized to their maximum intensity and offset for clarity.	158
4.12	Nitrogen physisorption isotherms for (top) TS-1(73), (middle) TS-1(126), and (bottom) S-1, offset by 200 cm ³ _{STP} g ⁻¹ , 75 cm ³ _{STP} g ⁻¹ , and 0 cm ³ _{STP} g ⁻¹ , respectively.	159

4.13	DRUV-Vis spectra in Kubelka-Munk units (normalized to the maximum $F(R)$ intensity) for (a) TS-1(126) and (b) TS-1(73), collected under (i) ambient conditions (solid line) and (ii) after dehydration at 523 K in flowing dry helium. . . .	160
4.14	Tauc plots for (a) TS-1(126) and (b) TS-1(73) measured after dehydration at 523 K in flowing dry helium.	161
4.15	Rates of PO generation (triangles) and CO ₂ generation (circles) during (a) propylene epoxidation reaction conditions and (b-d) hydrogen oxidation reaction conditions.	167
4.16	Sample mass (solid line) and temperature program (dashed line) in initial TGA experiment for 0.083Au-PVP/TS-1(126). 20-30 mg of catalyst sample was held in flowing air ($1.67 \text{ cm}^3 \text{ s}^{-1}$) first at ambient temperature for 0.5 h, 423 K for 2 h, followed by 473 K, 523 K, 573 K, 623 K, 673 K, 723 K, and 1073 K, each for 0.5 h.	168
4.17	Net rate of PO generation during a PO reaction order experiment with co-fed PO (co-feeds: 0% PO, 0.18% PO, 0.07% PO, 0.13% PO, 0% PO) (10/10/10/0-0.18/bal. mol% C ₃ H ₆ /H ₂ /O ₂ /PO/N ₂ , SV = $26,000 \text{ cm}^3 \text{ h}^{-1} \text{ g}_{cat}^{-1}$, 473 K, 101.3 kPa)	169
4.18	Example cubo-octahedron crystal model (edge length, m , = 4) used for Au nanoparticles. The red line indicates the truncation line used to create the truncated cubo-octahedron model with a (100) top facet. Atoms bisected by the line are included in the model. Labeled and color-filled atoms (purple, blue, green) indicate gold atoms with unique coordination to other gold atoms. Subscripts on labels denote Au-Au coordination numbers. Superscripts denote FCC lattice position of missing neighboring atoms (see [38] for further examples). Adapted from [38] with permission from Surface Science.	170
4.19	Example cubo-octahedron crystal model (edge length, m , = 4) used for Au nanoparticles. The red line indicates the truncation line used to create the truncated cubo-octahedron model with a (111) top facet (leftmost portion of nanoparticle retained for model). Atoms bisected by the line are included in the model. Labeled and color-filled atoms (red, orange) indicate gold atoms with unique coordination to other gold atoms. Subscripts on labels denote Au-Au coordination numbers. Superscripts denote FCC lattice position of missing neighboring atoms (see [38] for further examples). Adapted from [38] with permission from Surface Science.	172
4.20	TEM-derived gold nanoparticle size distribution for 0.083Au-PVP/TS-1(126). The distribution was determined from 210 gold nanoparticles. The average size is $7.6 \pm 3.3 \text{ nm}$, with 3.3 nm representing the standard deviation of the measured diameters.	174

4.21	TEM-derived gold nanoparticle size distribution for 0.083Au-PVP/TS-1(126) (repeat). The distribution was determined from 498 gold nanoparticles. The average size is 6.5 ± 2.9 nm, with 2.9 nm representing the standard deviation of the measured diameters.	175
4.22	TEM-derived gold nanoparticle size distribution for 0.11Au-PVP/TS-1(73). The distribution was determined from 315 gold nanoparticles. The average size is 7.4 ± 2.9 nm, with 2.9 nm representing the standard deviation of the measured diameters.	176
4.23	TEM-derived gold nanoparticle size distribution for 0.082Au-PVP/S-1. The distribution was determined from 327 gold nanoparticles. The average size is 6.6 ± 2.5 nm, with 2.5 nm representing the standard deviation of the measured diameters.	177
4.24	2-D grid illustrating the proximal Ti model, with unit cell side lengths, Au nanoparticle radius (R), and interaction range (D) shown. The gold nanoparticle is represented by the yellow/gold circle labeled “Au” and surface-accessible Ti-containing sites are represented by green circles. In this example, the gold nanoparticle has four Ti-containing sites within the interaction range.	180
4.25	Schematic showing the lengths of hydrogen peroxide used to generate the estimated maximum interaction range used for the proximal Ti model in the main text. $L1 = 0.255$ nm, $L2 = 0.181$ nm. Molecular internal coordinates obtained from the NIST Computational Chemistry Comparison and Benchmark Database (CCCBDB, https://cccbdb.nist.gov/introx.asp)	181
4.26	Example central unit cell with a 5x5 grid of sampling points (sampling resolution = 5/side).	182
4.27	The effect of increasing sampling resolution on the value of the average number of Au-Ti site pairs for a range of interaction ranges (0.1-15 nm, top). For all interaction ranges tested, the average number of Au-Ti sites per nanoparticle converged to within 5% of the value at a sampling resolution of 300 by a sampling resolution of 100.	183
4.28	Average number of proximal Ti per Au nanoparticle for Si/Ti of 73 (green circles), 96 (blue triangles), 100 (orange squares), and 126 (grey diamonds), for Au nanoparticles of diameters 0.5-20 nm.	184
4.29	Effect of increasing the interaction range for Au and Ti sites on the catalytic turnover frequency required to explain catalytic rates measured on a series of catalysts including 0.06Au-DP/TS-1(100), 0.12Au-DP/TS-1(100), 0.20Au-DP/TS-1(100), 0.24Au-DP/TS-1(100), 0.40Au-DP/TS-1(100) 0.083Au-PVP/TS-1(126), and 0.11Au-PVP/TS-1(73).	185

4.30	(Top left) Plot of PO rate normalized to gold mass vs. the molar proximal Ti per Au ratio. The average turnover frequency required for this model is shown in the top right corner of the plot. (Top right) Residual error plot for the top left plot. (Bottom) Lag plot for the residual error plot. These plots contain data for the Au-PVP/TS-1 catalysts from this work (0.083Au-PVP/TS-1(126) (black triangles) and 0.11Au-PVP/TS-1(73) (orange diamond)) as well as Au-DP/TS-1(100) (red circles) catalysts from [39].	186
4.31	(Top left) Model fit for the proximal Ti model to propylene epoxidation rate data as a function of average gold nanoparticle diameter. (Top right) Residual error plot for the model fit. (Bottom) Lag plot for the residual error plot. These plots contain data for the Au-PVP/TS-1 catalysts from this work (0.083Au-PVP/TS-1(126) (black triangles) and 0.11Au-PVP/TS-1(73) (orange diamond)) as well as Au-DP/TS-1(100) (red circles) catalysts from [39].	187
4.32	(Top left) Plot of PO rate normalized to gold mass vs. corner atom fraction. The average turnover frequency required for this model is shown in the top right corner of the plot. (Top right) Residual error plot for the top left plot. (Bottom) Lag plot for the residual error plot. These plots contain data for the Au-PVP/TS-1 catalysts from this work (0.083Au-PVP/TS-1(126) (black triangles) and 0.11Au-PVP/TS-1(73) (orange diamond)) as well as Au-DP/TS-1(100) (red circles) catalysts from [39].	188
4.33	(Top left) Model fit for the corner model to propylene epoxidation rate data as a function of average gold nanoparticle diameter. (Top right) Residual error plot for the model fit. (Bottom) Lag plot for the residual error plot. These plots contain data for the Au-PVP/TS-1 catalysts from this work (0.083Au-PVP/TS-1(126) (black triangles) and 0.11Au-PVP/TS-1(73) (orange diamond)) as well as Au-DP/TS-1(100) (red circles) catalysts from [39].	189
4.34	(Top left) Plot of PO rate normalized to gold mass vs. edge atom fraction. The average turnover frequency required for this model is shown in the top right corner of the plot. (Top right) Residual error plot for the top left plot. (Bottom) Lag plot for the residual error plot. These plots contain data for the Au-PVP/TS-1 catalysts from this work (0.083Au-PVP/TS-1(126) (black triangles) and 0.11Au-PVP/TS-1(73) (orange diamond)) as well as Au-DP/TS-1(100) (red circles) catalysts from [39].	190
4.35	(Top left) Model fit for the edge model to propylene epoxidation rate data as a function of average gold nanoparticle diameter. (Top right) Residual error plot for the model fit. (Bottom) Lag plot for the residual error plot. These plots contain data for the Au-PVP/TS-1 catalysts from this work (0.083Au-PVP/TS-1(126) (black triangles) and 0.11Au-PVP/TS-1(73) (orange diamond)) as well as Au-DP/TS-1(100) (red circles) catalysts from [39].	191

4.36	(Top left) Plot of PO rate normalized to gold mass vs. perimeter atom fraction. The average turnover frequency required for this model is shown in the top right corner of the plot. (Top right) Residual error plot for the top left plot. (Bottom) Lag plot for the residual error plot. These plots contain data for the Au-PVP/TS-1 catalysts from this work (0.083Au-PVP/TS-1(126) (black triangles) and 0.11Au-PVP/TS-1(73) (orange diamond)) as well as Au-DP/TS-1(100) (red circles) catalysts from [39].	192
4.37	(Top left) Model fit for the perimeter model to propylene epoxidation rate data as a function of average gold nanoparticle diameter. (Top right) Residual error plot for the model fit. (Bottom) Lag plot for the residual error plot. These plots contain data for the Au-PVP/TS-1 catalysts from this work (0.083Au-PVP/TS-1(126) (black triangles) and 0.11Au-PVP/TS-1(73) (orange diamond)) as well as Au-DP/TS-1(100) (red circles) catalysts from [39].	193
4.38	(Top left) Plot of PO rate normalized to gold mass vs. terrace atom fraction. The average turnover frequency required for this model is shown in the top right corner of the plot. (Top right) Residual error plot for the top left plot. (Bottom) Lag plot for the residual error plot. These plots contain data for the Au-PVP/TS-1 catalysts from this work (0.083Au-PVP/TS-1(126) (black triangles) and 0.11Au-PVP/TS-1(73) (orange diamond)) as well as Au-DP/TS-1(100) (red circles) catalysts from [39].	194
4.39	(Top left) Model fit for the terrace model to propylene epoxidation rate data as a function of average gold nanoparticle diameter. (Top right) Residual error plot for the model fit. (Bottom) Lag plot for the residual error plot. These plots contain data for the Au-PVP/TS-1 catalysts from this work (0.083Au-PVP/TS-1(126) (black triangles) and 0.11Au-PVP/TS-1(73) (orange diamond)) as well as Au-DP/TS-1(100) (red circles) catalysts from [39].	195
4.40	(Top left) Plot of PO rate normalized to gold mass vs. surface atom fraction. The average turnover frequency required for this model is shown in the top right corner of the plot. (Top right) Residual error plot for the top left plot. (Bottom) Lag plot for the residual error plot. These plots contain data for the Au-PVP/TS-1 catalysts from this work (0.083Au-PVP/TS-1(126) (black triangles) and 0.11Au-PVP/TS-1(73) (orange diamond)) as well as Au-DP/TS-1(100) (red circles) catalysts from [39].	196
4.41	(Top left) Model fit for the surface model to propylene epoxidation rate data as a function of average gold nanoparticle diameter. (Top right) Residual error plot for the model fit. (Bottom) Lag plot for the residual error plot. These plots contain data for the Au-PVP/TS-1 catalysts from this work (0.083Au-PVP/TS-1(126) (black triangles) and 0.11Au-PVP/TS-1(73) (orange diamond)) as well as Au-DP/TS-1(100) (red circles) catalysts from [39].	197

4.42	(Top left) Plot of PO rate normalized to gold mass vs. CN<8 atom fraction for a spherical nanoparticle model [41]. The average turnover frequency required for this model is shown in the top right corner of the plot. (Top right) Residual error plot for the top left plot. (Bottom) Lag plot for the residual error plot. These plots contain data for the Au-PVP/TS-1 catalysts from this work (0.083Au-PVP/TS-1(126) (black triangles) and 0.11Au-PVP/TS-1(73) (orange diamond)) as well as Au-DP/TS-1(100) (red circles) catalysts from [39].	198
4.43	(Top left) Model fit for CN<8 atoms from a spherical nanoparticle model [41] to propylene epoxidation rate data as a function of average gold nanoparticle diameter. (Top right) Residual error plot for the model fit. (Bottom) Lag plot for the residual error plot. These plots contain data for the Au-PVP/TS-1 catalysts from this work (0.083Au-PVP/TS-1(126) (black triangles) and 0.11Au-PVP/TS-1(73) (orange diamond)) as well as Au-DP/TS-1(100) (red circles) catalysts from [39].	199
4.44	(Top left) Plot of PO rate normalized to gold mass vs. CN=8 atom fraction for a spherical nanoparticle model [41]. The average turnover frequency required for this model is shown in the top right corner of the plot. (Top right) Residual error plot for the top left plot. (Bottom) Lag plot for the residual error plot. These plots contain data for the Au-PVP/TS-1 catalysts from this work (0.083Au-PVP/TS-1(126) (black triangles) and 0.11Au-PVP/TS-1(73) (orange diamond)) as well as Au-DP/TS-1(100) (red circles) catalysts from [39].	200
4.45	(Top left) Model fit for CN=8 atoms from a spherical nanoparticle model [41] to propylene epoxidation rate data as a function of average gold nanoparticle diameter. (Top right) Residual error plot for the model fit. (Bottom) Lag plot for the residual error plot. These plots contain data for the Au-PVP/TS-1 catalysts from this work (0.083Au-PVP/TS-1(126) (black triangles) and 0.11Au-PVP/TS-1(73) (orange diamond)) as well as Au-DP/TS-1(100) (red circles) catalysts from [39].	201
4.46	(Top left) Plot of PO rate normalized to gold mass vs. CN=9 atom fraction for a spherical nanoparticle model [41]. The average turnover frequency required for this model is shown in the top right corner of the plot. (Top right) Residual error plot for the top left plot. (Bottom) Lag plot for the residual error plot. These plots contain data for the Au-PVP/TS-1 catalysts from this work (0.083Au-PVP/TS-1(126) (black triangles) and 0.11Au-PVP/TS-1(73) (orange diamond)) as well as Au-DP/TS-1(100) (red circles) catalysts from [39].	202
4.47	(Top left) Model fit for CN=9 atoms from a spherical nanoparticle model [41] to propylene epoxidation rate data as a function of average gold nanoparticle diameter. (Top right) Residual error plot for the model fit. (Bottom) Lag plot for the residual error plot. These plots contain data for the Au-PVP/TS-1 catalysts from this work (0.083Au-PVP/TS-1(126) (black triangles) and 0.11Au-PVP/TS-1(73) (orange diamond)) as well as Au-DP/TS-1(100) (red circles) catalysts from [39].	203

4.48	(Top left) Plot of PO rate normalized to gold mass vs. CN>9 atom fraction for a spherical nanoparticle model [41]. The average turnover frequency required for this model is shown in the top right corner of the plot. (Top right) Residual error plot for the top left plot. (Bottom) Lag plot for the residual error plot. These plots contain data for the Au-PVP/TS-1 catalysts from this work (0.083Au-PVP/TS-1(126) (black triangles) and 0.11Au-PVP/TS-1(73) (orange diamond)) as well as Au-DP/TS-1(100) (red circles) catalysts from [39].	204
4.49	(Top left) Model fit for CN>9 atoms from a spherical nanoparticle model [41] to propylene epoxidation rate data as a function of average gold nanoparticle diameter. (Top right) Residual error plot for the model fit. (Bottom) Lag plot for the residual error plot. These plots contain data for the Au-PVP/TS-1 catalysts from this work (0.083Au-PVP/TS-1(126) (black triangles) and 0.11Au-PVP/TS-1(73) (orange diamond)) as well as Au-DP/TS-1(100) (red circles) catalysts from [39].	205
4.50	(Top left) Plot of hydrogen oxidation rate normalized to gold mass vs. molar proximal Ti to Au ratio. The average turnover frequency required for this model is shown in the top right corner of the plot. (Top right) Residual error plot for the top left plot. (Bottom) Lag plot for the residual error plot. These plots contain data for the Au-PVP/TS-1 catalysts from this work (0.083Au-PVP/TS-1(126) (black triangles) and 0.11Au-PVP/TS-1(73) (orange diamond)) as well as Au-DP/TS-1(100) (red circles) catalysts from [39].	206
4.51	(Top left) Model fit for the proximal Ti model to hydrogen oxidation rate data as a function of average gold nanoparticle diameter. (Top right) Residual error plot for the model fit. (Bottom) Lag plot for the residual error plot. These plots contain data for the Au-PVP/TS-1 catalysts from this work (0.083Au-PVP/TS-1(126) (black triangles) and 0.11Au-PVP/TS-1(73) (orange diamond)) as well as Au-DP/TS-1(100) (red circles) catalysts from [39].	207
4.52	(Top left) Plot of hydrogen oxidation rate normalized to gold mass vs. corner atom fraction. The average turnover frequency required for this model is shown in the top right corner of the plot. (Top right) Residual error plot for the top left plot. (Bottom) Lag plot for the residual error plot. These plots contain data for the Au-PVP/TS-1 catalysts from this work (0.083Au-PVP/TS-1(126) (black triangles) and 0.11Au-PVP/TS-1(73) (orange diamond)) as well as Au-DP/TS-1(100) (red circles) catalysts from [39].	208
4.53	(Top left) Model fit for the corner model to hydrogen oxidation rate data as a function of average gold nanoparticle diameter. (Top right) Residual error plot for the model fit. (Bottom) Lag plot for the residual error plot. These plots contain data for the Au-PVP/TS-1 catalysts from this work (0.083Au-PVP/TS-1(126) (black triangles) and 0.11Au-PVP/TS-1(73) (orange diamond)) as well as Au-DP/TS-1(100) (red circles) catalysts from [39].	209

4.54	(Top left) Plot of hydrogen oxidation rate normalized to gold mass vs. edge atom fraction. The average turnover frequency required for this model is shown in the top right corner of the plot. (Top right) Residual error plot for the top left plot. (Bottom) Lag plot for the residual error plot. These plots contain data for the Au-PVP/TS-1 catalysts from this work (0.083Au-PVP/TS-1(126) (black triangles) and 0.11Au-PVP/TS-1(73) (orange diamond)) as well as Au-DP/TS-1(100) (red circles) catalysts from [39].	210
4.55	(Top left) Model fit for the edge model to hydrogen oxidation rate data as a function of average gold nanoparticle diameter. (Top right) Residual error plot for the model fit. (Bottom) Lag plot for the residual error plot. These plots contain data for the Au-PVP/TS-1 catalysts from this work (0.083Au-PVP/TS-1(126) (black triangles) and 0.11Au-PVP/TS-1(73) (orange diamond)) as well as Au-DP/TS-1(100) (red circles) catalysts from [39].	211
4.56	(Top left) Plot of hydrogen oxidation rate normalized to gold mass vs. perimeter atom fraction. The average turnover frequency required for this model is shown in the top right corner of the plot. (Top right) Residual error plot for the top left plot. (Bottom) Lag plot for the residual error plot. These plots contain data for the Au-PVP/TS-1 catalysts from this work (0.083Au-PVP/TS-1(126) (black triangles) and 0.11Au-PVP/TS-1(73) (orange diamond)) as well as Au-DP/TS-1(100) (red circles) catalysts from [39].	212
4.57	(Top left) Model fit for the perimeter model to hydrogen oxidation rate data as a function of average gold nanoparticle diameter. (Top right) Residual error plot for the model fit. (Bottom) Lag plot for the residual error plot. These plots contain data for the Au-PVP/TS-1 catalysts from this work (0.083Au-PVP/TS-1(126) (black triangles) and 0.11Au-PVP/TS-1(73) (orange diamond)) as well as Au-DP/TS-1(100) (red circles) catalysts from [39].	213
4.58	(Top left) Plot of hydrogen oxidation rate normalized to gold mass vs. terrace atom fraction. The average turnover frequency required for this model is shown in the top right corner of the plot. (Top right) Residual error plot for the top left plot. (Bottom) Lag plot for the residual error plot. These plots contain data for the Au-PVP/TS-1 catalysts from this work (0.083Au-PVP/TS-1(126) (black triangles) and 0.11Au-PVP/TS-1(73) (orange diamond)) as well as Au-DP/TS-1(100) (red circles) catalysts from [39].	214
4.59	(Top left) Model fit for the terrace model to hydrogen oxidation rate data as a function of average gold nanoparticle diameter. (Top right) Residual error plot for the model fit. (Bottom) Lag plot for the residual error plot. These plots contain data for the Au-PVP/TS-1 catalysts from this work (0.083Au-PVP/TS-1(126) (black triangles) and 0.11Au-PVP/TS-1(73) (orange diamond)) as well as Au-DP/TS-1(100) (red circles) catalysts from [39].	215

4.60	(Top left) Plot of hydrogen oxidation rate normalized to gold mass vs. surface atom fraction. The average turnover frequency required for this model is shown in the top right corner of the plot. (Top right) Residual error plot for the top left plot. (Bottom) Lag plot for the residual error plot. These plots contain data for the Au-PVP/TS-1 catalysts from this work (0.083Au-PVP/TS-1(126) (black triangles) and 0.11Au-PVP/TS-1(73) (orange diamond)) as well as Au-DP/TS-1(100) (red circles) catalysts from [39].	216
4.61	(Top left) Model fit for the surface model to hydrogen oxidation rate data as a function of average gold nanoparticle diameter. (Top right) Residual error plot for the model fit. (Bottom) Lag plot for the residual error plot. These plots contain data for the Au-PVP/TS-1 catalysts from this work (0.083Au-PVP/TS-1(126) (black triangles) and 0.11Au-PVP/TS-1(73) (orange diamond)) as well as Au-DP/TS-1(100) (red circles) catalysts from [39].	217
4.62	(Top left) Plot of hydrogen oxidation rate normalized to gold mass vs. CN<8 atom fraction for a spherical nanoparticle model [41]. The average turnover frequency required for this model is shown in the top right corner of the plot. (Top right) Residual error plot for the top left plot. (Bottom) Lag plot for the residual error plot. These plots contain data for the Au-PVP/TS-1 catalysts from this work (0.083Au-PVP/TS-1(126) (black triangles) and 0.11Au-PVP/TS-1(73) (orange diamond)) as well as Au-DP/TS-1(100) (red circles) catalysts from [39].	218
4.63	(Top left) Model fit for CN<8 atoms from a spherical nanoparticle model [41] to hydrogen oxidation rate data as a function of average gold nanoparticle diameter. (Top right) Residual error plot for the model fit. (Bottom) Lag plot for the residual error plot. These plots contain data for the Au-PVP/TS-1 catalysts from this work (0.083Au-PVP/TS-1(126) (black triangles) and 0.11Au-PVP/TS-1(73) (orange diamond)) as well as Au-DP/TS-1(100) (red circles) catalysts from [39].	219
4.64	(Top left) Plot of hydrogen oxidation rate normalized to gold mass vs. CN=8 atom fraction for a spherical nanoparticle model [41]. The average turnover frequency required for this model is shown in the top right corner of the plot. (Top right) Residual error plot for the top left plot. (Bottom) Lag plot for the residual error plot. These plots contain data for the Au-PVP/TS-1 catalysts from this work (0.083Au-PVP/TS-1(126) (black triangles) and 0.11Au-PVP/TS-1(73) (orange diamond)) as well as Au-DP/TS-1(100) (red circles) catalysts from [39].	220
4.65	(Top left) Model fit for CN=8 atoms from a spherical nanoparticle model [41] to hydrogen oxidation rate data as a function of average gold nanoparticle diameter. (Top right) Residual error plot for the model fit. (Bottom) Lag plot for the residual error plot. These plots contain data for the Au-PVP/TS-1 catalysts from this work (0.083Au-PVP/TS-1(126) (black triangles) and 0.11Au-PVP/TS-1(73) (orange diamond)) as well as Au-DP/TS-1(100) (red circles) catalysts from [39].	221

- 4.66 (Top left) Plot of hydrogen oxidation rate normalized to gold mass vs. CN=9 atom fraction for a spherical nanoparticle model [41]. The average turnover frequency required for this model is shown in the top right corner of the plot. (Top right) Residual error plot for the top left plot. (Bottom) Lag plot for the residual error plot. These plots contain data for the Au-PVP/TS-1 catalysts from this work (0.083Au-PVP/TS-1(126) (black triangles) and 0.11Au-PVP/TS-1(73) (orange diamond)) as well as Au-DP/TS-1(100) (red circles) catalysts from [39]. 222
- 4.67 (Top left) Model fit for CN=9 atoms from a spherical nanoparticle model [41] to hydrogen oxidation rate data as a function of average gold nanoparticle diameter. (Top right) Residual error plot for the model fit. (Bottom) Lag plot for the residual error plot. These plots contain data for the Au-PVP/TS-1 catalysts from this work (0.083Au-PVP/TS-1(126) (black triangles) and 0.11Au-PVP/TS-1(73) (orange diamond)) as well as Au-DP/TS-1(100) (red circles) catalysts from [39]. 223
- 4.68 (Top left) Plot of hydrogen oxidation rate normalized to gold mass vs. CN>9 atom fraction for a spherical nanoparticle model [41]. The average turnover frequency required for this model is shown in the top right corner of the plot. (Top right) Residual error plot for the top left plot. (Bottom) Lag plot for the residual error plot. These plots contain data for the Au-PVP/TS-1 catalysts from this work (0.083Au-PVP/TS-1(126) (black triangles) and 0.11Au-PVP/TS-1(73) (orange diamond)) as well as Au-DP/TS-1(100) (red circles) catalysts from [39]. 224
- 4.69 (Top left) Model fit for CN>9 atoms from a spherical nanoparticle model [41] to hydrogen oxidation rate data as a function of average gold nanoparticle diameter. (Top right) Residual error plot for the model fit. (Bottom) Lag plot for the residual error plot. These plots contain data for the Au-PVP/TS-1 catalysts from this work (0.083Au-PVP/TS-1(126) (black triangles) and 0.11Au-PVP/TS-1(73) (orange diamond)) as well as Au-DP/TS-1(100) (red circles) catalysts from [39]. 225

ABSTRACT

Propylene oxide (PO), is a key intermediate in the production of value-added products, such as polyurethanes and propylene glycol. Current industrially practiced methods of propylene epoxidation, including hydrochlorination, epoxidation by organic peroxides, and the Hydrogen Peroxide to Propylene Oxide (HPPO) process either produce PO unselectively, necessitating energy intensive separation processes, produce environmentally damaging byproducts, or require several sequential reaction vessels. A potential solution for these issues exists in the form of a single-step, highly selective gas phase reaction to produce PO. Industrial adoption of a process utilizing this technology has not occurred due to the failure of state-of-the-art Au/TS-1 catalysts, consisting of gold supported on titanium MFI, to meet economic targets for hydrogen use efficiency, selectivity to PO, and PO rate-per-mass, improvement on all of which has been hindered by a lack of understanding of how Au-TS-1 catalysts fundamentally operate. Therefore, the goal of this work has been to understand the active site requirements and reaction kinetics with the aim of lowering barriers to commercialization of this more environmentally benign process.

Once we had developed a general understanding of product inhibition, we applied this knowledge to the kinetics of propylene epoxidation over Au/TS-1 catalysts. We measured gas phase kinetics in a continuous stirred tank reactor (CSTR) free from temperature and concentration gradients. Apparent reaction orders measured at 473 K for H_2 , O_2 , and propylene for a series of Au-DP/TS-1 with varied Au and Ti contents were consistent with those reported previously. Co-feeding propylene oxide enabled measurement of the apparent reaction order in propylene oxide and the determination that relevant pressures of propylene oxide reversibly inhibit propylene epoxidation over Au-DP/TS-1, while co-feeding carbon dioxide and water had no effect on the propylene epoxidation rate. The measured reaction orders for propylene epoxidation, after corrected to account for propylene oxide inhibition, are consistent with a ‘simultaneous’ mechanism requiring two distinct, but adjacent, types of sites. H_2 oxidation rates are not inhibited by propylene oxide, implying that the sites required for hydrogen oxidation are distinct from those required for propylene epoxidation.

We then shifted focus to elucidate structural details of gold active sites and their interaction with Ti active sites. To determine whether the roles of extracrystalline and intracrystalline gold nanoparticles supported on titanasilicate-1 on direct propylene epoxidation are intrinsically different, the kinetics of direct propylene epoxidation were measured in a gas-phase continuous stirred tank reactor (CSTR) over PVP-coated gold nanoparticles (Au-PVP/TS-1) deposited on TS-1 supports. The PVP-coated gold nanoparticles were too large to fit into the micropores of TS-1, even after ligands were removed in situ by a series of pretreatments, as confirmed by both TEM and TGA-DSC. The activation energy and reaction orders for H_2 , O_2 , propylene, propylene oxide, carbon dioxide, and water for propylene epoxidation measured on Au-PVP/TS-1 catalysts were consistent with those reported for Au/TS-1 prepared via deposition-precipitation (Au-DP/TS-1). However, while the reaction orders for hydrogen oxidation on Au-PVP/TS-1 were similar to those measured on Au-DP/TS-1, a decrease in activation energy from approximately 30 kJ mol^{-1} for Au-DP/TS-1 to $4\text{-}5 \text{ kJ mol}^{-1}$ for Au-PVP/TS-1 suggests there is a change in mechanism, rate-limiting step, and/or active site for hydrogen oxidation. Additionally, an active site model was developed which determines the number of Ti within an interaction range of the perimeter of extracrystalline Au nanoparticles (i.e., the number of Au-Ti active site pairs). Turnover frequencies estimated for this active site model for a dataset containing both Au-DP/TS-1 and Au-PVP/TS-1 were $\sim 20\times$ higher than any previous report (80 s^{-1} vs. $1\text{-}5 \text{ s}^{-1}$ at 473 K) for catalytic oxidation on noble metals, suggesting that the simultaneous mechanism occurring over proximal Au-Ti sites alone is incapable of explaining the observed rate of propylene epoxidation and that short-range migration of hydrogen peroxide is necessary to account for the catalytic rate. The agreement of reaction orders, activation energy, and active site model for propylene epoxidation on both Au-DP/TS-1 and Au-PVP/TS-1 suggests a common mechanism for propylene epoxidation on both catalysts containing small intraporous gold clusters and catalysts with exclusively larger extracrystalline nanoparticles. Rates of hydrogen oxidation were found to vary proportionally to the amount of surface gold atoms. This is also consistent with the hypothesis that the observed decrease in hydrogen efficiency and PO site-time-yield per gold mass with increasing gold loading are driven primarily by the gold dispersion in Au/TS-1 catalysts.

1. INTRODUCTION

Propylene oxide (PO) is an important chemical intermediate used in industrial polyurethane production, as well as industrial and consumer products such as adhesives, solvents, and structural components [source 1 from PVP paper]. With worldwide demand for PO increasing, reaching an estimated 8.6 million tons in 2010 [1], the drawbacks of current industrial processes, such as hydrogen peroxide to propylene oxide (HPPO), epoxidation by organic peroxides, or hydrochlorination, are becoming magnified [2], [3]. These drawbacks, specifically the generation of environmentally harmful byproducts, low selectivity to PO, or the requirement for liquid-liquid separations [2], [3], can be circumvented by the creation of a new process consisting of the gas-phase, single-step epoxidation of propylene by co-feeding propylene, hydrogen, and oxygen over a gold/titanium catalyst, as was first reported by Haruta in the late 1990s [4]. While this process holds potential for the next generation of epoxidation catalysis, development has lagged due to low PO selectivity, hydrogen efficiency, stability on stream, and site-time yield (STY).

After the initial discovery of gold/titanium catalysts for partial oxidations, much effort was put into determining the optimal makeup of these catalysts. After initial interest in Au/TiO₂ catalysts, which suffered from rapid deactivation, focus was placed on catalysts limiting Ti to isolated, tetrahedrally-coordinated species [5]–[9] incorporated into silicious supports, such as the titanium zeotype titanosilicate-1 (TS-1). These efforts have resulted in dramatic increases in catalytic epoxidation rates, from approximately 11 g_{PO} kg_{cat}⁻¹ h⁻¹ on Au/TiO₂ [10] to approximately 150 g_{PO} kg_{cat}⁻¹ h⁻¹ on Au/TS-1 [11], as well as improved stability under reaction conditions. Studies focusing on the effects of various promoters [12]–[18] were carried out, with Au/TS-1 catalysts eventually reaching steady state formation rates of approximately 300 g_{PO} kg_{cat}⁻¹ h⁻¹ with a selectivity to PO of approximately 80% [12]. Efforts to find an 'optimal' gold nanoparticle size were carried out, however no optimal size was determined [19]–[25] beyond the general observation that increasing the gold loading of Au/TS-1 catalysts resulted in a decrease in selectivity to PO, hydrogen efficiency, and PO rate normalized to gold mass [11].

Understanding this observation by learning more about the intrinsic kinetics of propylene epoxidation and structural details of the gold active sites is a goal of this work. The first chapter sets the foundation for a later kinetic analysis of propylene epoxidation by discussing the technique for correctly measuring the intrinsic kinetic parameters of a catalytic reaction in systems where inhibition due to a product is significant, meaning that differential kinetic behavior is not guaranteed by maintaining reactant conversions of less than 10%. In the second chapter, this technique is applied to propylene epoxidation on Au/TS-1 catalysts, where an example discrimination between two of the proposed mechanisms for propylene epoxidation on Au/TS-1 is demonstrated and the physical separation of active sites for propylene epoxidation and hydrogen oxidation is suggested by the data. In the third chapter, the second chapter's kinetic analysis is used in conjunction with a variety of active site models for gold nanoparticles to gain information about the catalytic roles of gold nanoparticles, how they change with nanoparticle size, and what active site models for propylene epoxidation gold active sites are reasonable.

Chapter 1 has been reprinted from (James W. Harris, Anuj A. Verma, Jeremy W. Arvay, Arthur J. Shih, W. Nicholas Delgass, and Fabio H. Ribeiro, "Consequences of product inhibition in the quantification of kinetic parameters", *Journal of Catalysis* 389 (2020) 468-475) Copyright (2020) Elsevier.

Chapter 2 has been reprinted from (James. W. Harris, Jeremy Arvay, Garrett Mitchell, W. Nicholas Delgass, and Fabio H. Ribeiro, "Propylene oxide inhibits propylene epoxidation over Au/TS-1", *Journal of Catalysis* 365 (2018) 105-114) Copyright (2018) Elsevier.

References

- [1] H. Baer, M. Bergamo, A. Forlin, L. H. Pottenger, and J. Lindner, "Propylene oxide," in *Ullmann's Encyclopedia of Industrial Chemistry*, John Wiley & Sons, Ltd, 2012, ISBN: 978-3-527-30673-2. DOI: [10.1002/14356007.a22_239.pub3](https://doi.org/10.1002/14356007.a22_239.pub3). [Online]. Available: https://onlinelibrary.wiley.com/doi/abs/10.1002/14356007.a22_239.pub3.
- [2] T. A. Nijhuis, M. Makkee, J. A. Moulijn, and B. M. Weckhuysen, "The production of propene oxide: catalytic processes and recent developments," *Ind. Eng. Chem. Res.*, vol. 45, no. 10, pp. 3447–3459, May 1, 2006, ISSN: 0888-5885. DOI: [10.1021/ie0513090](https://doi.org/10.1021/ie0513090). [Online]. Available: <http://dx.doi.org/10.1021/ie0513090>.
- [3] J. Lu, X. Zhang, J. J. Bravo-Suárez, T. Fujitani, and S. T. Oyama, "Effect of composition and promoters in au/TS-1 catalysts for direct propylene epoxidation using h₂ and o₂," *Catalysis Today*, Special Issue dedicated to Marc Jacques Ledoux on the occasion of his 60th birthday, vol. 147, no. 3, pp. 186–195, Oct. 15, 2009, ISSN: 0920-5861. DOI: [10.1016/j.cattod.2008.09.005](https://doi.org/10.1016/j.cattod.2008.09.005). [Online]. Available: <http://www.sciencedirect.com/science/article/pii/S0920586108004239>.
- [4] M. Haruta, B. S. Uphade, S. Tsubota, and A. Miyamoto, "Selective oxidation of propylene over gold deposited on titanium-based oxides," *Res. Chem. Intermed.*, vol. 24, no. 3, pp. 329–336, Mar. 1, 1998, ISSN: 0922-6168, 1568-5675. DOI: [10.1163/156856798X00276](https://doi.org/10.1163/156856798X00276). [Online]. Available: <https://link.springer.com/article/10.1163/156856798X00276>.
- [5] J. J. Bravo-Suárez, Lu, C. G. Dallos, T. Fujitani, and S. T. Oyama, "Kinetic study of propylene epoxidation with h₂ and o₂ over a gold/mesoporous titanasilicate catalyst," *J. Phys. Chem. C*, vol. 111, no. 46, pp. 17 427–17 436, Nov. 1, 2007, ISSN: 1932-7447. DOI: [10.1021/jp075098j](https://doi.org/10.1021/jp075098j). [Online]. Available: <http://dx.doi.org/10.1021/jp075098j>.
- [6] A. K. Sinha, S. Seelan, M. Okumura, T. Akita, S. Tsubota, and M. Haruta, "Three-dimensional mesoporous titanasilicates prepared by modified sol–gel method: ideal gold catalyst supports for enhanced propene epoxidation," *J. Phys. Chem. B*, vol. 109, no. 9, pp. 3956–3965, Mar. 1, 2005, ISSN: 1520-6106. DOI: [10.1021/jp0465229](https://doi.org/10.1021/jp0465229). [Online]. Available: <http://dx.doi.org/10.1021/jp0465229>.
- [7] B. S. Uphade, T. Akita, T. Nakamura, and M. Haruta, "Vapor-phase epoxidation of propene using h₂ and o₂ over au/ti-MCM-48," *Journal of Catalysis*, vol. 209, no. 2, pp. 331–340, Jul. 25, 2002, ISSN: 0021-9517. DOI: [10.1006/jcat.2002.3642](https://doi.org/10.1006/jcat.2002.3642). [Online]. Available: <http://www.sciencedirect.com/science/article/pii/S0021951702936420>.
- [8] B. S. Uphade, Y. Yamada, T. Akita, T. Nakamura, and M. Haruta, "Synthesis and characterization of ti-MCM-41 and vapor-phase epoxidation of propylene using h₂ and o₂ over au/ti-MCM-41," *Applied Catalysis A: General*, vol. 215, no. 1, pp. 137–148, Jul. 13, 2001, ISSN: 0926-860X. DOI: [10.1016/S0926-860X\(01\)00527-0](https://doi.org/10.1016/S0926-860X(01)00527-0). [Online]. Available: <http://www.sciencedirect.com/science/article/pii/S0926860X01005270>.

- [9] J. Lu, X. Zhang, J. J. Bravo-Suárez, K. K. Bando, T. Fujitani, and S. T. Oyama, “Direct propylene epoxidation over barium-promoted au/ti-TUD catalysts with h₂ and o₂: Effect of au particle size,” *Journal of Catalysis*, vol. 250, no. 2, pp. 350–359, Sep. 10, 2007, ISSN: 0021-9517. DOI: [10.1016/j.jcat.2007.06.006](https://doi.org/10.1016/j.jcat.2007.06.006). [Online]. Available: <http://www.sciencedirect.com/science/article/pii/S0021951707002345>.
- [10] T. Hayashi, K. Tanaka, and M. Haruta, “Selective vapor-phase epoxidation of propylene over au/TiO₂ catalysts in the presence of oxygen and hydrogen,” *Journal of Catalysis*, vol. 178, no. 2, pp. 566–575, Sep. 10, 1998, ISSN: 0021-9517. DOI: [10.1006/jcat.1998.2157](https://doi.org/10.1006/jcat.1998.2157). [Online]. Available: <http://www.sciencedirect.com/science/article/pii/S0021951798921571>.
- [11] W.-S. Lee, M. Cem Akatay, E. A. Stach, F. H. Ribeiro, and W. Nicholas Delgass, “Reproducible preparation of au/TS-1 with high reaction rate for gas phase epoxidation of propylene,” *Journal of Catalysis*, vol. 287, pp. 178–189, Mar. 2012, ISSN: 0021-9517. DOI: [10.1016/j.jcat.2011.12.019](https://doi.org/10.1016/j.jcat.2011.12.019). [Online]. Available: <http://www.sciencedirect.com/science/article/pii/S0021951711004222>.
- [12] W.-S. Lee, M. Cem Akatay, E. A. Stach, F. H. Ribeiro, and W. Nicholas Delgass, “Enhanced reaction rate for gas-phase epoxidation of propylene using h₂ and o₂ by cs promotion of au/TS-1,” *Journal of Catalysis*, 50th Anniversary Special Issue, vol. 308, pp. 98–113, Dec. 2013, ISSN: 0021-9517. DOI: [10.1016/j.jcat.2013.05.023](https://doi.org/10.1016/j.jcat.2013.05.023). [Online]. Available: <http://www.sciencedirect.com/science/article/pii/S0021951713001966>.
- [13] Z. Li, Y. Wang, J. Zhang, D. Wang, and W. Ma, “Better performance for gas-phase epoxidation of propylene using h₂ and o₂ at lower temperature over au/TS-1 catalyst,” *Catalysis Communications*, vol. 90, pp. 87–90, Feb. 2017, ISSN: 1566-7367. DOI: [10.1016/j.catcom.2016.12.002](https://doi.org/10.1016/j.catcom.2016.12.002). [Online]. Available: <http://www.sciencedirect.com/science/article/pii/S1566736716304484>.
- [14] Z. Song, X. Feng, Y. Liu, C. Yang, and X. Zhou, “Advances in manipulation of catalyst structure and relationship of structure-performance for direct propene epoxidation with h₂ and o₂,” *Progress in Chemistry*, vol. 28, no. 12, pp. 1762–1773, 2016. DOI: [10.7536/PC160803](https://doi.org/10.7536/PC160803).
- [15] J. Huang, T. Takei, T. Akita, H. Ohashi, and M. Haruta, “Gold clusters supported on alkaline treated TS-1 for highly efficient propene epoxidation with o₂ and h₂,” *Applied Catalysis B: Environmental*, vol. 95, no. 3, pp. 430–438, Apr. 6, 2010, ISSN: 0926-3373. DOI: [10.1016/j.apcatb.2010.01.023](https://doi.org/10.1016/j.apcatb.2010.01.023). [Online]. Available: <http://www.sciencedirect.com/science/article/pii/S0926337310000378>.
- [16] J. Huang, E. Lima, T. Akita, A. Guzmán, C. Qi, T. Takei, and M. Haruta, “Propene epoxidation with o₂ and h₂: Identification of the most active gold clusters,” *Journal of Catalysis*, vol. 278, no. 1, pp. 8–15, Feb. 14, 2011, ISSN: 0021-9517. DOI: [10.1016/j.jcat.2010.11.012](https://doi.org/10.1016/j.jcat.2010.11.012). [Online]. Available: <http://www.sciencedirect.com/science/article/pii/S0021951710003982>.

- [17] J. Lu, X. Zhang, J. J. Bravo-Suárez, T. Fujitani, and S. T. Oyama, “Effect of composition and promoters in au/TS-1 catalysts for direct propylene epoxidation using h₂ and o₂,” *Catalysis Today*, Special Issue dedicated to Marc Jacques Ledoux on the occasion of his 60th birthday, vol. 147, no. 3, pp. 186–195, Oct. 15, 2009, ISSN: 0920-5861. DOI: [10.1016/j.cattod.2008.09.005](https://doi.org/10.1016/j.cattod.2008.09.005). [Online]. Available: <http://www.sciencedirect.com/science/article/pii/S0920586108004239>.
- [18] T. Liu, P. Hacırlıoğlu, S. T. Oyama, M.-F. Luo, X.-R. Pan, and J.-Q. Lu, “Enhanced reactivity of direct propylene epoxidation with h₂ and o₂ over ge-modified au/TS-1 catalysts,” *Journal of Catalysis*, vol. 267, no. 2, pp. 202–206, Oct. 25, 2009, ISSN: 0021-9517. DOI: [10.1016/j.jcat.2009.08.002](https://doi.org/10.1016/j.jcat.2009.08.002). [Online]. Available: <http://www.sciencedirect.com/science/article/pii/S0021951709002577>.
- [19] T. Hayashi, K. Tanaka, and M. Haruta, “Selective vapor-phase epoxidation of propylene over au/TiO₂ catalysts in the presence of oxygen and hydrogen,” *Journal of Catalysis*, vol. 178, no. 2, pp. 566–575, Sep. 10, 1998, ISSN: 0021-9517. DOI: [10.1006/jcat.1998.2157](https://doi.org/10.1006/jcat.1998.2157). [Online]. Available: <http://www.sciencedirect.com/science/article/pii/S0021951798921571>.
- [20] C. Qi, J. Huang, S. Bao, H. Su, T. Akita, and M. Haruta, “Switching of reactions between hydrogenation and epoxidation of propene over au/ti-based oxides in the presence of h₂ and o₂,” *Journal of Catalysis*, vol. 281, no. 1, pp. 12–20, Jul. 1, 2011, ISSN: 0021-9517. DOI: [10.1016/j.jcat.2011.03.028](https://doi.org/10.1016/j.jcat.2011.03.028). [Online]. Available: <http://www.sciencedirect.com/science/article/pii/S0021951711001114>.
- [21] J. Huang, T. Takei, T. Akita, H. Ohashi, and M. Haruta, “Gold clusters supported on alkaline treated TS-1 for highly efficient propene epoxidation with o₂ and h₂,” *Applied Catalysis B: Environmental*, vol. 95, no. 3, pp. 430–438, Apr. 6, 2010, ISSN: 0926-3373. DOI: [10.1016/j.apcatb.2010.01.023](https://doi.org/10.1016/j.apcatb.2010.01.023). [Online]. Available: <http://www.sciencedirect.com/science/article/pii/S0926337310000378>.
- [22] W.-S. Lee, M. Cem Akatay, E. A. Stach, F. H. Ribeiro, and W. Nicholas Delgass, “Enhanced reaction rate for gas-phase epoxidation of propylene using h₂ and o₂ by cs promotion of au/TS-1,” *Journal of Catalysis*, 50th Anniversary Special Issue, vol. 308, pp. 98–113, Dec. 2013, ISSN: 0021-9517. DOI: [10.1016/j.jcat.2013.05.023](https://doi.org/10.1016/j.jcat.2013.05.023). [Online]. Available: <http://www.sciencedirect.com/science/article/pii/S0021951713001966>.
- [23] L. Barrio, P. Liu, J. A. Rodriguez, J. M. Campos-Martin, and J. L. G. Fierro, “Effects of hydrogen on the reactivity of o₂ toward gold nanoparticles and surfaces,” *J. Phys. Chem. C*, vol. 111, no. 51, pp. 19 001–19 008, Dec. 1, 2007, ISSN: 1932-7447. DOI: [10.1021/jp073552d](https://doi.org/10.1021/jp073552d). [Online]. Available: <https://doi.org/10.1021/jp073552d>.
- [24] S. M. Lang, T. M. Bernhardt, R. N. Barnett, B. Yoon, and U. Landman, “Hydrogen-promoted oxygen activation by free gold cluster cations,” *J. Am. Chem. Soc.*, vol. 131, no. 25, pp. 8939–8951, Jul. 1, 2009, ISSN: 0002-7863. DOI: [10.1021/ja9022368](https://doi.org/10.1021/ja9022368). [Online]. Available: <https://doi.org/10.1021/ja9022368>.
- [25] D. G. Barton and S. G. Podkolzin, “Kinetic study of a direct water synthesis over silica-supported gold nanoparticles,” *J. Phys. Chem. B*, vol. 109, no. 6, pp. 2262–2274, Feb. 1, 2005, ISSN: 1520-6106. DOI: [10.1021/jp048837u](https://doi.org/10.1021/jp048837u). [Online]. Available: <http://dx.doi.org/10.1021/jp048837u>.

2. CONSEQUENCES OF PRODUCT INHIBITION IN THE QUANTIFICATION OF KINETIC PARAMETERS

2.1 Introduction

Inhibition of the forward rate by products of the reaction is prevalent in heterogeneous catalysis. Examples include the combustion of methane on Pd [1], [2], hydro-dechlorination of chlorocarbons on Pd [3], [4], the water-gas shift on Pd [5], Pt [6], [7], and CuO/ZnO/Al₂O₃ [8], SO₂ oxidation on Pt [9], NO oxidation on Cu, Fe-zeolites [10], [11] and Pt [12], [13], NO decomposition on Cu-zeolites [14], epoxidation of ethylene to ethylene oxide on Ag/a-Al₂O₃ [15], epoxidation of propylene to propylene oxide on Au/TS-1 [16], cyclohexene epoxidation on Ti, Ta, and Nb containing molecular sieves of the Beta topology [17], ketonization of acetic acid on both Ru/TiO₂ [18] and on H-ZSM-5 [19], and dehydrogenation of methanol to methyl formate [20]. Failure to account for product inhibition in the planning and analysis of kinetic experiments can produce significant errors in calculated kinetic parameters. The source of these errors is demonstrated in the following qualitative argument. Consider a monomolecular transformation of reactant A to product B taking place in a wellmixed, continuous stirred tank reactor (CSTR) with pure A as the sole component of the inlet stream. A typical set of experiments would vary temperature at constant concentration and flow rate of A and vary the concentration of A ([A]) by diluting in inert gas at constant temperature. The slope of a plot of the natural log of the rate versus inverse temperature equals the negative apparent activation energy divided by the gas constant R, and the slope of a log-log plot of rate vs. concentration of A equals the apparent reaction order of A. We will assume that even though the conversion of A is below 10% for all data gathered, the rate is inverse order in B for all measurements, and that this fact is not known to the investigator. In the activation energy experiments, as the temperature is increased the conversion will increase, increasing the concentration of B ([B]). At higher [B] the rate will decrease, thus diminishing the increase in rate caused by higher temperature and leading to lower apparent activation energy. This was experimentally verified by Mulla et al. [12] and Hamzehlouyan et al. [9], who studied the effect of product inhibition on the kinetics of NO oxidation and SO₂ oxidation, respectively, over supported Pt clusters and recorded a lower value of the

apparent activation energy in the absence of product co-feeds. Similarly, increases in the concentration of A at constant temperature will yield more B, which will diminish the rate increase caused by A and lead to a lower than expected order in A. Most commonly, the errors above are generated by the assumption that product inhibition of the forward rate can always be ignored when operating under conditions which maintain differential conversion of the reactants. While it is true that there will always be a conversion below which product inhibition can be ignored, we will show in the discussion below that this value of the conversion is often too low for practical experiments and that no reactor type is immune from this problem. Using NO oxidation over copper-exchanged chabazite zeolites (Cu-SSZ-13) as an example, we show that co-feeding products with the reactant mixture avoids these potential errors. We then illustrate the quantitative consequences of ignoring product inhibition. We further generalize the analysis for any power law rate expression and show that the need for co-feeding products with the reactant mixture to avoid falsification of kinetic parameter measurements can be evaluated with conversion versus space time (or, in a batch reactor, elapsed time) data. The focus of this analysis is on measurement of initial rates of reaction at conversions that are intended to be low enough to minimize effects of products on the rates. The objective of the power law rate expressions obtained from such measurements is to provide guidance, through the values of the apparent orders of reaction and the apparent activation energy and entropy, to a Langmuir-Hinshelwood, Hougen-Watson rate expression representing a sequence of elementary reaction steps at the molecular level [21]. Analyses of complex reactions with kinetically important reversible steps also require data obtained with products in the feed but are beyond the scope of this paper. Detailed examples of such reactions can be found in Marin et al. [22]. We note, however, that if the reaction is irreversible and products do not undergo subsequent reactions, the analysis presented here would also apply to any incremental change in conversion with the inlet mixture representative of a specific reactant conversion. In what follows, we present a straightforward example of the issues that can arise when product inhibition is not accounted for, a simple experimental test to determine if product inhibition is occurring, and experimental strategies to accurately measure kinetic parameters in spite of inhibitory reaction products.

2.2 Experimental Methods

2.2.1 Catalyst preparation

The methods for catalyst synthesis and characterization have been provided in detail elsewhere [10], [23]. In brief, SSZ-13 was synthesized by following the recipe of Fickel and Lobo [24], [25]. The XRD pattern, N₂ adsorption isotherms, ²⁷Al magic-angle spinning NMR, and H⁺:Al ratios are reported by Bates et al. and confirm the zeolite structure and Al coordination [23]. Copper ions were deposited by a liquid phase ion exchange method by using copper nitrate as the Cu ion precursor. The catalyst used for kinetic studies reported in the main text of this manuscript had $28 \pm 5\%$ of the Cu present as Cu_xO_y species, as quantified under in-situ NO oxidation from separate X-ray absorption results, and the Cu:Al_{total} ratio was 0.35 as measured by AAS [10].

2.2.2 Catalyst characterization

Atomic absorption spectroscopy (AAS) was used to quantify bulk Si, Al, and Cu concentrations. Approximately 20 mg of sample were dissolved in 2 mL of HF (Mallenkrodt, 40 wt%) for >8 hours in a high-density-polyethylene (HDPE) bottle, then diluted with between 50 and 120 mL deionized water (Millipore, Synergy UV Water Purification System, 18.2 MΩcm resistivity at 298 K). Proper PPE, engineering controls, and emergency exposure precautions must be taken as HF is an extremely corrosive chemical and will directly attack calcium in human tissue. 1000 ppm standards for copper (Sigma Aldrich TraceCERT, 1000 mg/L Cu in nitric acid), silicon (Sigma Aldrich TraceCERT, 1000 mg/L Si in NaOH), aluminum (Sigma Aldrich TraceCERT, 1000 mg/L Al in nitric acid), and sodium (Sigma Aldrich TraceCERT, 1000 mg/L Na in nitric acid) were diluted to two to three concentrations within the linear calibration range in clean HDPE bottles for use as standards. Elemental analysis to measure the Cu wt%, Cu:Al, and Si:Al of the dissolved sample was performed using atomic absorption spectroscopy (AAS) on a Perkin-Elmer AAnalyst 300. A calibration (absorbance vs concentration) was generated at the beginning and end of each run to ensure that absorbances did not drift by more than 5% throughout the run. Each calibration and

sample bottle was shaken vigorously before collecting concentrations to eliminate possible concentration gradients due to gravimetric separation. The results of these elemental analyses are reported in Table 2.2 and determined that the catalysts reported in this study had Cu weight loadings of 0–18.93 wt% Cu, Cu:Al atomic ratios of 0–1.6, and Si:Al atomic ratios of 4.3–4.5.

Powder X-ray diffraction (XRD) data were collected on a Rigaku SmartLab diffractometer using a Cu K(α) radiation source operated at 1.76 kW. Two sample holders were used. For one, approximately 0.6 g of sample were loaded in a sample holder with a depth of 2 mm. The second, about 0.05 g of sample were loaded in a sample holder with a depth of 0.2 mm. Patterns were obtained from 4 to 40 2θ using a step size of $0.01^\circ 2\theta$ and scan rate $0.05^\circ 2\theta \text{ min}^{-1}$ at ambient conditions. XRD patterns were used to confirm the presence of peaks characteristic of the CHA framework. Representative XRD patterns are reported in Fig. 2.6.

Argon (87 K) adsorption isotherms were collected on a Micromeritics Accelerated Surface Area and Porosimetry (ASAP) 2020 system. Samples were first pelleted and sieved to retain particles between 180 and 250 μm in diameter, degassed by heating 0.03–0.05 g of sample to 393 K (0.167 K s^{-1}) under high vacuum ($<5 \mu\text{mHg}$) for 2 h, and then further heated to 623 K (0.167 K s^{-1}) under high vacuum ($<5 \mu\text{mHg}$) for 8 h. Extrapolation of the linear volumetric uptake during mesopore filling ($0.08\text{--}0.30 P/P_0$) to zero relative pressure gave an estimate for the volume of adsorbed gas in micropores ($\text{cm}^3 (\text{gcat})^{-1}$ at STP). An example Ar isotherm is reported in Fig. 2.7.

UV–Visible–NIR spectra of H- and Cu-zeolites were taken at ambient conditions (calcined beforehand in air at 823 K for 6 h and exposed to air at 298 K) with a Varian Cary 5000 UV–VIS–NIR spectrophotometer and Harrick-Scientific Praying-Mantis diffuse reflectance optics and cell. Barium sulfate (BaSO_4 , SigmaAldrich, 99%) was used for zero-absorbance background scans for background correction. UV–Visible–NIR spectra were collected with a scan speed of $2000 \text{ cm}^{-1} \text{ min}^{-1}$ from 4000 to 50000 cm^{-1} . Approximately 0.1 to 0.2 g of each sample were packed and flattened in a sample cup using a clean microscope slide followed by sealing of the *in situ* cell and collection of UV–Visible–NIR spectra. For Cu-zeolites, UV–Vis–NIR spectra show two bands, which are assigned to a Cu^{2+} d-d transition at $\sim 12000 \text{ cm}^{-1}$

and a charge transfer ($\text{O} \rightarrow \text{Cu}$) at $\sim 47000 \text{ cm}^{-1}$, as reported in the literature [23], [26], [27]. Representative UV–Vis–NIR spectra are shown in Fig. 2.8.

Ambient X-ray absorption spectroscopy (XAS) experiments were carried out at Sector 10 of the Advanced Photon Source at Argonne National Laboratory [28], [29]. For Cu-SSZ-13 and CuO spectra using a six-shooter cell that allows the simultaneous treatment of six samples, 10–15 mg of each sample were loaded. All spectra were collected in the step scan mode. An XAS spectrum of aqueous $\text{Cu}(\text{NO}_3)_2$ was collected in a glass cuvette. For experiments using either the six-shooter cell and the glass cuvette, the Cu metal foil spectrum was calibrated to 8979 eV for the Cu K-edge. In addition, a Cu metal foil spectrum was simultaneously collected while measuring sample spectra in the energy range from 8700 eV to 9890 eV. All spectra were normalized using a first-order polynomial in the pre-edge region. XAS spectra are shown in Fig. 2.9.

2.2.3 Catalytic testing

The reactor used for testing the kinetic effect of product co-feeding on NO oxidation was described in detail by Verma et al. [10]. In brief, kinetic experiments were performed in a plug flow reactor system which had the capability of measuring gas concentrations either from the reactor outlet or through a bypass loop. An online gas phase FTIR instrument (MKS Multigas 2030) was used with factory supplied calibrations to quantify the gas concentrations. Calibrations were validated by flowing NO and NO_2 standards (Praxair). In previous work, we have shown that catalytic dry NO oxidation (0.304 kPa NO, 0.015 kPa NO_2 , 10.13 kPa O_2 , 90.876 kPa N_2 , 543 K) is catalyzed by Cu ion clusters (Cu_xO_y species, $x \geq 2$, $y \geq 1$), and that Cu ions electrostatically tethered to two proximal anionic framework sites in Cu-SSZ-13 are inactive for this reaction [10], [30]. These results are reported in Fig. 2.10, in which the NO oxidation rate is zero for samples without Cu_xO_y clusters. As a result, a candidate Cu-SSZ-13 catalyst with high Cu_xO_y content was selected for this inhibition study from a series of Cu-SSZ-13 catalysts prepared by a liquid phase ion exchange method using copper nitrate as the Cu ion precursor. Two sets of experiments were performed for this study. The first set involved quantifying the kinetics of NO oxidation in the presence of

product (NO_2) co-feeding. The standard gas concentrations in this set were 0.304 kPa NO (Praxair, 3% NO in balance Ar), 0.015 kPa NO_2 (Praxair, 1.5% NO_2 in balance Ar), 10.13 kPa O_2 (Indiana Oxygen, 99.5% commercial grade), 90.876 kPa N_2 (Linde, liquid N_2 boiloff), at 543 K. The total flowrate was $1500 \text{ std cm}^3 \text{ min}^{-1}$ and the NO conversion was kept to less than 10% by varying the mass of catalyst between 30 mg and 300 mg, with most samples between 50 and 100 mg. Cu-SSZ-13 catalysts were calcined in 20% O_2 in balance N_2 at 773 K. The NO_2 inhibition was quantified by measuring the apparent reaction order with respect to NO_2 , and the rate of reaction was calculated at the respective inlet concentrations on the assumption that the differential plug flow reactor could be treated as a continuous stirred tank reactor (CSTR) [31]–[33]. The second set of experiments involved no NO_2 co-feeding. The standard conditions were 0.304 kPa NO, 10.13 kPa O_2 , 90.891 kPa N_2 , at 543 K. Once again, the NO conversion was less than 10%. The inhibition effect of NO_2 was ignored and a CSTR model was used to calculate the NO oxidation rates. In both kinetic data-sets, the NO_x mass balance, defined as $(\text{NO} + \text{NO}_2)_{\text{inlet}} - (\text{NO} + \text{NO}_2)_{\text{outlet}}$ was better than $\pm 3 \text{ ppm}$ (0.0003 kPa), which is within error of the detection limit of the FTIR instrument (MKS Multigas 2030, for which the standard deviation is $\pm 0.5 \text{ ppm}$ for both NO and NO_2). Lastly, all experiments were performed far away from equilibrium as quantified by $0.0002 < \beta \leq 0.04$, where $\beta = \frac{[\text{NO}_2]^2}{K[\text{NO}]^2[\text{O}_2]}$ is the approach to equilibrium and K is the equilibrium constant.

2.3 Results

2.3.1 Kinetic experiments in presence of NO_2 in the feed stream

When product inhibition is present, accurate kinetic parameters can only be obtained when the inhibiting product is included in the feed mixture. In order to show that NO oxidation on Cu-SSZ-13 was indeed inhibited by NO_2 , the rate of NO oxidation was first evaluated on the catalyst with NO_2 co-feeding (results are designated as “dataset 1”). The NO conversion, X , was less than 10% and the overall rate of reaction was calculated using the inlet NO concentration, the space time (τ) and a CSTR model, which is valid in this instance because conversion of reactants was differential, allowing the assumption that the

concentrations and reaction rate were constant across the catalyst bed. Therefore, the mass balance for a differential PFR can be simplified to that of a CSTR, and the following equations were used to calculate the rate of reaction for $\text{NO} + \frac{1}{2} \text{O}_2 \rightarrow \text{NO}_2$.

$$r_{fwd} = \frac{(F_{\text{NO}_0} - F_{\text{NO}})}{N} = \frac{F_{\text{NO}_0} X}{N} = \frac{[\text{NO}]_0 X}{\tau} \quad (2.1)$$

where $\tau = \frac{N}{Q}$ is space time $[(\text{mol Cu}) \text{ s L}^{-1}]$, F_{NO_0} is the inlet molar flow rate of NO $[(\text{mol NO}) \text{ s}^{-1}]$, F_{NO} is the outlet molar flow rate of NO $[(\text{mol NO}) \text{ s}^{-1}]$, NO_0 is the inlet concentration of NO $[(\text{mol NO}) \text{ L}^{-1}]$, N is the number of moles of Cu in the catalyst $[(\text{mol Cu})]$, Q is the total volumetric flow rate of gas from the reactor outlet $[\text{L s}^{-1}]$, and r_{fwd} is the moles of NO converted per mole of Cu per second $[(\text{mol NO}) (\text{mol Cu})^{-1} \text{ s}^{-1}]$. Note that Q is assumed to be independent of conversion because even though moles are not conserved in the NO oxidation reaction, the concentrations of NO_x are very small relative to those of N_2 and O_2 , and, at 10% NO conversion, the total flow rate would deviate by only 0.0015%, within error of the flow measurement. The rate was calculated for the standard feed conditions at each test temperature and the corresponding Arrhenius plot is displayed in Fig. 2.1. The apparent activation energy is $45 \pm 3 \text{ kJ mol}^{-1}$, in agreement with values reported previously by Verma et al. [10] and identical, within error, to the apparent activation energies measured across Cu-SSZ-13 samples with a range of Cu loadings (Fig. 2.11). The rate of NO oxidation at 543 K was also investigated with varied feed compositions with NO_2 included, and the apparent reaction orders with respect to NO, NO_2 , and O_2 pressure were 1.5 ± 0.1 , -0.9 ± 0.1 , and 1.1 ± 0.1 , respectively (Fig. 2.2). Reaction order measurements on Cu-SSZ-13 samples of varied Cu content were similar to those in Fig. 2.2 and are reported in Figs. 2.12 - 2.14.

This analysis shows that NO_2 inhibits the forward rate of NO oxidation over Cu-SSZ-13. It is important to once again emphasize that this analysis rests on the assumption that the plug flow reactor is operating at a sufficiently low conversion such that the rate across the catalyst bed is invariant and therefore can be approximated as a CSTR. Since we have assumed a power law expression for the rate,

$$r_{fwd} = k_{eff}[NO]^a[O_2]^b[NO_2]^c$$

$$= k_{eff}([NO]_0(1 - X))^a([O_2]_0 - [NO]_0 \frac{X}{2})^b([NO_2]_0 + [NO]_0 X)^c \quad (2.2)$$

Thus, for X sufficiently small, i.e. differential conversion, r_{fwd} is constant as shown below.

$$r_{fwd} = k_{eff}[NO]_0^a[O_2]_0^b[NO_2]_0^c \quad (2.3)$$

2.3.2 Kinetic experiments in absence of NO₂ in the feed stream

To illustrate the effect of NO₂ co-feeding on the measured kinetic parameters, data were obtained without co-feeding NO₂ for comparison to the data from Section 2.3.1.

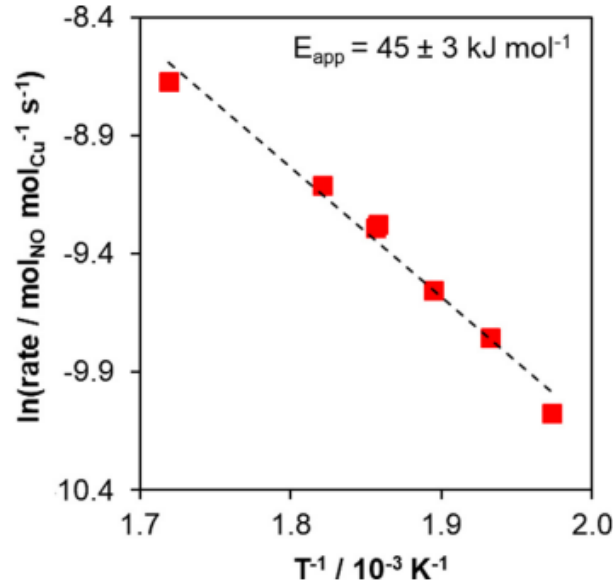


Figure 2.1. Arrhenius plot for NO oxidation with NO₂ in the feed (0.304 kPa NO, 0.015 kPa NO₂, 10.13 kPa O₂, 90.876 kPa N₂, 500 to 585 K). Differential conversion in the PFR makes the measured performance equivalent to that of a CSTR. Space velocities were maintained at 1300 s⁻¹.

The NO conversion was less than 10% and the rate of NO oxidation was evaluated with the CSTR formalism described in Eq. 2.1, i.e. on the assumption that the reactor can be

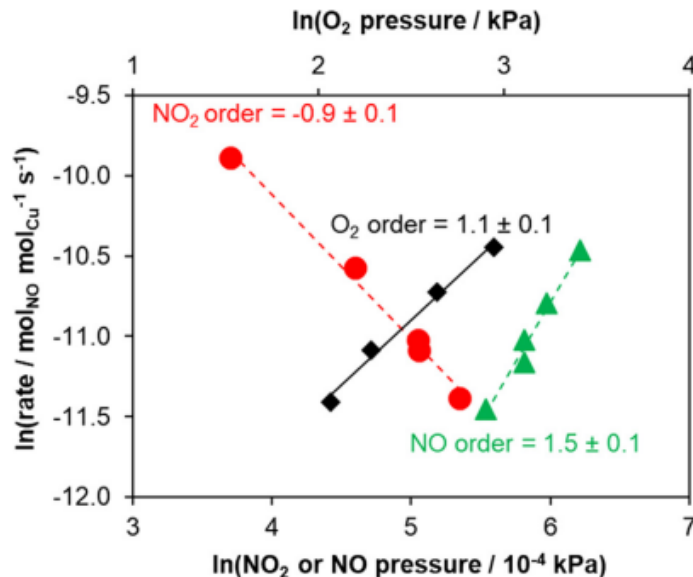


Figure 2.2. Natural log of the NO oxidation rate at 543 K as a function of NO₂ pressure (red circles), O₂ pressure (black diamonds), and NO pressure (green triangles). All kinetic data points included in this plot were obtained with NO₂ co-feeding. NO₂ pressures between 0.004 and 0.022 kPa were used for NO₂ orders. NO pressure between 0.02 and 0.05 kPa were used for NO orders, O₂ pressures between 8 and 20 kPa were used for O₂ orders. Space velocities were maintained at 1300 s⁻¹.

considered differential but ignoring the possible effect of NO₂ inhibition on the rate. The resulting Arrhenius plot is shown in Fig. 2.3. The apparent activation energy for the no NO₂ cofeeding case was 22 ± 1 kJ mol⁻¹. This value was lower than the apparent activation energy measured from NO oxidation experiments in the absence of NO₂ co-feeding by Metkar et al. (56 kJ mol⁻¹) [11] but similar to those reported by Akter et al. (17–35 kJ mol⁻¹, 500 ppm NO, 10% O₂, 373–523 K, 0.5–6 wt% Cu) [34] over Cu-CHA catalysts. Fig. 2.4 shows that when NO₂ inhibition was ignored and Eq. 2.1 was assumed to be valid, the apparent reaction orders with respect to NO and O₂ at 543 K are 0.8 ± 0.1 and 0.5 ± 0.1 respectively. These numbers, however, differ markedly from similar kinetic estimations performed with NO₂ co-feeding in the feed stream (set 1). The ratio of kinetic parameters obtained from NO₂ co-feeding versus no co-feeding ($n_{cofeed} : n_{nocofeed}$) for apparent activation energy, NO order, and O₂ order are 2 ± 0.2 , 1.9 ± 0.2 , and 2.2 ± 0.2 respectively. This systematic

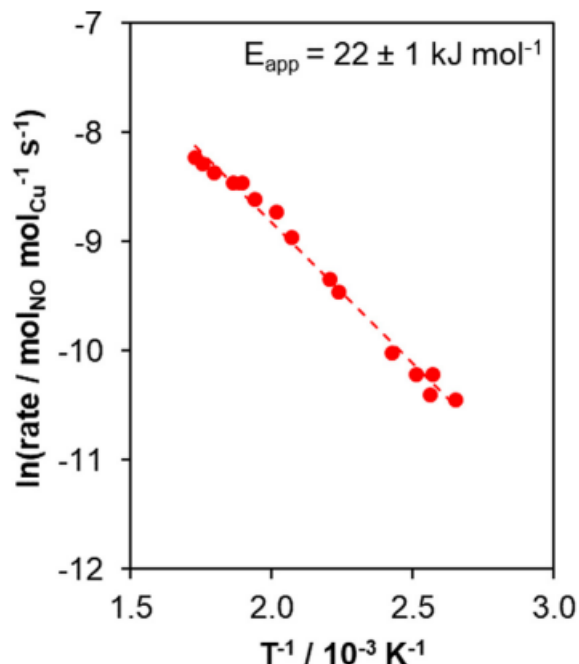


Figure 2.3. Variation of the rate of NO oxidation per mole Cu with temperature, in the absence of NO₂ co-feeding, evaluated with a CSTR model and ignoring product inhibition. Feed conditions: 0.304 kPa NO, 10.13 kPa O₂, 90.891 kPa N₂, at 380–580 K. Space velocities were maintained at 1300 s⁻¹.

trend is addressed below. We note that studies of NO oxidation on Cu-SSZ-13 at 563 K gave NO, O₂, and NO₂ orders of 0.85 to 1.0, 0.47 to 0.51, and -0.89 to -1.0, respectively [11]. In contrast to our findings at 543 K, the NO and O₂ orders did not change much in the absence of NO₂ in the feed in that study [11]. The lack of effect of the product in the feed and the relatively high value of the of the activation energy, 56 kJ mol⁻¹, measured in the 563 K range suggest that the higher temperature can contribute to making the rate insensitive to product inhibition in the 12% conversion range, but the inhibition was clearly present at the high concentrations of NO₂ used in the apparent reaction order study [11]. A reaction order for NO of approximately unity has also been reported for NO oxidation over Cu-chabazite in the 573–673 K range in the absence of NO₂ in the feed [35]. These two studies suggest that the NO reaction order is a function of temperature and that NO₂ inhibition is significantly decreased at higher temperature but it cannot be ruled out that the detailed structure of the Cu sites is not identical to that presented here.

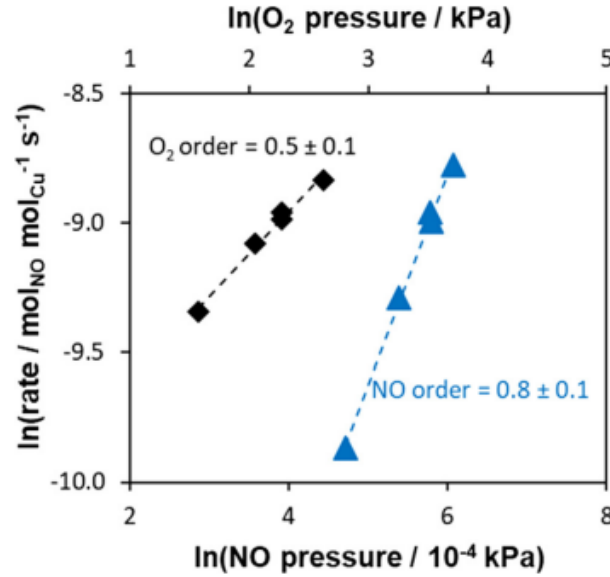


Figure 2.4. Variation of the \ln of the rate of NO oxidation per mole Cu, with the \ln of the NO and O₂ concentrations during dry NO oxidation conditions (0.304 kPa NO, 10.13 kPa O₂, 90.891 kPa N₂, 543 K). O₂ concentrations were varied between 80 and 270 kPa while holding NO and NO₂ gas pressures constant. NO concentrations were varied between 0.024 and 0.05 kPa while holding O₂ and NO₂ gas pressure constant. NO₂ was not co-fed in the feed stream.

2.4 Discussion

2.4.1 Quantitative analysis of the NO₂ inhibition effect

The analysis of the data for NO oxidation in the absence of product NO₂ in the feed in Section 2.3.2 above starts with the assumption that the PFR can be presumed to be differential and therefore approximated as a CSTR. To examine this assumption more closely, we start with the general design equation for a PFR, Eq. 2.4.

$$\tau = [NO]_0 \int_0^X \frac{dX}{r_{fwd}} \quad (2.4)$$

This equation reduces to the CSTR equation (Eq. 2.1) only if r_{fwd} is constant over the range of X . If we start with the power law rate expression in Eq. 2.2 and note that in this

case $[\text{NO}_2]_0 = 0$, then at small X the rate expression becomes:

$$r_{fwd} = k_{eff}[\text{NO}]_0^{a+c}[\text{O}_2]_0^b X^c \quad (2.5)$$

Eq. 2.5 illustrates the source of the error that originates from neglect of product inhibition, which is specifically that the rate is a function of X and therefore of position in the plug flow reactor. Thus, integration of Eq. 2.4 is necessary and leads to:

$$\tau = k_{eff}^{-1}[\text{NO}]_0^{1-a-c}[\text{O}_2]_0^{-b} \int_0^X \frac{dX}{X^c} = k_{eff}^{-1}[\text{NO}]_0^{1-a-c}[\text{O}_2]_0^{-b} \left(\frac{X^{1-c}}{1-c} \right) \quad (2.6)$$

Solving Eq. 2.6 for X then leads to:

$$X = \tau^{1/(1-c)}(1-c)^{1/(1-c)} k_{eff}^{1/(1-c)} [\text{NO}]_0^{-1+a/(1-c)} [\text{O}_2]_0^{b/(1-c)} \quad (2.7)$$

As is true in general for plug flow reactors, since the rate changes with conversion (Eq. 2.5) and conversion changes down the length of the reactor, the rate of reaction, r_{fwd} , is not directly defined by any measured parameters of the PFR experiment. If, however, we were to mistakenly assume that the reactor is differential and described by the CSTR approximation, then the forward rate of reaction would be given as $\frac{[\text{NO}]_0 X}{\tau}$. Then both the order plot, Fig. 2.4, and the Arrhenius plot, Fig. 2.3, have $\ln\left[\frac{[\text{NO}]_0 X}{\tau}\right]$ as the ordinate. The true expression for X , however, is given by Eq. 2.7 and the expression for $\frac{[\text{NO}]_0 X}{\tau}$ is given by Eq. 2.8.

$$\frac{[\text{NO}]_0 X}{\tau} = \tau^{c/(1-c)} A^{1/(1-c)} e^{-E_{app}/(RT(1-c))} [\text{NO}]_0^{a/(1-c)} [\text{O}_2]_0^{b/(1-c)} (1-c)^{1/(1-c)} \quad (2.8)$$

We see from Eq. 2.8 that the NO and O_2 orders produced from Fig. 2.4 are actually $a/(1-c)$ and $b/(1-c)$, respectively. Similarly, the Arrhenius plot of the log of $\frac{[\text{NO}]_0 X}{\tau}$ versus $1/T$ when $[\text{NO}]_0$ and $[\text{O}_2]_0$ are held constant, Fig. 2.3, yields an apparent activation energy of $E_{app}/(1-c)$ from Eq. 2.8. Furthermore, the ratio of the true values of the orders and apparent activation energy to those measured in the absence of the inhibition product NO_2 will in each case be $1-c$. Recalling that c has been found to have the value -0.9 ± 0.1 , yields a value of $n_{cofeed} : n_{nocofeed} = 1.9 \pm 0.1$, in agreement with the measured kinetic ratios presented at the end of Section 2.3.2 above.

Finally, we show in Section 2.6.7 that if we relax the approximation that the PFR is differential and numerically integrate the PFR equations using Eq. 2.2 for the rate with the values of a , b , and c extracted from the NO₂ co-feeding analysis above, the data give activation energy values in the agreement with those from the co-feeding experiment. This is the expected result because, as discussed, the CSTR approximation for the PFR is valid when NO₂ is co-fed.

Two important observations arise from this NO oxidation example. First, when product inhibition is present, but is overlooked, and data are obtained without the inhibiting product in the feed, serious errors are incurred in all measured kinetic parameters. This problem can be avoided by including the products in the feed at concentrations high enough that the product concentrations are also differential axially within the bed. The expected prevalence of product inhibition, generalization of the analysis, and a simple experimental test for the presence of inhibition are discussed in turn below.

2.4.2 Product inhibition is more likely than expected

To evaluate the likelihood of encountering product inhibition, we must first examine its origin. We begin with the simplest case. A Langmuir Hinshelwood Hougen Watson (LHHW) analysis of $A \rightarrow B$ on a catalytic surface yields:

$$r_B = \frac{kK_AP_A}{1 + K_AP_A + K_BP_B} \quad (2.9)$$

where k is the rate constant for the rate-determining step of A to B on the surface and K_A and K_B are adsorption equilibrium constants for A and B . For simplicity, assume that K_AP_A is very much less than 1. If K_BP_B is large with respect to 1, the rate will be first inverse order in B and will be decreased by the presence of B unless P_B is small enough to make $K_BP_B \ll 1$. Since $P_B = P_{A0}X_A$, where X_A is the conversion of A , there is a value of X_A below which the rate is independent of B , and that value depends on the value of K_B . Thus, it is true, as many assume, that there will always be a conversion low enough to remove the inhibition effect and guarantee differential conversion in a PFR. The question

is, how low does X_A have to be? To estimate a typical value of K_B in units of atm^{-1} , we take the correlation suggested by Vannice et al. [36] for the upper bound of $-\Delta S_{ads}^0$ as $51.0 - 0.0014\Delta H_{ads}^0$, where the entropy units are $\text{J}(\text{mol K})^{-1}$ and the enthalpy units are J mol^{-1} . For a typical value of ΔH_{ads}^0 of 84 kJ mol^{-1} (20 kcal mol^{-1}), the upper bound for $-\Delta S_{ads}^0$ would be $168 \text{ J}(\text{mol K})^{-1}$. The lower bound reported by Vannice et al. was $41.8 \text{ J mol}^{-1} \text{ K}^{-1}$ [36]. If we approximate ΔS_{ads}^0 as $105 \text{ J}(\text{mol K})^{-1}$ (the average of 41.8 and $168 \text{ J mol}^{-1} \text{ K}^{-1}$) and assume that the onset of inhibition will occur when $K_B P_B = 0.1$ (i.e., when the term for coverage of B in the denominator of a Langmuir Hinshelwood rate expression approaches the order of magnitude of unity), Eq. 2.10 shows the relation between P_B (with units of Pa), ΔH_B^0 (ΔH_{ads}^0 for species B, J mol^{-1}), R (ideal gas constant, units $\text{J mol}^{-1} \text{ K}^{-1}$) and T (K) at that point:

$$P_B = 0.1 \cdot 101325 \cdot \exp\left(\left(105 + \frac{\Delta H_B^0}{T}\right)R^{-1}\right) \quad (2.10)$$

At 600 K , the rate of reaction of 1 atm of A (to form B) would be suppressed by competitive adsorption from B (i.e., product inhibited) at a conversion of 0.15% . This value for a reaction at atmospheric pressure shows that the standard assumption that product inhibition does not impact measured kinetic parameters at 10% conversion is not reliable and suggests that one should assume that inhibition will corrupt the observed kinetics until experiments prove otherwise. Further evaluation of the effects of parameter choice are included in the Supporting Information, Fig 2.17, and those results further support the conclusion that it is not safe to assume that an arbitrary low conversion is adequate to guarantee that inhibition can be ignored.

For our example of NO oxidation on Cu-zeolites, however, the situation is more complex, because the partial pressures of the limiting reagent are low and the reaction mechanism must be considered more carefully to include the possibility of product inhibition. We can first attempt to apply the same approach represented by Eq. 2.10 for the simplest general LHHW reaction $A \rightarrow B$, however, as we see below this approach fails as the mechanism for NO oxidation is not as simple as this example reaction. Metkar et al. [11] estimated that the adsorption enthalpy for NO_2 on Cu-CHA was $141.5 \text{ kJ mol}^{-1}$ by regressing parameters

in a kinetic model. The upper bound of $-\Delta S_{ads}^0$ calculated from the Vannice correlation [36] using $\Delta H_{ads,NO_2}^0 = -141.5 \text{ kJ mol}^{-1}$ would be $249 \text{ J (mol K)}^{-1}$. Given the similarity between this value and the tabulated value of $-\Delta S^0$ from NIST of $269 \text{ J (mol K)}^{-1}$ [35], this approximation is not non-physical, though it would equate to near-complete entropy loss upon adsorption. Assuming the onset of inhibition occurs when the product of the adsorption constant for NO_2 and the NO_2 pressure, $(K_{NO_2} \cdot P_{NO_2})$, is equal to 0.1 leads to Eq. 2.11 if we use the upper bound value for $-\Delta S_{ads}^0$ of $249 \text{ J (mol K)}^{-1}$,

$$P_{NO_2} = 0.1 \cdot 101325 \cdot \exp\left(\left(249 + \frac{\Delta H_{ads,NO_2}^0}{T}\right)R^{-1}\right) \quad (2.11)$$

At 543 K with an NO partial pressure of 32 Pa, Eq. 2.11 predicts no inhibition even when the conversion approaches 100%. Inhibition is clearly present at conversions below 10%, however (Fig. 2.2). To see why the simple analysis behind Eq. 2.11 breaks down in this case, we need to look more closely at the mechanism for NO oxidation. As reported previously by Verma et al. [10], and as is compared to the series of elementary steps reported by Metkar et al. [11] in Section 2.6.10 of the Supporting Information, a sequence of elementary steps consistent with the data is given in figure 2.5.

Assuming that the first, third, and fourth steps in figure 2.5 are in quasi-equilibrium and that $*$, $O*$, and NO_2* are the most abundant surface intermediates leads to the following rate expression:

$$r = \frac{k_2 K_1 L [O_2]}{\frac{1}{[NO]} + \frac{K_3^{-1} K_4^{-1} [NO_2]}{[NO]^2} + \frac{K_4^{-1} [NO_2]}{[NO]}} \quad (2.12)$$

where L is the total number of active sites, k_2 is the rate constant for step 2, and K_1 , K_3 , and K_4 are equilibrium constants. This expression does not have the simple LHHW form discussed above, and therefore Eq. 2.11 does not apply since both Eqs. 2.10 and 2.11 are derived for cases in which the inhibiting term in the denominator of the rate law follows the $K_B P_B$ format. We see that the inhibiting terms in the denominator of Eq. 2.12 are ratios of equilibrium constants and the ratio of NO_2 and NO concentrations, and that product inhibition will be significant when $[NO_2]/K_4[NO]$ is large. Specifically, product inhibition

will be apparent when the following equation is satisfied:

$$0.1 \cdot \left(\frac{1}{[NO]} \right) = \frac{K_3^{-1} K_4^{-1} [NO_2]}{[NO]^2} + \frac{K_4^{-1} [NO_2]}{[NO]} \quad (2.13)$$

Multiplying Eq. 2.13 by $[NO]$ leads to:

$$0.1 = \frac{K_3^{-1} K_4^{-1} [NO_2]}{[NO]} + K_4^{-1} [NO_2] \quad (2.14)$$

1. $O_{2(g)} + * \leftrightarrow O_2^*$
2. $NO_{(g)} + O_2^* \rightarrow O^* + NO_{2(g)}$
3. $NO_{(g)} + O^* \leftrightarrow NO_2^*$
4. $NO_2^* \leftrightarrow * + NO_{2(g)}$

Figure 2.5. Series of elementary steps consistent with the data collected in this manuscript and the data reported previously by Verma et al. [10].

While it is still possible to apply an equation of the same general form as Eqs. 2.10 and 2.11 for this more complex case of equilibrium-controlled inhibition, as shown in Eq. 2.14, we need to know how K_3 and K_4 depend on temperature. Metkar et al. [11] provide estimates for the value of K_3 and K_4 , though we note that Verma et al. [10] wrote step four in the opposite direction versus than of Metkar et al., such that K_4^{-1} in Verma et al. [10] is equivalent to the values of K_4 reported by Metkar et al. The value $K_3^{-1} K_4^{-1}$ was estimated as $12.7 \cdot \exp(5200/RT)$ (see derivation in Section 2.6.10), therefore the value of the second term in the denominator of Eq. 2.12 is equivalent to $40.2([NO_2]/[NO]^2)$ at 543 K. The value of K_4^{-1} is calculated as $1.27 \cdot 10^{-8} \cdot \exp(141500/RT)$ and the right hand side of Eq. 2.14 equal to 0.1 when the conversion of NO to NO_2 is 0.05% (assuming an inlet NO pressure of 32 Pa and a total pressure of 101,325 Pa). Thus, inhibition would be expected when conversion is equal to or greater than 0.05%. This analysis also shows clearly that increasing temperature will decrease the coverage of O^* and NO_2^* and, thus, decrease the inhibition effect. Another interesting case of quasi-equilibrium control of an active intermediate by products is given

was reported by Huang et al. [20]. This case shows that when the rate expression is not yet determined from data, prediction of the presence or absence of product inhibition can be difficult, and it emphasizes the need for direct experimental verification of the effect of products on the rate.

These examples serve to illustrate that the limit on conversion below which the influence of the products on the rate can be ignored can be substantially lower than is usually invoked in the literature (which is usually set at 10% conversion of reactant). Finally, we note that though we have used the simple $A \rightarrow B$ reaction as an example, any sequence of steps that involves multiple products competing for sites will generate a LHHW rate equation that will have $K_j P_j$ terms in the denominator for each product, j , and that any time a $K_j P_j$ term is order 1 or higher it has the potential to affect the rate and will do so unless a reactant term $K_i P_i$ for adsorption of reactant i is substantially greater than $K_j P_j$. As also shown above, more complex sequences of steps can lead to more complex relations that determine the influence of the products on the rate.

2.4.3 Generalization of the analysis

First we consider a general reaction of two reactants going to two products, $A + B \rightarrow C + D$. From the discussion above, one cannot assume, *a priori*, that the forward rate will be independent of the product concentrations, so we express the generalized power law rate as

$$r_{fwd} = k_{app} C_A^a C_B^b C_C^c C_D^d \quad (2.15)$$

A comparison of this rate expression to that shown in Eq. 2.2 shows just one additional term, involving C_D . Following the same logic as used for Eq. 2.2 but adding C_{D0} as well as C_{C0} to the feed to ensure differential PFR behavior, and comparing that case to the case where the effects of products are ignored leads to $n_{cofeed} : n_{nocofeed} = 1\text{-c-d}$. This result shows that all products that affect the forward rate but are not included in the feed in kinetic experiments will lead to substantial error in the values of all measured kinetic parameters.

The analysis has so far been applied to a plug flow reactor run at low, presumed differential, conversion. The analysis of a low conversion batch reactor is identical to that shown

here with s replaced by the elapsed reaction time, t . For an ideal CSTR, where the reaction medium is well-mixed, the rate is identical at all spatial positions in the reactor and the concentrations of reactants and products are each equal to those in the reactor effluent. Under these conditions, Eq. 2.3 is not an approximation, but is the true representation of the rate for all conversions. For the power law rate in Eq. 2.15,

$$r_{fwd} = C_{A0}X/\tau = k_{app}C_A^aC_B^bC_C^cC_D^d \quad (2.16)$$

where X is the conversion of A and the concentration values of the reactants and products are those measured at the reactor effluent. If products are included in the feed and the conversion is kept sufficiently low to allow $C_i = C_{i0}(1-X) = C_{i0}$ for reactants and $C_j = C_{j0} + C_{A0}X = C_{j0}$, then,

$$r_{fwd} = C_{A0}X/\tau = k_{app}C_{A0}^aC_{B0}^bC_{C0}^cC_{D0}^d \quad (2.17)$$

and conversions measured at constant τ with each of the reactant and product feed concentrations varied independently will produce the data for construction of the log/log reaction order plots to produce the true reaction orders, a , b , c , and d , analogously to the procedure for the truly differential PFR in Section 2.3.1. If the products are not fed, however, Eq. 2.17 becomes,

$$r_{fwd} = C_{A0}X/\tau = k_{app}C_{A0}^aC_{B0}^bC_{C0}^cC_{D0}^dX^{c+d} \quad (2.18)$$

The rate is still given by $r_{fwd} = C_{A0}X/\tau$, but the rate is no longer determined by the inlet concentration alone because of the X^{c+d} term. We can solve for X , however, to give,

$$X = \tau^{1/(1-c-d)}k_{app}^{1/(1-c-d)}C_{A0}^{(a+c+d-1)/(1-c-d)}C_{B0}^{b/(1-c-d)} \quad (2.19)$$

Substituting X into the expression for the rate gives,

$$r_{fwd} = \tau^{(c+d)/(1-c-d)} k_{app}^{1/(1-c-d)} C_{A0}^{a/(1-c-d)} C_{B0}^{b/(1-c-d)} \quad (2.20)$$

Thus, we see that regardless of reactor type, ignoring product inhibition and not including products in the feed produces the same error in all the measured kinetic parameters, i.e. $n_{cofeed} : n_{noco feed} = 1-c-d$.

2.4.4 A simple test for product inhibition

It is clear that ignoring product inhibition when it is in fact present produces inaccurate kinetic data. While the solution to this problem is straightforward - including the products in the feed – the solution is not without a cost in time and effort. Re-plumbing to accommodate controlled and measured feeds of the product components may be required and measuring small changes in product concentration in the outlet versus the inlet may challenge the detection scheme. These adjustments must be made if inhibition is present, but they could be avoided if it could be shown experimentally that product inhibition does not occur in the system under study. To generate such a test, we need only to consider Eq. 2.19. If we maintain constant inlet reactant concentrations and vary the space time (either by changing flowrate or amount of catalyst, or both) and measure conversion, while keeping X small, a plot of $\ln X$ versus $\ln s$ will have a slope of $1/(1-c-d)$. If the slope is less than 1, either c, or d, or both have measurable negative values, inhibition is indicated, and products must be fed in order to measure useful kinetic data. This approach has been demonstrated in a recent study of propylene epoxidation to propylene oxide [16]. Furthermore, it is straightforward to show that this approach also applies to a low conversion PFR or batch reactor.

The above procedure still requires that the analytical system be accurate enough to measure small conversions of reactants. One way to achieve the higher precision necessary for analysis is to add an internal standard to the feed and to measure the concentrations of reactants and products before and after the reactor for each process condition. Finally, it should be noted that this analysis is only valid for single reactions which can be defined by a power law model.

There are not many examples of direct accounting for product inhibition by comparing data in the presence and absence of products in the feed in the literature, but a few are shown below in Table 2.1.

2.5 Conclusions

In view of the importance of accurate interpretation of kinetic data to the science of catalysis and the rational design of improved catalyst formulations, the prevalence of product inhibition, and the falsification of kinetic parameters caused by overlooking product inhibition, it is prudent to account for the effects of products on the rate for all kinetic measurements. Including products in the feed is a reliable way to guarantee data integrity at a modest cost in analytical and reactor complexity. Such efforts are necessary for prediction of catalyst performance at elevated conversions (and product concentrations) relevant to industrial practice based on kinetic parameters measured in lab-scale reactors in the presence of relatively low (but consequential) product concentrations. Plotting the natural logarithm of conversion versus the natural logarithm of the space time is a simple way to check for product inhibition and a straightforward way to ascertain whether product co-feeding is necessary. We encourage inclusion of this test in all kinetic analyses that are reasonably approximated by power law rate expressions.

Table 2.1. Literature examples of the quantitative effects of inhibition of products.

Overall reaction stoichiometry	Catalyst	Parameter	$n_{co-feed}$	$n_{no\ co-feed}$	$\frac{n_{co-feed}}{n_{no\ co-feed}}$
$2\text{NO} + \text{O}_2 \rightleftharpoons 2\text{NO}_2$	Pt/Al ₂ O ₃ [12]; Pt/SiO ₂ [37]	E_{app} (kJ mol ⁻¹)	82 [12]	39 [12]; 41 [37]	2.1
		NO order	1 [12]	0.5 [37]	2
		O ₂ order	1 [12]	0.5 [37]	2
		NO ₂ order	-1 [12]	-	-
$\text{CH}_4 + 2\text{O}_2 \longrightarrow \text{CO}_2 + 2\text{H}_2\text{O}$	Pd/ZrO ₂ [2]	E_{app} (kJ mol ⁻¹)	170	80	2.1

2.6 Supplementary Information

2.6.1 Elemental Analysis

Table 2.2. Bulk elemental analysis of Si, Al, and Cu content in Cu-SSZ-13 catalysts measured using atomic absorption spectroscopy (AAS). Data for all samples except that with Cu wt% 7.40 were originally reported in Verma et al. [\[10\]](#)

Si:Al	Cu wt%	Cu:Al
4.5	0.00	0.00
4.3	0.31	0.02
4.3	0.82	0.04
4.5	1.74	0.09
4.5	3.04	0.16
4.5	3.75	0.20
4.5	5.64	0.31
4.5	6.39	0.35
4.5	7.40	0.39
4.5	18.93	1.60

2.6.2 X-ray Diffraction (XRD) Patterns

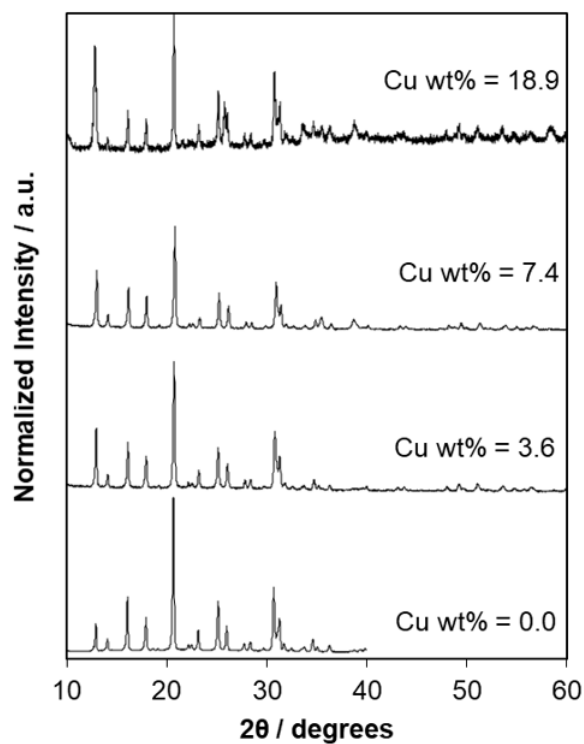


Figure 2.6. Ambient XRD patterns from 10° to 60° 2θ on Cu-SSZ-13 Si:Al = 4.5 with Cu wt% of 3.6, 7.4, and 18.9, and H-SSZ-13. All Cu-SSZ-13 materials were Si:Al = 4.5 and were calcined after Cu-exchange then cooled and exposed to ambient air prior to collecting ambient XRD spectra.

2.6.3 Sample Argon Adsorption Isotherms

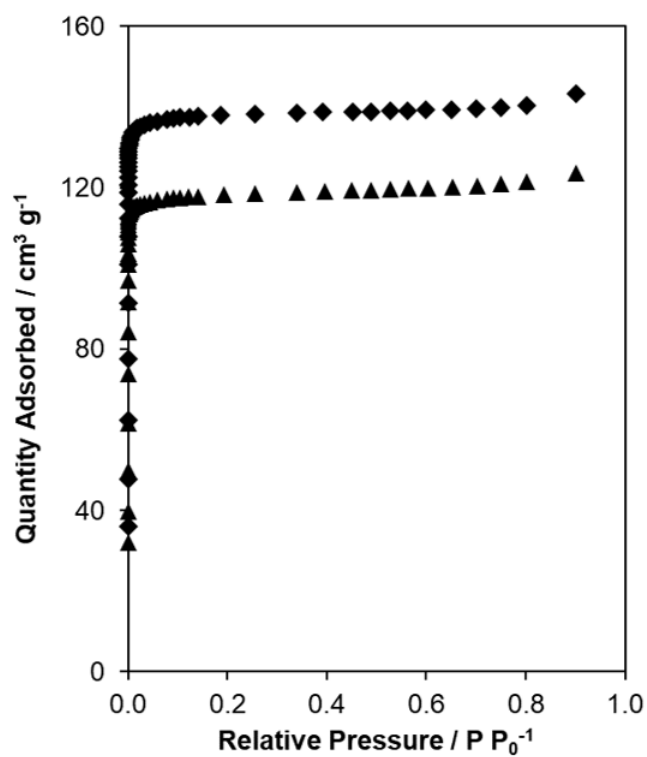


Figure 2.7. Argon adsorption isotherms (87 K) of H-SSZ-13 (diamonds) and Cu-SSZ-13 (Cu wt% = 3.75, triangles). Both samples are Si:Al = 4.5.

2.6.4 Diffuse Reflectance UV-Visible-NIR

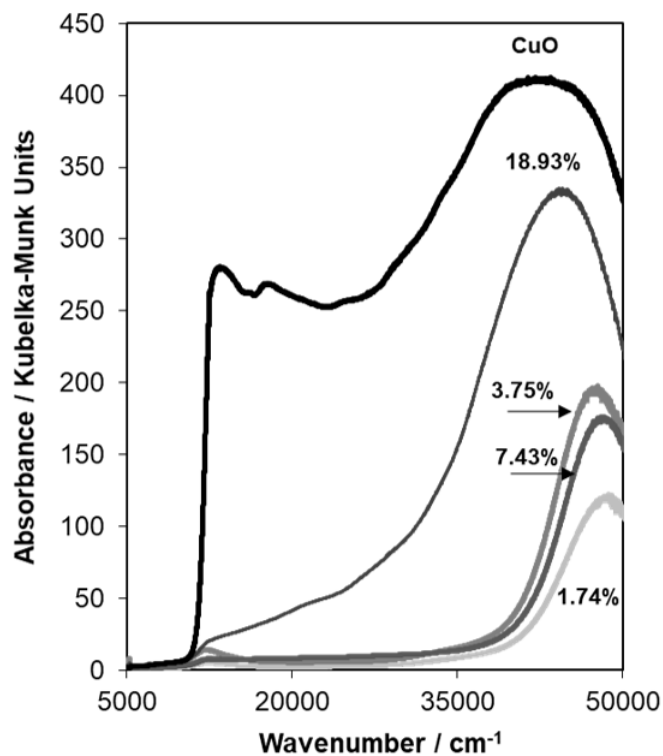


Figure 2.8. Diffuse reflectance UV-visible spectra of Cu-SSZ-13 samples with Cu wt% ranging from 1.74-18.93 and of CuO, collected under ambient conditions (298 K, ambient air).

2.6.5 Cu K-edge X-ray Absorption Spectroscopy (XAS)

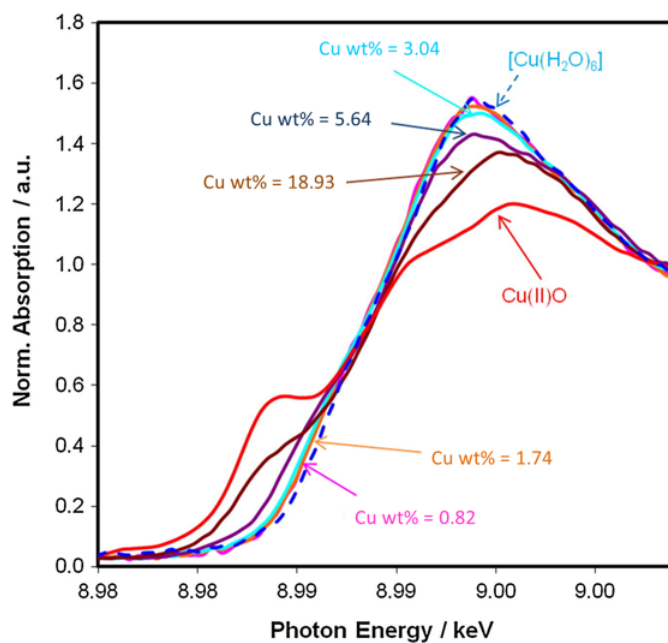


Figure 2.9. Ambient Cu K-edge X-ray absorption spectra collected on bulk Cu(II)O (red), aqueous Cu(NO₃)₂ (blue), and five Cu-SSZ-13 samples with Cu wt% from 0.82-18.93. All Cu-SSZ-13 materials were Si:Al = 4.5 and were calcined after Cu-exchange then cooled and exposed to ambient air prior to collecting ambient XAS spectra. These data were originally reported in Verma et al. [10].

2.6.6 Dry NO oxidation kinetics on Cu-SSZ-13 catalysts

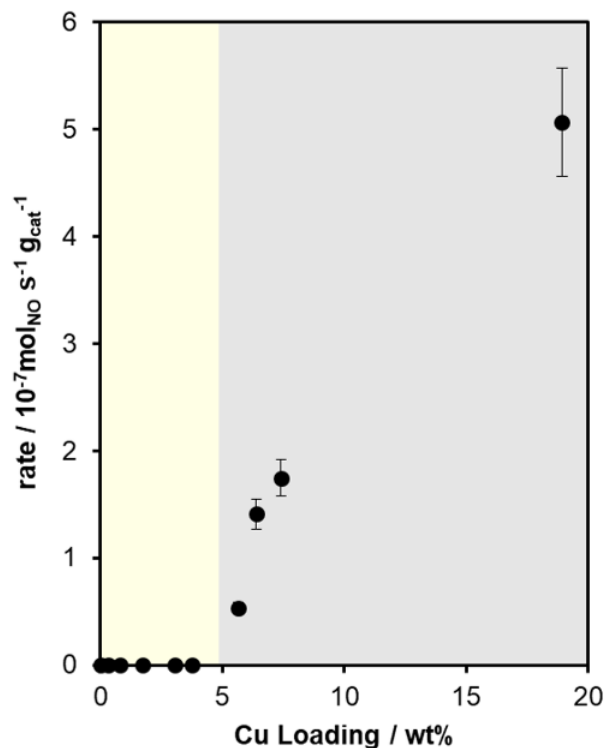


Figure 2.10. The dry NO oxidation reaction rate normalized per gram of catalyst plotted versus the Cu wt%. Dry NO oxidation conditions (300 ppm NO, 150 ppm NO₂, 10% O₂, in balance N₂, 543 K). Cu-SSZ-13 catalysts with a Si:Al molar ratio of 4.5 and Cu wt% from 0-19 were synthesized and used for this study. The yellow shaded area between 0 and 4 wt% represents samples with all Cu as ionic Cu²⁺/Cu¹⁺ species. The grey shaded area between 4 to 19 wt% represents samples that contain bulk Cu_xO_y species. Data for all samples except that with Cu wt% 7.40 were originally reported in Verma et al. [10].

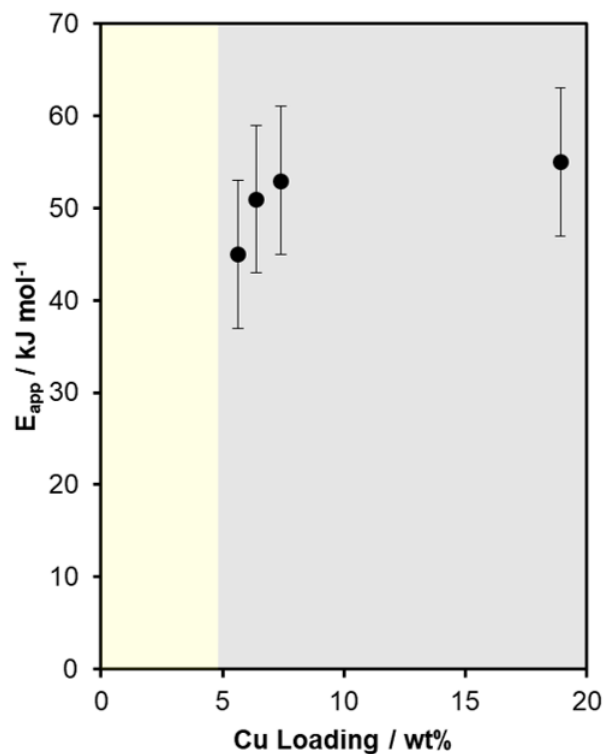


Figure 2.11. The dry NO oxidation apparent activation energy plotted versus the Cu wt%. Dry NO oxidation conditions (300 ppm NO, 150 ppm NO₂, 10% O₂, in balance N₂, 543 K). Cu-SSZ-13 catalysts with a Si:Al molar ratio of 4.5 and Cu wt% from 0-19 were synthesized and used for this study. The yellow shaded area between 0 and 4 wt% represents samples with all Cu as ionic Cu²⁺/Cu¹⁺ species. The grey shaded area between 4 to 19 wt% represents samples that contain bulk Cu_xO_y species. Data for all samples except that with Cu wt% 7.40 were originally reported in Verma et al. [10].

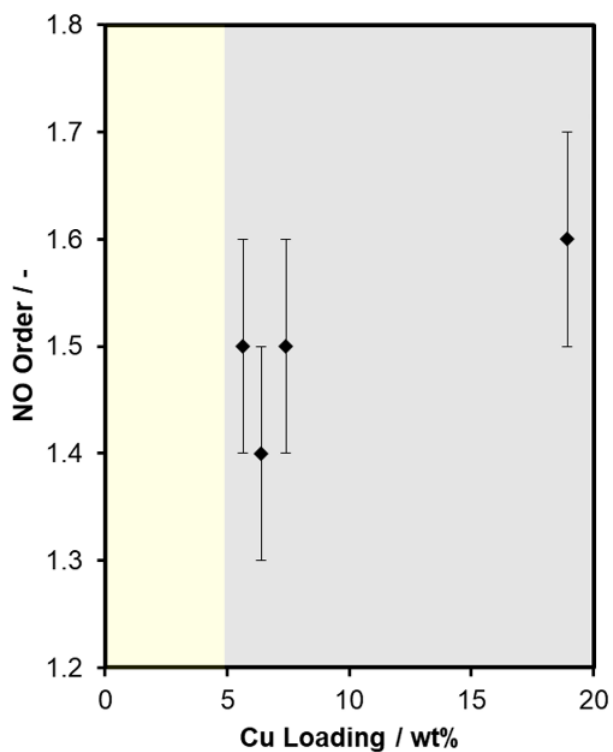


Figure 2.12. NO reaction orders plotted versus the Cu wt% under dry NO oxidation conditions (300 ppm NO, 150 ppm NO₂, 10% O₂, in balance N₂, 543 K). Cu-SSZ-13 catalysts with a Si:Al molar ratio of 4.5 and Cu wt% from 0-19 were synthesized and used for this study. The yellow shaded area between 0 and 4 wt% represents samples with all Cu as ionic Cu²⁺/Cu¹⁺ species. The grey shaded area between 4 to 19 wt% represents samples that contain bulk Cu_xO_y species. Data for all samples except that with Cu wt% 7.40 were originally reported in Verma et al. [10].

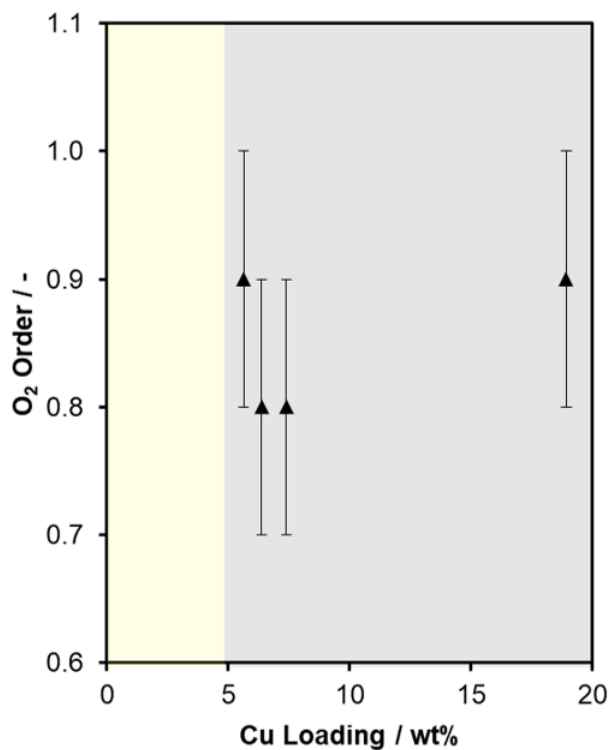


Figure 2.13. O₂ reaction orders plotted versus the Cu wt% under dry NO oxidation conditions (300 ppm NO, 150 ppm NO₂, 10% O₂, in balance N₂, 543 K). Cu-SSZ-13 catalysts with a Si:Al molar ratio of 4.5 and Cu wt% from 0-19 were synthesized and used for this study. The yellow shaded area between 0 and 4 wt% represents samples with all Cu as ionic Cu²⁺/Cu¹⁺ species. The grey shaded area between 4 to 19 wt% represents samples that contain bulk Cu_xO_y species. Data for all samples except that with Cu wt% 7.40 were originally reported in Verma et al. [10].

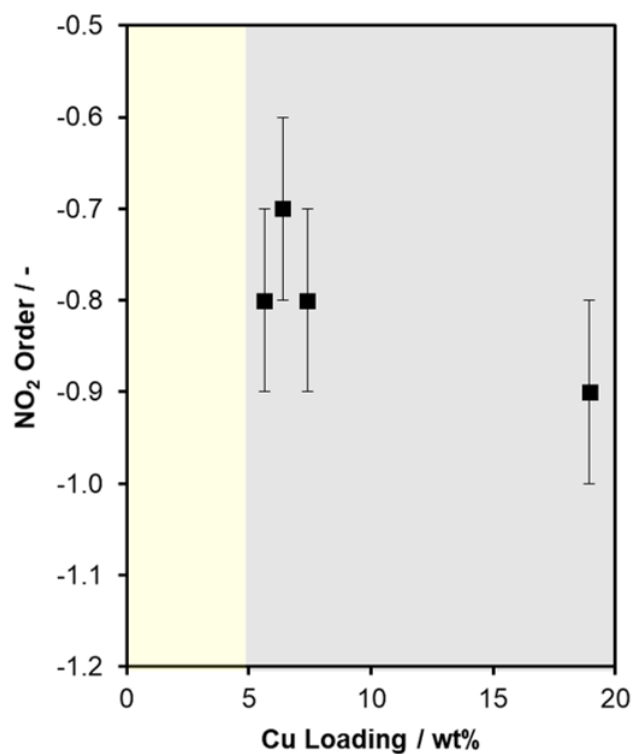


Figure 2.14. NO₂ reaction orders plotted versus the Cu wt% under dry NO oxidation conditions (300 ppm NO, 150 ppm NO₂, 10% O₂, in balance N₂, 543 K). Cu-SSZ-13 catalysts with a Si:Al molar ratio of 4.5 and Cu wt% from 0-19 were synthesized and used for this study. The yellow shaded area between 0 and 4 wt% represents samples with all Cu as ionic Cu²⁺/Cu¹⁺ species. The grey shaded area between 4 to 19 wt% represents samples that contain bulk Cu_xO_y species. Data for all samples except that with Cu wt% 7.40 were originally reported in Verma et al. [10].

2.6.7 Relaxation of differential assumption for PFR

Here, we relax the approximation that the PFR is differential and numerically integrate the PFR equations in Eq. 2.2 for the rate with the values of a, b, and c of $1.5/(1-(-0.9))$, $1.1/(1-(-0.9))$, and -0.9, respectively, extracted from the co-feeding analysis in Section 2.4.1. We start with equation 2.2:

$$r_{fwd} = k_{eff}([NO]_0(1 - X))^a([O_2]_0 - [NO]_0X/2)^b([NO_2]_0 + [NO]_0X)^c \quad (2.2)$$

And we note that $[NO_2]_0$ is equal to zero, giving:

$$r_{fwd} = k_{eff}([NO]_0(1 - X))^a([O_2]_0 - [NO]_0X/2)^b([NO]_0X)^c \quad (2.21)$$

or,

$$r_{fwd} = k_{eff}([NO]_0(1 - X))^{0.79}([O_2]_0 - [NO]_0X/2)^{0.58}([NO]_0X)^{-0.9} \quad (2.22)$$

We reintroduce equation 2.4, the design equation for a PFR.

$$\tau = [NO]_0 \int_0^X \frac{dX}{r_{fwd}} \quad (2.4)$$

In the main text, we next simplified equation 2.21 by assuming small X, but here we will not make this simplification. Therefore:

$$\tau = [NO]_0 \int_0^x \frac{dX}{k_{eff}([NO]_0(1 - X))^{0.79}([O_2]_0 - [NO]_0X/2)^{0.58}([NO]_0X)^{-0.9}} \quad (2.23)$$

Next, we integrate this expression numerically to give the trend in X with respect to τ shown in Figure 2.15.

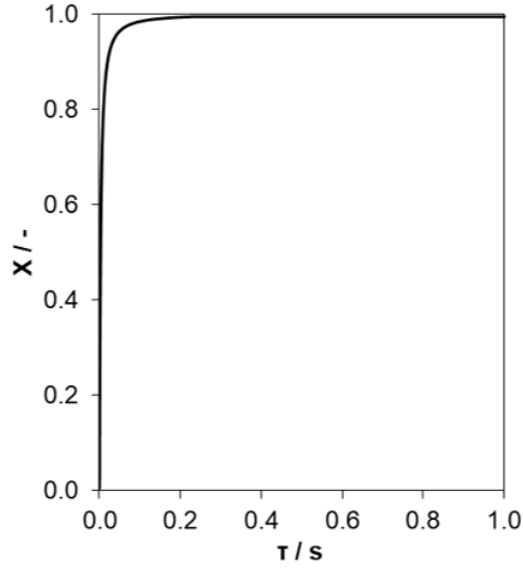


Figure 2.15. Conversion as a function of τ as determined by numerical integration of Eq. 2.23 using trapezoid rule with 200 mesh points.

We find that the exponent of k_{eff} will lead to apparent activation energies in agreement with those from the co-feeding experiment. For instance, if we vary the value of k_{eff} and then plot the value of X observed at fixed τ , we find that k_{eff} has an exponent of 0.5187. Now, the expected value is k_{eff} raised to a power of $1/(1-c)$, and in this case c is -0.9, giving k_{eff} raised to 0.53, which is similar to the exponent shown in in Figure 2.16.

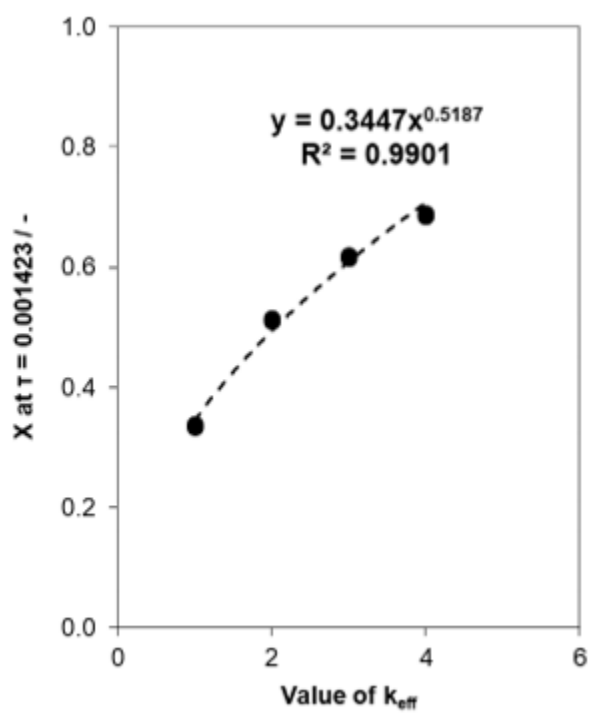


Figure 2.16. Conversion at a fixed value of τ as a function of k_{eff} .

2.6.8 Derivation of equation 2.10

From the definition of the equilibrium constant, K:

$$K = \exp\left(\frac{-\Delta G_B^o}{RT}\right) \quad (2.24)$$

With ΔG_B^o as the free energy for adsorption of B. When $K_B P_B = 0.1$, as was assumed in Section 2.4.2, we can solve for P_B in terms of thermodynamic quantities as follows:

$$K_B P_B = 0.1 \quad (2.25)$$

Combining equations 2.24 and 2.25 gives:

$$\exp\left(\frac{-\Delta G_B^o}{RT}\right) P_B = 0.1 \quad (2.26)$$

Rearranging equation 2.26 and substituting for ΔG :

$$P_B = 0.1 \exp\left(\frac{\Delta H_B^o - T \Delta S_B^o}{RT}\right) \quad (2.27)$$

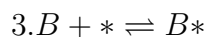
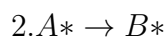
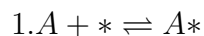
Where ΔH_B^o and ΔS_B^o are the enthalpy and entropy of adsorption of B. For adsorption of B with ΔS_{ads} assumed to be $105 \text{ J (mol K)}^{-1}$, this equation simplifies to:

$$P_B = 0.1 \cdot \exp\left(\left(105 + \frac{\Delta H_B^o}{T}\right) R^{-1}\right) \quad (2.10)$$

Which is equation 10.

2.6.9 Range of parameter space where errors from neglecting product inhibition are significant

In the main text, an approximate entropy value of 84 kJ mol^{-1} was used. In this section, we discuss the effect of the enthalpy and entropy of product adsorption on the measured rate in the context of a simple example, the irreversible surface-catalyzed reaction of $A \rightarrow B$. The set of elementary steps we will use are as follows:



Step 1 and 3 are assumed to be quasi-equilibrated, and step 2 is considered the sole rate limiting step, and we consider vacant sites (*) and adsorbed species B (B^*) as the most abundant surface intermediates (MASI), which can result in inhibition by species B depending on the magnitude of $K_3 P_B$. Those assumptions result in the following rate law, r_{inh} , for the case that B inhibits the reaction:

$$r_{inh} = \frac{k_2 K_1 P_A L}{1 + K_3 P_B} \quad (2.28)$$

Where K_1 and K_3 are the equilibrium constants for steps 1 and 3, k_2 is the rate constant for step 2, L is the total number of active sites, and P_A and P_B are dimensionless pressures for species A and B, respectively. We can then derive an expression for the case that product inhibition is neglected, in which case at low pressures where the coverage of A is considered low and vacant sites are the sole MASI and the rate expression for the uninhibited reaction, r_u , is given by:

$$r_u = k_2 K_1 P_A L \quad (2.29)$$

The relative percent error between the measured rates is given by:

$$\%error = \frac{100(r_{un} - r_{inh})}{r_{inh}} \quad (2.30)$$

Based on the form of eq. 2.30, we need not specify a value for $k_2K_1P_A$, as this term fortuitously cancels upon further simplification of eq. 2.30.

And finally, from thermodynamics we know that K_3P_B is equivalent to:

$$K_3P_B = P_B \cdot \exp\left(\frac{-\Delta H_{ads,B}^o}{RT}\right) \cdot \exp\left(\frac{\Delta S_{ads,B}^o}{R}\right) \quad (2.31)$$

In Figure 2.17, we show the impact of inhibitory product pressure and the adsorption enthalpy of the inhibitory product on the error that results when product inhibition is ignored. Each of the three rows illustrates the error in the rate using a different enthalpy-dependent formula for the adsorption entropy, as discussed in section 2.4.2 of the main text. The magnitude of the entropy loss upon adsorption increases going from the bottom row to the top row. As expected for exothermic adsorption events, the error is less significant for all pressures and adsorption enthalpies at higher temperatures, reflecting decreases in the coverage of the inhibitory product. Assuming a feed of 100% of A at atmospheric pressure, a reactor temperature of 600 K, and 10% conversion of A (10 kPa B formed), inhibition would result in ten percent error or more if the negative adsorption enthalpy were -50 kJ mol^{-1} or higher, using the lower bound estimate for the entropy of adsorption of $-41.8 \text{ J (mol K)}^{-1}$.

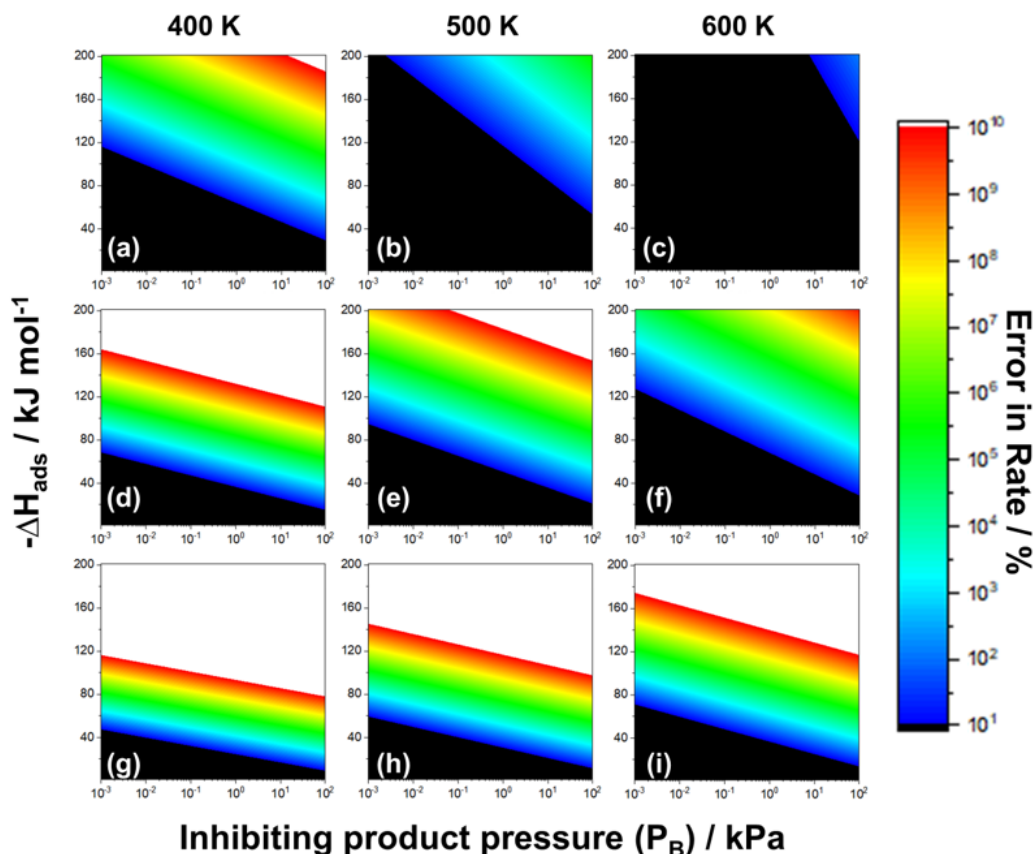


Figure 2.17. Percent difference in the rate of reaction when product inhibition is not included in the rate expression, as a function of the pressure of the inhibiting product (B) and the enthalpy of adsorption of species B. Plots (a)-(c) use the upper bound for entropy of adsorption as reported by Vannice et al. [36] (see Section 2.4.2 of the main text), plots (d)-(f) use the average of the upper bound and lower bound adsorption entropy, and plots (g)-(i) use the lower bound for adsorption entropy ($-41.8 \text{ J (mol K)}^{-1}$) at 400 K (a,d,e), 500 K (b,e,h), and 600 K (c, f, i).

2.6.10 Derivations for Section 2.4.2

The full rate law given by Verma et al. [10] is:

$$-r_{NO} = \frac{k_2 K_1 L [NO]^2 [O_2]}{[NO] + K_3^{-1} K_4^{-1} [NO_2] + K_1 [NO] [O_2] + K_4^{-1} [NO] [NO_2]} \quad (2.32)$$

Where the rate and equilibrium constants refer to the steps from figure 2.5 in the main text. If the numerator and denominator of the equation 2.32 are multiplied by (*), the first term in the resulting denominator the coverage of vacant sites (*), the second term is the coverage of O*, the third term is the coverage of O₂*, and the fourth term is the coverage of NO₂*. Given the near unity reaction order for oxygen reported in Figure 2.2, we conclude that the coverage of O₂* is 0. With that assumption, the rate law becomes:

$$-r_{NO} = \frac{k_2 K_1 L [NO] [O_2]}{1 + \frac{K_3^{-1} K_4^{-1} [NO_2]}{[NO]} + K_4^{-1} [NO_2]} \quad (2.33)$$

By taking the derivative of the natural log of the rate with respect to the natural log of the concentration of each species in the system [10], the reaction orders with respect to NO, O₂, and NO₂ reflect the coverages of these intermediates as defined in equations 2.34 - 2.36:

$$n_{NO} = 2 - \theta_* - \theta_{NO_2*} \quad (2.34)$$

$$n_{O_2} = 1 \quad (2.35)$$

$$n_{NO_2} = -(\theta_{O*} + \theta_{NO_2*}) \quad (2.36)$$

Based on the measured reaction orders for NO, O₂, and NO₂ of 1.5±0.1, 1.1±0.1, and -0.9 ± 0.1, respectively, we calculate that the coverage of NO₂ is 0.4, the coverage of O* is 0.5, and the coverage of * is 0.1, resulting in the required sum of coverages of one. This coverage

of NO_2^* , measured here at 543 K, is twice as high as that reported by Verma et al. [10] for measurements performed at 573 K, and the coverage of O^* reported here is slightly smaller (by 0.1) than that reported by Verma et al., while the coverage of $*$ is identical in both cases. The coverage of O_2^* is zero here, whereas it was 0.1 in Verma et al. [10]. A higher coverage of NO_2^* would be expected given the lower reaction temperature used in this study. In summary, the reaction orders measured in this study are consistent with the rate expression reported in eq. 2.33 and eq. 2.12 in the main text and with the results of Verma et al. [10]. The elementary steps proposed by Metkar et al. [11] are given in figure 2.5. We note that

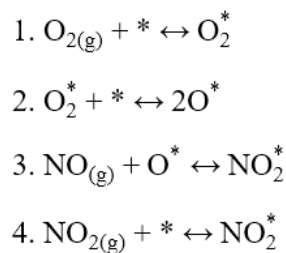


Figure 2.18. Series of elementary steps reported by Metkar et al. [11].

this scheme is not consistent with our data, because it cannot give NO orders greater than 1. Steps 3 and 4, however are the same as steps 3 and 4 in our figure 2.5, but we have assumed that step 3 is quasi-equilibrated as well as step 4. Metkar et al. assumed steps 1, 2, and 4 in figure 2.5 were equilibrated. Using the steps in Scheme 2.18, the following definitions were reported by Metkar et al. [11]:

$$K_i = \frac{k_{f,i}}{k_{b,i}} \quad (2.37)$$

Where $k_{f,i}$ is the forward rate constant for step i and $k_{b,i}$ is the reverse rate constant for step. Each rate constant is defined as:

$$k_i = A_i \cdot \exp\left(\frac{-E_i}{RT}\right) \quad (2.38)$$

where A_i is the pre-exponential factor, E_i is the activation energy for each step, R is the ideal gas constant ($8.314 \text{ J (mol K)}^{-1}$), and T is the temperature in K.

Thus, based on eqs. 2.37 and 2.38, K_4/K_3 is given by:

$$\frac{K_4}{K_3} = \frac{\left(\frac{A_{f,4} \cdot \exp\left(\frac{-E_{f,4}}{RT}\right)}{A_{b,4} \cdot \exp\left(\frac{-E_{b,4}}{RT}\right)} \right)}{\left(\frac{A_{f,3} \cdot \exp\left(\frac{-E_{f,3}}{RT}\right)}{A_{b,3} \cdot \exp\left(\frac{-E_{b,3}}{RT}\right)} \right)} \quad (2.39)$$

The given values for $A_{f,3}$, $A_{b,3}$, $A_{f,4}$, $A_{b,4}$, $E_{f,3}$, $E_{b,3}$, $E_{f,4}$, and $E_{b,4}$ from Metkar et al. [11] are reported in Table 2.3.

Table 2.3. Values for pre-exponential factors and activation energies reported by Metkar et al. [11].

Step (i)	Pre-exponential factor, A_i , $\text{mol m}_{washcoat}^{-3} \text{ s}^{-1}$	Activation energy, E_i , kJ mol^{-1}
f,3	$6.41 \pm 0.6 \cdot 10^5$	29.11 ± 5
b,3	$6.38 \cdot 10^{14}$	165.41 ± 5
f,4	$4.33 \pm 1 \cdot 10^6$	0
b,4	$3.41 \cdot 10^{14}$	141.5

Using the values from Table 2.3 and eq. 2.37, the computed value of K_4/K_3 is:

$$\frac{K_4}{K_3} = 12.7 \cdot \exp\left(\frac{5200}{RT}\right) \quad (2.40)$$

We note that step 4 was written in the opposite direction by Verma et al. [10], such that the left hand side of eq. 2.40 would be $K_3^{-1} K_4^{-1}$ using the notation of Verma et al. that is also used here in the main text.

We can also compute the value of K_4^{-1} itself, using the notation of Verma et al. [10], based

on the values reported by Metkar et al. [11] in Table 2.3:

$$K_4 = \frac{k_{f,4}}{k_{b,4}} = 1.27 \cdot 10^{-8} \cdot \exp\left(\frac{141500}{RT}\right) \quad (2.41)$$

References

- [1] Y.-H. Chin, C. Buda, M. Neurock, and E. Iglesia, "Selectivity of chemisorbed oxygen in c-h bond activation and co oxidation and kinetic consequences for CH_4 - O_2 catalysis on pt and rh clusters," *J. Catal.*, vol. 283, pp. 10–24, 1 2011. DOI: <https://doi.org/10.1016/j.jcat.2011.06.011>.
- [2] F. H. Ribeiro, M. Chow, and R. A. Dallabetta, "Kinetics of the complete oxidation of methane over supported palladium catalysts," *J. Catal.*, vol. 146, pp. 537–544, 1 1994. DOI: <https://doi.org/10.1006/jcat.1994.1092>.
- [3] F. Ribeiro, C. Gerken, G. Rupprechter, G. Somorjai, C. Kellner, G. Coulston, L. Manzer, and L. Abrams, "Structure insensitivity and effect of sulfur in the reaction of hydrodechlorination of 1,1-dichlorotetrafluoroethane ($\text{CF}_3\text{-CFCl}_2$) over pd catalysts," *J. Catal.*, vol. 176, pp. 352–357, 1998. DOI: <https://doi.org/10.1006/jcat.1998.2059>.
- [4] C. Thompson, R. Rioux, N. Chen, and F. Ribeiro, "Turnover rate, reaction order, and elementary steps for the hydrodechlorination of chlorofluorocarbon compounds on palladium catalysts," *J. Phys. Chem. B*, vol. 104, pp. 3067–3077, 2000. DOI: <https://doi.org/10.1021/jp992888n>.
- [5] L. Bollmann, J. Ratts, A. Joshi, W. Williams, J. Pazmino, Y. Joshi, J. Miller, A. Kropf, W. Delgass, and F. Ribeiro, "Effect of zn addition on the water-gas shift reaction over supported palladium catalysts," *J. Catal.*, vol. 257, pp. 43–54, 2008. DOI: <https://doi.org/10.1016/j.jcat.2008.04.005>.
- [6] B. Zugic, S. Zhang, D. Bell, F. (Tao, and M. Flytzani-Stephanopoulos, "Probing the low-temperature water-gas shift activity of alkali-promoted platinum catalysts stabilized on carbon supports," *J. Am. Chem. Soc.*, vol. 136, pp. 3238–3245, 2014. DOI: <https://doi.org/10.1021/ja4123889>.
- [7] A. Phatak, N. Koryabkina, S. Rai, J. Ratts, W. Ruettinger, R. Farrauto, G. Blau, W. Delgass, and F. Ribeiro, "Kinetics of the water-gas shift reaction on pt catalysts supported on alumina and ceria," *Catal. Today*, vol. 123, pp. 224–234, 2007. DOI: <https://doi.org/10.1016/j.cattod.2007.02.031>.
- [8] N. Koryabkina, A. Phatak, W. Ruettinger, R. Farrauto, and F. Ribeiro, "Determination of kinetic parameters for the water-gas shift reaction on copper catalysts under realistic conditions for fuel cell applications," *J. Catal.*, vol. 217, pp. 233–329, 2003. DOI: [https://doi.org/10.1016/S0021-9517\(03\)00050-2](https://doi.org/10.1016/S0021-9517(03)00050-2).
- [9] T. Hamzehlouyan, C. Sampara, J. Li, A. Kumar, and W. Epling, "Experimental and kinetic study of SO_2 oxidation on a pt/c- Al_2O_3 catalyst," *Appl. Catal. B Environ.*, vol. 152–153, pp. 108–116, 2014. DOI: <https://doi.org/10.1016/j.apcatb.2014.01.005>.
- [10] A. Verma, S. Bates, T. Anggara, C. Paolucci, A. Parekh, K. Kamasamudram, A. Yezerecs, J. Miller, W. Delgass, W. Schneider, and F. Ribeiro, "No oxidation: A probe reaction on cu-ssz-13," *J. Catal.*, vol. 312, pp. 179–190, 2014. DOI: <https://doi.org/10.1016/j.jcat.2014.01.017>.

- [11] P. Metkar, V. Balakotaiah, and M. Harold, “Experimental and kinetic modeling study of no oxidation: Comparison of fe and cu-zeolite catalysts,” *Catal. Today*, vol. 184, pp. 115–128, 2012. DOI: <https://doi.org/10.1016/j.cattod.2011.11.032>.
- [12] S. Mulla, N. Chen, W. Delgass, W. Epling, and F. Ribeiro, “No₂ inhibits the catalytic reaction of no and o₂ over pt,” *Catal. Lett.*, vol. 100, pp. 267–270, 2005. DOI: <https://doi.org/10.1007/s10562-004-3466-1>.
- [13] J. Pazmiño, J. Miller, S. Mulla, W. N. Delgass, and F. Ribeiro, “Kinetic studies of the stability of pt for no oxidation: Effect of sulfur and long-term aging,” *J. Catal.*, vol. 282, pp. 13–24, 2011. DOI: <https://doi.org/10.1016/j.jcat.2011.05.007>.
- [14] B. Modén, P. D. Costa, B. Fonfé, D. Lee, and E. Iglesia, “Kinetics and mechanism of steady-state catalytic no decomposition reactions on cu-zsm5,” *J. Catal.*, vol. 209, pp. 75–86, 2002. DOI: <https://doi.org/10.1006/jcat.2002.3622>.
- [15] C.-J. Chen, J. Harris, and A. Bhan, “Kinetics of ethylene epoxidation on a promoted ag/ α -al₂o₃ catalyst—the effects of product and chloride co-feeds on rates and selectivity,” *Chem. – Eur. J.*, vol. 24, pp. 12 405–12 415, 2018. DOI: <https://doi.org/10.1002/chem.201801356>.
- [16] J. Harris, J. Arvay, G. Mitchell, W. Delgass, and F. Ribeiro, “Propylene oxide inhibits propylene epoxidation over au/ts-1,” *J. Catal.*, vol. 365, pp. 105–114, 2018. DOI: <https://doi.org/10.1016/j.jcat.2018.06.015>.
- [17] D. Bregante and D. Flaherty, “Periodic trends in olefin epoxidation over group iv and v framework-substituted zeolite catalysts: A kinetic and spectroscopic study,” *J. Am. Chem. Soc.*, vol. 139, pp. 6888–6898, 2017. DOI: <https://doi.org/10.1021/jacs.7b01422>.
- [18] T. Pham, D. Shi, and D. Resasco, “Kinetics and mechanism of ketonization of acetic acid on ru/tio₂ catalyst,” *Top. Catal.*, vol. 57, pp. 706–714, 2014. DOI: <https://doi.org/10.1007/s11244-013-0227-7>.
- [19] A. Gumidyala, T. Sooknoi, and S. Crossley, “Selective ketonization of acetic acid over hzsm-5: The importance of acyl species and the influence of water,” *J. Catal.*, vol. 340, pp. 76–84, 2016. DOI: <https://doi.org/10.1016/j.jcat.2016.04.017>.
- [20] X. Huang, N. Cant, M. Wainwright, and L. Ma, “The dehydrogenation of methanol to methyl formate: Part i: Kinetic studies using copper-based catalysts,” *Chem. Eng. Process. Process Intensif.*, vol. 44, pp. 393–402, 2005.
- [21] M. Boudart, “Kinetics on ideal and real surfaces,” *AIChE J.*, vol. 2, pp. 62–64, 1956. DOI: <https://doi.org/10.1002/aic.690020113>.
- [22] G. Marin, G. Yablonsky, and D. Constales, *Kinetics of Chemical Reactions. Decoding Complexity*. Wiley-VCH, 2019.
- [23] S. Bates, A. Verma, C. Paolucci, A. Parekh, T. Anggara, A. Yezerets, W. Schneider, J. Miller, W. Delgass, and F. Ribeiro, “Identification of the active cu site in standard selective catalytic reduction with ammonia on cu-ssz-13,” *J. Catal.*, vol. 312, pp. 87–97, 2014. DOI: <https://doi.org/10.1016/j.jcat.2014.01.004>.

- [24] D. Fickel and R. Lobo, "Copper coordination in cu-ssz-13 and cu-ssz-16 investigated by variable-temperature xrd," *J. Phys. Chem. C*, vol. 114, pp. 1633–1640, 2010. DOI: <https://doi.org/10.1021/jp9105025>.
- [25] D. Fickel, E. D’Addio, J. Lauterbach, and R. Lobo, "The ammonia selective catalytic reduction activity of copper-exchanged small-pore zeolites," *Appl. Catal. B Environ.*, vol. 102, pp. 441–448, 2011. DOI: <https://doi.org/10.1016/j.apcatb.2010.12.022>.
- [26] S. Korhonen, D. Fickel, R. Lobo, B. Weckhuysen, and A. Beale, "Isolated cu²⁺ ions: Active sites for selective catalytic reduction of no," *Chem. Commun.*, vol. 47, pp. 800–802, 2010. DOI: <https://doi.org/10.1039/C0CC04218H>.
- [27] M. Groothaert, J. van Bokhoven, A. Battiston, B. Weckhuysen, and R. Schoonheydt, "Bis(μ -oxo)dicopper in cu-zsm-5 and its role in the decomposition of no: A combined in situ xafs, uv-vis-near-ir, and kinetic study," *J. Am. Chem. Soc.*, vol. 125, pp. 7629–7640, 2003. DOI: <https://doi.org/10.1021/ja029684w>.
- [28] C. Segre, N. Leyarovska, L. Chapman, W. Lavender, P. Plag, A. King, A. Kropf, B. Bunker, K. Kemner, P. Dutta, R. Duran, and J. Kaduk, "The mrcat insertion device beamline at the advanced photon source," *AIP Conf. Proc.*, vol. 521, pp. 419–422, 2000. DOI: <https://doi.org/10.1063/1.1291825>.
- [29] A. Kropf, J. Katsoudas, S. Chattopadhyay, T. Shibata, E. Lang, V. Zyryanov, B. Ravel, K. McIvor, K. Kemner, K. Scheckel, S. Bare, J. Terry, S. Kelly, B. Bunker, and C. Segre, "The new mrcat (sector 10) bending magnet beamline at the advanced photon source," *AIP Conf. Proc.*, vol. 1234, pp. 299–302, 2010. DOI: <https://doi.org/10.1063/1.3463194>.
- [30] C. Paolucci, A. Parekh, I. Khurana, J. D. Iorio, H. Li, J. A. Caballero, A. Shih, T. Anggara, W. Delgass, J. Miller, F. Ribeiro, R. Gounder, and W. Schneider, "Catalysis in a cage: Condition-dependent speciation and dynamics of exchanged cu cations in ssz-13 zeolites," *J. Am. Chem. Soc.*, vol. 138, pp. 6028–6048, 2016. DOI: <https://doi.org/10.1021/jacs.6b02651>.
- [31] D. Hickman, J. Degenstein, and F. Ribeiro, "Fundamental principles of laboratory fixed bed reactor design," *Curr. Opin. Chem. Eng.*, vol. 13, pp. 1–9, 2016. DOI: <https://doi.org/10.1016/j.coche.2016.07.002>.
- [32] V. Cybulskis, A. Smeltz, Y. Zvinevich, R. Gounder, W. Delgass, and F. Ribeiro, "Learning the fundamentals of kinetics and reaction engineering with the catalytic oxidation of methane," *Chem. Eng. Educ.*, vol. 50, pp. 202–210, 2016.
- [33] H. Massaldi and J. Maymó, "Error in handling finite conversion reactor data by the differential method," *J. Catal.*, vol. 14, pp. 61–68, 1969. DOI: [https://doi.org/10.1016/0021-9517\(69\)90356-X](https://doi.org/10.1016/0021-9517(69)90356-X).
- [34] N. Akter, X. Chen, J. Parise, J. Boscoboinik, and T. Kim, "Effects of copper loading on nh₃-scr and no oxidation over cu impregnated cha zeolite," *Korean J. Chem. Eng.*, vol. 35, pp. 89–98, 2018. DOI: <https://doi.org/10.1007/s11814-017-0268-x>.
- [35] J. Kwak, D. Tran, J. Szanyi, C. Peden, and J. Lee, "The effect of copper loading on the selective catalytic reduction of nitric oxide by ammonia over cu-ssz-13," *Catal. Lett.*, vol. 142, pp. 395–301, 2012. DOI: <https://doi.org/10.1007/s10562-012-0771-y>.

- [36] M. Vannice, S. Hyun, B. Kalpakci, and W. Liah, “Entropies of adsorption in heterogeneous catalytic reactions,” *J. Catal.*, vol. 56, pp. 358–362, 1979. DOI: [https://doi.org/10.1016/0021-9517\(79\)90128-3](https://doi.org/10.1016/0021-9517(79)90128-3).
- [37] Y. Ji, T. Toops, U. Graham, G. Jacobs, and M. Crocker, “A kinetic and drifts study of supported pt catalysts for no oxidation,” *Catal. Lett.*, vol. 110, pp. 29–37, 2006. DOI: <https://doi.org/10.1007/s10562-006-0100-4>.

3. PROPYLENE OXIDE INHIBITS PROPYLENE EPOXIDATION OVER AU/TS-1

3.1 Introduction

Propylene epoxidation is a critical step in industrial polyurethane production and has an estimated annual production of 8.6 million tons per year [1]. Since the first report of titania-supported Au catalysts for the partial oxidation catalysis by Haruta and co-workers [2], propylene epoxidation rates (per kg catalyst) over Au-Ti catalysts have increased dramatically. These increases have been achieved by limiting the TiO_2 domains to single Ti atoms by incorporation in SiO_2 substrates, particularly Ti-Si zeolites such as TS-1, leading to increased epoxidation rate (from 11 $\text{g}_{\text{PO}} \text{kg}_{\text{cat}}^{-1} \text{h}^{-1}$ over Au/ TiO_2 at 323 K to 150 $\text{g}_{\text{PO}} \text{kg}_{\text{cat}}^{-1} \text{h}^{-1}$ over Au/TS-1 at 473 K) and with selectivity (from 70% to 80% [3]) that approaches that of Au/ TiO_2 (99% [2]). Further steady-state rate and selectivity increases were achieved by judicious choice of promoters [4]–[10], resulting in steady state propylene oxide (PO) formation rates of 300 $\text{g kg}_{\text{cat}}^{-1} \text{h}^{-1}$ with a PO selectivity of 80% [4]. Similarly, reduction of zeolite crystal size and addition of mesoporosity resulted in steady state PO formation rates of 140 $\text{g kg}_{\text{cat}}^{-1} \text{h}^{-1}$ over 50 h on stream with a propylene oxide selectivity of 95% [11].

Despite increases in reaction rates, comparatively minor increases (from 10% to 40%) [2], [3] in hydrogen efficiency (S_{H_2} = mol PO produced per mol H_2 consumed) over Au/TS-1 catalysts compared to the industrially required value of 50% continue to limit the utility of these catalysts [12]. While S_{H_2} values between 35 and 40% have been reported for Au/TS-1 with $\text{Si}/\text{Ti} > 100$ and Au loadings of 0.009–0.03 wt%, the steady state propylene epoxidation rates over these catalysts range from 22 to 80 $\text{g kg}_{\text{cat}}^{-1} \text{h}^{-1}$ [3], [9]. A S_{H_2} of 99% has been reported for a 0.005 wt% Au supported on TS-1 with a Si/Ti ratio of 170 (TS-1(170)), though the propylene epoxidation rate was 4.8 $\text{g kg}_{\text{cat}}^{-1} \text{h}^{-1}$ [9]. The S_{H_2} values measured over 0.04 wt% Au catalysts supported on uncalcined TS-1 (U-TS-1) catalysts at steady state are 40%, compared to 2% for their calcined counterparts at this Au loading [13]. While state-of-the-art Au-Ti catalysts for direct gas-phase epoxidation of propylene lack the combination of PO selectivity, H_2 selectivity, and PO formation rate per mass of catalyst necessary to compete with existing processes, this catalyst system is of interest for the opportunity

it presents to unravel the complex catalytic chemistry and kinetics of *in situ* hydrogen peroxide formation on coordinatively unsaturated Au clusters and epoxidation reactions of such species in proximity to isolated Ti atoms. In addition, understanding these Au-Ti catalysts may accelerate realization of the potential environmental and safety benefits of this approach to PO production. Without accurate measurement of the reaction kinetics, it is not tractable to determine whether the most active sites for propylene oxide production have inherently low S_{H_2} , or if there are separate, low epoxidation rate, high H_2 oxidation rate sites that could be limited during catalyst synthesis. Further, efforts to determine the most active Au-Ti sites in order to stabilize these sites via new synthetic procedures for operation at industrially relevant pressures [14] are not possible without first understanding the reaction kinetics.

Development of reaction mechanisms consistent with all data measured in the literature has lagged behind improvements in maximum propylene epoxidation rates and selectivities. Measured H_2/D_2 kinetic isotope effects on Au/TiO₂ catalysts [15] indicate the breaking of a bond to hydrogen in the rate determining step, consistent with kinetically relevant hydroperoxy intermediates observed spectroscopically over Au/TiO₂ catalysts previously [16]. Raman spectroscopy combined with measurement of H_2O_2 formation over colloidal palladium catalysts with either $^{16}O_2$ or $^{18}O_2$ reactants confirmed that oxygen was present as molecular oxygen during H_2O_2 formation over these catalysts [17]. An experimental study of activation energies and apparent reaction orders by Taylor et al. [18] determined reaction orders (H_2 : 0.5, O_2 : 0.3, C_3H_6 : 0.2) across Au/TS-1 catalysts with a range of molar Si/Ti ratios (36–144), Au loadings (0.02–0.06 wt%), and at a range of feed partial pressures (H_2 : 8–24 mol% O_2 : 2–8 mol%; C_3H_6 : 8–24 mol%) and temperatures (413–473 K), similar to those reported elsewhere [19], [20]. These findings are consistent with a two-site ‘simultaneous’ mechanism, where a hydroxperoxy intermediate forms on a Au site and reacts with propylene adsorbed on an adjacent framework Ti site in TS-1 [18], [21]. A second mechanism first proposed by Lu et al. [19] and reaffirmed by Kanungo et al. [22] includes two kinetically relevant steps, the first of which forms HOOH adsorbed at one of two Au sites required and the second involves decomposition of a C_3H_6 -HOOH-Ti species into PO and water. The mechanism presented by Lu et al. and Kanungo et al. includes separate

Au regions involved in either H_2 oxidation only or both H_2 oxidation and combustion [19], [22]. This mechanism is consistent with reaction orders reported by Taylor et al. [18], and notably involves adsorption of C_3H_6 at Au rather than Ti sites. Additionally, the reaction orders reported by Taylor et al. [18] are inconsistent with a sequential two-site mechanism, in which H_2O_2 forms on Au particles prior to desorbing intact, co-adsorbing with propylene on Ti-defect sites ((OH)-Ti-(OSi)₃) and reacting, as has been proposed as the mechanism for liquid-phase epoxidation reactions over TiO_2 and TS-1 [23], since such a mechanism would result in reaction orders for hydrogen and oxygen being equal, which has not been observed [18].

Joshi et al. calculated lower energy barriers for the simultaneous mechanism than the sequential mechanism over Au clusters supported within TS-1 pores [21]. The predominance of the simultaneous mechanism over small Au clusters in the pores of TS-1 is also consistent with the observations of Lee et al., in which Au deposition on a TS-1 catalyst over-coated with an S-1 shell followed by measurement of propylene epoxidation rates leads to reaction rates (per kg TS-1) that are 4x higher than those measured over Au/TS-1, with similar measured apparent activation energy to conventional Au/TS-1 [24]. Furthermore, physical mixtures of TS-1 and Au supported on S-1 are not reactive [24]. These results demonstrate that the Au sites located within the pores of TS-1 are the active Au species for this reaction. Propylene epoxidation over Au supported on U-TS-1 results in reactivity that slowly increases with time on stream (over 20 h at reaction temperature), concurrent with increases in BET surface area, suggesting that small Au ensembles can migrate into TS-1 pores excavated by removal of confined tetrapropylammonium cations in the presence of H_2O_2 , H_2O , and O_2 at 473 K [13]. Although the epoxidation rate appears to increase over Au clusters confined in TS-1 pores, the H_2O_2 decomposition rate over Au/ TiO_2 catalysts has been reported to increase as Au cluster size decreases [25], suggesting that the desirable clusters for PO production may be undesirable for maintaining high hydrogen selectivity.

Despite these experimental and theoretical efforts to determine the gas-phase propylene epoxidation mechanism, accurate experimental measurement of kinetic parameters for reactions with product inhibition, as has been reported recently for liquid-phase cyclohexene epoxidation with H_2O_2 over Nb^{5+} , Ta^{5+} , and Ti^{4+} sites in Beta zeolites (313 K, [26]), requires

either product co-feeding or correction of kinetic parameters for known product inhibition [27]. For gas-phase propylene epoxidation, inhibition has not been observed previously, though deactivation due to irreversible site blockage by polymeric propylene oxide derivatives on Au/TS-1 was reported by Nijhuis et al. [28]. To our knowledge, neither propylene epoxidation experiments in a CSTR with correction for product inhibition, nor gas-phase propylene oxide co-feed experiments in plug-flow reactors has been reported.

Here, we report apparent activation energies and apparent reaction orders (measured by varying each component independently) for carbon dioxide, hydrogen, oxygen, propylene, propylene oxide, and water, and provide a clear demonstration that propylene oxide reversibly inhibits rates of propylene oxidation, but not hydrogen oxidation. We demonstrate that this product inhibition occurs at all space velocities measured, and that inhibition at low space velocity results exclusively from propylene oxide and not from the major reaction byproducts (CO_2 and water). A careful reexamination of the proposed mechanisms for direct gas-phase propylene epoxidation is presented, which accounts for inhibition by propylene oxide and provides evidence that propylene oxide binds to both sites invoked in the simultaneous mechanism. The reaction orders measured for hydrogen, oxygen, and propylene are consistent with the simultaneous mechanism for propylene epoxidation, and rule out a two-site sequential mechanism under the conditions studied here. The lack of propylene oxide inhibition of H_2 oxidation rates implies that there are multiple sites or site ensembles present on conventional Au/TS-1 catalysts.

3.2 Experimental methods

3.2.1 Catalyst synthesis

TS-1 synthesis

Synthesis of titanium silicalite-1 (TS-1) was performed according to previously reported procedures [29]. Briefly, synthesis was performed by first mixing 3.85 g of polyoxyethylene 20-sorbitan monolaurate (Tween 20, Fischer Scientific, enzyme grade) and 61.56 g of deionized water (DI water) (Millipore, Synergy UV Water Purification System, 18.2 $\text{M}\Omega/\text{cm}$ resistivity) and stirring (~ 300 RPM) for 900 s at ambient temperature. Then, 29.38 g of

tetrapropylammonium hydroxide (TPAOH, Alfa Aesar, 40 wt%) and 70.00 g of tetraethylorthosilicate (TEOS, Sigma Aldrich, 98%) were added, followed by stirring (~ 300 RPM) under ambient conditions for 1–2 h. In a separate 15 cm³ disposable centrifuge tube (VWR, sterile polypropylene), 1.14 g of titanium (IV) butoxide (TBOT, Alfa Aesar, 99%+) and 17.26 g of isopropyl alcohol (IPA, Sigma Aldrich, 99.5%) were combined and stirred with a vortex mixer (VWR Mini Vortex Mixer) and subsequently added dropwise to the synthesis gel, with stirring (~ 300 RPM), under ambient conditions. The final molar ratio of the synthesis gel was 1 SiO₂/0.01 TiO₂/0.17 TPA⁺/13.1 H₂O/0.0093 Tween 20/0.04 C₄H₁₀O/0.85 C₃H₈O. The solution was then stirred (350 RPM), for at least 1 h at 313–318 K before addition to a Teflon-lined stainless-steel autoclave (45 cm³, Parr Instrument Company model 4744) and placement in an isothermal oven (Yamato DKN402C Constant Temperature Oven) and heated without agitation at 413 K for at least 18 h. The resulting solid was separated from the slurry via centrifugation (Thermo Scientific Heraeus Megafuge 16, 5000 RPM for 1800 s), and then washed twice with DI water, twice with acetone (Sigma Aldrich, 99.5%+), and one more time with DI water, with each wash using 15 cm³ of DI water or acetone per gram of TS-1 and a vortex mixing time of ~ 30 s. Once washed, the solid was dried for approximately 48 h at 363 K. The dried TS-1 was then treated in flowing air (100 cm³ min⁻¹ g_{cat}⁻¹) at 853 K for 10 h (1 K min⁻¹ ramp).

Gold deposition

A typical gold deposition onto TS-1 was performed according to previously published protocols [30]. First, approximately 0.040 g of hydrogen tetrachloroaurate(III) trihydrate (HAuCl₄·3H₂O, Alfa Aesar, 99.99% (metals basis)) were mixed with 8.0 g of DI water followed by addition of 0.40 g of calcined TS-1. The slurry (water, gold precursor, and TS-1) was mixed under ambient conditions at 900 RPM for 1800 s. An appropriate amount of 0.5 M (1 N) sodium carbonate (Sigma Aldrich, 99.5%+) solution was then added to the slurry to bring the Na/Au molar ratio to a value chosen based on the desired final pH of the solution. Typically, this ratio was between 5.5 and 7.5 for a target final pH of the slurry was ~ 7 –7.5, measured via pH probe calibrated before each Au deposition (Mettler Toledo FiveEasy pH

meter). The slurry was stirred at 900 RPM for another 10 h at ambient conditions. The Au/TS-1 was then separated from the slurry liquid via centrifugation (Thermo Scientific Heraeus Megafuge 16, 5000 RPM for 1800 s) and washed with approximately 25 cm³ of DI water per g of Au/TS-1 for ~90 s with vigorous stirring. The resulting solid was then dried overnight under vacuum at room temperature.

Catalyst characterization

Bulk elemental compositions of samples were determined using atomic absorption spectroscopy (AAS) performed with a Perkin Elmer AAnalyst 300 Atomic Absorption Spectrometer. 1000 ppm AAS standards (Alfa Aesar, TraceCERT, ± 4 ppm) for each metal were diluted to create calibration standards, and the instrument was calibrated for each element prior to collecting measurements. Au/TS-1 samples (typically 0.10 g) were dissolved in 2 g of HF (48 wt%, Alfa Aesar) and 2.5 g of aqua regia (aqua regia prepared from a 2:1 v/v ratio of 37 wt% HCl, Mallinckrodt Chemicals and 70 wt% HNO₃, Mallinckrodt Chemicals) overnight and then further diluted with 30 g of deionized water. Absorbance values were measured at 399.9 nm in an acetylene/nitrous oxide flame for Ti, and at 267.6 nm in an air/acetylene flame for Au. Na content was determined by measuring absorbance values at 589.0 nm in an air/acetylene flame. Titanium AAS measurements were taken after calcination but before gold deposition. The Ti weight fraction was used along with the unit cell formula for zeolite MFI to calculate the Si/Ti ratios for each sample.

Powder X-ray diffraction (XRD) patterns were collected on a Rigaku Smartlab X-ray diffractometer equipped with an ASC-6 automated sample changer and a Cu Ka X-ray source (1.76 kW). Typically, 0.01 g of sample were packed within zero background, low dead volume sample holders (Rigaku) and diffraction patterns were measured from 4 to 40° at a scan rate of 0.00417° s⁻¹ with a step size of 0.02°.

N₂ (77 K) adsorption isotherms were measured on samples (~0.03 g, sieved to 180–250 μ m diameter particle size) using a Micromeritics ASAP2020 Surface Area and Porosity Analyzer. Prior to measurement of isotherms, samples were degassed under vacuum (<0.005 Torr) by heating to 393 K (0.0167 K s⁻¹) for 2 h, then heating under vacuum to 623 K (0.0167 K

s⁻¹) for 8 h. Micropore volumes were determined from a semi-log derivative analysis of N₂ isotherms ($\delta(V_{ads}/g)/\delta(\log(P/P_0))$ vs. $\log(P/P_0)$) to identify the completion of micropore filling.

Diffuse reflectance UV-Vis (DRUV-Vis) spectra were collected on a Varian Cary 5000 UV-Vis-NIR using a Harrick Praying Mantis *in situ* diffuse reflectance cell. Spectra were collected on samples: (i) first exposed to ambient conditions and held in flowing dry He (4.17 cm³ s⁻¹ (g zeolite)⁻¹) ("ambient" spectra) and (ii) after subsequent treatment to 523 K (~ 0.5 K s⁻¹) for 1800 s in flowing dry He (4.17 cm³ s⁻¹ (g zeolite)⁻¹) ("dehydrated" spectra). Spectra were collected at a scan rate of 10 nm s⁻¹, using poly(tetrafluoroethylene) (PTFE, 1 μ m powder, Sigma-Aldrich) as a 100% reflectance standard, and then converted to an absorption spectrum using the Kubelka-Munk (F(R)) function. Absorption edge energies were calculated from the x-intercepts of Tauc plots of $[F(R)h\nu]^2$ vs. $h\nu$ (additional details in Section 3.5.4) [31]–[33].

Kinetic studies of propylene epoxidation

The gas-phase reaction kinetic data were obtained in a continuous stirred tank reactor (CSTR), which ensures isoconcentration throughout the catalyst bed under all feed conditions and reactant conversions. This setup, detailed in Fig. 3.6, facilitates quantitative study of orders of reaction, including product inhibition, as discussed for H₂O inhibition in the methane oxidation reaction by Cybulskis et al. [27]. The piping and instrumentation diagram (P + ID) shown on the right-hand side of Fig. 3.6 shows that by choosing the proper valve configuration the reactor can be operated as a U-tube PFR, or, with the recirculating pump (Metal Bellows MB-21), as a CSTR, thus facilitating the advantages of the CSTR configuration and allowing direct comparison with previously reported data collected in plug flow reactors.

Measurement of the kinetics was performed on as-deposited Au/TS-1 catalysts by sieving the Au/TS-1 samples to a 125–250 μ m size range, followed by loading 0.080–0.400 g into a Pyrex U-tube reactor (diagram and photograph shown in Fig. 3.7) equipped with a coiled inlet to allow for preheating the reaction gases, and placement of this reactor in a

furnace controlled by a Eurotherm 2408 controller and protected by an over temperature thermocouple and controller (Omega CN9000A). Reaction temperature was measured by a thermocouple (Omega) inserted within a quartz thermowell that was located in the radial and vertical centers of the catalyst bed. The reactor was connected to the glass manifold that serves as a recirculating volume (Fig. 3.6) using $\frac{1}{4}$ " ultra-torr fittings (Swagelok). The top of the furnace was insulated, and the reactor checked for leaks at ambient temperature by pressurizing to 3 PSI gauge with N₂. The reactor was considered sealed when no change in pressure occurred over a period of 600 s. Next, flow of the reactant mixture, typically 10% H₂, 10% O₂, 10% C₃H₆, and 70% N₂ at a total flowrate of either 0.6 cm³ s⁻¹ during an initial day of catalyst activation or 1.1 cm³ s⁻¹ for kinetic experiments was started using mass flow controllers connected to H₂ (Praxair, 99.999%), air (Indiana Oxygen, Air Zero Grade, <1 ppm total hydrocarbon content), N₂ (Indiana Oxygen, 99.999%) and C₃H₆ (Matheson, Research Purity, 99.99%) cylinders. Care was taken such that hydrogen and propylene were introduced after nitrogen and air flow began, and that H₂ and C₃H₆ never exceeded 10 mol% of the flow to avoid operation in an explosive regime. After reactant flow begins and the total flowrate was confirmed using a bubble flowmeter, the reaction test was initiated by increasing the temperature to a standard temperature of 473 K (0.017 K s⁻¹ ramp rate) prior to an initial period of ~3 h, during which the PO formation rate decreased to ~80% of its initial value, followed by a period of slower deactivation. Kinetic studies were performed by independently varying either the H₂, O₂, air, or C₃H₆ flowrates while maintaining constant total flowrate by varying the N₂ flowrate. CO₂ and propylene oxide co-feed experiments were performed using a pure CO₂ (Indiana Oxygen) cylinder and a 1% PO/N₂ cylinder (Airgas, 1.032 ± 0.02% PO/N₂, Certified Standard Grade), while H₂O co-feed experiments were performed by flowing N₂ through a vapor-liquid-equilibrium (VLE) saturator at ambient temperature (295 K). To avoid creating a dangerous, explosive feed mixture, H₂, O₂, C₃H₆ order measurements were performed by decreasing the concentrations from the standard 10% flowrate in a non-monotonic fashion. Apparent activation energy measurements were performed starting from the standard 473 K reaction temperature by varying the temperature in a non-monotonic fashion from 443 to 483 K. In both apparent reaction order and apparent activation energy measurements, a minimum of three repeated GC injections were taken at

each condition and the reported data represented the average of the last two (or more) of these injections.

Products were injected into an on-line Agilent 6890 GC equipped with a Supelcowax-10 capillary column (Agilent, 60 m x 530 μ m x 1 mm) connected to a flame-ionization detector (FID) and a 60/80 Chromosorb 102 packed column connected to a thermal-conductivity detector (TCD) with N₂ used as the carrier gas for both columns and detectors. GC peak areas were quantified using pre-measured response factor calibrations for propylene, propanal, ethanal, acetone, acrolein, and propylene oxide on the FID and H₂, O₂, and CO₂ for the TCD. Propylene conversions measured using the propylene peak were typically less than 5%, near the accuracy of the instrument. Thus, reported C₃H₆ conversions ($X_{C_3H_6}$) were calculated as moles of carbon containing products detected divided by the moles of C₃H₆ fed (3.1)

$$X_{C_3H_6} = \frac{\text{total moles carbon in products}}{\text{moles } C_3H_6 \text{ fed}} / 3 \quad (3.1)$$

The product carbon selectivity for a given product i ($S_{c,i}$) was defined on a carbon basis as:

$$S_{c,i} = \frac{\text{moles of product i formed}}{\text{total moles C in products}} \times (\text{number of carbon atoms in i}) \quad (3.2)$$

while the hydrogen selectivity (S_{H_2}) was defined as:

$$S_{H_2} = \frac{\text{moles of PO formed}}{\text{total moles } H_2 \text{ consumed}} \quad (3.3)$$

The H₂ oxidation rate (r_{H_2O}) was defined as:

$$r_{H_2O} = \frac{\text{moles } H_2 \text{ consumed} - \text{moles of PO formed}}{g_{cat} \cdot s} \quad (3.4)$$

assuming one mole of H₂ is consumed in water formation per mole of propylene oxide formed.

3.3 Results and discussion

3.3.1 Structural characterization of titanosilicates

XRD patterns, N₂ isotherms, and UV–Visible spectra (523 K) after dehydration for all TS-1 samples used in this study are reported in Figs. 3.8, 3.9, and 3.10, respectively. The XRD patterns and N₂ micropore volumes (Table 3.1) for all TS-1 samples were consistent with those reported previously for TS-1 (MFI micropore volumes 0.135–0.146 cm³ g^{−1} [3]).

UV–VIS peak centers for dehydrated, isolated Ti⁴⁺ sites in TS-1 were between 215 nm and 225 nm, similar to those previously reported under ambient conditions for TS-1 synthesized in our lab [3] and for Ti-Beta-F zeolites reported previously [34]. The UV–VIS edge energies of >4.9 eV for all dehydrated TS-1 samples (Tauc plots shown in Fig. 3.11, edge energies reported in Table 3.1), are characteristic of primarily isolated, dehydrated Ti⁴⁺ sites in zeolites, but that does not exclude the possibility of a minority of nano-sized octahedral TiO₂ domains [35], [36] whose edge energies increase with decreasing domain size due to quantum confinement effects [37]. The lack of distinct peaks at 25.7°, 27.9°, and 31° is characteristic of TS-1 XRD patterns without larger (>3 nm [38]) TiO₂ domains [39]. Bulk Ti, Au, and Na contents measured by atomic absorption spectroscopy (AAS) for Au-loaded TS-1 samples are reported in Table 3.1, and demonstrate the low Au loadings typical of Au/TS-1 catalysts performed by careful deposition-precipitation procedures [3]. Despite the use of 4–5 mol Na per mol Au for pH control during the Au DP step, the final Na/Au ratios measured using AAS range from 11 to 140 for the samples reported in Table 3.1. To our knowledge, Na contents for samples prepared by this method have not been reported previously, and may underlie the low Au efficiency during the DP procedure as well as the possibility of Na covered Au particles, Ti defect sites, or Na exchanged SiOH groups in Au/TS-1 catalysts reported here. Na exchange on TS-1 (Na/Ti 3.5) has been reported to eliminate oxidation and epoxidation activity, as well as hydroperoxo complex formation, for epoxidation of n-octane over TS-1 in the presence of aqueous H₂O₂ at 353 K [40]. No clear effects of Na were observed in this work, but we note that the Na/Au ratio may be a variable worth considering in future studies.

Table 3.1. Characterization data for all catalyst samples used in this study.

Catalyst	Si/Ti ^a	Au wt% ^b	Na wt% ^b	Au/Ti ^a	Na/Ti ^a	Na/Au ^a	V_{ads} (N ₂ , 77 K) ^c (cm ³ g ⁻¹)	DRUV Band Center (nm) ^d	DRUV Edge Energy (eV) ^d	PO Rate (10 ⁻⁷ mol PO g _{cat} ⁻¹ s ⁻¹) ^e
0.110Au/TS-1(81)	81	0.110	n.m.*	0.042	n.m.	n.m.	0.170	220	5.07	3.3
0.092Au/TS-1(75)	75	0.092	0.13	0.030	0.36	12	0.148	225	4.94	4.7
0.063Au/TS-1(75)	75	0.063	0.13	0.020	0.35	17	0.148	225	4.94	3.7
0.100Au/TS-1(143)	143	0.10	0.14	0.060	0.67	11	0.147	215	5.18	4.3
0.022Au/TS-1(143)	143	0.022	0.089	0.013	0.44	35	0.147	215	5.18	2.4
0.019Au/TS-1(143)	143	0.019	0.31	0.011	1.53	140	0.147	215	5.18	1.6
0.040Au/TS-1(81)	81	0.040	n.m.	0.016	n.m.	n.m.	0.170	220	5.07	3.1
0.030Au/TS-1(81)	81	0.030	n.m.	0.013	n.m.	n.m.	0.170	220	5.07	3.1
0.044Au/TS-1(81)	81	0.044	n.m.	0.015	n.m.	n.m.	0.170	220	5.07	4.0
0.033Au/TS-1(143)	143	0.033	n.m.	0.013	n.m.	n.m.	0.147	215	5.18	2.4
0.069Au/TS-1(143)	143	0.069	n.m.	0.046	n.m.	n.m.	0.147	215	5.18	4.5
0.064Au/TS-1(143)	143	0.064	n.m.	0.043	n.m.	n.m.	0.147	215	5.18	4.7

^a Ratios reported are molar ratios determined by atomic absorption spectroscopy (AAS). Errors are $\pm 21\%$.

^b Bulk composition determined by AAS. Errors are $\pm 15\%$.

^c Micropore volume determined from total N₂ uptake at the end of micropore filling in adsorption isotherms measured at 77 K (Section 3.5.3).

^d Diffuse reflectance UV-Vis spectra (band center at maximum F(R) intensity) and Tauc plots for samples after dehydration at 523 K (Section 3.5.4).

^e Average PO rates are reported as the average values between 3rd and 5th hour on stream during the initial activation day (SV = 14,000 cm³ g_{cat}⁻¹ h⁻¹, T = 200°C, 10% C₃H₆/10% H₂/10% O₂/70% N₂ by volume). Multiply by 2.09 x 10⁸ to convert units to g_{PO} kg_{cat}⁻¹ h⁻¹.

* n.m. not measured.

3.3.2 Measurement of reaction kinetics of over Au/TS-1 catalysts

Propylene epoxidation

Fig. 3.1 shows the typical time on stream behavior for Au/TS-1 catalysts under reactant flow (10% H₂/10% O₂/10% C₃H₆/70% N₂ by volume at 473 K). After reaching reaction temperature, the PO formation rate showed an initial rapid deactivation ($k_{deactivation} = 0.029$ h⁻¹) which decelerated after 3–4 h on stream ($k_{deactivation} = 0.002$ h⁻¹, Fig. 3.12). Measurement of reaction orders was performed after the temperature ramp and initial deactivation, with measured reaction rates corrected for the slow deactivation thereafter, enabled by intermittent measurements at the standard conditions and by assuming first order exponential decay (example shown in Fig. 3.13, Supporting Information).

Measurement of apparent H₂, O₂, and C₃H₆ reaction orders in the absence of products in the feed resulted in similar reaction orders as those reported elsewhere (Table 3.2, example data shown in Fig. 3.14), of 0.6, 0.2, and 0.2 respectively, while measured apparent activation energies were also similar to those reported elsewhere (30 kJ mol⁻¹, Fig. 3.15, vs. 28 kJ

mol^{-1} [24]). The similarity of reaction orders measured on various supports (TS-1 and Ti-TUD), at various Au loadings (0.02–0.10 wt%), a range of space velocities ($7,000\text{--}26,000 \text{ cm}^3 \text{ g}_{\text{cat}}^{-1} \text{ h}^{-1}$), and in both PFR and CSTR configurations implies that these reaction orders are not measured under mass transfer limited conditions.

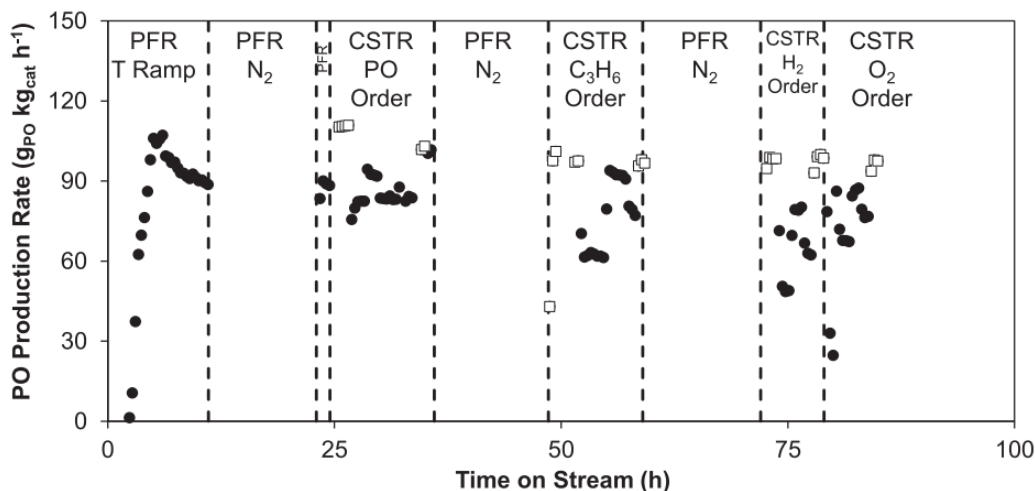


Figure 3.1. Time on stream (TOS) profile for 0.092Au/TS-1(75). Initial rate increase occurs during temperature ramp (0.0083 K s^{-1}) until reaction temperature (473 K) is reached. Returns to 10% H_2 /10% O_2 /10% C_3H_6 /70% N_2 (by volume) are represented by white boxes after the initial activation under these conditions. Reaction orders are measured by non-monotonically varying the reactant (or product) flow rate of interest while keeping the total flow rate constant ($\text{SV} = 14,000 \text{ cm}^3 \text{ g}_{\text{cat}}^{-1} \text{ h}^{-1}$ up to 25 h, then 26,000 for $\text{TOS} > 25 \text{ h}$) and varying the balance N_2 flow rate to compensate. N_2 flow at reaction temperature maintained between each experiment to maintain O_2 - and moisture-free atmosphere.

The space velocity employed here is in a similar range to that used previously ($7,000\text{--}14,000 \text{ cm}^3 \text{ g}_{\text{cat}}^{-1} \text{ h}^{-1}$), conditions under which the external mass transfer limitations were negligible (Mears criterion ~ 0.15) and the presence of internal mass transfer limitations was excluded by estimation of a Thiele modulus between 10^{-1} and 10^{-3} [18], [24] (Derivation shown in Section S.5, Supporting Information). Further, these results suggest similar active Au/Ti species across the range of titanosilicate topologies and Au weight loadings tested.

Measurement of the PO reaction order while co-feeding controlled amounts of PO (0.06–0.30 vol% PO) and correcting for deactivation yielded a reaction order of, for example, -0.6 ± 0.02

Table 3.2. Measured reaction orders compared to those reported in literature.

Source	Molar Si/Ti Ratio	SV ($\text{cm}^3 \text{ g}_{\text{cat}}^{-1} \text{ h}^{-1}$)	Au loading (wt%)	H ₂ Order	O ₂ Order	C ₃ H ₆ Order	PO Order ^e
[19] ^a	33	7000	0.11	0.5	0.2	0.4	–
[18]	36, 143	7000	0.02, 0.04, 0.06	0.6	0.3	0.2	–
[20] ^b	33	7000	0.02	0.5	0.3	0.2	–
Au/TS-1	75–143	26,000	0.02–0.09	0.6 ± 0.08^c	0.2 ± 0.01^c	0.2 ± 0.08^c	-0.6 ± 0.2
Au/TS-1, corrected for inhibition	75–143	26,000	0.02–0.09	1 ± 0.2^d	0.4 ± 0.06^d	0.4 ± 0.1^d	-0.6 ± 0.2

^a Catalyst used was Au/Ti-TUD.

^b Orders measured in packed-bed catalytic membrane reactor with Au/TS-1 at higher O₂ and H₂ partial pressures (up to 40 vol% each, respectively).

^c Average values for our measured reaction orders (c: H₂, O₂, and C₃H₆ not PO corrected; d: Orders corrected by 1.6 to account for dependence of the rate on [PO]^{−0.6}. Errors determined from standard deviation of the measured reaction orders across eight TS-1 samples listed in Table 3.1.

^d Average values for our measured reaction orders (c: H₂, O₂, and C₃H₆ not PO corrected; d: Orders corrected by 1.6 to account for dependence of the rate on [PO]^{−0.6}. Errors determined from standard deviation of the measured reaction orders across eight TS-1 samples listed in Table 3.1.

^e Average value of measured PO orders.

(0.030Au/TS-1(81), Fig. 3.2) or, on average for all Au/TS-1 samples, -0.6 ± 0.2 (Table 3.2).

We note that we measured a range of PO orders from -0.4 to -0.8 over samples with varying Au loading and Si/Ti ratios, apparently reflecting a change in PO coverage, but have not yet been able to establish a clear correlation to catalyst properties. The active site geometry may vary from catalyst to catalyst due to differences in Au-Ti proximity, Au particle size, and Au location, resulting in the observed variations in the measured PO order. The inverse dependence of PO production rate on PO concentration implies substantial surface coverage of PO on kinetically relevant catalytic sites. The decrease in PO rate with PO concentration observed on all catalysts included in this study, including data collected without PO co-feeds at propylene conversions as low as 0.6%, demonstrates that operation of plug flow reactors at low reactant conversion (<1%) in the absence of co-fed products does not guarantee such reactors can be considered differential. Varying the space velocity from 5,200 to 62,000 $\text{cm}^3 \text{ g}_{\text{cat}}^{-1} \text{ h}^{-1}$ by varying the mass of catalyst loaded to the reactor and the total flowrate led to the trend reported in Fig. 3.3a, where the rate of PO production decreases with increased space time. The effect of space time on rate was reported previously by Nijhuis et al., but was not considered as an effect of product inhibition but rather of irreversible site-blocking due to formation of propylene oxidederived oligomers [28]. The H₂ oxidation rate is independent of space time as expected for a lack of inhibition for H₂ oxidation. The high scatter

at low conversion, i.e. low space time, results from quantification of H_2 oxidation rates via subtraction of PO formation rates from H_2 consumption rates which are more difficult to quantify at low conversion, but the values average to the more accurate value at high conversion. The trend in H_2 oxidation rate is also complicated by changes in H_2 selectivity (from 41% to 19%) across this data set.

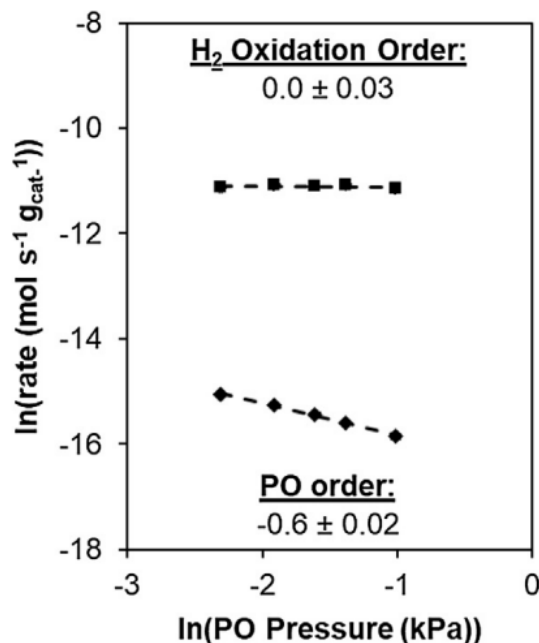


Figure 3.2. Natural log of the net PO rate ($\text{mol g}_{cat}^{-1} \text{s}^{-1}$ total minus $\text{mol g}_{cat}^{-1} \text{s}^{-1}$ fed) (diamonds) and natural log of the H_2 oxidation rate ($\text{mol g}_{cat}^{-1} \text{s}^{-1}$ H_2 consumed minus net $\text{mol g}_{cat}^{-1} \text{s}^{-1}$ PO formed) (squares) as a function of the natural log of the total gas phase PO mol fraction over 0.030Au/TS-1(81) at 473 K with gas composition 10% H_2 /10% O_2 /10% C_3H_6 , balance N_2 and PO (PO mol fraction in feed 0–0.003) at a SV of $26,000 \text{ cm}^3 \text{ g}_{cat}^{-1} \text{h}^{-1}$. The dashed lines show the linear regressions to the data resulting in the reported reaction orders. Error bars represent one standard deviation.

To test for product inhibition, we invoke the following simple analysis. A mole balance on a CSTR produces the relation:

$$r_A = -C_{A0}X/\tau \quad (3.5)$$

where X is the conversion of A and τ is the space time (reactor volume divided by the volumetric flow rate, the inverse of the space velocity). If we then assume a power law rate expression for the general reaction:



we determine that the forward rate is equal to:

$$r_A = -kC_A^a C_B^b C_C^c C_D^d \quad (3.7)$$

where a, b, c, and d are the orders of reaction for A, B, C, and D for the forward reaction. We can then express the concentrations in terms of conversion, X , to derive:

$$r_A = -k((C_{A0}(1 - X))^a (C_{B0}(1 - C_{A0}X/C_{B0}))^b (C_{C0} + C_{A0}X)^c (C_{D0} + C_{A0}X)^d \quad (3.8)$$

If we then assume that X is small with respect to 1, as is usually done when the reactor is assumed to be running at differential conversion and that $C_{C0} = C_{D0} = 0$, then

$$r_A = -C_1 X^{c+d} \quad (3.9)$$

where C_1 is a constant equal to $kC_{A0}^{a+c+d}C_{B0}^b$. This expression shows the often-overlooked conclusion that when there is product influence on the forward rate, the rate is not independent of conversion even at low values typical of expected differential behavior. This leads to the final result, $C_{A0}X^{1-c-d}/\tau = C_1$, or:

$$X = C_2 \tau^{1/(1-c-d)} \quad (3.10)$$

where $C_2 = (C_1/C_{A0})^{1/(1-c-d)}$.

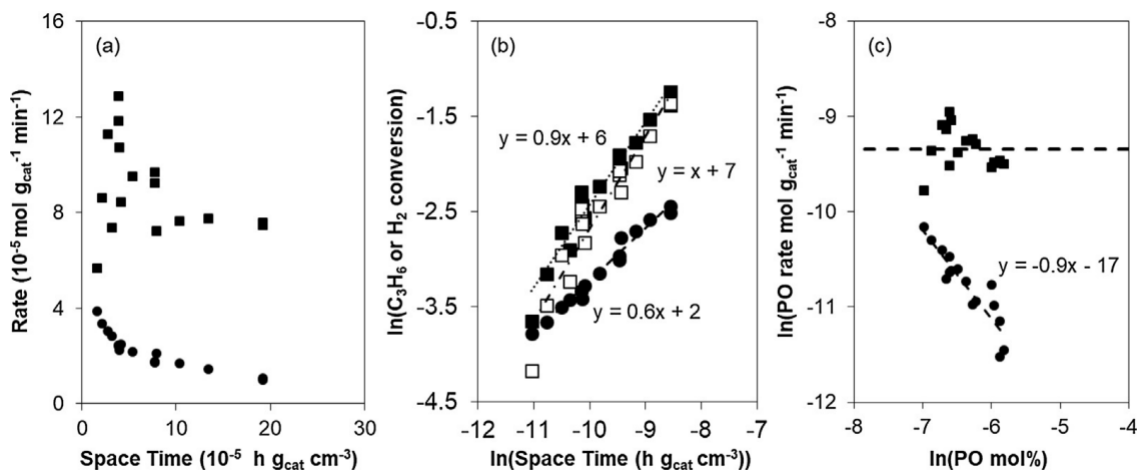


Figure 3.3. (a) PO production rate (circles) and H_2 oxidation rate (squares) in a gas-phase CSTR as a function of space time (b) natural log of C_3H_6 conversion (circles), natural log of H_2 conversion (filled squares), and natural log of H_2 oxidation computed from the H_2 conversion by subtracting PO formation (open squares) as functions of the natural log of space time (c) natural log of PO production rate (circles) and natural log of H_2 oxidation rate (squares) as functions of the natural log of the total gas phase PO mol%. Dotted lines in (b) and (c) are linear trendlines fit to the data resulting in the reported equations, while the thick dotted line in (c) is the average of the natural log of the H_2 oxidation rates included to guide the eye. Mass of catalyst ranged from 0.080 to 0.400 g 0.10Au/TS-1(143), 473 K, 10% H_2 /10% O_2 /10% C_3H_6 / 70% N_2 (vol%) and the total flow rate was varied from 0.6 to 1.4 $\text{cm}^3 \text{ s}^{-1}$, resulting in a range of space times from 1.6 to $19 \times 10^5 \text{ h g}_{\text{cat}} \text{ cm}^{-3}$.

If there is no product inhibition, then c and d will be zero and X will be a linear function of τ with a slope equal to unity. Thus, the presence or absence of product effects on the forward rate are easily detected in a plot of $\ln(X)$ versus $\ln(\tau)$. For our data on PO, the slope of the plot in Fig. 3.3b is 0.55 ± 0.02 , giving $c + d = -0.8 \pm 0.03$ and showing clear product inhibition. A plot of the natural log of the PO rate with respect to PO concentration across the entire data set for the 0.10Au/TS-1(143) catalyst gives an apparent PO reaction order of -0.9 ± 0.1 (Fig. 3.3c), consistent with the result of Fig. 3.3b (-0.8 ± 0.03). Co-feeding 16% CO_2 in the inlet had no effect on the measured PO formation rate, suggesting that CO_2 does not inhibit the PO production rate (See Fig. 3.17). Co-feeding 0.3–0.9% H_2O during measurement of the H_2O reaction order over various samples (See Table 3.7,

Fig. 3.18) confirms that H_2O does not inhibit the rate of PO production, and thus the observed production inhibition can be plausibly ascribed to inhibition by PO. While these data do not exclude the possibility of reversible inhibition by propylene glycol or another species derived from reaction of propylene oxide, we note that we have not seen evidence for any such potential species in the product distribution. Fig. 3.3b shows that the predicted inhibition of H_2 conversion is ~ -0.1 order, though if the H_2 conversion is replaced by H_2 oxidation alone (determined from the rate of H_2 consumption less the rate of PO formation) is considered, this inhibition is removed (slope for H_2 conversion in Fig. 3.3b changes from -0.9 to -1). Some inhibition to H_2 conversion with increasing space time is expected, as formation of PO requires consumption of H_2 , and we have demonstrated that PO formation, and not H_2 oxidation, is inhibited by increasing PO concentration via co-fed PO (Fig. 3.2). Finally, Fig. 3.3c shows that while there is a clear linear dependence of the natural log of the PO formation rate as a function of the natural log of the PO pressure when space time is varied, there is no clear monotonic trend in the log-log plot of the H_2 oxidation rate as a function of PO pressure. The scatter in these data reflects the convolution of decreased H_2 oxidation rates with decreased H_2 pressure (Section 3.3.2), changes in H_2 selectivity with increasing space time (from 40% to 17%), and scatter resulting from quantification of H_2 oxidation rates by measurement of H_2 consumption rather than H_2O formation.

The average values for the apparent reaction orders (0.6, 0.2, and 0.2 for H_2 , O_2 , and C_3H_6 , respectively, Table 3.2) are all non-integer and difficult to rationalize mechanistically for a single site Langmuir-Hinshelwood mechanism, but they are also not the intrinsic reaction orders, because they do not account for product inhibition. Assuming a power rate law (3.11), the true (PO inhibition corrected) reaction orders for H_2 , O_2 , and C_3H_6 require multiplication of the orders observed in absence of PO by the factor 1-d, or in this case 1.6 [27].

$$r_{PO} = k[H_2]^\alpha [O_2]^\beta [C_3H_6]^\gamma [PO]^\delta \quad (3.11)$$

Taking into account correction of the reaction orders for PO inhibition is also shown in Table 2. The corrected reaction orders for H_2 , O_2 , and C_3H_6 (1 ± 0.2 , 0.4 ± 0.06 , and $0.4 \pm$

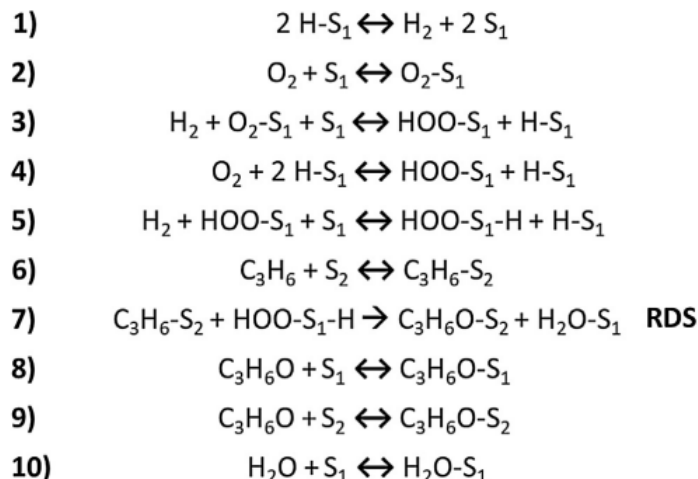


Figure 3.4. Proposed reaction mechanism for propylene oxide synthesis over Au/TS-1 catalysts. S_1 is a Au site, S_2 is an Au-Ti interfacial site, and that they are neighboring sites.

0.1, respectively) are near 1 for H_2 but non-integer for O_2 and C_3H_6 . These are the values that must be reconciled with any proposed mechanism.

The mechanism proposed by our group previously [18] involves HOOH formation on Au sites (denoted as S_1 sites in Figure 3.4) that reacts in a single step with C_3H_6 adsorbed at the interface between small Au clusters and framework Ti atoms (denoted as S_2 sites in Figure 3.4). Pulido et al. [41] proposed a similar H-Au-OOH species during gas-phase propylene epoxidation over isolated Au atoms supported on graphene. The interface site as the binding location for C_3H_6 is consistent with DFT calculations that predict stronger adsorption of C_3H_6 at the interface between small Au clusters and framework Ti atoms ($\Delta E_{\text{ads}} \sim -20 \text{ kcal mol}^{-1}$) than at framework Ti atoms alone ($\Delta E_{\text{ads}} \sim -10 \text{ kcal mol}^{-1}$) [21]. The exact nature of the Ti site is not known, and could include titanium atom with three Si-O-Ti bonds and one -OH ligand, with a neighboring Si-OH group (i.e., $(\text{SiO})_3\text{-Ti-OH-HO-Si}$) in addition to framework Ti atoms with four Si-O-Ti bonds. Our previously proposed mechanism was consistent with the observed D_2 kinetic isotope effect for PO formation on Au/ TiO_2 catalysts [15], DFT calculations of sequential and simultaneous mechanisms [21], and the measured apparent reaction orders from multiple research groups (Table 3.2), but it did not account for PO inhibition. Figure 3.4 adds steps 8 and 9 for adsorption of PO at Au and Ti sites to

correct this omission. We note that the kinetic relevance of H-H bond breaking is assumed on the basis of DFT predictions of a predominant "simultaneous" epoxidation mechanism involving H-Au-OOH intermediates over Au/TS-1 [21] as well as the kinetic isotope effect seen for Au/TiO₂ [17].

If we take step 7 as the sole rate determining elementary step, in agreement with theoretical calculations that suggest the free energy barriers are lower for this step than for the equivalent step in the sequential reaction pathway (discussed in the ensuing paragraphs) [21], we arrive at the following rate expression:

$$r_{PO} = k_7(C_3H_6 - S_2) \frac{(HOO - S_1 - H)}{L_1} \quad (3.12)$$

If all other steps are considered quasi-equilibrated, and if empty S₁ sites, O₂-S₁, PO-S₁, and HOO-S₁-H, are the most abundant surface species (MASIs) for S₁, then [HOO-S₁-H] becomes:

$$\frac{(HOO - S_1 - H)}{L_1} = \frac{K_5 K_4 P_{H_2} P_{O_2}}{1 + K_2 P_{O_2} + K_8 P_{PO} + K_5 K_4 P_{O_2} P_{H_2}} \quad (3.13)$$

where L₁ is the total number of covered plus empty S₁ sites, each K_i represents the equilibrium constant for elementary step i, and P_j represents the bulk gas phase partial pressure of a species j. The [C₃H₆-S₂] term can be derived by assuming that step 6 is quasi-equilibrated, that only empty S₂ sites, C₃H₆-S₂ and PO-S₂ are MASIs on S₂, and that L₂ is the total number of covered and empty S₂ sites:

$$C_3H_6 - S_2 = \frac{K_6 P_{C_3H_6} L_2}{1 + K_6 P_{C_3H_6} + K_9 P_{PO}} \quad (3.14)$$

Combining 3.12, 3.13, and 3.14 yields the rate expression:

$$r_{PO} = \frac{k_7 K_6 K_5 K_4 P_{C_3H_6} P_{O_2} P_{H_2} L_2}{(1 + K_2 P_{O_2} + K_5 K_4 P_{O_2} P_{H_2} + K_8 P_{C_3H_6O})(1 + K_6 P_{C_3H_6} + K_9 P_{C_3H_6O})} \quad (3.15)$$

The numerator of 3.15 is directly proportional to the gas phase pressures of hydrogen, oxygen, and propylene, resulting in maximum apparent reaction orders of unity for each

reactant. Depending on the coverage of S_1 and S_2 , any of the three reactants can have an apparent reaction order less than one. By taking the derivative of the natural log of the rate with respect to the natural log of the gas phase pressure of each species in the rate expression, one can derive relationships between the apparent reaction order and the surface coverage of each species (derivation shown in Section 3.5.6), resulting in the expressions for each reaction order are shown in Table 3.3.

Thus, in order to match the average measured reaction orders (Table 3.2), the coverage of HOOH on S_1 is approximately zero, the coverage of O_2 on S_1 is 0.6, the coverage of C_3H_6 on S_2 is 0.6, and the coverage of C_3H_6O is $0.2 \leq \theta_{PO-S_1} \leq 0.4$ on S_1 and $0.2 \leq \theta_{PO-S_2} \leq 0.4$ on S_2 , with the sum of $\theta_{PO-S_1} + \theta_{PO-S_2} = 0.6$, resulting in an apparent C_3H_6O reaction order of -0.6. This analysis confirms that the observed orders could reasonably arise from the rate expression derived from Eqs. 3.12-3.14 without violating the requirement that the coverage must be ≤ 1 on each of the two active sites. The mechanism reported here is consistent with the observed reaction orders for H_2 , O_2 , C_3H_6 , and PO. An alternative mechanism reported by Kanungo et al. [22] invokes two kinetically relevant steps, the first of which forms HOOH over two types of non-competing Au sites, which then migrates to an adjacent Ti site and reacts with C_3H_6 adsorbed at an adjacent Au site to form C_3H_6 -HOOH-Ti, which produces PO and H_2O in a second kinetically relevant step. This mechanism assumes C_3H_6 will not adsorb directly to a Ti site, and thus C_3H_6 must adsorb on Au adjacent to Ti-HOOH before formation of C_3H_6 -HOOH-Ti and subsequent formation of PO and H_2O . Adsorption of C_3H_6 at Au sites is consistent with C_3H_6 inhibition of H_2 oxidation over Au sites reported by Kanungo et al. [22] and observed in this study (*vide infra*). We note however that we have previously found adsorption of C_3H_6 on a Au-Ti interfacial site to be a feasible elementary step on the basis of density-functional theory calculations [21]. Whether or not there are three sites and multiple kinetically relevant steps and migration of HOOH from Au to Ti prior to adsorption of C_3H_6 at a Au site neighboring the HOOH-Ti species and subsequent reaction, or two sites and a reaction of a Au-HOOH species with C_3H_6 -(Au-Ti) in a single kinetically relevant step (as reported here, Scheme 1) cannot be determined on the basis of kinetics alone and requires additional spectroscopic and/ or computational evidence. Another difference in the two mechanisms that remains to be resolved is pathway

for HOOH formation. Kanungo et al. [22] accommodate the experimental observation that the hydrogen order is roughly double that for oxygen by invoking an independent oxygen adsorption site. Our mechanism has been guided by both DFT [21] and our reluctance to invoke additional sites unless required. Given that both mechanisms are consistent with observed kinetic measurement data and our previous DFT results support the mechanism described in Figure 3.4, we report this mechanism in the present study. Our continuing efforts will attempt to differentiate between these two plausible mechanisms.

In the two-site sequential mechanism, hydrogen peroxide forms on a Au site prior to desorbing intact and adsorbing at a Ti-OH site where C_3H_6 has already adsorbed. This latter step mimics the proposed steps for liquid-phase epoxidation over TS-1 and TiO_2 [23]. In the sequential mechanism, assuming the epoxidation of propylene is the rate-limiting step, the numerator of the rate expression will be first order in C_3H_6 , H_2 , and O_2 , and the denominator can contain coverage terms for C_3H_6 , C_3H_6O , and H_2O_2 . This results in apparent reaction orders for hydrogen and oxygen that are equal, which was not observed for any sample in this study (Table 3.2, Table 3.7). The equivalence of the hydrogen and oxygen reaction orders is a direct result of the desorption from Au and readsorption on Ti of H_2O_2 , and therefore any mechanism which includes this step can be removed from consideration on the basis of the kinetic data presented in this study (Table 3.2, Table 3.7). Thus, from the kinetic results presented here, it is clear that the two-site sequential mechanism is ruled out by the measured kinetic parameters, and that the two-site simultaneous mechanism occurring over adjacent Au-Ti sites, proposed by previous experimental and theoretical reports, can explain the measured kinetics.

Table 3.3. Relation between the true reaction order and the coverages of the most abundant surface species, according to the mechanism shown in Figure 3.4 and the mechanistic assumptions resulting in Eq. 3.15.

Reaction order	Function
H_2	$1-\theta_{HOO-S_1-H}$
O_2	$1-\theta_{S_1-O_2}-\theta_{HOO-S_1-H}$
C_3H_6	$1-\theta_{C_3H_6-S_2}$
C_3H_6O	$-(\theta_{PO-S_1}+\theta_{PO-S_2})$

Measurement of reaction orders and activation energies for hydrogen oxidation over Au/TS-1

The H₂ oxidation rate was indirectly calculated according to Eq. 3.4, which assumes that all hydrogen consumed other than for PO formation (which produces one mole of H₂O per mole of PO) is consumed in direct H₂ oxidation to H₂O, as it was not possible in our experimental apparatus to quantify water in the reactor effluent via GC. Considering that the side products observed in this reaction do not include saturated oxygenates (e.g., alcohols) or hydrocarbons (e.g., ethane, propane), this assumption is reasonable. The highest H₂ oxidation rate measured here (3×10^{-6} mol H₂ consumed per g_{cat} (0.069Au/TS-1(143)) per s, 10.1 kPa H₂, 10.1 kPa O₂, 2.53 kPa C₃H₆, T = 473 K) was significantly lower than that measured by Barton and Podkolzin over 0.15Au/TS-1(51) (1.5×10^{-1} mol H₂O formed g_{cat}⁻¹ s⁻¹, 2.5 kPa O₂, 5.0 kPa H₂, 433 K). As reported in Table 3.4, the apparent reaction orders for H₂ oxidation are 0.9 ± 0.1 for H₂, 0.3 ± 0.1 for O₂, -0.3 ± 0.07 for C₃H₆, and 0.0 ± 0.2 for PO, apparent orders that are markedly different from those for PO production reported here and elsewhere (Table 3.2). Barton and Podkolzin reported apparent orders for H₂O synthesis over Au catalysts of 0.7–0.8 for H₂, 0.1–0.2 for O₂, and zero for H₂O over Au/SiO₂ and Au/TS-1 catalysts at 433 K [42], while experiments over solid gold found orders of 1 for H₂ and 0.5 for O₂, and over gold gauze found orders of 1 for H₂ and zero for O₂ [43], [44]. The hydrogen and oxygen orders measured over Au/TS-1 in this study are similar to those reported by Barton and Podkolzin, but the vast difference in rate and the differences in Au loading and deposition method between their catalyst in the absence and ours in the presence of propylene and propylene oxide make it difficult to draw meaningful comparisons. The O₂ order for H₂ oxidation over Au/TS-1 reported here suggests that the sites for this reaction are partially covered with O₂. The apparent propylene order that is slightly below zero can be explained by a small coverage of adsorbed propylene on the active sites for hydrogen oxidation.

Figure 3.5 shows the mechanism for hydrogen oxidation over Au/TS-1 catalysts proposed by Barton and Podkolzin [42]. In agreement with observations over 3-atom Au particles simulated by Wells et al. [45], H₂ dissociation proceeds with assistance by adsorbed molecular

oxygen (reaction (4), Figure 3.5). However, Barton and Podkolzin also included unassisted dissociative hydrogen adsorption (reaction (2), Figure 3.5) in order to simplify the definition of kinetic model parameters and the derivation of rate expressions [42]. H_2O_2 decomposition proceeds through breakage of the O-O bond to form 2 -OH species on the surface (reaction (5), Figure 3.5). The OH surface species can then react with adsorbed H to form water (reaction (6), Figure 3.5). Adsorbed OOH and H species were reported to be more stable on smaller Au particles [42], rendering these particles unreactive for hydrogen oxidation but active in oxygen-assisted hydrogen dissociation. H_2O_2 decomposition on intermediate-size (13–55 Au atoms) and large Au particles (>55 Au atoms) was predicted to occur by breaking an O-O bond (reaction (5), Figure 3.5) [42]. This mechanism results in a hydrogen and oxygen reaction orders of 1 assuming exclusively empty sites, and can result in a hydrogen order of 1 and oxygen order of 0.3, as reported here (Table 4), if O_2^* has a coverage of 0.7.

Table 3.4. Apparent and PO-inhibition-corrected reaction orders and activation energies for propylene oxide formation and H_2 oxidation determined by averaging the measured kinetic parameters for eight separate Au/TS-1 samples (0.092Au/TS-1(75), 0.019Au/TS-1(143), 0.040Au/TS-1(81), 0.030Au/TS-1(81), 0.044Au/TS-1(81), 0.033Au/TS-1(143), 0.069Au/TS-1(143), and 0.064Au/TS-1(143)).

Product	Reaction orders						E_{app} (kJ mol ⁻¹)
	H_2	O_2	C_3H_6	PO	CO_2	H_2O	
PO ^a	0.6 ± 0.08	0.2 ± 0.01	0.2 ± 0.08	-0.6 ± 0.2	0	0	33 ± 0.9
PO ^b	1 ± 0.2	0.4 ± 0.06	0.4 ± 0.1	-0.6 ± 0.2	0	0	52 ± 6
H_2O^a from H_2 oxidation	0.9 ± 0.1	0.3 ± 0.1	-0.3 ± 0.07	0.0 ± 0.2	0	-0.1 ± 0.07	31 ± 10

^a Not corrected for inhibition

^b Reactant orders and E_{app} corrected by a factor of 1.6 to account for PO inhibition [27].

Nijhuis et al. observed that propylene adsorbed to Au sites in Au/SiO₂ catalysts during pre-adsorption experiments at 353 K, partially poisoning the hydrogen oxidation reaction, though to a lesser extent than when propylene was co-fed with hydrogen and oxygen (conditions under which PO was formed) over Au/TiO₂ catalysts [46], similar to the observation of Hayashi and Haruta that the presence of C_3H_6 in the feed stream decreased the rate of H_2 consumption over Au/TiO₂/SiO₂ catalysts between 273 and 400 K [2]. These results imply that propylene adsorbs to active sites for H_2 oxidation in Au-Ti catalysts at 353 K and

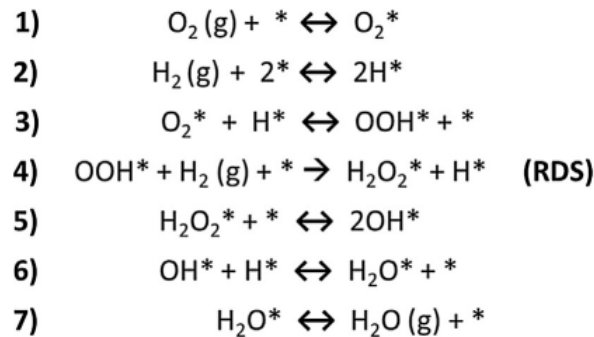


Figure 3.5. Single-site reaction mechanism proposed by Barton and Podkolzin for hydrogen oxidation over Au/Ts-1 catalysts [42].

are consistent with the observed slightly negative apparent reaction order in propylene for hydrogen oxidation reported here. While the H_2 and O_2 order differences compared to those for PO formation could be explained by different kinetically relevant steps over the same active sites involved from the PO formation mechanism, the lack of PO inhibition for the H_2 oxidation reaction(s), a surface intermediate which occupies the surface on both sites in the PO formation mechanism (Section 3.3.2), suggests that H_2 oxidation occurs primarily on a site that is not involved in PO formation. A distribution of Au and Ti sites over Au/Ti-SiO₂ that form PO and water over Au sites in the vicinity of Ti sites and that form H_2O over Au sites that are not near Ti sites was proposed by Kanungo et al. [22]. The data presented here suggest a similar collection of sites is present over Au/TS-1, wherein Au sites that form water from H_2 oxidation must be distinct from those that form water along with PO, as the coverages of PO and C_3H_6 required for the observed reaction orders in PO and C_3H_6 would exceed 1 if PO were only bound to Ti sites and propylene and oxygen were only bound to Au sites. Thus, PO apparently binds to Au sites that are relevant for PO formation, but not those that are relevant for H_2O formation by H_2 oxidation, resulting in a zero order dependence on PO pressure for H_2 oxidation. The data presented here do not exclude the possibility that a minority of the H_2 oxidation events could occur over PO formation sites, but the dominant sites for H_2 oxidation must be distinct from those involved in formation of PO.

3.4 Conclusions

Apparent reaction orders and activation energies consistent with those reported previously over titanosilicate-supported Au catalysts were measured for a series of Au/TS-1 catalysts in a gas-phase CSTR reactor. Measurement of product inhibition by co-feeding propylene oxide has revealed significant inhibition by propylene oxide in the Au/TS-1 system, while CO_2 and H_2O do not inhibit propylene epoxidation rates. Previous reports of apparent reaction orders have not accounted for product inhibition, and thus these reaction orders for propylene oxide formation over Au/TS-1 and similar catalysts reported in the literature are incorrect by substantial amounts (a factor of 1.6) and, therefore, can lead to incorrect mechanistic interpretations. We have found, however, that reaction orders corrected for propylene oxide inhibition are consistent with the previously proposed two-site simultaneous mechanism in which an $\text{HOO-S}_1\text{-H}$ species reacts with propylene adsorbed on a neighboring site, but rule out a two-site sequential mechanism in which H_2O_2 formed on Au sites desorbs and reacts with propylene adsorbed on Ti sites. The precise nature of the active species that we designate as $\text{HOO-S}_1\text{-H}$ is not yet clear and is a subject of continuing study. H_2 oxidation is not inhibited by propylene oxide, suggesting this reaction occurs on sites other than the sites responsible for PO formation. This finding implies the possibility of improved catalyst formulations in which the H_2 oxidation sites are minimized while the epoxidation sites are maximized, resulting in a catalyst with high epoxidation rates and H_2 selectivity, as required for industrial application of this reaction. Without accurate measurement of kinetics, in this case enabled by use of a gas-phase CSTR, discovering the physical identity of the active site, the use of mechanistic conclusions to guide new catalyst formulations, and the pairing of molecular-level theory with experiments would all not be possible.

3.5 Supplementary Information

3.5.1 Reactor Apparatus

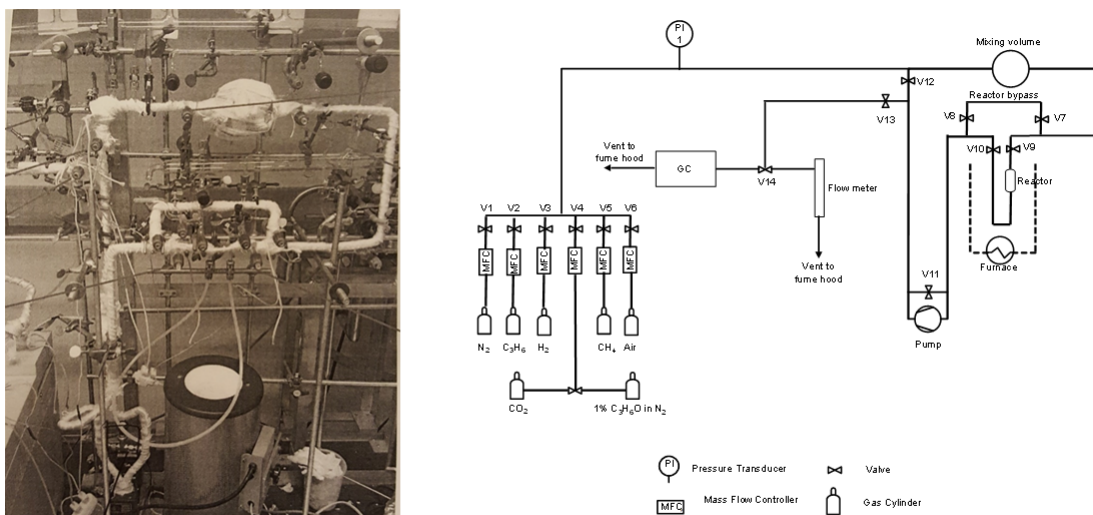


Figure 3.6. Photograph of gas-phase CSTR system with heat-traced recirculation loop (left). P&ID diagram for gas-phase PFR/CSTR system (right).

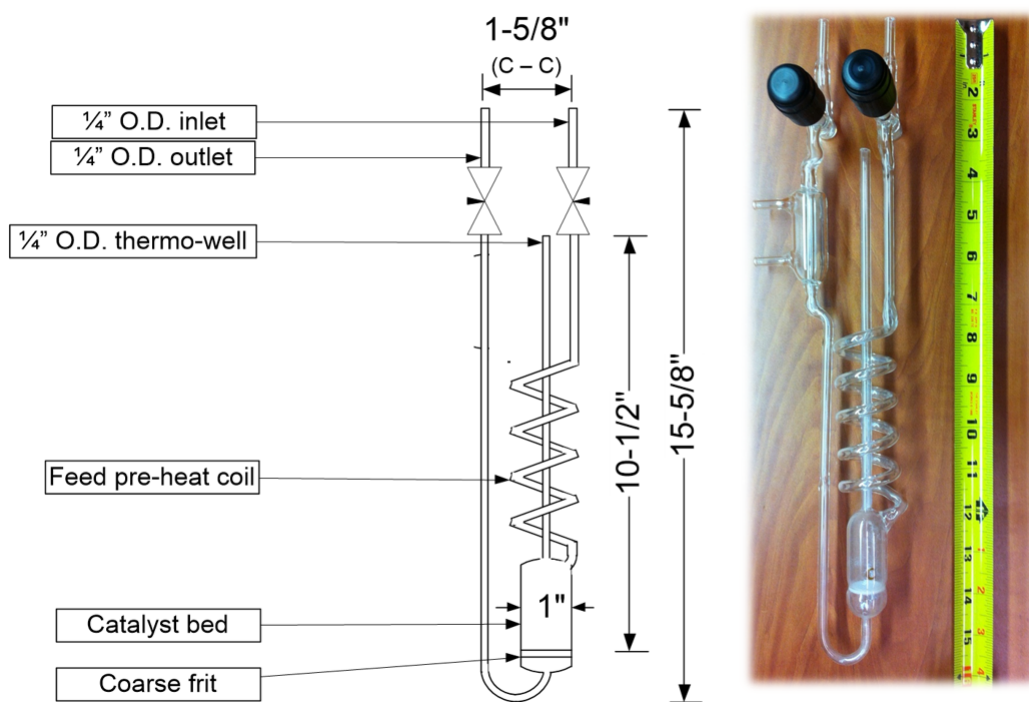


Figure 3.7. Diagram of Pyrex reactor (left). Photograph of pyrex reactor (right).

3.5.2 XRD Patterns

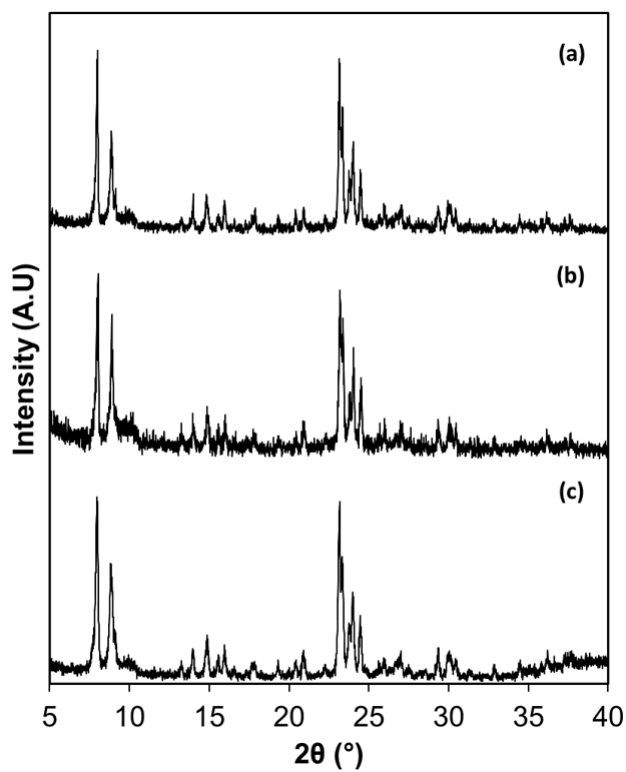


Figure 3.8. XRD patterns for calcined (a) TS-1(75) and (b) TS-1(81) and (c) TS-1(143). Patterns are normalized to their maximum intensity and offset vertically for clarity.

3.5.3 Nitrogen Isotherms

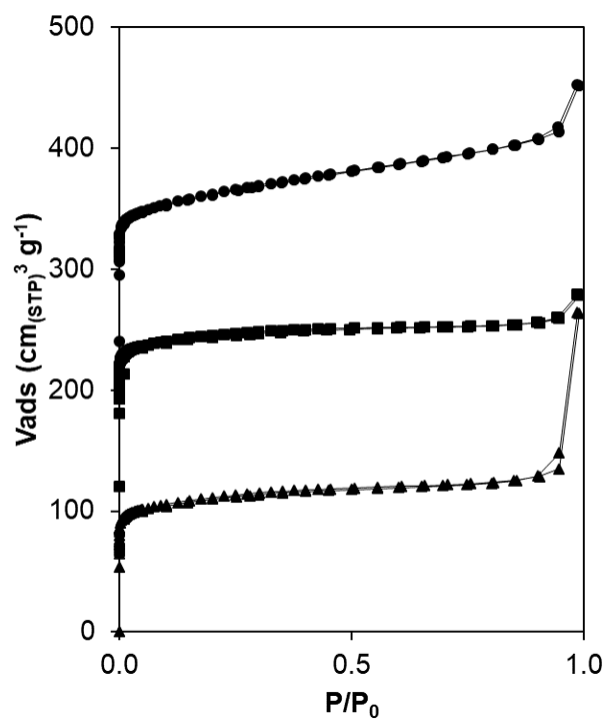


Figure 3.9. N₂ adsorption isotherms for TS-1(75) (circles) and TS-1(81) (squares) TS-1(143) (triangles). Isotherms are offset by 120 cm_(STP)³ g⁻¹ for clarity. Micropore volumes are reported in Table 3.1.

3.5.4 Diffuse Reflectance UV-Visible Spectroscopy

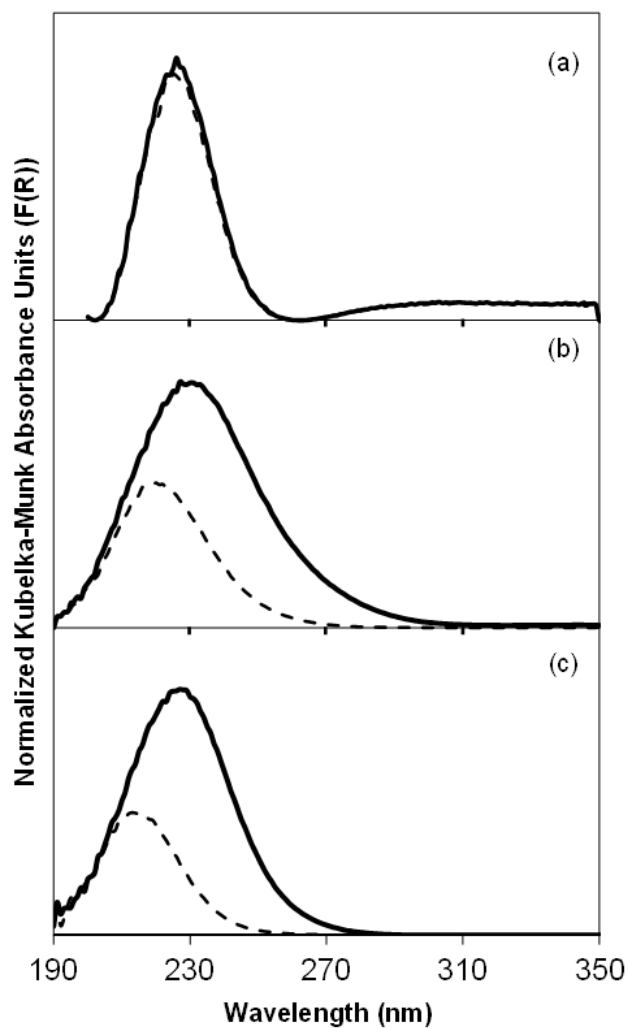


Figure 3.10. DRUV-Vis spectra in Kubelka-Munk units (normalized to the maximum $F(R)$ intensity) for (a) TS-1(75) (b) TS-1(81) and (c) TS-1(143), collected (i) under ambient conditions (solid line), (ii) after dehydration at 523 K (dashed line).

DRUV-Vis spectra of dehydrated TS-1 samples (Figure 3.10) were used to produce the Tauc plots shown in Figure 3.11 for each TS-1 sample. The lowest energy x-intercepts of these plots (~ 5 eV) correspond to the Ti edge energies [31]–[33] and are reported in Table 3.1.

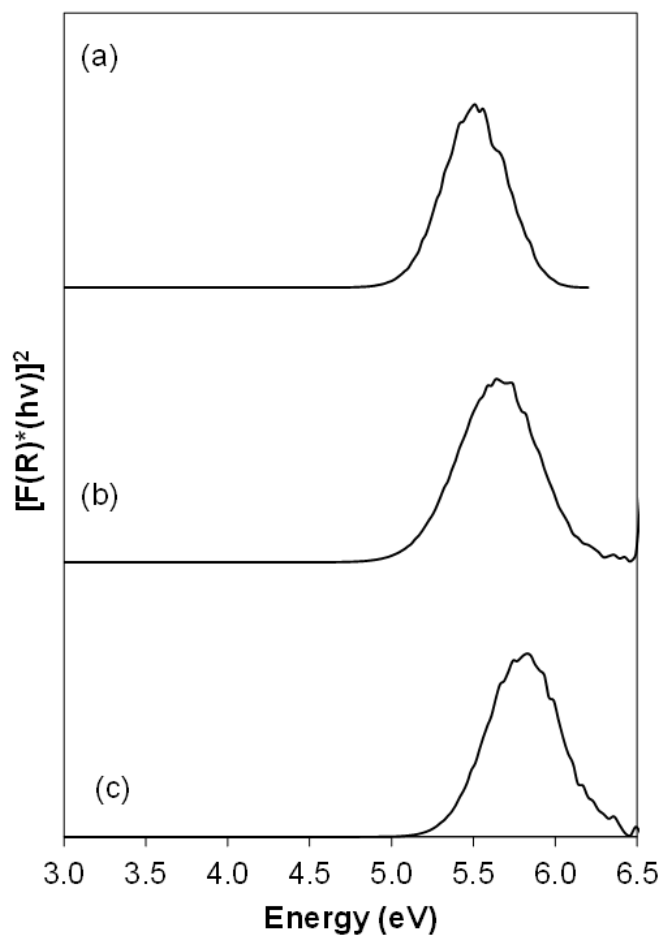


Figure 3.11. Tauc plots for (a) TS-1(75) and (b) TS-1(81) and (c) TS-1(143) measured under dehydrated conditions (He flow, 523 K).

3.5.5 Additional Kinetic Data and Derivations

The absence of diffusion limitations was confirmed by calculation of the Mears criterion and the Thiele Modulus for the Au/TS-1 catalysts studied here, as adapted from the derivation in Lee et al. [24]. The absence of external diffusion limitations is confirmed if the Mears criterion (Eq. 3.16) is met, specifically that:

$$\frac{-r_{A(obs)} \cdot \rho_b \cdot R \cdot n}{k_c \cdot C_{Ab}} < 0.15 \quad (3.16)$$

where $-r_{A(obs)}$ is the observed reaction rate ($\text{kmol kg}_{cat}^{-1} \text{ s}^{-1}$); R is the catalyst pellet radius (m); n is the reaction order of reactant A; C_{Ab} is the concentration of reactant A in the bulk gas phase at 473 K (kmol m^{-3}); and k_c is the mass transfer coefficient for reactant A (m s^{-1}). Finally, ρ_b is the catalyst bed density (kg m^{-3}), defined as:

$$\rho_b = (1 - \Phi)\rho_c \quad (3.17)$$

where ρ_c is the pellet bulk density (kg m^{-3}) and Φ is the porosity of the catalyst bed. The Reynolds number for this system is defined as:

$$Re = 2U \cdot R \cdot \rho / \mu \quad (3.18)$$

where U is superficial velocity (m s^{-1}), ρ is the density of the reactant mixture (kg m^{-3} , approximated by air at 473 K), μ is the viscosity of the reactant mixture ($\text{kg (m}\cdot\text{s)}^{-1}$, approximated by air at 473 K). Since the Reynolds number is much smaller than 1, the mass transfer coefficient (k_c) can be estimated by assuming that the Sherwood number, Sh , defined as:

$$Sh = k_c \cdot (2R) / De \quad (3.19)$$

is equal to 2, where De is estimated diffusivity of reactant A in the bulk gas phase [47]. All parameters used in these equations are listed in Table 3.5.

Table 3.5. Parameters used to calculate the Mears criterion for Au/TS-1 catalysts used in this study.

Parameter	Value	Units
Highest observed PO rate at 473 K	$\sim 7.2 \times 10^{-7}$	$\text{kmol kg}_{cat}^{-1} \text{s}^{-1}$
Density of catalyst pellet	500	kg m^{-3}
Catalyst bed density (estimated bed porosity 0.3)	~ 350	kg m^{-3}
Radius of catalyst pellet	7.5×10^{-5}	m
Bulk gas concentration of propylene at 473 K	2.6×10^{-3}	kmol m^{-3}
Reynolds number ^a	$\sim 1.3 \times 10^{-2}$	unitless
Estimated gas phase diffusivity of propylene in air at 473 K [24], [47]	$\sim 3 \times 10^{-5}$	$\text{m}^2 \text{s}^{-1}$
Mass transfer coefficient for propylene ^b	0.4	m s^{-1}
Reaction order of C_3H_6	~ 0.5	unitless
Estimated Mears criterion	9.1×10^{-6}	unitless

^a Superficial velocity = 0.0021 m s^{-1} (flow rate = $65 \text{ cm}^3 \text{ min}^{-1}$ through a reactor with inner diameter $\sim 0.025 \text{ m}$), estimated fluid kinematic viscosity (air at 473 K): $\sim 3.7 \times 10^{-5} \text{ (m}^2 \text{ s}^{-1})$

^b Since $Re \ll 1$, mass transfer coefficient was estimated by assuming Sh (Sherwood number) = 2 (Eq. 3.19)

The absence of internal diffusion limitations was confirmed by estimating the Thiele modulus for the Au/TS-1 catalysts used here under the standard reaction conditions employed. The catalysts were sieved to pellets of approximately $150 \mu\text{m}$ diameter, but each pellet contains many TS-1 crystallites with an average diameter of $\sim 200 \text{ nm}$. Thus, calculations related to internal mass transfer assumed that this diameter was the relevant characteristic diameter. The Thiele modulus is defined as:

$$\Phi = \frac{-r_{A(obs)} \cdot \rho_c \cdot R^2}{D_e \cdot C_{As}} = \eta \phi^2 \quad (3.20)$$

where $-r_{A(obs)}$ is the observed reaction rate ($\text{kmol kg}_{cat}^{-1} \text{ s}^{-1}$), ρ_c is the TS-1 crystallite density (kg m^{-3}), R is TS-1 crystallite radius (m), De is the effective gas-phase diffusivity at 473 K (estimated from the Knudsen equation assuming that the constriction factor, tortuosity and pellet porosity were 0.8, 6 and 0.3 respectively [47], assuming a pore radius of 0.25 nm for the TS-1 crystallites), ($\text{m}^2 \text{ s}^{-1}$), C_{As} is the gas concentration of A at the catalyst surface (kmol m^{-3}), η is the internal effectiveness factor and ϕ is the Thiele modulus. If $\phi \ll 1$, then $\eta \approx 1$ and ϕ is easily calculated. The parameters used for the Thiele modulus estimation are listed in Table 3.6.

Table 3.6. Parameters used to calculate the Mears criterion for Au/TS-1 catalysts used in this study.

Parameter	Value	Units
Density	1.7×10^3	kg m^{-3}
TS-1 crystallite size	1.0×10^{-7}	m
Effective gas phase diffusivity	3.3×10^{-9}	$\text{m}^2 \text{ s}^{-1}$
Estimated Thiele modulus	1.2×10^{-3}	—

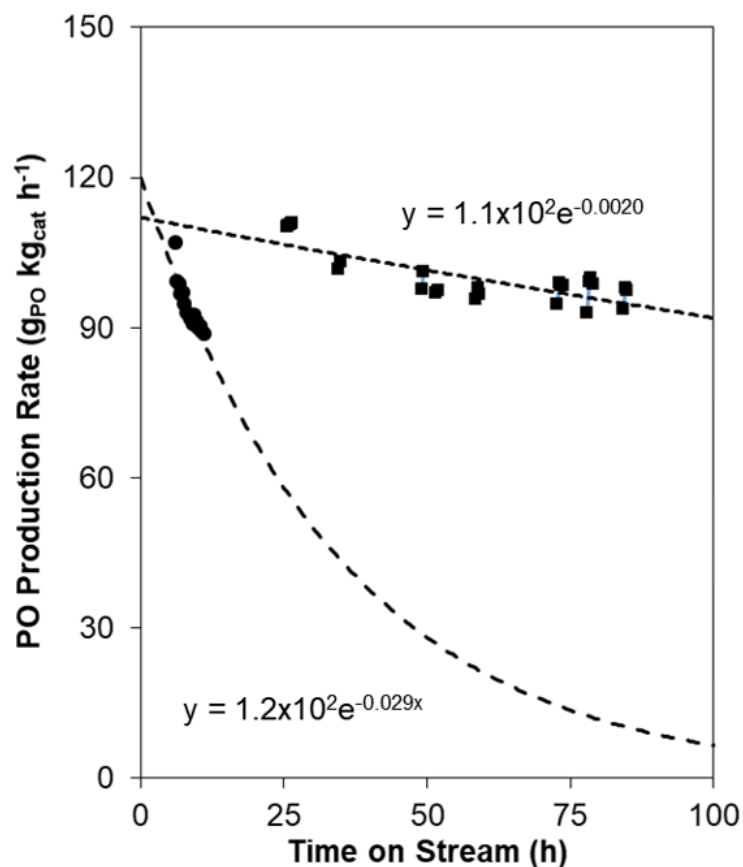


Figure 3.12. Determination of the deactivation rate constants in the initial deactivation (large dashed line, circles) and the steady-state deactivation (small dashed lines, squares) regimes for 0.092Au/TS-1(75). Note that after 24 h time on stream, the space velocity was changed from 14,000 to 26,000 $\text{cm}^3 \text{g}_{cat}^{-1} \text{h}^{-1}$ and the reactor operating mode changed from PFR to CSTR, resulting in an increased reaction rate at 25 h time on stream. ($T = 473 \text{ K}$, feed was 10% H_2 / 10% O_2 / 10% C_3H_6 / 70% N_2 by volume).

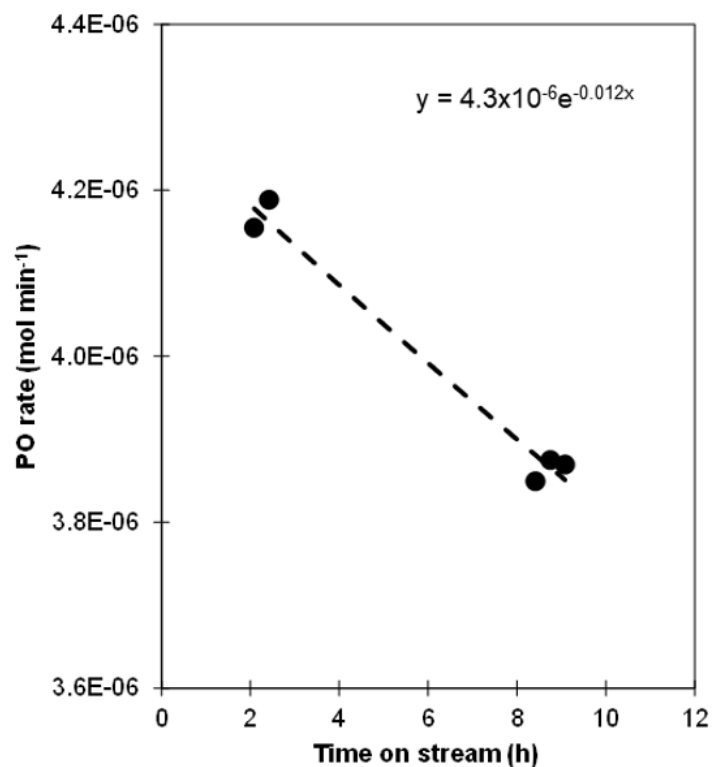


Figure 3.13. Example determination of the first-order exponential decay constant for correction of steady-state reaction rates during PO order measurement on 0.063Au/TS-1(75). Data collected in CSTR mode, $SV = 26,000 \text{ cm}^3 \text{ g}_{cat}^{-1} \text{ h}^{-1}$, $T = 473 \text{ K}$, feed = 10% H_2 /10% O_2 /10% C_3H_6 /0-0.012% PO/Balance N_2 over 0.063Au/TS-1(75) and represent returns to the standard condition with 0% PO co-feed. Over the time scale studied, the deactivation is approximately linear.

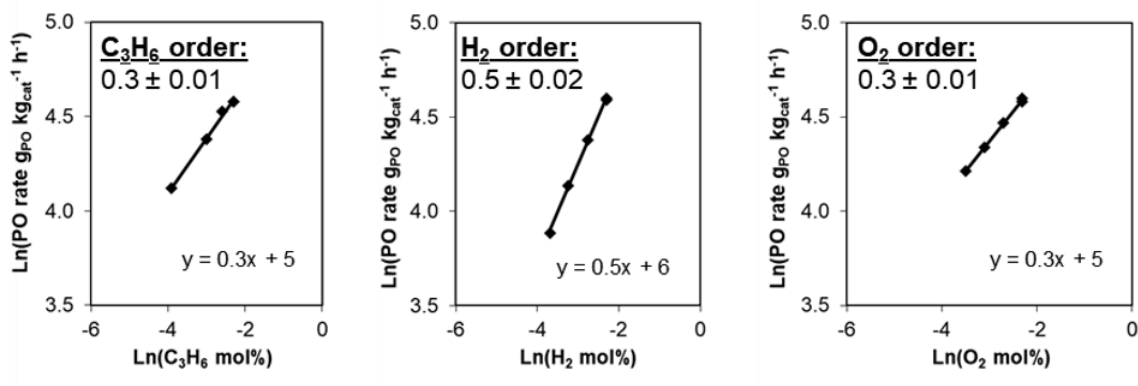


Figure 3.14. Apparent (a) H_2 , (b) O_2 , and (c) C_3H_6 reaction orders measured over 0.092Au/TS-1(75) at 473 K and a space velocity of $26,000 \text{ cm}^3 \text{ g}_{\text{cat}}^{-1} \text{ h}^{-1}$ in a gas-phase CSTR.

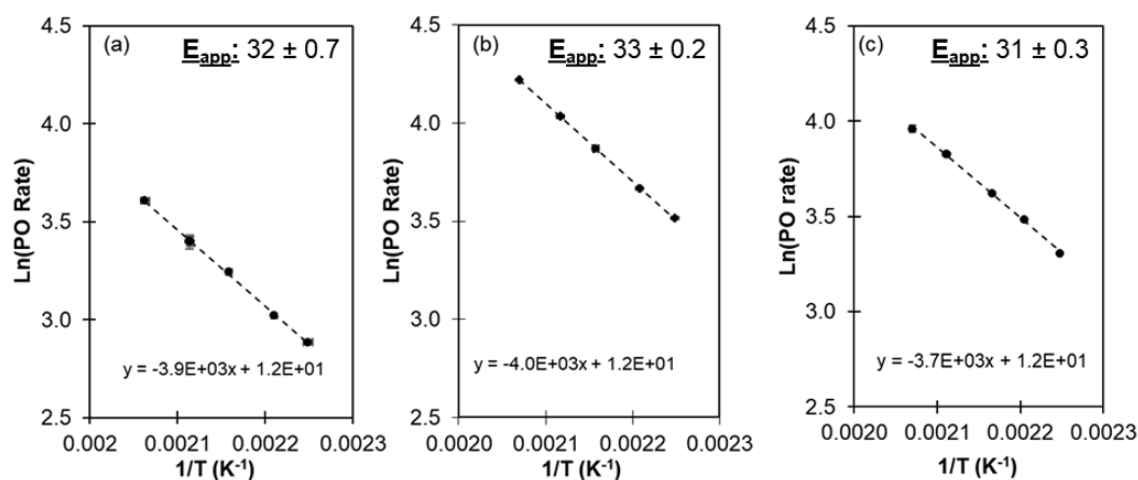


Figure 3.15. Apparent activation energies (deactivation corrected, not PO corrected) for PO formation measured over (a) 0.019Au/TS-1(143), (b) 0.040Au/TS-1(81), and (c) 0.022Au/TS-1(143) from 443-483 K with a feed composition of 10% H_2 / 10% O_2 / 10% C_3H_6 / 70% N_2 and a space velocity of $26,000 \text{ cm}^3 \text{ g}_{\text{cat}}^{-1} \text{ h}^{-1}$ in a gas-phase CSTR.

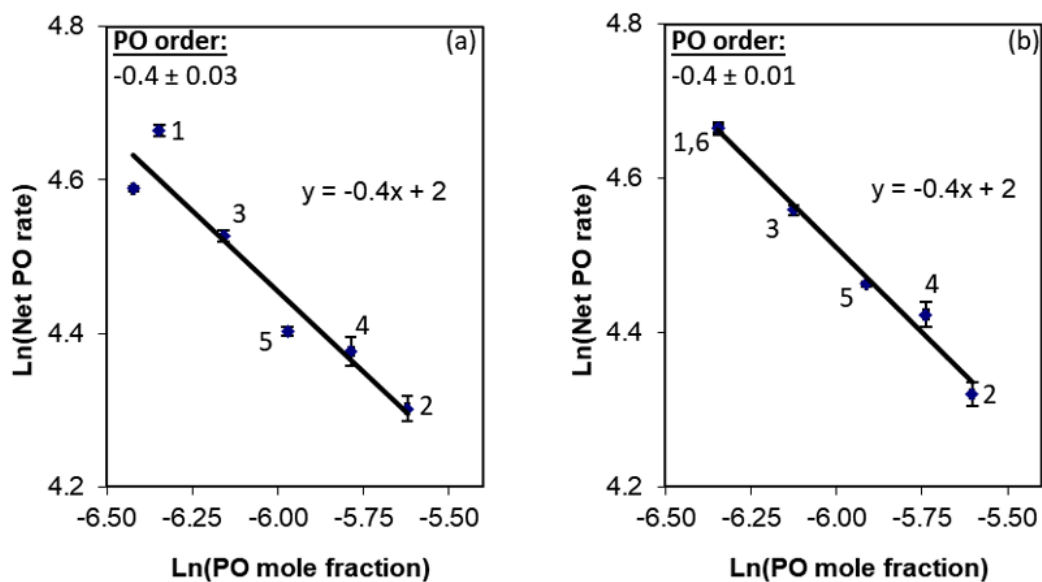


Figure 3.16. Example PO order measurement (a) before and (b) after correction for deactivation over time on stream. Numbers near each data point represent the non-monotonic order in which the data were collected (data points 1 and 6 represent no PO co-feed). Data collected in CSTR mode, $SV = 26,000 \text{ cm}^3 \text{ g}_{cat}^{-1} \text{ h}^{-1}$, $T = 473 \text{ K}$, feed = 10% H_2 /10% O_2 /10% C_3H_6 /0-0.024% PO/Balance N_2 over 0.069Au/TS-1(143).

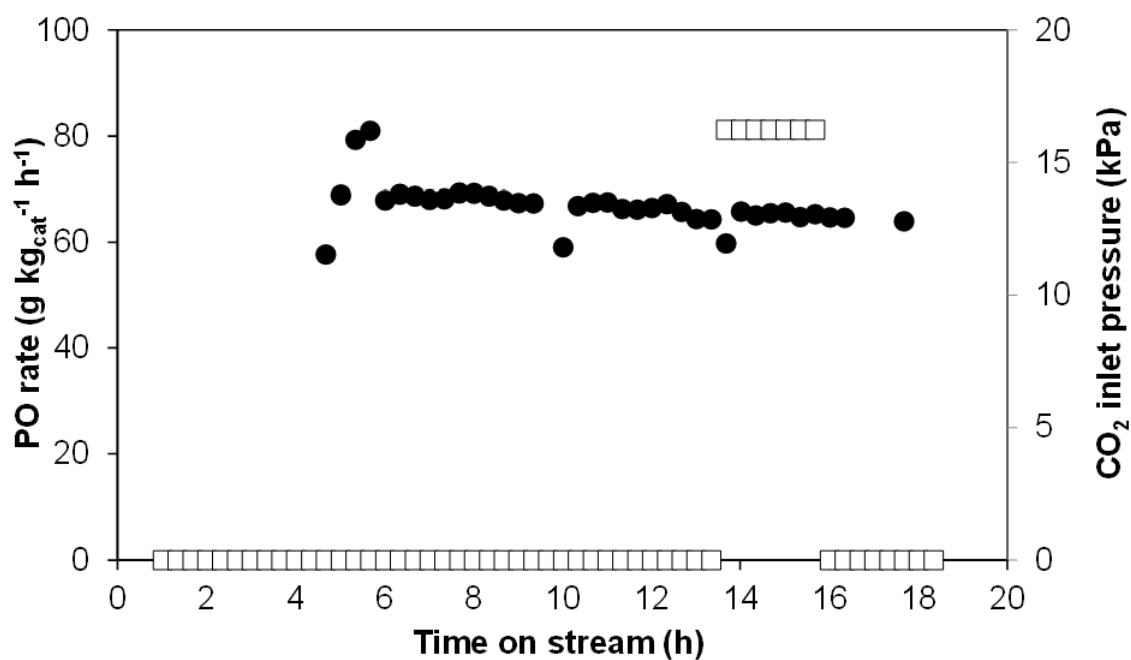


Figure 3.17. Propylene oxide formation rate as a function of time on stream (filled circles) and CO₂ inlet pressure (open squares) over 0.11Au/TS-1(81) with 10% H₂, 10% O₂, 10% propylene, and balance N₂ flow (SV = 14,000 cm³ g_{cat} h⁻¹, T = 473 K).

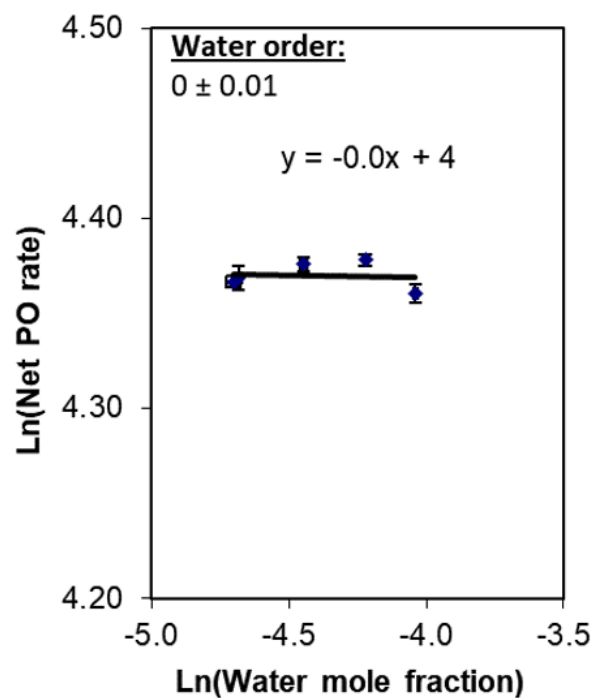


Figure 3.18. Apparent water order measured over 0.069Au/TS-1(143) at 473 K, $SV = 26,000 \text{ cm}^3 \text{ g}_{cat}^{-1} \text{ h}^{-1}$, 10% H_2 , 10% O_2 , 10% C_3H_6 , 0-0.86% H_2O , and balance N_2 in a gas phase CSTR.

Table 3.7. Apparent reaction orders and activation energies for PO formation measured over all catalysts in this study. Activation energies were measured in the temperature range 443-483 K with a feed composition of 10% H₂/ 10% O₂/ 10% C₃H₆/ 70% N₂ and a space velocity of 26,000 cm³ g_{cat}⁻¹ h⁻¹ in a gas-phase CSTR. Reaction orders were measured at 473 K with a feed composition of 2.5-10% H₂/ 2.5-10% O₂/ 2.5-10% C₃H₆/ 0-0.3% PO/ balance N₂ and a space velocity of 26,000 cm³ g_{cat}⁻¹ h⁻¹ in a gas-phase CSTR.

Catalyst	Reaction orders						E _{app} (kJ mol ⁻¹)
	H ₂	O ₂	C ₃ H ₆	PO	CO ₂	H ₂ O	
0.092Au/TS-1(75)	0.5	0.2	0.3	-0.8	n.m.*	n.m.	n.m.
0.019Au/TS-1(143)	0.7	0.2	0.2	-0.5	n.m.	n.m.	32
0.040Au/TS-1(81)	0.7	0.2	0.2	-0.8	n.m.	n.m.	33
0.030Au/TS-1(81)	0.7	0.2	0.1	-0.6	n.m.	n.m.	34
0.044Au/TS-1(81)	0.7	0.2	0.2	-0.7	n.m.	n.m.	34
0.033Au/TS-1(143)	0.7	0.2	0.2	-0.4	n.m.	0.0	34
0.069Au/TS-1(143)	0.6	0.2	0.3	-0.4	n.m.	0.0	32
0.064Au/TS-1(143)	0.6	0.2	0.3	-0.5	n.m.	0.0	33

* n.m., not measured

The reaction orders measured for each of the minor products are reported in Table 3.8, along with the reaction orders for propylene oxide and H₂ oxidation for comparison. Of the products, acetone, ethanal, propanal, and CO₂ had average measured H₂ reaction orders of 0.3, 0.7, 0.4, and 0.2 respectively, while the acrolein rate was not affected by changing the H₂ inlet pressure.

The oxygen reaction orders are similar to that for PO formation (0.2) for acrolein, acetone, and ethanal (0.4, 0.3, 0.2, respectively), while the reaction orders for propanal (0.1) and CO₂ (0.1) formation are notably lower.

Differences in apparent propylene orders, from slightly positive to slightly negative, were observed over all species and imply differences in common intermediates or differences in the sites in which side products are formed. For instance, acrolein (0.3 order) and propanal (0.1 order) were promoted by increased propylene pressure, while acetone (0), ethanal (-0.2), and CO₂ (-0.1) were unaffected or slightly inhibited by propylene, similar to the observed kinetics for H₂ oxidation (-0.3 order).

Differences in apparent propylene oxide orders, from slightly positive to slightly negative, were observed over all species and imply differences in common intermediates or differences

in the sites in which side products are formed. Propanal (0.4 order) in particular appears to be a series product from propylene oxide similar to acetone (0.2 order), as might be expected for these two ring opening products. In contrast, acrolein (0), CO₂ (0), and ethanal (0.1) formation rates were less dependent on PO pressure, suggesting the possibility of alternate pathways to forming these products than via propylene oxide.

The apparent activation energies for acrolein, acetone, ethanal, and propanal (72, 40, 57, and 63 kJ mol⁻¹, respectively) were distinct from that for CO₂ (20 kJ mol⁻¹). Those for acrolein, ethanal, and propanal were higher, outside of experimental error, than those for propylene oxide formation (33 kJ mol⁻¹) and H₂ oxidation (31 kJ mol⁻¹).

Table 3.8. Apparent reaction orders and activation energies for PO formation measured over all catalysts in this study. Activation energies were measured in the temperature range 443-483 K with a feed composition of 10% H₂/ 10% O₂/ 10% C₃H₆/ 70% N₂ and a space velocity of 26,000 cm³ g_{cat}⁻¹ h⁻¹ in a gas-phase CSTR. Reaction orders were measured at 473 K with a feed composition of 2.5-10% H₂/ 2.5-10% O₂/ 2.5-10% C₃H₆/ 0-0.3% PO/ balance N₂ and a space velocity of 26,000 cm³ g_{cat}⁻¹ h⁻¹ in a gas-phase CSTR.

Product	Reaction orders						E _{app} (kJ mol ⁻¹)
	H ₂	O ₂	C ₃ H ₆	PO	CO ₂	H ₂ O	
PO	0.6 ± 0.08	0.2 ± 0.01	0.2 ± 0.08	-0.6 ± 0.2	0	0.02 ± 0.03	33 ± 0.9
corrected ^a	1 ± 0.2	0.4 ± 0.06	0.4 ± 0.1	—	0	—	52 ± 6
Acrolein	0.00 ± 0.09	0.4 ± 0.9	0.3 ± 0.04	-0.06 ± 0.04	0	-0.05 ± 0.08	72 ± 9
Acetone	0.3 ± 0.2	0.3 ± 0.2	0.0 ± 0.1	0.2 ± 0.2	0	-0.01 ± 0.03	40 ± 20
Ethanal	0.7 ± 0.08	0.2 ± 0.05	-0.2 ± 0.04	0.1 ± 0.05	0	0.02 ± 0.04	57 ± 4
Propanal	0.4 ± 0.04	0.1 ± 0.03	0.1 ± 0.02	0.4 ± 0.06	0	0.03 ± 0.04	63 ± 9
CO ₂	0.2 ± 0.07	0.1 ± 0.03	-0.1 ± 0.04	0.03 ± 0.06	0	0.04 ± 0.01	20 ± 5
H ₂ oxidation	0.9 ± 0.1	0.3 ± 0.1	-0.3 ± 0.07	-0.01 ± 0.2	0	-0.14 ± 0.07	31 ± 10

^a Corrected for PO inhibition (-0.6 order).

3.5.6 Example Log Derivative Derivation

As derived in section ??, the rate of PO formation is:

$$r_{PO} = \frac{k_7 K_6 K_5 K_4 P_{C_3H_6} P_{O_2} P_{H_2} L_2}{(1 + K_2 P_{O_2} + K_5 K_4 P_{O_2} P_{H_2} + K_8 P_{C_3H_6O})(1 + K_6 P_{C_3H_6} + K_9 P_{C_3H_6O})} \quad (3.21)$$

For example, to arrive at the equivalence of the H_2 reaction order with $1 - \theta_{HOOH}$, we first note that:

$$\frac{d \ln(r_{PO})}{d \ln(P_{H_2})} = \frac{P_{H_2}}{r_{PO}} \cdot \frac{d(r_{PO})}{d(P_{H_2})} \quad (3.22)$$

Then, taking the derivative of the rate expression with respect to hydrogen pressure results in:

$$\begin{aligned} & \frac{k_7 K_6 K_5 K_4 P_{C_3H_6} P_{O_2}}{(1 + K_2 P_{O_2} + K_5 K_4 P_{O_2} P_{H_2} + K_8 P_{PO})(1 + K_6 P_{C_3H_6} + K_9 P_{PO})} \\ & \cdot \left(1 - \frac{K_5 K_4 P_{O_2} P_{H_2}}{1 + K_2 P_{O_2} + K_5 K_4 P_{O_2} P_{H_2} + K_8 P_{PO}} \right) \end{aligned} \quad (3.23)$$

And thus:

$$\frac{P_{H_2}}{r_{PO}} \cdot \frac{d(r_{PO})}{d(P_{H_2})} = \left(1 - \frac{K_5 K_4 P_{O_2} P_{H_2}}{1 + K_2 P_{O_2} + K_5 K_4 P_{O_2} P_{H_2} + K_8 P_{PO}} \right) \quad (3.24)$$

Or equivalently:

$$\frac{d \ln(r_{PO})}{d \ln(P_{H_2})} = 1 - \theta_{HOOH} \quad (3.25)$$

3.5.7 Sequential Mechanism, Rate Law, and Log Derivatives

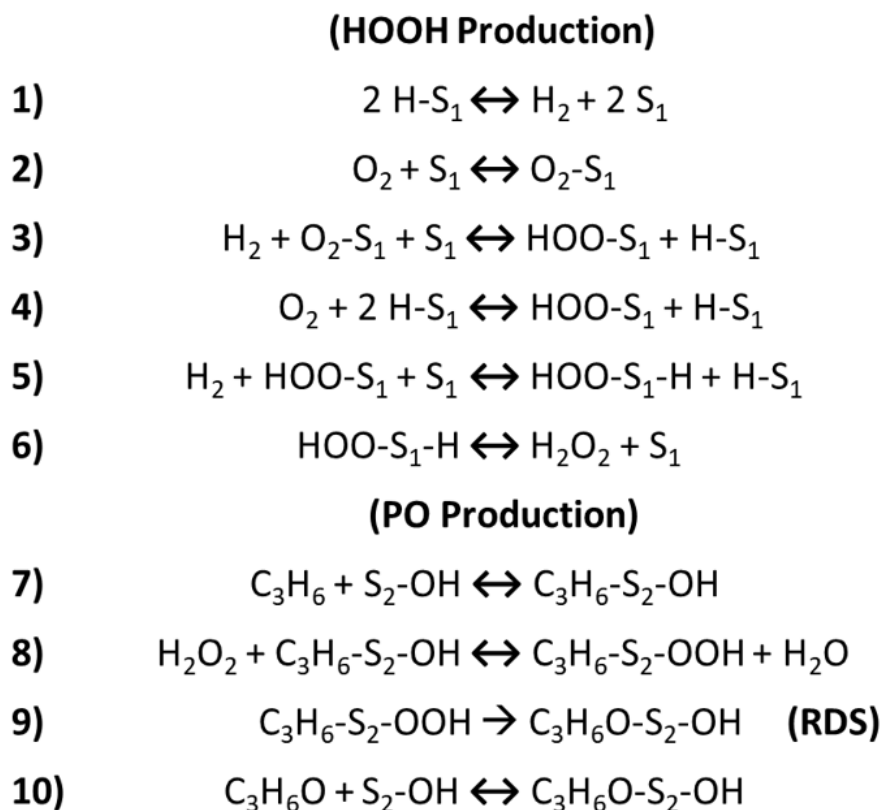


Figure 3.19. One variation of the sequential mechanism. In this mechanism, S_1 refers to a Au site, and S_2 refers to a Ti site.

In general, the sequential mechanism (Figure 3.19) features hydrogen peroxide production on gold sites (S_1), which then desorbs and adsorbs to titanium sites (in this case, $\text{S}_2\text{-OH}$) to form a hydroperoxy species, which then epoxidizes propylene.

Assuming steps 1-8 and 10 are quasi-equilibrated, step 9 is the rate determining step, and that the MASIs on the Ti site (in order of appearance in the denominator of the rate law) are empty sites ($\text{S}_2\text{-OH}$), $\text{C}_3\text{H}_6\text{-S}_2\text{-OH}$, $\text{C}_3\text{H}_6\text{-S}_2\text{-OOH}$, and $\text{C}_3\text{H}_6\text{O-S}_2\text{-OH}$ results in the rate

expression shown in equation 3.26.

$$r = \frac{r_{PO}}{L_2} = \frac{k_9 K_8 K_7 K_6 K_5 K_4 P_{C_3H_6} P_{H_2} P_{O_2} / P_{H_2O}}{1 + K_7 P_{C_3H_6} + \frac{K_8 K_7 K_6 K_5 K_4 P_{C_3H_6} P_{H_2} P_{O_2}}{P_{H_2O}} + K_{10} P_{C_3H_6O}} \quad (3.26)$$

Where k_{11} is the forward rate constant for step 11, K_i is the equilibrium constant for step i, P_j is the partial pressure of component j, and L_2 is the number of Ti sites.

This rate law results in the following log derivative relationships (Equations 3.27 - 3.30), describing the relationship between surface coverages and reaction orders. An example derivation is shown above (section 3.5.6, equations 3.22 - 3.25). Based on these log derivatives, the coverages required for the sequential model to reproduce the measured kinetics presented in this study (Table 3.2, Table 3.7) necessitate a coverage on the Ti-OH site that is greater than 1.

$$\frac{\partial \ln(r)}{\partial \ln(P_{O_2})} = 1 - \theta_{C_3H_6-S_2-OOH} \quad (3.27)$$

$$\frac{\partial \ln(r)}{\partial \ln(P_{H_2})} = 1 - \theta_{C_3H_6-S_2-OOH} \quad (3.28)$$

$$\frac{\partial \ln(r)}{\partial \ln(P_{C_3H_6})} = 1 - \theta_{C_3H_6-S_2-OH} - \theta_{C_3H_6-S_2-OOH} \quad (3.29)$$

$$\frac{\partial \ln(r)}{\partial \ln(P_{C_3H_6O})} = -\theta_{C_3H_6O-S_2-OH} \quad (3.30)$$

References

- [1] H. Baer, M. Bergamo, A. Forlin, L. H. Pottenger, and J. Lindner, "Propylene oxide," in *Ullmann's Encyclopedia of Industrial Chemistry*, John Wiley & Sons, Ltd, 2012, ISBN: 978-3-527-30673-2. DOI: [10.1002/14356007.a22_239.pub3](https://doi.org/10.1002/14356007.a22_239.pub3). [Online]. Available: https://onlinelibrary.wiley.com/doi/abs/10.1002/14356007.a22_239.pub3.
- [2] T. Hayashi, K. Tanaka, and M. Haruta, "Selective vapor-phase epoxidation of propylene over au/TiO₂ catalysts in the presence of oxygen and hydrogen," *Journal of Catalysis*, vol. 178, no. 2, pp. 566–575, Sep. 10, 1998, ISSN: 0021-9517. DOI: [10.1006/jcat.1998.2157](https://doi.org/10.1006/jcat.1998.2157). [Online]. Available: <http://www.sciencedirect.com/science/article/pii/S0021951798921571>.
- [3] W.-S. Lee, M. Cem Akatay, E. A. Stach, F. H. Ribeiro, and W. Nicholas Delgass, "Reproducible preparation of au/TS-1 with high reaction rate for gas phase epoxidation of propylene," *Journal of Catalysis*, vol. 287, pp. 178–189, Mar. 2012, ISSN: 0021-9517. DOI: [10.1016/j.jcat.2011.12.019](https://doi.org/10.1016/j.jcat.2011.12.019). [Online]. Available: <http://www.sciencedirect.com/science/article/pii/S0021951711004222>.
- [4] W.-S. Lee, M. Cem Akatay, E. A. Stach, F. H. Ribeiro, and W. Nicholas Delgass, "Enhanced reaction rate for gas-phase epoxidation of propylene using h₂ and o₂ by cs promotion of au/TS-1," *Journal of Catalysis*, 50th Anniversary Special Issue, vol. 308, pp. 98–113, Dec. 2013, ISSN: 0021-9517. DOI: [10.1016/j.jcat.2013.05.023](https://doi.org/10.1016/j.jcat.2013.05.023). [Online]. Available: <http://www.sciencedirect.com/science/article/pii/S0021951713001966>.
- [5] Z. Li, Y. Wang, J. Zhang, D. Wang, and W. Ma, "Better performance for gas-phase epoxidation of propylene using h₂ and o₂ at lower temperature over au/TS-1 catalyst," *Catalysis Communications*, vol. 90, pp. 87–90, Feb. 2017, ISSN: 1566-7367. DOI: [10.1016/j.catcom.2016.12.002](https://doi.org/10.1016/j.catcom.2016.12.002). [Online]. Available: <http://www.sciencedirect.com/science/article/pii/S1566736716304484>.
- [6] Z. Song, X. Feng, Y. Liu, C. Yang, and X. Zhou, "Advances in manipulation of catalyst structure and relationship of structure-performance for direct propene epoxidation with h₂ and o₂," *Progress in Chemistry*, vol. 28, no. 12, pp. 1762–1773, 2016. DOI: [10.7536/PC160803](https://doi.org/10.7536/PC160803).
- [7] J. Huang, T. Takei, T. Akita, H. Ohashi, and M. Haruta, "Gold clusters supported on alkaline treated TS-1 for highly efficient propene epoxidation with o₂ and h₂," *Applied Catalysis B: Environmental*, vol. 95, no. 3, pp. 430–438, Apr. 6, 2010, ISSN: 0926-3373. DOI: [10.1016/j.apcatb.2010.01.023](https://doi.org/10.1016/j.apcatb.2010.01.023). [Online]. Available: <http://www.sciencedirect.com/science/article/pii/S0926337310000378>.
- [8] J. Huang, E. Lima, T. Akita, A. Guzmán, C. Qi, T. Takei, and M. Haruta, "Propene epoxidation with o₂ and h₂: Identification of the most active gold clusters," *Journal of Catalysis*, vol. 278, no. 1, pp. 8–15, Feb. 14, 2011, ISSN: 0021-9517. DOI: [10.1016/j.jcat.2010.11.012](https://doi.org/10.1016/j.jcat.2010.11.012). [Online]. Available: <http://www.sciencedirect.com/science/article/pii/S0021951710003982>.

- [9] J. Lu, X. Zhang, J. J. Bravo-Suárez, T. Fujitani, and S. T. Oyama, “Effect of composition and promoters in au/TS-1 catalysts for direct propylene epoxidation using h₂ and o₂,” *Catalysis Today*, Special Issue dedicated to Marc Jacques Ledoux on the occasion of his 60th birthday, vol. 147, no. 3, pp. 186–195, Oct. 15, 2009, ISSN: 0920-5861. DOI: [10.1016/j.cattod.2008.09.005](https://doi.org/10.1016/j.cattod.2008.09.005). [Online]. Available: <http://www.sciencedirect.com/science/article/pii/S0920586108004239>.
- [10] T. Liu, P. Hacırlıoğlu, S. T. Oyama, M.-F. Luo, X.-R. Pan, and J.-Q. Lu, “Enhanced reactivity of direct propylene epoxidation with h₂ and o₂ over ge-modified au/TS-1 catalysts,” *Journal of Catalysis*, vol. 267, no. 2, pp. 202–206, Oct. 25, 2009, ISSN: 0021-9517. DOI: [10.1016/j.jcat.2009.08.002](https://doi.org/10.1016/j.jcat.2009.08.002). [Online]. Available: <http://www.sciencedirect.com/science/article/pii/S0021951709002577>.
- [11] X. Feng, N. Sheng, Y. Liu, X. Chen, D. Chen, C. Yang, and X. Zhou, “Simultaneously enhanced stability and selectivity for propene epoxidation with h₂ and o₂ on au catalysts supported on nano-crystalline mesoporous TS-1,” *ACS Catal.*, pp. 2668–2675, Feb. 27, 2017. DOI: [10.1021/acscatal.6b03498](https://doi.org/10.1021/acscatal.6b03498). [Online]. Available: <http://dx.doi.org/10.1021/acscatal.6b03498>.
- [12] A. K. Sinha, S. Seelan, S. Tsubota, and M. Haruta, “A three-dimensional mesoporous titanasilicate support for gold nanoparticles: Vapor-phase epoxidation of propene with high conversion,” *Angewandte Chemie International Edition*, vol. 43, no. 12, pp. 1546–1548, Mar. 12, 2004, ISSN: 1521-3773. DOI: [10.1002/anie.200352900](https://doi.org/10.1002/anie.200352900). [Online]. Available: <http://onlinelibrary.wiley.com/doi/10.1002/anie.200352900/abstract>.
- [13] W.-S. Lee, M. Cem Akatay, E. A. Stach, F. H. Ribeiro, and W. Nicholas Delgass, “Gas-phase epoxidation of propylene in the presence of h₂ and o₂ over small gold ensembles in uncalcined TS-1,” *Journal of Catalysis*, vol. 313, pp. 104–112, May 2014, ISSN: 0021-9517. DOI: [10.1016/j.jcat.2014.02.013](https://doi.org/10.1016/j.jcat.2014.02.013). [Online]. Available: <http://www.sciencedirect.com/science/article/pii/S0021951714000529>.
- [14] E. E. Stangland, K. B. Stavens, R. P. Andres, and W. N. Delgass, “Characterization of gold–titania catalysts via oxidation of propylene to propylene oxide,” *Journal of Catalysis*, vol. 191, no. 2, pp. 332–347, Apr. 25, 2000, ISSN: 0021-9517. DOI: [10.1006/jcat.1999.2809](https://doi.org/10.1006/jcat.1999.2809). [Online]. Available: <https://www.sciencedirect.com/science/article/pii/S002195179928099>.
- [15] E. Stangland, D. Barton, R. Schroden, and K. Watson, “Deactivation of au/TS-1 catalysts during the epoxidation of propylene in the presence of h₂/o₂,” *AIChE Annual Meeting, Salt Lake City, UT*, 2015.
- [16] C. Sivadinarayana, T. V. Choudhary, L. L. Daemen, J. Eckert, and D. W. Goodman, “The nature of the surface species formed on au/TiO₂ during the reaction of h₂ and o₂: an inelastic neutron scattering study,” *J. Am. Chem. Soc.*, vol. 126, no. 1, pp. 38–39, Jan. 1, 2004, ISSN: 0002-7863. DOI: [10.1021/ja0381398](https://doi.org/10.1021/ja0381398). [Online]. Available: <https://doi.org/10.1021/ja0381398>.
- [17] D. P. Dissanayake and J. H. Lunsford, “The direct formation of h₂o₂ from h₂ and o₂ over colloidal palladium,” *Journal of Catalysis*, vol. 214, no. 1, pp. 113–120, Feb. 15, 2003, ISSN: 0021-9517. DOI: [10.1016/S0021-9517\(02\)00171-9](https://doi.org/10.1016/S0021-9517(02)00171-9). [Online]. Available: <http://www.sciencedirect.com/science/article/pii/S0021951702001719>.

- [18] B. Taylor, J. Lauterbach, G. E. Blau, and W. N. Delgass, "Reaction kinetic analysis of the gas-phase epoxidation of propylene over au/TS-1," *Journal of Catalysis*, vol. 242, no. 1, pp. 142–152, Aug. 15, 2006, ISSN: 0021-9517. DOI: [10.1016/j.jcat.2006.06.007](https://doi.org/10.1016/j.jcat.2006.06.007). [Online]. Available: <http://www.sciencedirect.com/science/article/pii/S002195170600203X>.
- [19] J. Lu, X. Zhang, J. J. Bravo-Suárez, S. Tsubota, J. Gaudet, and S. T. Oyama, "Kinetics of propylene epoxidation using h₂ and o₂ over a gold/mesoporous titanosilicate catalyst," *Catalysis Today*, M. Albert Vannice Festschrift, vol. 123, no. 1, pp. 189–197, May 30, 2007, ISSN: 0920-5861. DOI: [10.1016/j.cattod.2007.02.005](https://doi.org/10.1016/j.cattod.2007.02.005). [Online]. Available: <http://www.sciencedirect.com/science/article/pii/S0920586107001009>.
- [20] S. T. Oyama, X. Zhang, J. Lu, Y. Gu, and T. Fujitani, "Epoxidation of propylene with h₂ and o₂ in the explosive regime in a packed-bed catalytic membrane reactor," *Journal of Catalysis*, vol. 257, no. 1, pp. 1–4, Jul. 1, 2008, ISSN: 0021-9517. DOI: [10.1016/j.jcat.2008.04.023](https://doi.org/10.1016/j.jcat.2008.04.023). [Online]. Available: <http://www.sciencedirect.com/science/article/pii/S0021951708001681>.
- [21] A. M. Joshi, W. N. Delgass, and K. T. Thomson, "Mechanistic implications of aun/ti-lattice proximity for propylene epoxidation," *J. Phys. Chem. C*, vol. 111, no. 22, pp. 7841–7844, Jun. 1, 2007, ISSN: 1932-7447. DOI: [10.1021/jp072873m](https://doi.org/10.1021/jp072873m). [Online]. Available: <http://dx.doi.org/10.1021/jp072873m>.
- [22] S. Kanungo, D. M. Perez Ferrandez, F. Neira d'Angelo, J. C. Schouten, and T. A. Nijhuis, "Kinetic study of propene oxide and water formation in hydro-epoxidation of propene on au/ti–SiO₂ catalyst," *Journal of Catalysis*, vol. 338, pp. 284–294, Jun. 1, 2016, ISSN: 0021-9517. DOI: [10.1016/j.jcat.2016.03.019](https://doi.org/10.1016/j.jcat.2016.03.019). [Online]. Available: <http://www.sciencedirect.com/science/article/pii/S0021951716001159>.
- [23] M. G. Clerici, G. Bellussi, and U. Romano, "Synthesis of propylene oxide from propylene and hydrogen peroxide catalyzed by titanium silicalite," *Journal of Catalysis*, vol. 129, no. 1, pp. 159–167, May 1, 1991, ISSN: 0021-9517. DOI: [10.1016/0021-9517\(91\)90019-Z](https://doi.org/10.1016/0021-9517(91)90019-Z). [Online]. Available: <http://www.sciencedirect.com/science/article/pii/002195179190019Z>.
- [24] W.-S. Lee, L.-C. Lai, M. Cem Akatay, E. A. Stach, F. H. Ribeiro, and W. N. Delgass, "Probing the gold active sites in au/TS-1 for gas-phase epoxidation of propylene in the presence of hydrogen and oxygen," *Journal of Catalysis*, vol. 296, pp. 31–42, Dec. 2012, ISSN: 0021-9517. DOI: [10.1016/j.jcat.2012.08.021](https://doi.org/10.1016/j.jcat.2012.08.021). [Online]. Available: <http://www.sciencedirect.com/science/article/pii/S0021951712002783>.
- [25] M. Okumura, Y. Kitagawa, K. Yamaguchi, T. Akita, S. Tsubota, and M. Haruta, "Direct production of hydrogen peroxide from h₂ and o₂ over highly dispersed au catalysts," *Chem. Lett.*, vol. 32, no. 9, pp. 822–823, Aug. 11, 2003, ISSN: 0366-7022. DOI: [10.1246/cl.2003.822](https://doi.org/10.1246/cl.2003.822). [Online]. Available: <http://www.journal.csj.jp/doi/abs/10.1246/cl.2003.822>.
- [26] D. T. Bregante and D. W. Flaherty, "Periodic trends in olefin epoxidation over group IV and v framework substituted zeolite catalysts: A kinetic and spectroscopic study," *J. Am. Chem. Soc.*, Apr. 28, 2017, ISSN: 0002-7863. DOI: [10.1021/jacs.7b01422](https://doi.org/10.1021/jacs.7b01422). [Online]. Available: <http://pubs.acs.org/doi/abs/10.1021/jacs.7b01422>.

- [27] V. Cybulskis, A. Smeltz, Y. Zvinevich, R. Gounder, W. N. Delgass, and F. Ribeiro, "Learning the fundamentals of kinetics and reaction engineering with the catalytic oxidation of methane," *Chemical Engineering Education*, vol. 50, no. 3, pp. 202–210, Aug. 1, 2016, ISSN: 2165-6428. [Online]. Available: <http://journals.fcla.edu/cee/article/view/88296>.
- [28] T. A. Nijhuis, B. J. Huizinga, M. Makkee, and J. A. Moulijn, "Direct epoxidation of propene using gold dispersed on TS-1 and other titanium-containing supports," *Ind. Eng. Chem. Res.*, vol. 38, no. 3, pp. 884–891, Mar. 1, 1999, ISSN: 0888-5885. DOI: [10.1021/ie980494x](https://doi.org/10.1021/ie980494x). [Online]. Available: <http://dx.doi.org/10.1021/ie980494x>.
- [29] R. B. Khomane, B. D. Kulkarni, A. Paraskar, and S. R. Sainkar, "Synthesis, characterization and catalytic performance of titanium silicalite-1 prepared in micellar media," *Materials Chemistry and Physics*, vol. 76, no. 1, pp. 99–103, Jul. 28, 2002, ISSN: 0254-0584. DOI: [10.1016/S0254-0584\(01\)00507-7](https://doi.org/10.1016/S0254-0584(01)00507-7). [Online]. Available: <http://www.sciencedirect.com/science/article/pii/S0254058401005077>.
- [30] B. Taylor, J. Lauterbach, and W. N. Delgass, "Gas-phase epoxidation of propylene over small gold ensembles on TS-1," *Applied Catalysis A: General*, Catalysis by Gold, vol. 291, no. 1, pp. 188–198, Sep. 12, 2005, ISSN: 0926-860X. DOI: [10.1016/j.apcata.2005.02.039](https://doi.org/10.1016/j.apcata.2005.02.039). [Online]. Available: <http://www.sciencedirect.com/science/article/pii/S0926860X05002504>.
- [31] J. Tauc, "Optical properties and electronic structure of amorphous ge and si," *Materials Research Bulletin*, vol. 3, no. 1, pp. 37–46, Jan. 1, 1968, ISSN: 0025-5408. DOI: [10.1016/0025-5408\(68\)90023-8](https://doi.org/10.1016/0025-5408(68)90023-8). [Online]. Available: <http://www.sciencedirect.com/science/article/pii/0025540868900238>.
- [32] J. Tauc, R. Grigorovici, and A. Vancu, "Optical properties and electronic structure of amorphous germanium," *physica status solidi (b)*, vol. 15, no. 2, pp. 627–637, 1966, ISSN: 1521-3951. DOI: [10.1002/pssb.19660150224](https://doi.org/10.1002/pssb.19660150224). [Online]. Available: <https://onlinelibrary.wiley.com/doi/abs/10.1002/pssb.19660150224>.
- [33] E. A. Davis and N. F. Mott, "Conduction in non-crystalline systems v. conductivity, optical absorption and photoconductivity in amorphous semiconductors," *The Philosophical Magazine: A Journal of Theoretical Experimental and Applied Physics*, vol. 22, no. 179, pp. 0903–0922, Nov. 1, 1970, ISSN: 0031-8086. DOI: [10.1080/14786437008221061](https://doi.org/10.1080/14786437008221061). [Online]. Available: <https://doi.org/10.1080/14786437008221061>.
- [34] R. Gounder and M. E. Davis, "Titanium-beta zeolites catalyze the stereospecific isomerization of d-glucose to l-sorbose via intramolecular c5–c1 hydride shift," *ACS Catal.*, vol. 3, no. 7, pp. 1469–1476, Jul. 5, 2013. DOI: [10.1021/cs400273c](https://doi.org/10.1021/cs400273c). [Online]. Available: <https://doi.org/10.1021/cs400273c>.
- [35] G. Petrini, A. Cesana, G. D. Alberti, F. Genoni, G. Leofanti, M. Padovan, G. Paparatto, and P. Roffia, "Deactivation phenomena on ti-silicalite," in *Studies in Surface Science and Catalysis*, ser. Catalyst Deactivation 1991, C. H. Bartholomew and J. B. Butt, Eds., vol. 68, Elsevier, Jan. 1, 1991, pp. 761–766. DOI: [10.1016/S0167-2991\(08\)62710-X](https://doi.org/10.1016/S0167-2991(08)62710-X). [Online]. Available: <http://www.sciencedirect.com/science/article/pii/S016729910862710X>.

- [36] X. Gao, S. R. Bare, J. L. G. Fierro, M. A. Banares, and I. E. Wachs, "Preparation and in-situ spectroscopic characterization of molecularly dispersed titanium oxide on silica," *J. Phys. Chem. B*, vol. 102, no. 29, pp. 5653–5666, Jul. 1, 1998, ISSN: 1520-6106. DOI: [10.1021/jp981423e](https://doi.org/10.1021/jp981423e). [Online]. Available: <https://doi.org/10.1021/jp981423e>.
- [37] X. Xue, W. Ji, Z. Mao, H. Mao, Y. Wang, X. Wang, W. Ruan, B. Zhao, and J. R. Lombardi, "Raman investigation of nanosized TiO₂: Effect of crystallite size and quantum confinement," *J. Phys. Chem. C*, vol. 116, no. 15, pp. 8792–8797, Apr. 19, 2012, ISSN: 1932-7447. DOI: [10.1021/jp2122196](https://doi.org/10.1021/jp2122196). [Online]. Available: <https://doi.org/10.1021/jp2122196>.
- [38] M. Behrens and R. Schlögl, "X-ray diffraction and small angle x-ray scattering," in *Characterization of Solid Materials and Heterogeneous Catalysts*, John Wiley & Sons, Ltd, 2012, pp. 609–653, ISBN: 978-3-527-64532-9. DOI: [10.1002/9783527645329.ch15](https://doi.org/10.1002/9783527645329.ch15). [Online]. Available: <https://onlinelibrary.wiley.com/doi/abs/10.1002/9783527645329.ch15>.
- [39] H. Zhang and J. F. Banfield, "Understanding polymorphic phase transformation behavior during growth of nanocrystalline aggregates: insights from TiO₂," *J. Phys. Chem. B*, vol. 104, no. 15, pp. 3481–3487, Apr. 1, 2000, ISSN: 1520-6106. DOI: [10.1021/jp000499j](https://doi.org/10.1021/jp000499j). [Online]. Available: <http://dx.doi.org/10.1021/jp000499j>.
- [40] C. B. Khouw, C. B. Dartt, J. A. Labinger, and M. E. Davis, "Studies on the catalytic-oxidation of alkanes and alkenes by titanium silicates," *Journal of Catalysis*, vol. 149, no. 1, pp. 195–205, Sep. 1, 1994, ISSN: 0021-9517. DOI: [10.1006/jcat.1994.1285](https://doi.org/10.1006/jcat.1994.1285). [Online]. Available: <https://www.sciencedirect.com/science/article/pii/S0021951784712851>.
- [41] A. Pulido, M. Boronat, and A. Corma, "Propene epoxidation with h₂/h₂O/o₂ mixtures over gold atoms supported on defective graphene: A theoretical study," *J. Phys. Chem. C*, vol. 116, no. 36, pp. 19355–19362, Sep. 13, 2012, ISSN: 1932-7447. DOI: [10.1021/jp3055125](https://doi.org/10.1021/jp3055125). [Online]. Available: <https://doi.org/10.1021/jp3055125>.
- [42] D. G. Barton and S. G. Podkolzin, "Kinetic study of a direct water synthesis over silica-supported gold nanoparticles," *J. Phys. Chem. B*, vol. 109, no. 6, pp. 2262–2274, Feb. 1, 2005, ISSN: 1520-6106. DOI: [10.1021/jp048837u](https://doi.org/10.1021/jp048837u). [Online]. Available: <http://dx.doi.org/10.1021/jp048837u>.
- [43] W. Bone and R. Wheeler, "The combination of hydrogen and oxygen in contact with hot surfaces," *Philosophical Transactions of the Royal Society A: Mathematical, Physical and Engineering Sciences*, vol. 206, pp. 1–67, 1906.
- [44] A. F. Benton and J. C. Elgin, "THE CATALYTIC SYNTHESIS OF WATER VAPOR IN CONTACT WITH METALLIC GOLD¹," *J. Am. Chem. Soc.*, vol. 49, no. 10, pp. 2426–2438, Oct. 1, 1927, ISSN: 0002-7863. DOI: [10.1021/ja01409a012](https://doi.org/10.1021/ja01409a012). [Online]. Available: <https://doi.org/10.1021/ja01409a012>.
- [45] D. H. Wells, W. N. Delgass, and K. T. Thomson, "Evidence of defect-promoted reactivity for epoxidation of propylene in titanosilicate (TS-1) catalysts: a DFT study," *J. Am. Chem. Soc.*, vol. 126, no. 9, pp. 2956–2962, Mar. 1, 2004, ISSN: 0002-7863. DOI: [10.1021/ja037741v](https://doi.org/10.1021/ja037741v). [Online]. Available: <https://doi.org/10.1021/ja037741v>.

- [46] T. A. Nijhuis, E. Sacaliuc, A. M. Beale, A. M. J. van der Eerden, J. C. Schouten, and B. M. Weckhuysen, “Spectroscopic evidence for the adsorption of propene on gold nanoparticles during the hydro-epoxidation of propene,” *Journal of Catalysis*, vol. 258, no. 1, pp. 256–264, Aug. 15, 2008, ISSN: 0021-9517. DOI: [10.1016/j.jcat.2008.06.020](https://doi.org/10.1016/j.jcat.2008.06.020). [Online]. Available: <http://www.sciencedirect.com/science/article/pii/S0021951708002455>.
- [47] R. B. Bird, W. E. Steward, and E. N. Lightfoot, *Transport Phenomena*. New York: John Wiley & Sons, 2002.

4. KINETICS OF PROPYLENE EPOXIDATION OVER EXTRA-CRYSTALLINE GOLD ACTIVE SITES ON AU/TS-1 CATALYSTS

4.1 Introduction

Propylene oxide (PO) is an important chemical intermediate used in the manufacture of a variety of industrial and consumer products, such as polyurethanes and functional fluids [1]. However, current industrial processes for the production of PO, such as hydrochlorination, hydrogen peroxide to propylene oxide (HPPO), or epoxidation with organic peroxides, all have significant drawbacks, including generation of environmentally harmful byproducts, low selectivity to PO, or the requirement for expensive liquid-liquid separations [2], [3]. An opportunity to address these challenges exists in the form of a highly selective gas phase epoxidation reaction, with water as the only major byproduct, using co-fed propylene, hydrogen, and oxygen over gold- and titanium-containing catalysts, as first reported by Haruta and co-workers in the late 1990s [4]. While these catalysts present a unique opportunity, their integration into industrial processes has lagged due to low site-time yield (STY), low hydrogen efficiency, and poor stability with time on stream.

Efforts to increase the active site density and stabilize active sites remain hindered by a lack of fundamental understanding of the reaction kinetics and active site requirements, specifically for the gold species in the active sites. Earlier studies focused on the importance of titanium dispersion in support materials, where gold supported on Al-free MFI with framework titanium heteroatoms (TS-1), prepared by deposition-precipitation (DP) (Au/TS-1), was observed to consistently give higher STY per catalyst mass (10/10/10/70 mol% C₃H₆/H₂/O₂/N₂, 473 K, 101.3 kPa) than other gold-loaded titanium-containing materials tested, such as Au supported on crystalline mesoporous and amorphous Ti-SiO₂ [5]–[9]. Others have endeavored to determine if an optimal gold nanoparticle size exists (i.e., a size which minimizes both direct hydrogen oxidation and unselective propylene oxidation reactions), using both experimental [10]–[13] and computational [14]–[16] techniques; such efforts resulted in a general agreement that smaller gold nanoparticles or clusters were cor-

related with increased STY per TEM-derived gold surface area or catalyst mass, however no optimal size was identified.

Lee et al. later observed a continuous decrease in PO rate normalized to gold mass, PO selectivity, and hydrogen efficiency with increasing gold loading [17]. Lee et al. also observed a PO rate normalized to TS-1 mass in a core/shell catalyst consisting of a TS-1 core surrounded by an S-1 shell which was then gold loaded via DP, approximately four times greater than of a conventional Au/TS-1 catalyst with the same gold and titanium composition [18]. These results implied that active sites that include small gold clusters inside the micropores of TS-1 are the predominant PO active sites. However, the origin of this kinetic variation with gold loading, be it an intrinsic cluster size effect or merely improved Au dispersion, has not been conclusively determined. These results, in conjunction with kinetic data consistent with a two-site ‘simultaneous’ mechanism requiring Au-Ti proximity [19], [20], imply that in addition to large gold nanoparticles observable via TEM on extracrystalline TS-1 surfaces, some fraction of the gold deposited on TS-1 by DP exists as small, intraporous clusters in proximity to intraporous Ti sites.

Harris et al. determined that mechanisms requiring an equilibration with gas phase hydrogen peroxide produced in situ were inconsistent with the measured reaction orders in oxygen and hydrogen (H_2 : 1 ± 0.2 , O_2 : 0.4 ± 0.06 , 473 K, 101.3 kPa, 2.5-10 mol% O_2 , 2.5-10 mol% H_2), while a simultaneous mechanism in which intact hydrogen peroxide diffusion is unnecessary due to proximity between Au and Ti sites could not be ruled out by these measurements [20]. These results suggested that gold and Ti sites located in close proximity are necessary for PO production under the reaction conditions used (473 K, 101.3 kPa, 10/10/10/70 mol% $\text{C}_3\text{H}_6/\text{H}_2/\text{O}_2/\text{N}_2$, $14,000 \text{ cm}^3 \text{ g}_{\text{cat}}^{-1} \text{ h}^{-1}$). However, due to the lack of control of Au location when DP is used to deposit gold on TS-1, the catalytic contributions of intraporous gold clusters could not be distinguished from those of extracrystalline gold nanoparticles too large to fit into the pores of TS-1 (i.e., those $> 0.6 \text{ nm}$).

Here, we aim to independently elucidate the catalytic roles of both extracrystalline gold nanoparticles and intraporous gold clusters for both hydrogen oxidation and propylene epoxidation, by preparing Au-TS-1 catalysts using PVP-ligated Au nanoparticles (Au-PVP/TS-1) deposited onto TS-1 supports, with initial nanoparticle sizes too large to enter the micro-

pores of TS-1 (1 nm diameter) prior to ligand removal. We report apparent activation energies and reaction orders for hydrogen oxidation and intrinsic activation energies and reaction orders for propylene epoxidation, measured on both Au-PVP/TS-1 and Au/TS-1 prepared with DP (Au-DP/TS-1), as well as apparent propylene epoxidation reaction orders on Au-PVP/S-1. We evaluate active site models which assume, respectively, that corner, edge, terrace, perimeter, and all surface Au atoms are active sites for propylene epoxidation. We also evaluate a model assuming gold nanoparticles are spherical and non-faceted. Finally, we use an active site model which estimates the number of externally-accessible Ti-containing active sites within a specified interaction range of a gold nanoparticle perimeter, herein referred to as the ‘proximal Ti’ model.

We report that the kinetics of propylene epoxidation measured on both Au-PVP/TS-1 and Au-DP/TS-1 agree within error, suggesting that no significant differences in catalytic properties, exist when comparing PO active sites containing small intraporous gold clusters and sites containing large extracrystalline gold nanoparticles. The kinetics of hydrogen oxidation differ significantly between Au-DP/TS-1 and Au-PVP/TS-1 catalysts, suggesting a change in rate-determining step, reaction barrier, or active site. Additionally, rates of propylene epoxidation and hydrogen oxidation follow different trends when comparing rates normalized by either gold mass or average gold nanoparticle diameter, consistent with our previous results that suggested active sites for propylene epoxidation and hydrogen oxidation were distinct [20]. This finding suggests that there are distinct active sites for propylene epoxidation and hydrogen oxidation, which likely consist of different regions of the same Au nanoparticles.

4.2 Experimental methods

4.2.1 Catalyst synthesis

TS-1 and S-1 synthesis

Synthesis of TS-1 was performed according to previously reported procedures [21]. Briefly, synthesis began by mixing 3.85 g of polyoxyethylene 20-sorbitan monolaurate (Tween 20, Fischer Scientific, enzyme grade) and 61.56 g of deionized water (DI water) (Millipore, Synergy

UV Water Purification System, 18.2 M Ω /cm resistivity) and stirring (5 Hz) for 900 s at ambient temperature. Then, 29.38 g of tetrapropylammonium hydroxide (TPAOH, Alfa Aesar, 40 wt%) and 70.00 g of tetraethylorthosilicate (TEOS, Sigma Aldrich, 98%) were added, followed by stirring (5 Hz) under ambient conditions for 1–2 h. In a separate 15 cm³ disposable centrifuge tube (VWR, sterile polypropylene), 1.14 g of titanium (IV) butoxide (TBOT, Alfa Aesar, 99%+) and 17.26 g of isopropyl alcohol (IPA, Sigma Aldrich, 99.5%) were combined and stirred with a vortex mixer (VWR Mini Vortex Mixer) and subsequently added dropwise to the synthesis gel, with stirring (5 Hz), under ambient conditions. The final molar ratio of the synthesis gel was 1 SiO₂/0.01 TiO₂/0.17 TPA⁺/13.1 H₂O/0.0093 Tween 20/0.04 C₄H₁₀O/0.85 C₃H₈O. The solution was then stirred (6 Hz), for at least 1 h at 313–318 K before addition to a Teflon-lined stainless-steel autoclave (45 cm³, Parr Instrument Company model 4744) and placement in an isothermal oven (Yamato DKN402C Constant Temperature Oven) and heated without agitation at 413 K for at least 18 h. The resulting solid was separated from the slurry via centrifugation (Thermo Scientific Heraeus Megafuge 16, 83 Hz for 1800 s), and then washed twice with DI water, twice with acetone (Sigma Aldrich, 99.5%+), and once more with DI water, with each wash using 15 cm³ of DI water or acetone per gram of TS-1 and a vortex mixing time of 30 s. Once washed, the solid was dried for approximately 48 h at 363 K. The dried TS-1 was then treated in flowing air (100 cm³ min⁻¹ g_{cat}⁻¹) at 853 K for 10 h (0.0167 K s⁻¹ ramp).

S-1 synthesis was performed identically to TS-1 synthesis, except that the additions of titanium (IV) butoxide and isopropyl alcohol were omitted.

Preparation of Au-PVP/TS-1 and Au-PVP/S-1 samples

Polyvinylpyrrolidone (PVP) coated gold nanoparticles (Au-PVP) were deposited using the incipient wetness impregnation (IWI) method onto TS-1 and S-1 supports, as described in previous reports [22], [23]. A typical aqueous solution of Au-PVP was prepared by dissolving 0.02 g of hydrogen tetrachloroaurate(III) trihydrate (HAuCl₄ · 3H₂O, Alfa Aesar, 99.99% (metals basis)) in 50 g of DI water (Millipore, Synergy UV Water Purification System, 18.2 M Ω /cm resistivity). Then, 555 mg of PVP (40 kDa, Sigma-Aldrich) were added with

stirring (5 Hz) before the mixture was placed in a 273 K bath and stirred for an additional 30 minutes. Next, 5 mL of a 0.1 M aqueous solution of sodium borohydride (NaBH_4 , Sigma-Aldrich, 99.99% (trace metals basis)) were rapidly added to the solution while stirring at 273 K was continued. The resulting solution was then used for IWI of the TS-1 or S-1 support, followed by drying of the resulting Au-PVP/TS-1 or Au-PVP/S-1 in a vacuum oven overnight at ambient temperature. Due to the low concentration of gold in the Au-PVP solution, the IWI and vacuum drying procedures were repeated until the target gold loading was reached, which was then confirmed by elemental analysis.

4.2.2 Catalyst characterization

Powder X-ray diffraction (XRD) patterns were collected using a Rigaku Smartlab X-ray diffractometer equipped with an ASC-6 automated sample changer stage and a Cu $K\alpha$ X-ray source (1.76 kW). A typical measurement procedure consisted of packing 0.01 g of sample into a zero-background, low dead-volume sample holder (Rigaku), then scanning a 2θ range of $4\text{--}40^\circ$ at a scan rate of $0.000417^\circ \text{ s}^{-1}$ with a step size of 0.02° .

Nitrogen adsorption isotherms (77 K) were measured using a Micromeritics 3Flex Surface Characterization Analyzer. Prior to measuring isotherms, samples (0.05 g, sieved to 180–250 μm particle diameter) were degassed under vacuum (0.005 Torr) with heating to 393 K (0.0167 K s^{-1}) for 2 h, followed by heating to 623 K (0.0167 K s^{-1}) for 8 h. Micropore volumes were determined using a semi-log derivative analysis of N_2 isotherms ($\partial(V_{\text{ads}}/\text{g})/\partial(\log(P/P_0))$ vs $\log(P/P_0)$) to identify the end of micropore filling.

Bulk elemental compositions were determined using either atomic absorption spectroscopy (AAS) using a PerkinElmer model AAnalyst 300 or inductively coupled plasma optical emission spectroscopy with a Perkin Elmer ICP-OES (Thermo Scientific iCAP 7000 Plus Series ICP-OES). 1000 ppm standards (Sigma Aldrich TraceCERT) were used to create a series of diluted calibration standards, which were used to calibrate the instrument prior to measurement for each element. To prepare the samples for ICP-OES analysis, Au/TS-1 and Au/S-1 samples ($\sim 0.10 \text{ g}$) were dissolved in 2 g of HF (48 wt%, Alfa Aesar) and 2.5 g of aqua regia (prepared from a 2:1 v/v ratio of 37 wt% HCl, Mallinckrodt Chemicals, and 70 wt% HNO_3 ,

Mallinckrodt Chemicals) overnight before being diluted with 30 g of DI water. For elemental analysis with ICP-OES, samples were further acidified with 2.5 g of HNO₃ (70 wt%, Sigma Aldrich) before analysis. Titanium content was measured after calcination but before gold deposition. The Si/Ti ratio for each sample was calculated from the titanium mass fraction and the unit cell formula for the TS-1 zeotype.

Diffuse reflectance UV-Vis (DRUV-Vis) spectra were collected using a Varian Cary 5000 UV-Vis-NIR equipped with a Harrick Praying Mantis in-situ diffuse reflectance cell. Spectra were collected at a rate of 10 nm s⁻¹ on samples: (i) first exposed to ambient conditions and held in dry flowing helium 4.17 cm³ s⁻¹ (g sample)⁻¹ (referred to as “ambient spectra”) and (ii) after subsequent treatment to 523 K (0.167 K s⁻¹) for 1 h in dry flowing helium (4.17 cm³ s⁻¹ (g sample)⁻¹) (referred to as “dehydrated spectra”). Poly(tetrafluoroethylene) (PTFE, 1 μm powder, Sigma Aldrich) was used as a 100% reflectance standard, which then allowed conversion of the reflectance spectrum to an adsorption spectrum using the Kubelka-Munk (F(R)) function. Adsorption edge energies were calculated from the x-intercepts of Tauc plots ([F(R)hν]² vs. hν)[24]–[26].

Thermogravimetric analysis (TGA) experiments were performed on a TA instruments SDT Q600 thermogravimetric analyzer and differential scanning calorimeter (TGA-DSC) by heating 0.02 g of as-made Au-PVP/TS-1 or Au-PVP/S-1 in 83.3 cm³ s⁻¹ g_{cat}⁻¹ dry air (Indiana Oxygen, air zero grade, < 1 ppm total hydrocarbon content) to 423 K and holding for 2 h to remove any physisorbed water before further heating in air. To determine total PVP content, samples were heated to 1073 K (0.17 K s⁻¹) and held for 0.5 h. Combustion of PVP was characterized by a pair of exotherms and mass losses, centered at 625 K and 770 K, respectively (Section ??).

Transmission electron microscopy (TEM) and high-angle annular dark-field scanning transmission electron microscopy (HAADF-STEM) images were obtained on an FEI Talos F200X S/TEM with a 200kV X-FEG field-emission source. To prepare TEM samples, Au-PVP/TS-1 samples were sonicated in acetone and then drop-casted onto a carbon-coated Cu grid (Ted Pella).

4.2.3 Kinetic testing

Kinetic data for the gas-phase reactions examined herein were measured in an automated recycle reactor operated as a continuous stirred tank reactor (CSTR), which eliminates concentration gradients throughout the catalyst bed under all feed conditions and reactant conversions. Details of the reactor system, including details of the automation, can be found in the SI (Fig. S.1), as well as in a previous publication [20].

Kinetic measurements were performed on 0.15 g of as-deposited catalysts after sieving to 125-250 μm particle diameter, loading into a Pyrex U-tube reactor, and installing this reactor in a furnace controlled by a Eurotherm 2408 controller protected by an over-temperature thermocouple and controller (Omega CN9000A). Reaction temperatures were measured by a thermocouple (Omega, K type) housed in a quartz thermowell whose tip was in contact with the radial and axial center of the catalyst bed. The reactor is connected to a circular glass manifold serving as a recirculating volume (Fig. S.1) using 0.25" ultra-torr fittings (Swagelok). The top of the reactor and furnace were insulated using fiberglass insulation. A leak check was performed at ambient temperature by pressurizing the reactor and glass manifold to 3 psig with nitrogen, and the unit was considered leak free when no detectable change in pressure (0.1 psig) occurred over a period of 600 s.

For Au-PVP/TS-1 and Au-PVP/S-1 catalysts, flow of air was started ($\text{SV} = 10,000 \text{ cm}^3 \text{ h}^{-1} \text{ g}_{\text{cat}}^{-1}$) and the reactor temperature was increased to 573 K (0.017 K s^{-1}). This condition was maintained for 24 h before cooling to 473 K in a nitrogen purge of $0.8 \text{ cm}^3 \text{ s}^{-1}$ and switching to a 3/3/94 mol% $\text{H}_2/\text{O}_2/\text{N}_2$ flow ($\text{SV} = 10,000 \text{ cm}^3 \text{ h}^{-1} \text{ g}_{\text{cat}}^{-1}$). Care was taken to stay below the flammable regime of $\text{H}_2/\text{O}_2/\text{N}_2$ mixtures, as well as to avoid reaching the saturation pressure of water under ambient conditions. This condition was held until 12 h after the rate of hydrogen consumption reached steady state, typically about 48 h.

Kinetic experiments were performed by independently varying the flowrates of propylene, hydrogen, or air while maintaining a constant total flowrate by adjusting the nitrogen flow rate, following an activation procedure. The activation procedure for both Au-PVP/TS-1 and Au-DP/TS-1 catalysts consisted of exposing the pre-catalysts to reaction gases (10/10/10/70 mol% $\text{C}_3\text{H}_6/\text{H}_2/\text{O}_2/\text{N}_2$, 101.3 kPa, $14,000 \text{ cm}^3 \text{ h}^{-1} \text{ g}_{\text{cat}}^{-1}$) beginning at

ambient temperature and ramping to the initial reaction temperature of 473 K (0.0167 K s^{-1}). Catalysts were then held at these conditions until a steady state was achieved for both the propylene epoxidation and hydrogen oxidation rates. Propylene oxide and carbon dioxide co-feed experiments were performed using gases fed by digital mass flow controllers from a CO_2 (Indiana Oxygen) cylinder and a 1% PO/ N_2 cylinder (Airgas, $1 \pm 0.02\%$ PO in N_2 , certified standard grade), while water co-feed experiments were performed by flowing N_2 from a digital mass flow controller through a vapor-liquid-equilibrium saturator whose temperature was monitored by a thermocouple which was mounted in a quartz thermocouple well filled with water and sealed with parafilm. To avoid flammable or explosive gas mixtures, concentrations of propylene, hydrogen, and oxygen were decreased from the standard 10 mol% in a non-monotonic fashion. Apparent activation energy measurements were performed starting from the standard 473 K condition and varying the temperature in a non-monotonic fashion in the range 443-483 K. For both apparent reaction order and apparent activation energy experiments, a minimum of three repeated GC injections was taken at each condition and the reported data represent the average of the last two, or more, of these injections.

Products were injected into an on-line Agilent 6890 GC. C2 and C3 hydrocarbon products were quantified with a Supelcowax-10 capillary column (Agilent, 60 m x 530 μm , 1 μm film thickness) connected to a flame-ionization detector (FID). CO_2 , O_2 , and H_2 were quantified with a 60/80 Chromosorb 102 packed column connected to a thermal conductivity detector. Both columns and detectors used N_2 as the carrier gas. GC peak areas were quantified using pre-measured response factor calibrations for propylene, propanal, ethanal, acetone, acrolein, and propylene oxide on the FID, and H_2 , O_2 , and CO_2 for the TCD. Propylene conversions calculated based on the decrease in the effluent propylene concentration were typically less than 5%, which is within the uncertainty of the instrument. As a result, reported propylene conversions ($X_{\text{C}_3\text{H}_6}$) were calculated as the moles of C3 in the products divided by the moles of C_3H_6 in the feed (Eq. 4.1):

$$X_{\text{C}_3\text{H}_6} = \frac{\text{total moles carbon in products}}{\text{moles } \text{C}_3\text{H}_6 \text{ fed}} / 3 \quad (4.1)$$

The product carbon selectivity for each carbon-containing product was defined as:

$$S_{c,i} = \frac{\text{moles of product i formed}}{\text{total moles C in products}} \times (\text{number of carbon atoms in i}) \quad (4.2)$$

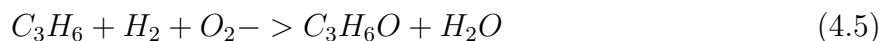
the hydrogen selectivity was defined as:

$$S_{H_2} = \frac{\text{moles of PO formed}}{\text{total moles } H_2 \text{ consumed}} \quad (4.3)$$

and the rate of hydrogen oxidation is calculated as:

$$r_{H_2O} = \frac{\text{moles } H_2 \text{ consumed} - \text{moles of PO formed}}{g_{cat} \cdot s} \quad (4.4)$$

assuming one mole of hydrogen is consumed in water formation per mole of propylene oxide formed, according to the overall reaction for PO formation (Eq. 4.5).



4.3 Results and discussion

4.3.1 Characterization of titanosilicate-1 and silicate-1

Structural characterization data (XRD, N₂ micropore, UV-Vis spectroscopy) for the TS-1 and S-1 samples used in this report can be found in figures 4.11-4.14. XRD patterns were consistent with those reported for titanium MFI zeotypes previously [17], [20]. The lack of splitting of the peak at $2\theta = 24.6^\circ$ indicates the presence of the orthorhombic unit cell [27] (see Fig. 4.11b). Nitrogen adsorption isotherms for TS-1 and S-1 samples were typical of the MFI structure, and micropore volumes were consistent with values typically reported for

TS-1 (micropore volumes: 0.16-0.18 cm³ g⁻¹) [17], [20], [28].

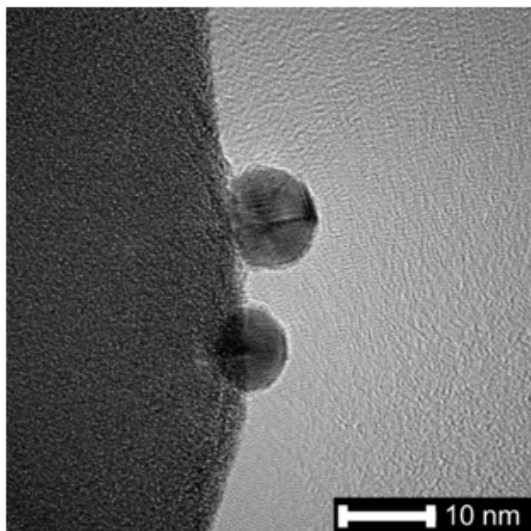


Figure 4.1. TEM micrograph of gold nanoparticles on 0.082Au-PVP/S-1, after kinetic experiments. The scale bar represents 10 nm.

UV-Vis spectroscopic data indicated the presence of primarily isolated Ti⁴⁺ sites in TS-1. UV-Vis peak centers were between 220 nm and 230 nm (Fig. 4.13), which is consistent with values reported previously for dehydrated, isolated Ti⁴⁺ in TS-1 [17], [20] as well as Ti-Beta-F zeolites [29]. The edge energies calculated from UV-Vis spectra for dehydrated TS-1 samples are all greater than 4.9 eV (Tauc plots shown in Fig. 4.14, edge energies reported in Table 4.5), which is characteristic of samples with primarily isolated, tetrahedrally coordinated Ti⁴⁺ sites. However, the existence of a minor fraction of the Ti in small, octahedrally coordinated TiO₂ domains cannot be ruled out, as the edge energies of such domains increases with decreasing size due to quantum confinement effects [30]. The presence of TiO₂ domains larger than three nanometers can be ruled out by the lack of distinct peaks in X-ray diffractograms at 25.7°, 27.9°, and 31° for TS-1(73) and TS-1(126) [31], [32] (Fig. 4.11). The gold nanoparticles on Au-PVP catalysts used in this work had similar geometries and particle size distributions to one another. For all samples used in this study, the gold nanoparticles have a size distribution centered around particles of 6 – 8 nm in diameter (Figs. 4.2, 4.20-4.23), with number averages and standard deviations shown in Table 4.1.

Table 4.1. Gold nanoparticle number average diameters and standard deviations calculated from TEM-derived particle size distributions for all samples used in this study. Particle size distributions were measured after air treatment, H₂/O₂/N₂ treatment, and the conclusion of all kinetic experiments for all samples.

Catalyst	Average diameter [nm]
0.083Au-PVP/TS-1(126)	7.6 ± 3.3
0.083Au-PVP/TS-1(126), repeat	6.5 ± 2.9
0.082Au-PVP/S-1	6.6 ± 2.5
0.11Au-PVP/TS-1(73)	7.4 ± 2.9

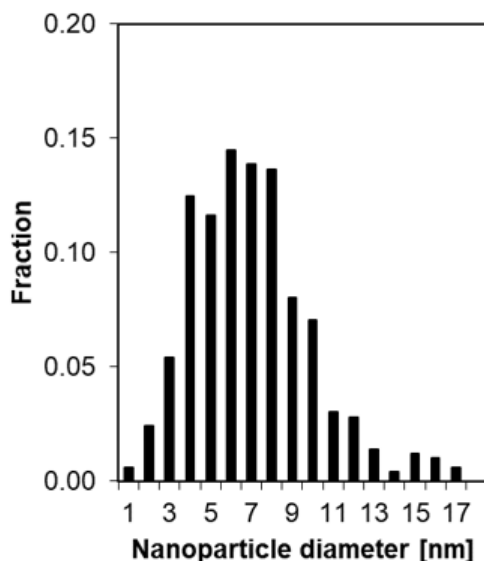


Figure 4.2. Gold nanoparticle size distribution, measured from TEM micrographs taken on 0.083Au-PVP/TS-1(126) after kinetic experiments. The number average gold nanoparticle diameter is 6.5 ± 2.9 nm and the distribution is based on a count of 498 gold nanoparticles.

4.3.2 In-situ removal of PVP ligands

PVP ligands were removed with a combination of *in situ* treatments, and their absence was confirmed with a combination of TGA and TEM data. Figures 4.3aa and 4.3b show TGA mass loss and heat flow data, respectively, for as-made (solid line), post-air treatment (long dashes), and air and H₂/O₂/N₂-treated (short dashes) samples. The air treatment consisted of flowing dry air at a space velocity of $10,000 \text{ cm}^3 \text{ g} + \text{cat}^{-1} \text{ h}^{-1}$ and temperature

of 573 K. These conditions were chosen because a ‘light off’ temperature of approximately 573 K for Au-PVP samples was observed in an initial TGA experiment with as-made 0.083Au-PVP/TS-1(126) (Figure 4.16). The conditions for the H₂/O₂/N₂ treatment were a mixture of 3/3/94 mol% H₂/O₂/N₂ at the same space velocity and a temperature of 473 K. These conditions were chosen based on previous experiments showing CO₂ evolution on Au-DP/TS-1 samples at 473 K flowing only H₂/O₂/N₂ after flowing C₃H₆/H₂/O₂/N₂ at 473 K (Fig. 4.15) and because they are close to the conditions used for measurement of

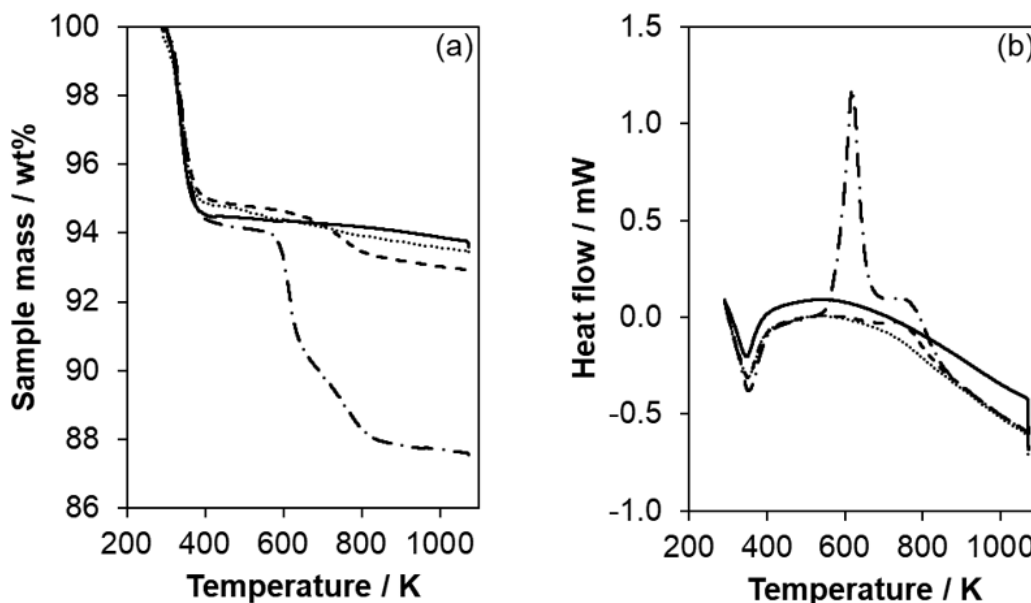


Figure 4.3. Sample mass (a) and heat flow (b) over the course of a TGA experiment. Calcined TS-1(126) (solid line), as-made 0.083Au-PVP/TS-1(126) (dash dot), post-air treatment (long dashes), and air and H₂/O₂/N₂-treated 0.083Au-PVP/TS-1(126) (dots) catalysts were held at ambient temperature with 1.67 cm³ s⁻¹ of dry air flowing for 900 s before ramping to 1073 K (10 K min⁻¹) and holding for 1800 s. The strong negative trend in the heat flow at high temperature is an artifact of the instrument.

propylene epoxidation rates. The data from TGA measurements on all samples (Fig. 4.3a) shows a rapid loss of mass in the temperature range 320-420 K corresponding to approximately 5% of the total sample masses. The heat flow data for all samples (Fig. 4.3b) show an endothermic feature in the same temperature range, thus these features are attributed to water desorption. In the sample mass data for the as-made Au-PVP/TS-1 two

additional mass losses are observed in the range 500 – 800 K sample (Fig. 4.3a, dashed-dotted line). These mass losses correspond to a pair of exothermic features in the heat flow data (Fig. 4.3b, dashed-dotted line) over the same temperature range, the first centered at approximately 625 K and the second centered at approximately 770 K. The feature centered at 625K can be attributed to thermal degradation of any inorganic salts and of PVP to a carbonaceous overlayer and lower molecular weight volatile species , while the feature centered at 770 K can be attributed to oxidation of the remaining carbonaceous species [33]. The air-treated Au-PVP/TS-1 sample (Figure 4.3, long dashes) lacks the initial mass loss and exothermic feature in the 500 – 800 K temperature range, however the second mass loss and exothermic feature centered at approximately 780 K are both observed. In the data for the post-H₂/O₂/N₂ treated Au-PVP/TS-1 sample (Figure 4.3, dots), neither of the features in the 500 – 800 K range associated with PVP decomposition and combustion is observed.

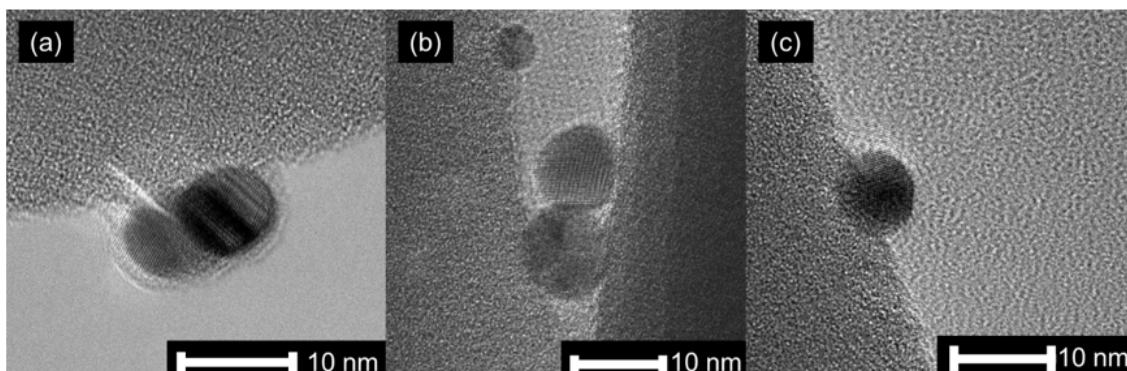


Figure 4.4. HRTEM micrographs of typical gold nanoparticles on (a) 0.08 Au-PVP/TS-1(126) after treatment in air and H₂/O₂/N₂, (b) 0.11Au-PVP/TS-1(73) after treatment in air and H₂/O₂/N₂ as well as an activation period in C₃H₆/H₂/O₂/N₂ (Fig. 5, below) , and (c) 0.08Au-PVP/TS-1(126) after all three treatments (air, H₂/O₂/N₂, and an activation period in C₃H₆/H₂/O₂/N₂) and the conclusion of all kinetic experiments. The scale bars represent 10 nm.

TEM images of the air-treated and post-H₂/O₂/N₂ treated Au-PVP/TS-1 samples were also used to track the progress of PVP removal from the catalyst surface. They reveal the presence of a 1-2 nm thick layer primarily covering the gold nanoparticles. This overlayer is

likely carbon from thermal PVP decomposition, due to the lack of regular atomic spacing and lesser intensity in the HRTEM images, both of which are consistent with an amorphous carbon-rich overlayer. An additional pretreatment under a standard set of reaction conditions (10/10/10/70 mol% C₃H₆/H₂/O₂/N₂, 14,000 cm³ h⁻¹ g_{cat}⁻¹ SV, and 473 K), removed this overlayer (Fig. 4.4). The rate of propylene epoxidation during this final treatment slowly increased until it plateaued at a maximum value (7 g_{PO} h⁻¹ kg_{cat}⁻¹) after approximately 15 ks (Fig. 4.5), which is consistent with the catalyst undergoing some structural or chemical change, such as loss of any remaining surface-bound species and/or rearrangement due to sintering. Further TEM images (Fig. 4.4c) do not show an overlayer, although we cannot rule out the presence of minute amounts of adatoms bound to gold surfaces. Although none was observed, any remaining carbon can also not be distinguished from carbon deposited during the propylene epoxidation reaction.

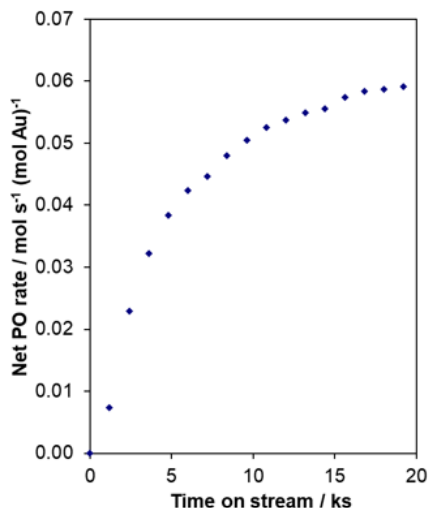


Figure 4.5. The rate of propylene epoxidation for 0.11Au-PVP/TS-1(73) during the first six hours of reaction time after treatment in air at 573 K and 3/3/94 mol% H₂/O₂/N₂ at 473 K. Reaction conditions: 10/10/10/70 mol% C₃H₆/H₂/O₂/N₂, T = 473 K, SV = 14,000 cm³ h⁻¹ g_{cat}⁻¹, P = 101.3 kPa.

4.3.3 Measurement of reaction kinetics on Au-PVP/TS-1 and Au-PVP/S-1

Propylene epoxidation

Measurement of reaction orders and activation energies was performed after *in situ* removal of PVP ligands, as described in Section 4.3.2. Internal and external mass transfer limitations were estimated to be negligible by calculation of the Mears criterion ($\ll 0.15$, Section 4.5.5) and the Thiele modulus (between 10^{-2} and 10^{-3} , Section 4.5.5), and internal mass transfer limitations for Au-PVP/TS-1 catalysts would be expected to be negligible given the location of gold nanoparticles on external crystallite surfaces. The measured reaction orders and activation energy for propylene epoxidation over Au-PVP/TS-1 catalysts were similar to previously reported values over Au-Ti catalysts (Table 4.2). Reaction orders for oxygen, hydrogen, and propylene, once corrected for the measured PO inhibition (reaction order for PO was -0.6) by multiplication by a factor of 1.6 (see [20]), were 0.5, 1.3, and 0.2, while the activation energy for propylene epoxidation was 51 kJ mol^{-1} .

Table 4.2. Apparent and PO-inhibition-corrected reaction orders and activation energies for propylene oxide formation and H_2 oxidation determined by averaging the measured kinetic parameters for eight separate Au/TS-1 samples (0.092Au/TS-1(75), 0.019Au/TS-1(143), 0.040Au/TS-1(81), 0.030Au/TS-1(81), 0.044Au/TS-1(81), 0.033Au/TS-1(143), 0.069Au/TS-1(143), and 0.064Au/TS-1(143)).

Catalyst	Reaction orders						E_{app} kJ mol $^{-1}$
	H_2	O_2	C_3H_6	PO	CO_2	H_2O	
Au-DP/TS-1 ^{a,b}	1 ± 0.2	0.4 ± 0.1	0.4 ± 0.1	-0.6 ± 0.2	0	0	52 ± 6
Au-PVP/TS-1 ^{a,c}	1.3 ± 0.2	0.5 ± 0.1	0.2 ± 0.1	-0.6 ± 0.1	0	0	51 ± 4
Au-PVP/S-1 ^d	0.6 ± 0.1	0.4 ± 0.1	0.5 ± 0.1	- ^e	0	0.7 ± 0.1	3 ± 3

^a Reactant orders and E_{app} corrected by a factor of $(1-d)$, where d is the PO order, to account for inhibition due to PO.

^b Kinetic parameters from Harris et al. [20]. Values are averages over eight separate catalysts.

^c Average values from two separate sets of kinetic experiments using 0.083Au-PVP/TS-1(126).

^d Not corrected for inhibition.

^e PO order for PO production not able to be measured due to excessive PO consumption.

While the reaction orders and activation energy for propylene epoxidation on Au-PVP/TS-1 catalysts are similar to values reported for conventional Au/TS-1 catalysts prepared by deposition-precipitation and are consistent with a ‘simultaneous’ mechanism [19], [20] requiring proximity of the Au and Ti active sites, the average value of the hydrogen reaction order is greater than one (1.3) and cannot be rationalized in the ‘simultaneous’ mechanism without including a third H₂(g)-derived hydrogen atom in the rate-determining step. Alternatively, mechanisms which include a second rate-determining step with three participating H₂(g)-derived hydrogen atoms are consistent with hydrogen reaction orders of up to 1.5; such a mechanism was proposed by Lu et al. that invoked H₂O₂ spillover from Au sites to Ti-OH [34]. Mechanisms such as the one proposed by Lu et al. are consistent with this requirement for explaining hydrogen reaction orders greater than unity for propylene epoxidation due to the inclusion of a second rate-determining step with three H₂(g)-derived hydrogen atoms (Eq. H-4, [34]).

Table 4.3. Comparisons of catalytic site-time yield (STY) of propylene epoxidation, unselective hydrogen oxidation (Eq. 4.4), and total C1-C3 byproduct generation on 0.11Au-PVP/TS-1(73), 0.083Au-PVP/TS-1(126) (averaged over two sets of experiments), and 0.082Au-PVP/S-1. Reaction conditions: 10/10/10/70 mol% C₃H₆/H₂/O₂/N₂, SV = 14,000 cm³ h⁻¹ g_{cat}⁻¹, T = 473 K, P = 101.3 kPa.

Catalyst	Site-Time Yields		
	C ₃ H ₆ epoxidation g _{PO} h ⁻¹ kg _{cat} ⁻¹	H ₂ oxidation μmol _{H₂} s ⁻¹ g _{cat} ⁻¹	Total C ₁ -C ₃ byproducts (mol C ₃) h ⁻¹ kg _{cat} ⁻¹
0.11Au-PVP/TS-1(73)	7	0.22	0.53
0.083Au-PVP/TS-1(126)	11	0.83	0.11
0.082Au-PVP/S-1	0.4	1.2	0.095

The rate of propylene epoxidation on Au-PVP/S-1 is 5-10% of the rate on Au-PVP/TS-1 catalysts, or roughly 1% of the rate on Au-DP/TS-1. The kinetics of propylene epoxidation on Au-PVP/S-1 are markedly different from those measured on Au-PVP/TS-1 and Au-DP/TS-1 (Table 4.2), which suggests the existence of secondary site(s) on gold surfaces and/or the gold-support interface capable of catalyzing propylene epoxidation by a reaction mechanism that differs from that over catalysts that contain both Au and Ti. The PO

reaction order for propylene epoxidation over Au-PVP/S-1 was not able to be measured due to apparent negative rates of propylene epoxidation upon co-feeding PO (Figure 4.17), presumably due to reactions of PO to form other products, although this reaction pathway was not investigated here.

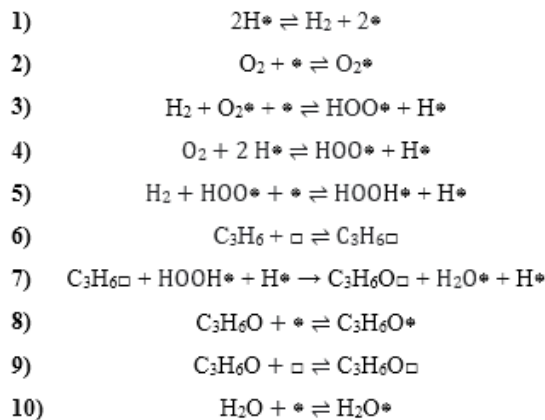


Figure 4.6. Proposed series of elementary steps for propylene epoxidation on Au/TS-1 catalysts known as the ‘simultaneous’ mechanism. Stars are Au sites and empty squares are Ti sites and they are assumed to be in proximity, such that a gold-adsorbed HOOH and titanium-adsorbed propylene can react to form propylene oxide.

Hydrogen oxidation kinetics

The kinetics of hydrogen oxidation were measured simultaneously with the kinetics of propylene epoxidation. The rate of direct hydrogen oxidation (i.e., H_2 consumption beyond the one mol H_2 consumed per mol PO produced) was measured indirectly according to equation 4.4, due to our inability to directly measure effluent water concentrations via GC. Our inability to measure gas-phase water concentrations is because the thermal conductivity of air saturated with water (298 K, 101.3 kPa) is nearly identical to the thermal conductivity of the GC carrier gas, N_2 , used here [35]. Equation 4.4 assumes that all hydrogen consumed in excess of the PO produced forms water, which is consistent with our observation of the absence of any other species to which hydrogen could go to (e.g., alcohols, saturated

hydrocarbons) in the reactor effluent.

$$r_{H_2O} = \frac{kK_{OOH}K_{O_2}P_{O_2}\sqrt{K_{H_2}P_{H_2}}P_{H_2}}{(1 + \sqrt{K_{H_2}P_{H_2}} + K_{O_2}P_{O_2} + K_{OOH}K_{O_2}P_{O_2}\sqrt{K_{H_2}P_{H_2}})(1 + \sqrt{K_{H_2}P_{H_2}})} \quad (4.6)$$

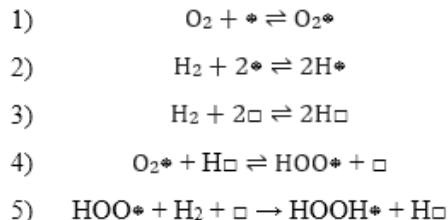


Figure 4.7. Dual-site reaction mechanism for hydrogen oxidation on gold nanoparticles, proposed by Barton and Podkolzin [16]. Stars represent Au sites accessible to all species, and squares represent Au sites accessible only to hydrogen.

The kinetics of hydrogen oxidation on Au-PVP catalysts differ from those previously reported for Au/TS-1 prepared by DP, for both feeds containing propylene and feeds containing only hydrogen, nitrogen, and oxygen (Table 4.4). While direct hydrogen oxidation reaction orders measured on Au-PVP/TS-1 (H_2 : 0.8, O_2 : 0, C_3H_6 : -0.3, PO: -0.1, CO_2 : 0, H_2O : -0.2) and Au-PVP/S-1 (H_2 : 0.9, O_2 : 0, C_3H_6 : -0.2, PO: -0.1, CO_2 : 0, H_2O : -0.3) are similar, the rate of hydrogen oxidation on both Au-PVP/TS-1 and Au-PVP/S-1 catalysts is relatively insensitive to temperature when compared to Au-DP/TS-1 catalysts, which is reflected in the difference in activation energies (4 kJ mol⁻¹ versus 30-40 kJ mol⁻¹). This is consistent with a difference in either the reaction barrier, rate-determining step, and/or active site between the smaller gold nanoparticles and clusters on Au-DP/TS-1 catalysts and the larger gold nanoparticles on Au-PVP/TS-1 and Au-PVP/S-1 catalysts discussed here. Additionally, the oxygen reaction order for hydrogen oxidation differs between Au-PVP/TS-1 and Au-DP/TS-1 catalysts (0 and 0.4, respectively), suggesting differences in either coverages of O_2 -derived surface species or rate-determining steps.

Table 4.4. Apparent and PO-inhibition-corrected reaction orders and activation energies for propylene oxide formation and H₂ oxidation determined by averaging the measured kinetic parameters for eight separate Au/TS-1 samples (0.092Au/TS-1(75), 0.019Au/TS-1(143), 0.040Au/TS-1(81), 0.030Au/TS-1(81), 0.044Au/TS-1(81), 0.033Au/TS-1(143), 0.069Au/TS-1(143), and 0.064Au/TS-1(143)).

Catalyst	Reaction orders						E_{app} kJ mol ⁻¹
	H ₂	O ₂	C ₃ H ₆	PO	CO ₂	H ₂ O	
Au-DP/TS-1 ^a	0.9 ± 0.1	0.3 ± 0.1	-0.3 ± 0.07	0 ± 0.2	0	-0.1 ± 0.07	31 ± 10
0.083Au-PVP/TS-1(126) ^b	0.8 ± 0.2	0 ± 0.2	-0.3 ± 0.2	-0.1 ± 0.1	0	-0.2 ± 0.1	4 ± 1
0.082Au-PVP/S-1 ^b	0.9 ± 0.1	0.1 ± 0.1	-0.2 ± 0.1	-0.1 ± 0.1	0	-0.3 ± 0.1	4 ± 1
Au-DP/TS-1 ^{c,d}	0.7 – 0.8	0.1 – 0.2	n.m. ^e	n.m.	n.m.	0	37 – 41

^a Kinetic parameters from Harris et al. [20]. Values are averages over eight separate catalysts.

^b Reaction conditions: T = 473 K (443-483 K for E_{app}), 2.5–10 / 2.5–10 / 2.5–10 / 0–0.24 / 0–5 / 0–0.3 / Bal. mol% H₂/O₂/C₃H₆/PO/CO₂/H₂O/N₂, SV = 26,000 cm³ h⁻¹ g_{cat}⁻¹, P = 101.3 kPa.

^c Kinetic parameters from Barton and Podkolzin [16].

^d Reaction conditions: T = 433 K (383-483 K for E_{app}), 0.5–19.7 / 0.5–39.5 / 0–3 / Bal. mol% H₂/O₂/H₂O/He, SV = 15,000 – 150,000 cm³ h⁻¹ g_{cat}⁻¹, P = 101.3 kPa.

^e n.m. = Not measured.

While the activation energy for hydrogen oxidation on Au-PVP catalysts is significantly lower than values reported for Au-DP catalysts, it is in rough agreement with the activation energy calculated for O₂ adsorption on gold wire by Kul’kova and Levchenko [36] and Choi et al. [37], who estimated values of 13 kJ mol⁻¹ and 12 kJ mol⁻¹ for this step, respectively, as well as the activation energy for O₂-assisted hydrogen dissociation on Au(211), estimated by Barton and Podkolzin to be 10 kJ mol⁻¹ [16]. Furthermore, we posit that it is unlikely that there are slower diffusion rates for H₂, O₂, and/or H₂O during H₂ oxidation on Au particles on the external surface of TS-1 than those for H₂ oxidation over Au particles within the micropores of TS-1, as would be required if mass transfer limitations were to explain the observed difference in apparent activation energies. This suggests that either i) the rate-determining step for hydrogen oxidation on gold surfaces changes as the size of the gold nanoparticle increases, or that ii) the barrier for hydrogen oxidation decreases on larger Au nanoparticles. Additionally, while non-zero hydrogen oxidation reaction orders for oxygen have been reported for Au-DP/TS-1 catalysts, no significant O₂-dependence on the rate of hydrogen oxidation was observed for Au-PVP/TS-1 catalysts, which, in the context of a

Langmuir-Hinshelwood type mechanism, suggests that the larger gold nanoparticles present on Au-PVP/TS-1 and Au-PVP/S-1 catalysts have higher coverages of adsorbed oxygen than the gold nanoparticles and small clusters on Au-DP/TS-1 catalysts studied by Harris et al. and by Barton and Podkolzin [16], [20]. This can be demonstrated using Eq. 4.6, derived from the two-site hydrogen oxidation mechanism proposed by Barton and Podkolzin [16].

Active site models and rate normalization for Au-DP/TS-1 and Au-PVP/TS-1

To further evaluate the hypothesis that the gold active sites responsible for propylene epoxidation on Au-DP/TS-1 and Au-PVP/TS-1 catalysts are similar, the rates of propylene epoxidation normalized to estimates of the fraction of gold which is in PO-producing active sites for several active site models were calculated for each catalyst considered here. Given that the geometry of gold nanoparticles on Au-PVP/TS-1 and Au-PVP/S-1 catalysts studied here was not able to be determined, we cannot propose a new physical model. However, we can use the model of a truncated cubo-octahedron [38] with a Au(111) top facet (Fig. 4.17) proposed for gold nanoparticles by Feng et al. [39] under propylene epoxidation reaction conditions, which is similar to the model proposed for gold nanoparticles by Williams et al. [40] for gold nanoparticles under water-gas shift reaction conditions, as a basis for comparison. Using this physical model in conjunction with TEM-derived gold nanoparticle size distributions and bulk gold loadings, we predicted the functional dependence of the PO rate on the prevalence of each atom type and evaluated the model regressions after minimizing the squared residuals for each case using equations 4.8 and ??, where r is the experimentally measured rate of propylene epoxidation, C_{site} is a fit parameter which is the rate per site for the site type being considered, $s(d)$ is the number of surface atoms of the given type (e.g., corner atoms) in a given particle, and $t(d)$ is the total number of atoms in a given particle.

$$r = C_{site}[\sum s(d)/\sum t(d)] \quad (4.7)$$

$$\min(r - C_{site}[\sum s(d)/\sum t(d)])^2 \quad (4.8)$$

Models for corner, edge, terrace, surface, and perimeter atoms on a truncated cuboctahedron with a Au(111) top facet were created (equations shown in Section 4.5.9). The corner, edge, and terrace atoms are mutually exclusive, however, the perimeter model includes a combination of corner, edge, and terrace atoms, and the surface model includes all accessible surface Au. These models assume that a single type of site (e.g., only 5- and 6-coordinate corner atoms closest to the support surface) makes up the vast majority of gold active sites. Further details of these models are shown in Sections 4.5.9 and ???. Additionally, a model of a non-faceted spherical nanoparticle [41] was considered, as the TEM data in section 4.3.2 shows no clear evidence of faceted nanoparticles. For the model regressions to propylene epoxidation rate data (Section ???), in general the residual plots exhibited trends which resulted in clustering around $y = x$ in the lag plots. This indicates the presence of systematic errors, meaning that the spherical nanoparticle model may not be a suitable fit for the data.

Since all the models mentioned so far only consider Au sites and do not consider Au-Ti interactions, we attempt to develop a new active site model here. Assuming a Langmuir-Hinshelwood-Hougen-Watson type mechanism, the reaction orders reported here, as well as all others reported previously [19], [20], [34], [42] are consistent with a reaction mechanism which requires the Au and Ti sites to be close enough to allow for interaction of Au- and Ti-bound reaction intermediates during the rate determining step. An alternative mechanistic proposal requires the desorption and migration of hydrogen peroxide [34]. All reported reaction orders for the gas phase epoxidation of propylene with oxygen and hydrogen over Au/TS-1 catalysts typically have a hydrogen order near unity and an oxygen order of approximately 0.5 [19], [20], [34], [42], if one assumes a PO reaction order of -0.6, as this is the approximate value reported by all those who have measured the reaction order with respect to PO and corrected measured H_2 and O_2 reaction orders accordingly. Therefore, given the hypothesis that Au-Ti proximity is necessary for PO-producing Au-Ti active sites, such proximity was used as a constraint for this active site model which we refer to as the ‘proximal Ti’ model in an attempt to test this hypothesis. This model predicts the number of Ti-containing sites on the external surfaces of TS-1 within a specified distance of the base of a gold nanoparticle which is itself on an external crystallite surface. We refer to the range

in which Ti are considered proximal to a gold nanoparticle as the interaction range, and the bounds on this range are as follows: the distance from the center of the gold nanoparticle to the Ti site must be greater than the nanoparticle's radius, such that it is not covered by the nanoparticle, but less than the combined lengths of propylene and hydrogen peroxide (Figure 4.25), which gives a maximum allowable distance of 0.44 nm before a gold nanoparticle and Ti site are no longer considered close enough to interact. This interaction range could be modified to increase physical accuracy in the future, but this was used as an initial guess to allow prediction of trends by the model. As a result of using the combined lengths of hydrogen peroxide and propylene for the maximum interaction range, turnover frequencies estimated using this assumption for the Au-Ti interaction range represent a minimum of the estimated catalytic turnover frequency required for the simultaneous mechanism alone to explain the observed rate of propylene epoxidation. Increasing this range decreases the predicted TOF, and decreasing this range increases the predicted TOF (Fig. 4.29). Using this model we can predict the approximate number of 'proximal Ti' per Au nanoparticle for a given Ti surface density (here, the surface Si/Ti ratio was assumed to be equal to the bulk Si/Ti ratio) and Au nanoparticle size. Further details of this model are shown in the SI (Section 4.20) and a comparison of the regressions for all models considered here is shown in Figure ??.

For each model considered, the regression to the dataset consisting of rate vs. average diameter data for both Au-PVP/TS-1 and Au-DP/TS-1 catalysts was determined (Fig. ??) by minimizing equation 4.8. For the catalyst samples in this study, the fraction of terrace and surface atoms scaled linearly with the average diameter and were therefore not considered. The corner, edge, perimeter, and 'proximal Ti' site densities were best approximated by power law relationships of $d^{-3.43}$, $d^{-2.31}$, $d^{-2.51}$, and $d^{-2.45}$, respectively. The rate of propylene epoxidation varies with the average diameter as $d^{-3.35}$. While the terrace and surface atom models can be disregarded due to their poor fits of the data, the corner, edge, perimeter, and proximal Ti models are difficult to distinguish and appear to all capture the trends in the data similarly (residual plots and lag plots in Section ??). Since the 'proximal Ti' model is a modified perimeter model which accounts for Ti effects, and the edge model is essentially a

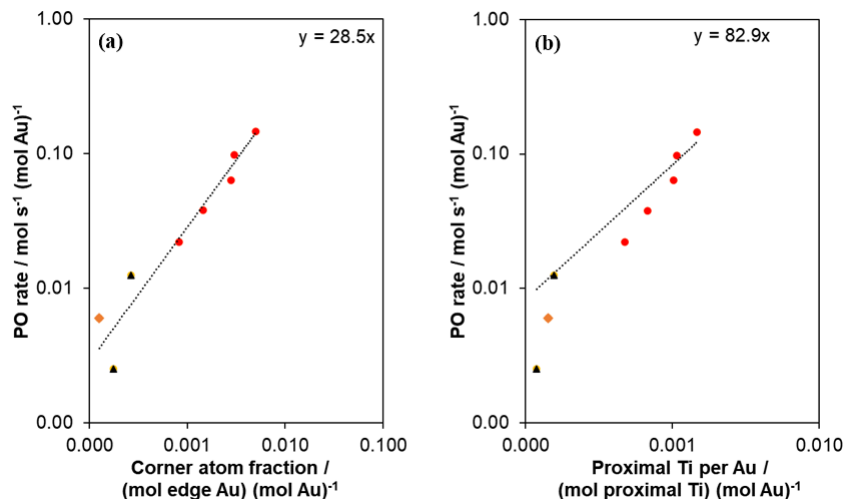


Figure 4.8. PO rate normalized to total gold mass vs. corner Au fraction (a) and proximal Ti per Au (b) for Au-PVP/TS-1 (Si/Ti = 126) (black triangles), Au-PVP/TS-1 (Si/Ti = 73) (Orange diamonds), and Au-DP/TS-1 ([17], red circles) catalysts. For the proximal Ti model, a Au-Ti interaction distance of 0.44 nm was used. The slope of the plotted line corresponds to the best-fit turnover frequency for the entire data set, which is shown in the upper right-hand corner of each plot. Reaction conditions: 10/10/10/70 mol% C₃H₆/H₂/O₂/N₂, SV = 14,000 cm³ h⁻¹ g_{cat}⁻¹, T = 473 K, P = 101.3 kPa.

perimeter model in which only a subset of perimeter Au atoms are considered (see Sections 4.5.7, 4.5.9), we chose to consider only the corner and proximal Ti models.

These active site models were used in conjunction with estimates of Ti densities on external crystallite surfaces and TEM measurements of the gold nanoparticle size distribution to calculate the catalytic turnover frequency required to explain the measured rate for each sample. Although there is the potential for Au clusters too small for detection by TEM on the ~200 nm TS-1 crystallites, the estimated turnover frequencies on Au-PVP/TS-1 catalysts, which have exclusively extracrystalline gold nanoparticles, span the range of predicted turnover frequencies for the Au-DP/TS-1 samples (Fig. ??). Therefore, it is unlikely that a subset of Au clusters which is undetectable by TEM for Au-DP/TS-1 samples significantly influences the predicted values of TOF for each model considered here, and any contributions from such sites would reduce the calculated TOF values. The range of these predicted TOFs as a function of the fraction of corner Au sites or proximal sites are shown in Figure

??, and the relationship between the estimated active site density and the rate of propylene epoxidation normalized to gold content is shown in Figure 4.8. For the reaction conditions used to measure catalytic rates of propylene epoxidation on Au/TS-1 catalysts (10/10/10/70 mol% C₃H₆/H₂/O₂/N₂, 473 K, SV = 14,000 cm³ g_{cat}⁻¹ h⁻¹), the upper limit on the turnover frequency set by collision theory (assuming every collision of gas-phase propylene with an active site results in product formation) is approximately 1.3x10⁴ mol s⁻¹ mol_{Ti}⁻¹ for the ‘proximal Ti’ model with a surface Ti density near 1/unit cell and 1.5x10⁴ mol s⁻¹ mol_{Au}⁻¹ for the corner model. These limits were calculated using equation 4.9 (adapted from [43]) with the assumption that propylene behaves as an ideal gas.

$$v_{coll} = \rho_n \sqrt{\frac{RT}{2\pi M}} \quad (4.9)$$

Both models predict turnover frequencies (30 and 80 for the corner and proximal Ti models, respectively) which are several orders of magnitude below the upper limit set by collision theory, however these estimated turnover frequencies are significantly higher than those reported previously for oxidation reactions on metal catalysts under similar reaction conditions, including estimates for propylene epoxidation on Au and Ag clusters (0.4 s⁻¹ and 2.5 s⁻¹, respectively, 473 K) [44,45], CO oxidation on Pt (0.002-0.05 s⁻¹, 473 K) [46], and WGS on Pt and Au (both 0.2 s⁻¹, 473 K) [47,48]. For the corner model, which was originally employed by Feng et al. [39] assuming a sequential mechanism involving hydrogen peroxide migration, this suggests that corner atoms alone are not capable of explaining the observed rates of propylene epoxidation. For the proximal Ti model, this implies that the simultaneous mechanism alone cannot explain the observed rates of propylene epoxidation, and that invoking short range migration of hydrogen peroxide over at least several nanometers is necessary to explain the observed rates with plausible calculated TOFs. Increasing the interaction range for Ti sites and Au nanoparticles in the proximal Ti model to 10 nanometers decreases the calculated TOF to values consistent with previous reports (Figure S.20). This suggests that while the simultaneous mechanism cannot be conclusively invalidated here, hydrogen peroxide migration is necessary to explain the observed catalytic rates

of propylene epoxidation on Au/TS-1 catalysts.

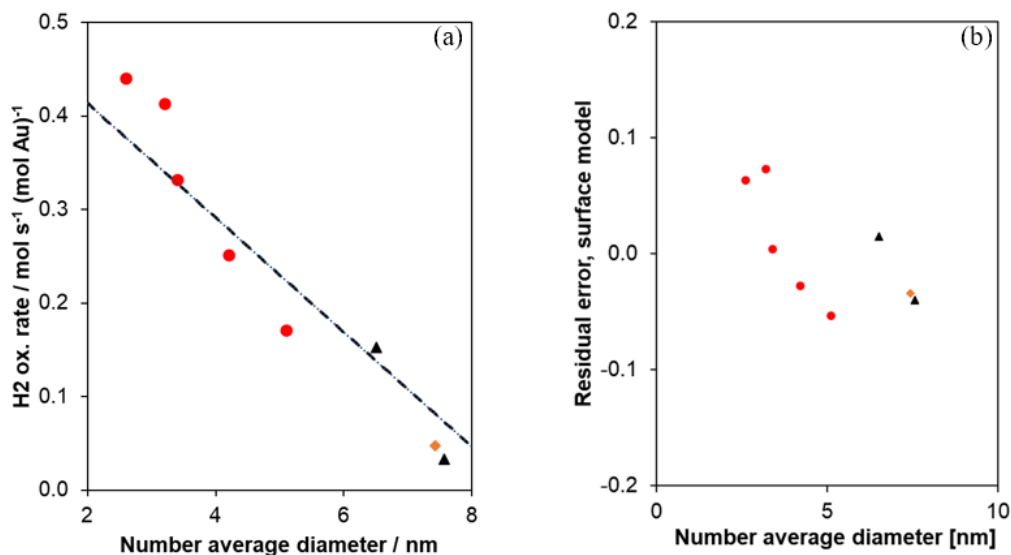


Figure 4.9. (a) Model fit of experimental data for the hydrogen oxidation rate data set consisting of 0.083Au-PVP/TS-1(126) catalysts (black triangles), 0.11Au-PVP/TS-1(73) (orange diamonds) and Au-DP/TS-1(100) catalysts (red circles) reported in [39] for the surface atom model (prediction shown by dashed line). (b) Residual plot for the model regression in (a). Reaction conditions: 10/10/10/70 mol% C₃H₆/H₂/O₂/N₂, SV = 14,000 cm³ h⁻¹ g_{cat}⁻¹, T = 473 K, P = 101.3 kPa.

The active site models discussed for propylene epoxidation were then regressed to the measured catalytic rates of hydrogen oxidation. The active site model which ‘best’ fit the hydrogen oxidation data, as determined by examination of the residual plots (Section ??), was the surface atom model, which assumes all surface Au atoms contribute to hydrogen oxidation (Fig. 4.9). Magnitudes of hydrogen oxidation turnover frequencies normalized per surface Au atoms are on the order of 1 s⁻¹, consistent with previous reports of oxidation reactions on noble or transition metal catalysts [44]–[47]. The agreement of this model across both Au-DP/TS-1 and Au-PVP/TS-1 catalysts suggests that differences observed in the activation energy and oxygen reaction order between these two types of samples (Table 4.4) are not due to a difference in active site type. We speculate that these observations may instead be rationalized by a change in either surface coverage regime or rate-determining

step, though further investigation into the origins of this discrepancy are beyond the scope of the present study. Additionally, the agreement of estimated turnover frequencies across these catalysts suggests that hydrogen oxidation on gold nanoparticles is a structure insensitive reaction that can potentially be used for estimation of accessible Au surface areas under these reaction conditions.

4.4 Conclusions

Au-PVP/TS-1 catalysts were synthesized by a repeated incipient wetness impregnation procedure and cleaned of organic PVP ligand residue by a series of in situ pretreatments. The reaction orders and activation energies for propylene epoxidation measured over Au-PVP/TS-1 catalysts were measured in a CSTR, free from temperature and concentration gradients, and were identical within experimental uncertainty to values previously reported for Au-DP/TS-1 catalysts. This agreement suggests that gold active sites on catalysts with some fraction of gold existing as small, intraporous clusters inside TS-1 (Au-DP/TS-1) and gold active sites on catalysts with exclusively larger, extracrystalline gold nanoparticles (Au-PVP/TS-1) are energetically similar (i.e., similar binding energies, reaction barriers, catalytic turnover frequencies). Additionally, this similarity demonstrates that propylene epoxidation on Au-PVP/TS-1 catalysts likely occurs through the same mechanism as on Au/TS-1 catalysts prepared by deposition-precipitation. Estimates of turnover frequencies for propylene epoxidation derived from model regressions considered herein suggest that models which assume a relatively constant number of active sites per gold nanoparticle (corner, proximal Ti models) are most capable of explaining measured catalytic propylene epoxidation rates on Au/TS-1 catalysts. The magnitude of the TOF predictions for the corner model suggest that corner atoms alone cannot produce hydrogen peroxide at a rate consistent with the observed rates of propylene epoxidation on the catalysts studied here. The estimated TOFs for propylene epoxidation via the simultaneous mechanism over active sites described by the proximal Ti model are much larger than those for previously reported metal-catalyzed oxidation reactions. This suggests that the simultaneous mechanism alone cannot explain the

measured data, and that hydrogen peroxide migration from Au sites to Ti sites is necessary to explain the observed rates of propylene epoxidation on the catalysts considered here.

The kinetics of hydrogen oxidation on Au-PVP/TS-1 and Au-DP/TS-1 catalysts primarily differ in the measured values of activation energy (Au-PVP/TS-1: ~ 4 kJ mol⁻¹, Au-DP/TS-1: ~ 30 kJ mol⁻¹) and oxygen reaction order (Au-PVP/TS-1: 0, Au-DP/TS-1: 0.4). The measured activation energy for hydrogen oxidation on Au-PVP/TS-1 catalysts is similar to estimates of the activation energy for O₂-assisted hydrogen dissociation on gold surfaces. Rates of hydrogen oxidation on both Au-PVP/TS-1 and Au-DP/TS-1 were regressed to the same active site models as discussed for propylene epoxidation. The rate of hydrogen oxidation correlates best with a surface Au atom model, suggesting that all surface gold atoms participate in hydrogen oxidation. Additionally, the agreement of active site model for hydrogen oxidation across both Au-DP/TS-1 and Au-PVP/TS-1 catalysts implies that there is no change in active site between the two catalysts, and that the difference in activation energy and oxygen order must be the result of a change in surface coverage regime or rate-determining step. Magnitudes of hydrogen oxidation turnover frequencies normalized per surface Au atoms are on the order of 1 s⁻¹, consistent with previous reports of oxidation reactions on noble or transition metal catalysts. These findings suggest that Au particle sizes should be minimized, in order to maximize the fraction of Au sites which participate in propylene oxide formation in conjunction with Ti sites, but that all Au sites on these Au particles will also participate in deleterious hydrogen oxidation, placing an upper limit on the possible H₂ selectivities over Au-Ti catalysts for direct propylene epoxidation.

4.5 Supplementary Information

4.5.1 Reactor schematic

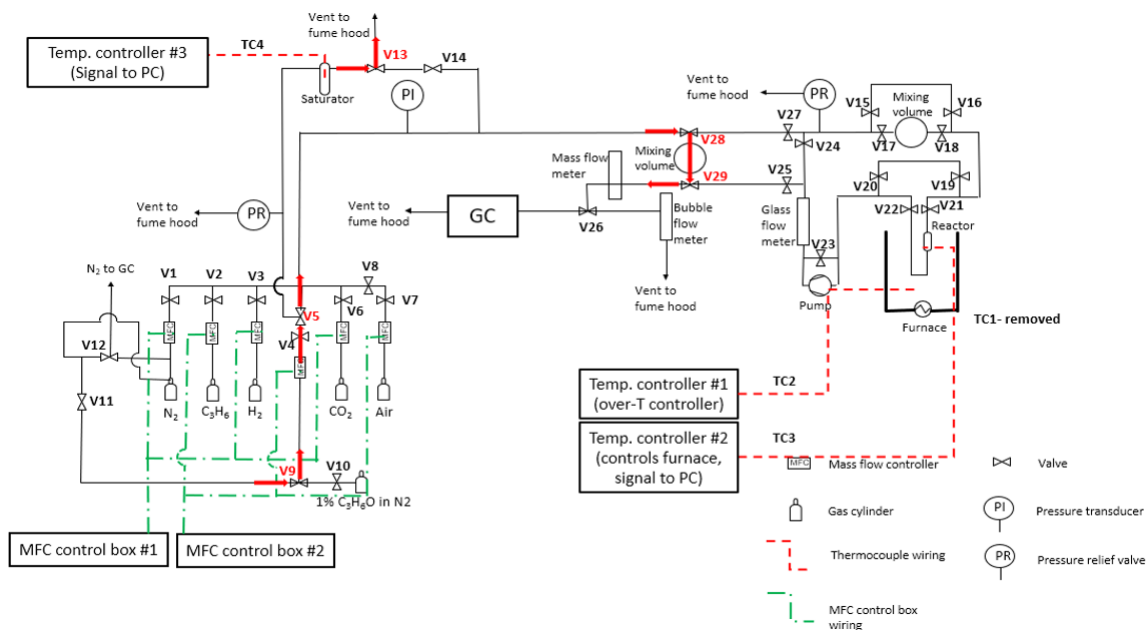


Figure 4.10. P&ID of gas-phase recycle reactor system, operated with a recycle ratio 30 so that the reactor behaves as a CSTR. The recirculation loop is heated to 323 K to prevent condensation of gas-phase products. Red arrows show the default positions of automated valves in the event of a power failure or alarm state. Temperatures from temperature controllers 2 and 3 are read out to a PC with Labview software, which is used to automatically carry out kinetic experiments according to user-written instructions. A mass balance across the system is closed by reading signals from MFC control boxes 1, 2 and the mass flow meter (left of recirculation loop) to detect leaks or malfunctioning mass flow controllers. A separate flammables gas detector is positioned over the glass recirculation loop and will put the system in an emergency shutdown state if triggered.

4.5.2 XRD patterns

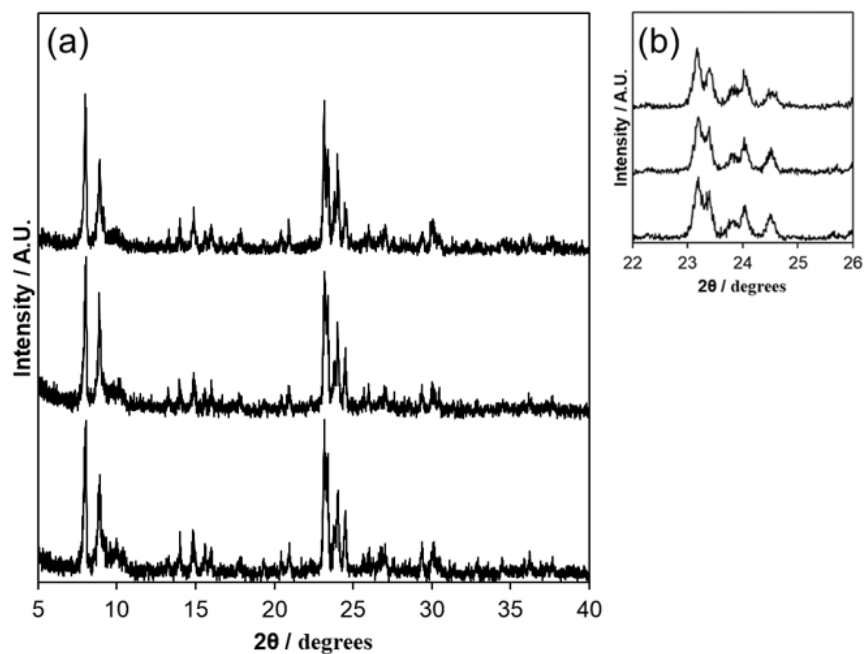


Figure 4.11. (a) XRD patterns for calcined (top) S-1, (middle) TS-1(73), and (bottom) TS-1(126). (b) Inset shows the peak at $2\theta = 24.6^\circ$ for calcined (top) S-1, (middle) TS-1(73), and (bottom) TS-1(126), the lack of splitting in which indicates the presence of an orthorhombic unit cell [27]. Patterns are normalized to their maximum intensity and offset for clarity.

4.5.3 Nitrogen physisorption isotherms

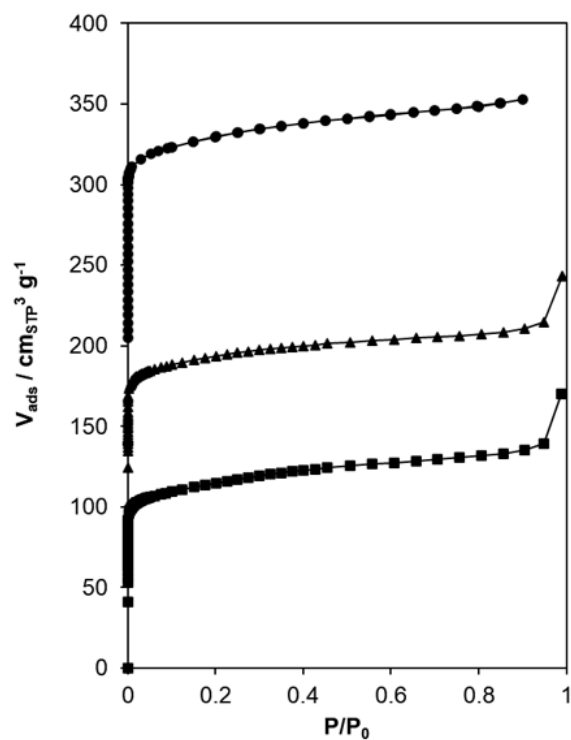


Figure 4.12. Nitrogen physisorption isotherms for (top) TS-1(73), (middle) TS-1(126), and (bottom) S-1, offset by $200 \text{ cm}_{\text{STP}}^3 \text{ g}^{-1}$, $75 \text{ cm}_{\text{STP}}^3 \text{ g}^{-1}$, and $0 \text{ cm}_{\text{STP}}^3 \text{ g}^{-1}$, respectively.

4.5.4 Diffuse reflectance UV-Visible spectroscopy

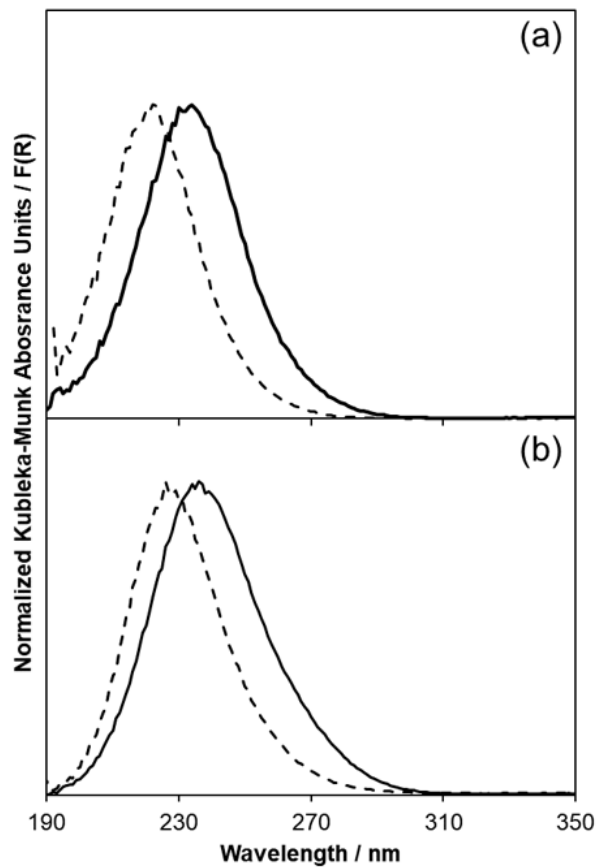


Figure 4.13. DRUV-Vis spectra in Kubelka-Munk units (normalized to the maximum $F(R)$ intensity) for (a) TS-1(126) and (b) TS-1(73), collected under (i) ambient conditions (solid line) and (ii) after dehydration at 523 K in flowing dry helium.

DRUV spectra of dehydrated TS-1 samples (Figure 4.13) were used to produce the Tauc plots shown in Figure 4.14 for both TS-1 samples. The lowest energy x-intercepts of these plots (~ 5 eV) correspond to the Ti edge energies and are reported in table 4.5 [24]–[26].

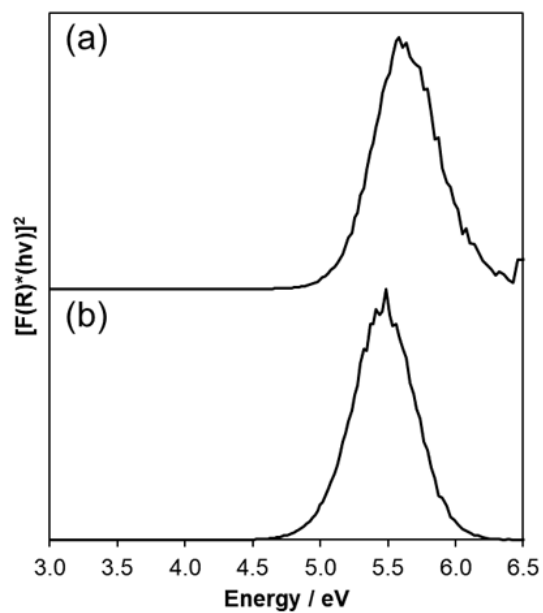


Figure 4.14. Tauc plots for (a) TS-1(126) and (b) TS-1(73) measured after dehydration at 523 K in flowing dry helium.

Table 4.5. UV-Vis peak centers and edge energies for TS-1 samples dehydrated using flowing dry He at 573 K.

Sample	Peak center [nm]	Edge energy [eV]
TS-1(126)	222	5.15
TS-1(73)	226	4.97

4.5.5 Estimation of internal and external mass transfer limitations

Calculation of the Mears criterion were used to confirm the absence of external mass transfer limitations in the Au-PVP/TS-1 and Au-DP/TS-1 catalysts considered here, and the derivations shown below are adapted from [18]. The Mears criterion is met, and external mass transfer limitations are insignificant, when the following relationship is satisfied:

$$\frac{-r_{A(obs)} \cdot \rho_b \cdot R \cdot n}{k_c \cdot C_{Ab}} < 0.15 \quad (4.10)$$

Where $-r_{A(obs)}$ is the experimentally measured net reaction rate ($\text{kmol kg}_{cat}^{-1} \text{s}^{-1}$), ρ_b is the catalyst bed density (kg m^{-3}), R is the catalyst pellet radius, n is the reaction order for reactant A (unitless), k_c is the mass transfer coefficient for reactant A (m s^{-1}), and C_{Ab} is the concentration of reactant A in the bulk gas phase under reaction conditions (kmol m^{-3}). The catalyst bed density, ρ_b , is defined as:

$$\rho_b = (1 - \phi)\rho_c \quad (4.11)$$

Where ρ_c is the catalyst pellet bulk density (kg m^{-3}), obtained by calculating the density of a single S-1 unit cell, and ϕ is the catalyst bed porosity (estimated to be ~ 0.3).

Calculation of the concentration of reactant A in the bulk gas phase, C_{Ab} , under reaction conditions was done by assuming reactant A, propylene, behaves as an ideal gas under the reaction conditions used (473 K, $P_A = 0.1 \text{ atm}$).

Calculation of the Reynolds number allows for selection of the method for estimation of k_c . Calculation of Re for the system is as follows:

$$Re = \frac{2U \cdot R \cdot \rho}{\mu} \quad (4.12)$$

Where U is the superficial gas velocity (m s^{-1}), R is the catalyst pellet radius (m), ρ is the density of the reactant mixture (kg m^{-3} , approximated as an ideal gas at 1 atm and 473 K), and μ is the dynamic viscosity of the reactant mixture ($\text{kg m}^{-1} \text{s}^{-1}$, approximated by air at 473 K). The superficial velocity used the recycle loop flow rate (~ 3.5 standard L min^{-1}), instead of the inlet flow rate ($65 \text{ cm}^3_{STP} \text{ min}^{-1}$), through the ~ 1 in. I.D. quartz reactor.

Given that the value of the Reynolds number is 0.55 and that the mass transfer coefficient, k_c , is estimated by assuming the catalyst pellets can be approximated as spheres, the Sherwood number, Sh , can be calculated and related to k_c as [48]:

$$Sh = 2 + 0.6515(Re \cdot Sc)^{1/2} = \frac{k_c \cdot 2R}{D_e} \quad (4.13)$$

Where D_e is the mass diffusivity of reactant A in the bulk gas phase and Sc is the Schmidt number, defined below:

$$Sc = \frac{\mu}{\rho D_e} \quad (4.14)$$

All parameters used in the calculation of the Mears criterion are listed in Table S.1.

Calculation of the Thiele modulus was used to confirm the absence of internal mass transfer limitations under the given reaction conditions for Au-PVP/TS-1 and Au-DP/TS-1 catalysts considered here. Although the catalysts were sieved to a diameter size distribution centered around $\sim 180 \mu\text{m}$, the individual catalyst crystallites had an average diameter of $\sim 200 \text{ nm}$. Therefore, calculation of the significance of internal mass transfer limitations used this dimension (200 nm) as the relevant characteristic diameter. The Thiele modulus is defined as:

$$\Phi = \frac{-r_{A(obs)} \cdot \rho_c \cdot R^2}{D_e \cdot C_{As}} = \eta \phi^2 \quad (4.15)$$

Table 4.6. Parameters used in the calculation of the Mears criterion.

Parameter and symbol	Value	Units
Highest measured PO rate at 473 K, $-r_{A(obs)}$	6.5×10^{-7}	$\text{kmol kg}_{cat}^{-1} \text{s}^{-1}$
Density of catalyst pellet, ρ_c	1.84×10^3	kg m^{-3}
Density of catalyst bed, ρ_b	1288	kg m^{-3}
Porosity of catalyst bed, ϕ	~ 0.3	—
Concentration of reactant A in the bulk gas phase, C_{Ab}	2.58×10^{-3}	kmol m^{-3}
Radius of catalyst pellet, R	9×10^{-5}	m
Superficial gas velocity, U	0.11	m s^{-1}
Density of reactant mixture, ρ	0.67	kg m^{-3}
Dynamic viscosity of reactant mixture, μ	2.573×10^{-5}	$\text{kg m}^{-1} \text{s}^{-1}$
Reynolds number, Re	0.55	—
Schmidt number, Sc	1.28	—
Mass diffusivity, D_e (estimated for propylene in air at 473 K)	3×10^{-5}	$\text{m}^2 \text{s}^{-1}$
Sherwood number, Sh	2.55	—
Mass transfer coefficient for propylene, k_c	0.43	m s^{-1}
Propylene reaction order	0.4	—
Mears criterion	2.7×10^{-5}	—

Where $-r_{A(obs)}$ is the highest observed reaction rate ($\text{kmol kg}_{cat}^{-1} \text{s}^{-1}$), ρ_c is the catalyst pellet density (kg m^{-3}), R is the catalyst pellet radius (m), D_e is the effective intracrystalline gas phase diffusivity of propylene at 473 K (estimated from the Knudsen equation assuming that the constriction factor, tortuosity, and pellet porosity were 0.8, 6, and 0.3 [18], respectively, and assuming a pore radius of 0.25 nm) ($\text{m}^2 \text{s}^{-1}$), C_{As} is the gas phase concentration of A at the catalyst surface (kmol m^{-3}), η is the internal effectiveness factor, and ϕ is the Thiele modulus. If $\Phi \ll 1$, then $\eta \approx 1$ and ϕ is calculated easily. All parameters used in the calculation of the Thiele modulus are in Table 4.6.

Table 4.7. Parameters used in the calculation of the Thiele modulus.

Parameter and symbol	Value	Units
Highest measured PO rate at 473 K, $-r_{A(obs)}$	6.5×10^{-7}	$\text{kmol kg}_{cat}^{-1} \text{s}^{-1}$
Density of catalyst pellet, ρ_c	1.84×10^3	kg m^{-3}
Radius of catalyst pellet, R	1.0×10^{-7}	m
Effective intracrystalline gas phase diffusivity, De	3.3×10^{-9}	$\text{m}^2 \text{s}^{-1}$
Gas phase concentration of A at the catalyst surface, C_{As}	2.6×10^{-3}	kmol m^{-3}
Estimated Thiele modulus	1.2×10^{-3}	—

4.5.6 CO₂ Generation during H₂/O₂/N₂ co-feed after propylene epoxidation

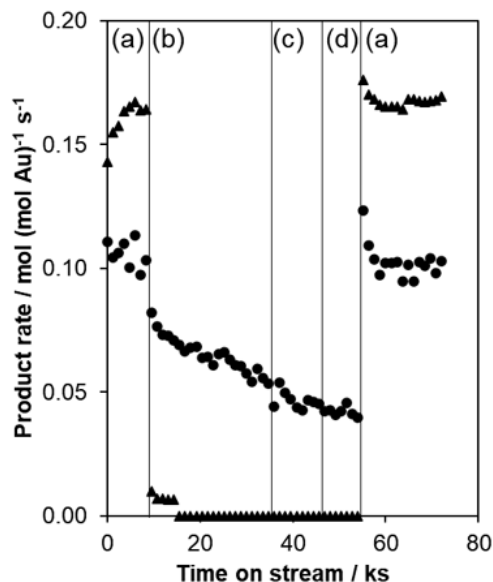


Figure 4.15. Rates of PO generation (triangles) and CO₂ generation (circles) during (a) propylene epoxidation reaction conditions and (b-d) hydrogen oxidation reaction conditions.

- (a) 10/10/10/70 mol% C₃H₆/H₂/O₂/N₂, SV = 26,000 cm³ g_{cat}⁻¹ h⁻¹, 498 K, 101.3 kPa
- (b) 4/4/92 mol% H₂/O₂/N₂, SV = 26,000 cm³ g_{cat}⁻¹ h⁻¹, 498 K, 101.3 kPa
- (c) 3/3/94 mol% H₂/O₂/N₂, SV = 24,000 cm³ g_{cat}⁻¹ h⁻¹, 498 K, 101.3 kPa
- (d) 2/2/96 mol% H₂/O₂/N₂, SV = 22,000 cm³ g_{cat}⁻¹ h⁻¹, 498 K, 101.3 kPa

The concentrations of hydrogen and oxygen were decreased in (b) to (d) to avoid reaching the saturation pressure of water as the conversion of hydrogen increased. The space velocity was decreased in (b) to (d) because the nitrogen mass flow controller was operating at its upper bound at SV = 26,000 cm³ g_{cat}⁻¹ h⁻¹.

4.5.7 Initial TGA experiment, stepped temperature program, Au-PVP/TS-1

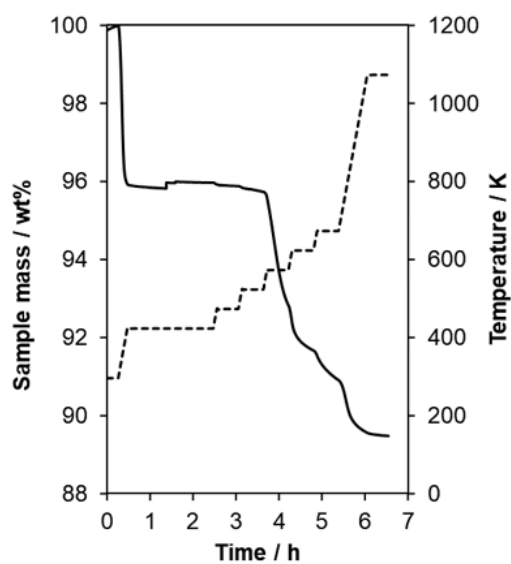


Figure 4.16. Sample mass (solid line) and temperature program (dashed line) in initial TGA experiment for 0.083Au-PVP/TS-1(126). 20-30 mg of catalyst sample was held in flowing air ($1.67 \text{ cm}^3 \text{ s}^{-1}$) first at ambient temperature for 0.5 h, 423 K for 2 h, followed by 473 K, 523 K, 573 K, 623 K, 673 K, 723 K, and 1073 K, each for 0.5 h.

4.5.8 Consumption of PO during PO reaction order experiment on 0.082Au-PVP/S-1

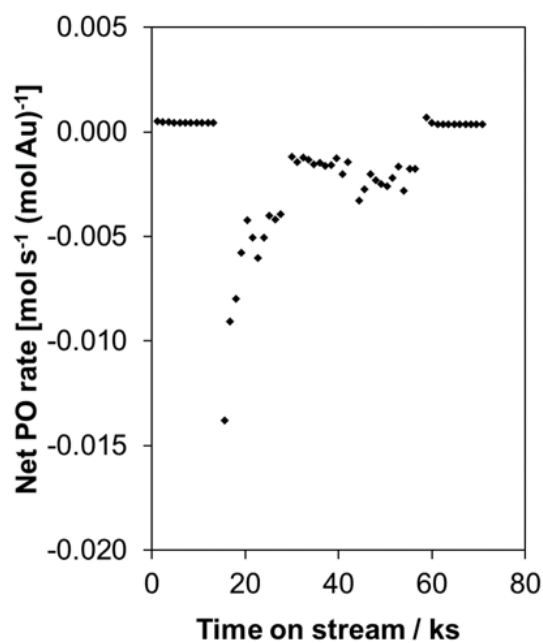


Figure 4.17. Net rate of PO generation during a PO reaction order experiment with co-fed PO (co-feeds: 0% PO, 0.18% PO, 0.07% PO, 0.13% PO, 0% PO) (10/10/10/0-0.18/bal. mol% C₃H₆/H₂/O₂/PO/N₂, SV = 26,000 cm³ h⁻¹ g_{cat}⁻¹, 473 K, 101.3 kPa)

4.5.9 Truncated cubo-octahedron crystal model and related active site models

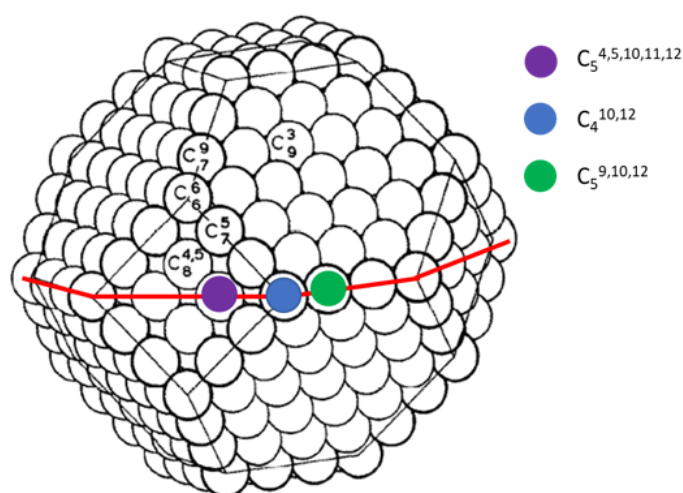


Figure 4.18. Example cubo-octahedron crystal model (edge length, m , = 4) used for Au nanoparticles. The red line indicates the truncation line used to create the truncated cubo-octahedron model with a (100) top facet. Atoms bisected by the line are included in the model. Labeled and color-filled atoms (purple, blue, green) indicate gold atoms with unique coordination to other gold atoms. Subscripts on labels denote Au-Au coordination numbers. Superscripts denote FCC lattice position of missing neighboring atoms (see [38] for further examples). Adapted from [38] with permission from Surface Science.

Table 4.8. Equations relating the edge length (m) of a given truncated cubo-octahedron with (100) top facet (Fig. 4.17) to the numbers of each type of surface atom, all surface atoms, and all atoms in the nanoparticle.

Atom identity	Number of atoms
	(as a function of edge length, m , for $m \geq 2$)
C_6^6	8
C_7^5	$12(m-2)$
C_7^9	$4(m-2)$
$C_8^{4,5}$	$2m^2-10m+12$
C_9^3	$4(3m^2-9m+7)$
$C_{10,12}^4$	8
$C_{5,9,10,12}^9$	$4(m-2)$
$C_5^{4,5,10,11,12}$	$4(m-2)$
Surface	$14m^2-22m+8$
Total	$8m^3-13m^2+7m-1$

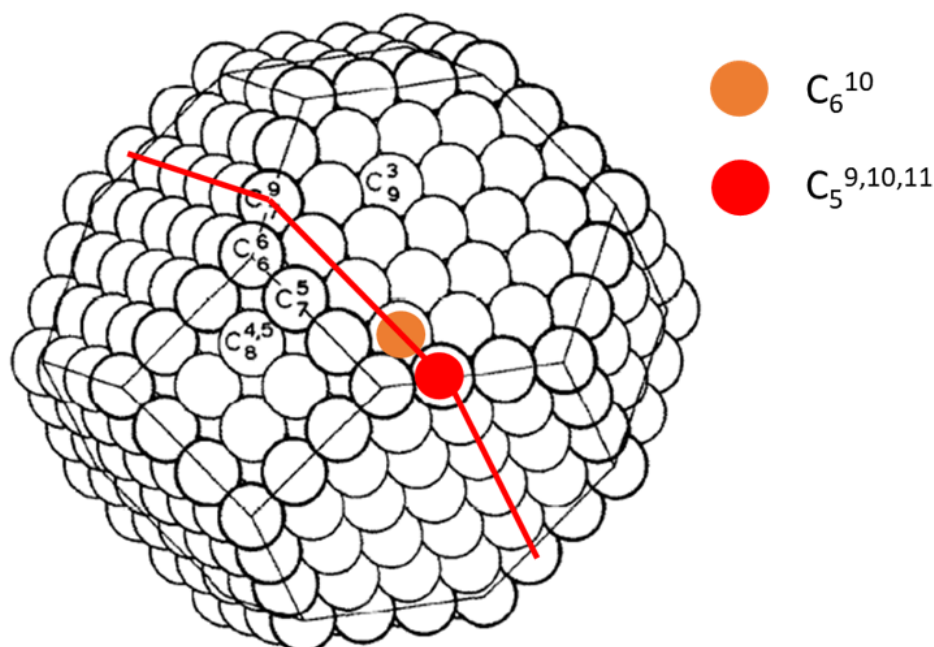


Figure 4.19. Example cubo-octahedron crystal model (edge length, m , = 4) used for Au nanoparticles. The red line indicates the truncation line used to create the truncated cubo-octahedron model with a (111) top facet (leftmost portion of nanoparticle retained for model). Atoms bisected by the line are included in the model. Labeled and color-filled atoms (red, orange) indicate gold atoms with unique coordination to other gold atoms. Subscripts on labels denote Au-Au coordination numbers. Superscripts denote FCC lattice position of missing neighboring atoms (see [38] for further examples). Adapted from [38] with permission from Surface Science.

Table 4.9. Equations relating the edge length (m) of a given truncated cubo-octahedron with (111) top facet (Fig. 4.18) to the numbers of each type of surface atom, all surface atoms, and all atoms in the nanoparticle.

Atom identity		Number of atoms	
		(as a function of edge length, m , for $m \geq 2$)	
	C_6^6		12
	C_7^5		$12(m-2)$
	C_7^9		$3(m-2)$
	$C_8^{4,5}$		$3(m-2)^2$
	C_9^3		$7.5m^2-19.5m+13$
	$C_5^{9,10,11}$		0 if $m = 2$, else: 6
	C_6^{10}		$3(2m-1)$
Surface		$10.5m^2-10.5m+4$ if $m = 2$, else: $10.5m^2-10.5m+10$	
Total		$(11/3)m^3+2m^2-(26/3)m+6$	

4.5.10 Gold nanoparticle size distributions

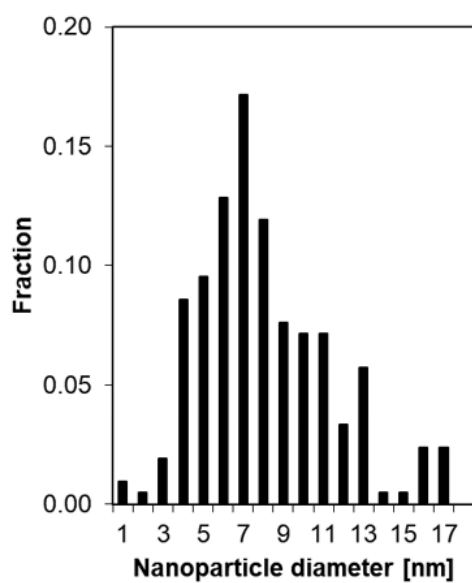


Figure 4.20. TEM-derived gold nanoparticle size distribution for 0.083Au-PVP/TS-1(126). The distribution was determined from 210 gold nanoparticles. The average size is 7.6 ± 3.3 nm, with 3.3 nm representing the standard deviation of the measured diameters.

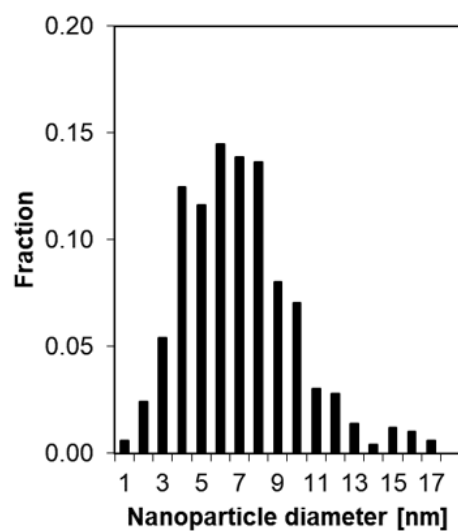


Figure 4.21. TEM-derived gold nanoparticle size distribution for 0.083Au-PVP/TS-1(126) (repeat). The distribution was determined from 498 gold nanoparticles. The average size is 6.5 ± 2.9 nm, with 2.9 nm representing the standard deviation of the measured diameters.

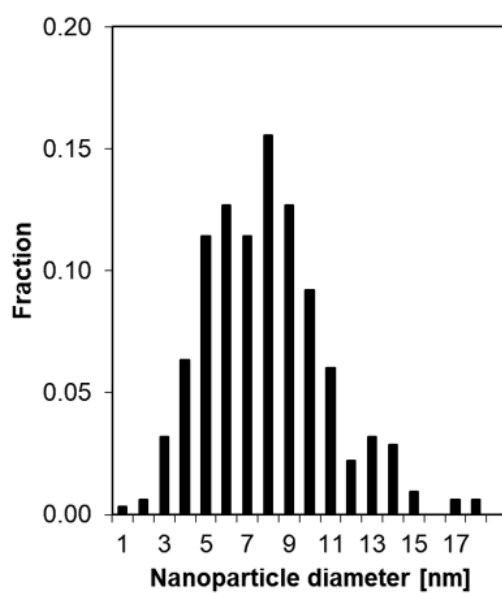


Figure 4.22. TEM-derived gold nanoparticle size distribution for 0.11Au-PVP/TS-1(73). The distribution was determined from 315 gold nanoparticles. The average size is 7.4 ± 2.9 nm, with 2.9 nm representing the standard deviation of the measured diameters.

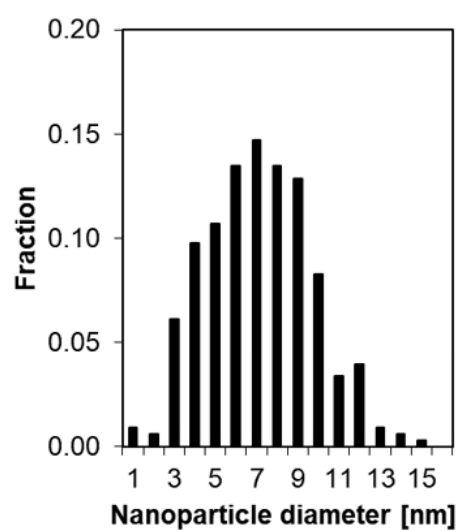


Figure 4.23. TEM-derived gold nanoparticle size distribution for 0.082Au-PVP/S-1. The distribution was determined from 327 gold nanoparticles. The average size is 6.6 ± 2.5 nm, with 2.5 nm representing the standard deviation of the measured diameters.

4.5.11 Proximal Ti active site model

The proximal Ti active site model is a tool used to test the hypothesis that all PO-producing active sites consist of an Au-containing active site and a Ti-containing active site, each with an adsorbed reactive intermediate involved in the rate-determining step (e.g., HOOH-S_{Au} and $\text{C}_3\text{H}_6\text{-S}_{Ti}$, where S_{Au} and S_{Ti} refer to gold- and titanium-containing active sites, respectively), and that they are close enough for these adsorbed intermediates to react and form PO and H_2O .

The model consists of a 2-D grid of unit cells ($20.09 \text{ \AA} \times 19.738 \text{ \AA}$), each with one accessible Ti-containing site placed at the center, and a gold nanoparticle, the footprint of which is approximated as a circle of radius R (Fig. 4.24). The width of the unit cell grid is determined by the radius of the nanoparticle, such that when the center of the nanoparticle is at an outer edge of the central unit cell, the distance between the nanoparticle's center and all outer edges of the unit cell grid will always be more than the sum of the nanoparticle radius and interaction range. Ti-containing sites are considered to be close enough to a gold nanoparticle to form a PO-producing Au-Ti active site if the Ti containing site is within an 'interaction range' (D , figure 4.24).

To determine the average number of Au-Ti sites for a given nanoparticle diameter and surface density of Ti-containing sites, the central unit cell is divided into a grid of sampling points (Figure 4.25). For each position, the number of Ti-containing sites within the interaction range is determined. After all points have been sampled, the number of Au-Ti sites for all points sampled is averaged to determine the average number of Au-Ti sites for that specific nanoparticle size and surface density of Ti-containing sites. As the number of sampling points increases, the value of the average number of Au-Ti sites converges to a final value (Figure 4.26). For the results discussed in the manuscript, 90,000 points (sampling resolution = 300/side) were used to sample the central unit cell. The average number of Au-Ti sites per nanoparticle can then be generated by this method for a range of Au nanoparticle diameters, Ti surface densities, and interaction ranges (Fig. 4.27).

The surface density of Ti-containing sites was approximated as being equal to the bulk Si/Ti molar ratio for the material. This is likely an overestimate, given that it may not

be likely that all unit cells of TS-1 at external crystallite surfaces which contain a Ti will have that Ti be externally accessible. For the model, this ratio is 95, corresponding to one Ti per unit cell, to simplify initial calculations. To account for surface densities of Ti-containing sites other than one per unit cell, the final average value of proximal Ti per Au nanoparticle is adjusted by a factor of $(\text{surface Ti density})_{\text{actual}}/(\text{surface Ti density})_{\text{model}}$, where the denominator is the value corresponding to 1 Ti per unit cell. This adjustment is discouraged for moving to higher Ti surface densities than 1 per unit cell, as this model does not capture any consequences of two Ti-containing sites being in proximity to one another, such as deactivation due to strong bipodal adsorption of propylene or propylene oxide [49], [50].

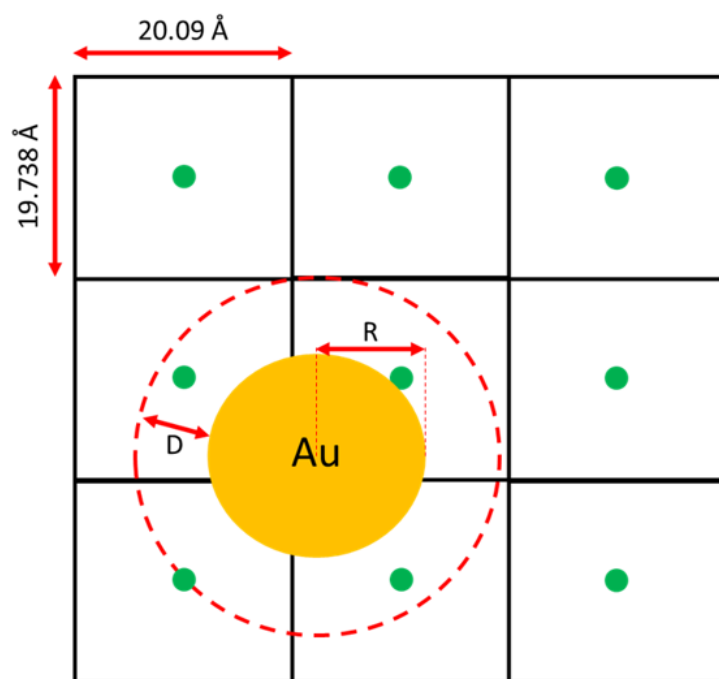


Figure 4.24. 2-D grid illustrating the proximal Ti model, with unit cell side lengths, Au nanoparticle radius (R), and interaction range (D) shown. The gold nanoparticle is represented by the yellow/gold circle labeled “Au” and surface-accessible Ti-containing sites are represented by green circles. In this example, the gold nanoparticle has four Ti-containing sites within the interaction range.

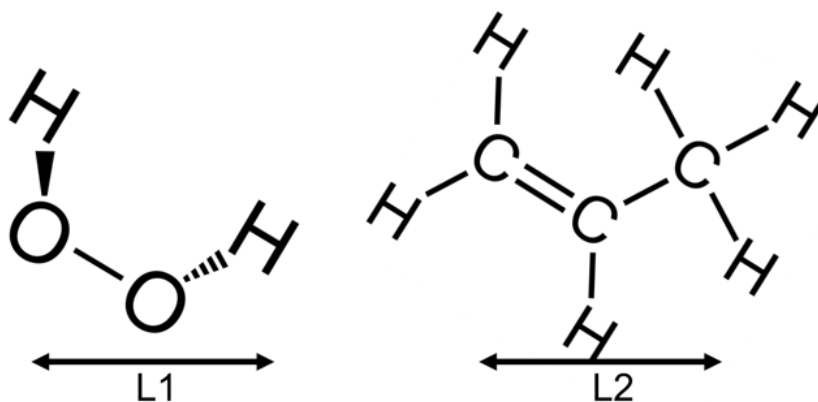


Figure 4.25. Schematic showing the lengths of hydrogen peroxide used to generate the estimated maximum interaction range used for the proximal Ti model in the main text. $L1 = 0.255$ nm, $L2 = 0.181$ nm. Molecular internal coordinates obtained from the NIST Computational Chemistry Comparison and Benchmark Database (CCCBDB, <https://cccbdb.nist.gov/introx.asp>)

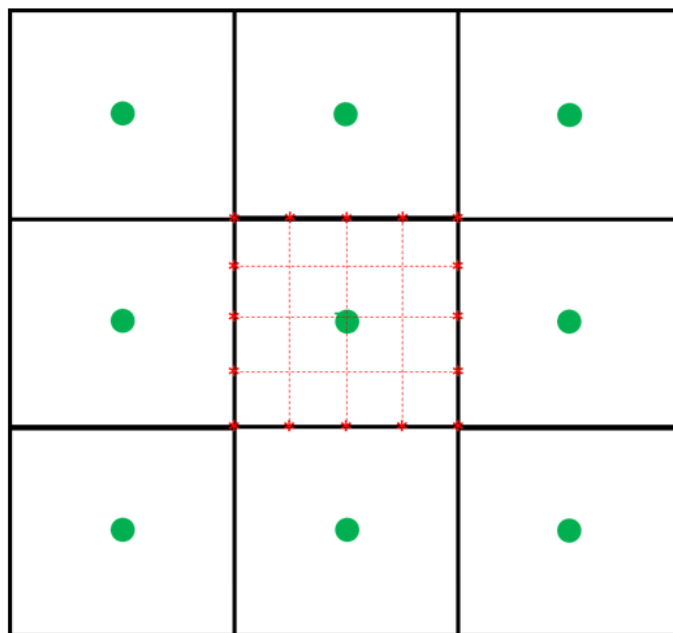


Figure 4.26. Example central unit cell with a 5x5 grid of sampling points (sampling resolution = 5/side).

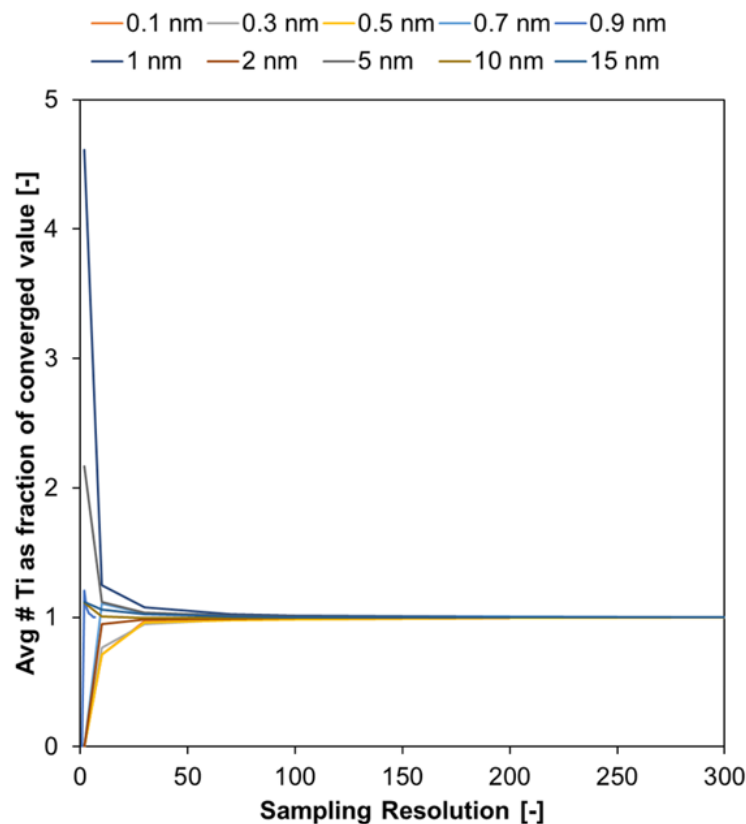


Figure 4.27. The effect of increasing sampling resolution on the value of the average number of Au-Ti site pairs for a range of interaction ranges (0.1-15 nm, top). For all interaction ranges tested, the average number of Au-Ti sites per nanoparticle converged to within 5% of the value at a sampling resolution of 300 by a sampling resolution of 100.

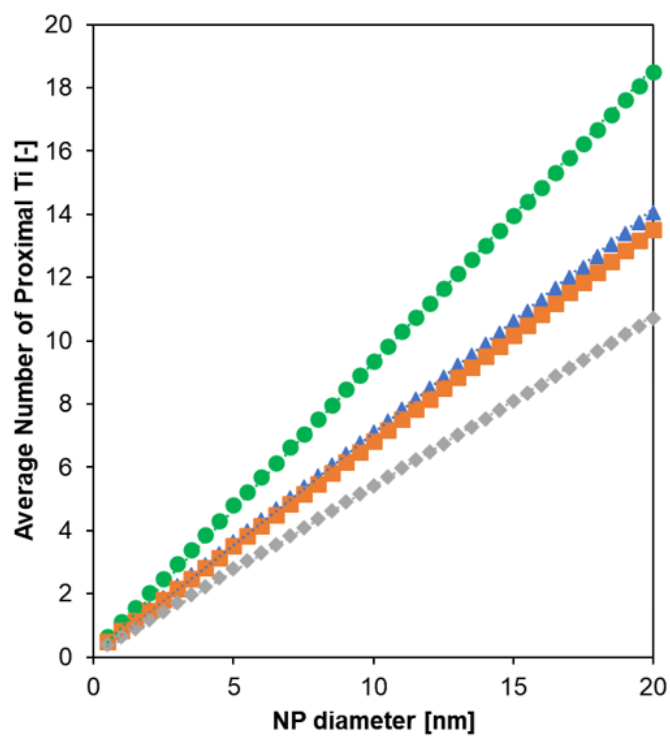


Figure 4.28. Average number of proximal Ti per Au nanoparticle for Si/Ti of 73 (green circles), 96 (blue triangles), 100 (orange squares), and 126 (grey diamonds), for Au nanoparticles of diameters 0.5-20 nm.

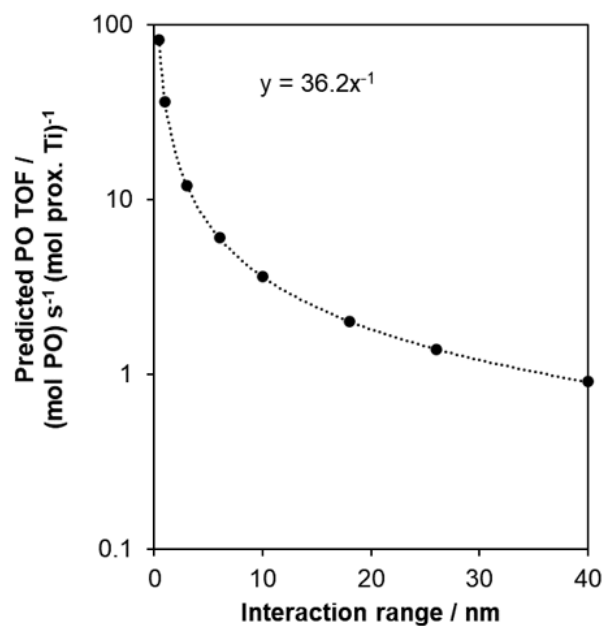


Figure 4.29. Effect of increasing the interaction range for Au and Ti sites on the catalytic turnover frequency required to explain catalytic rates measured on a series of catalysts including 0.06Au-DP/TS-1(100), 0.12Au-DP/TS-1(100), 0.20Au-DP/TS-1(100), 0.24Au-DP/TS-1(100), 0.40Au-DP/TS-1(100) 0.083Au-PVP/TS-1(126), and 0.11Au-PVP/TS-1(73).

4.5.12 Model fits of propylene epoxidation rate data

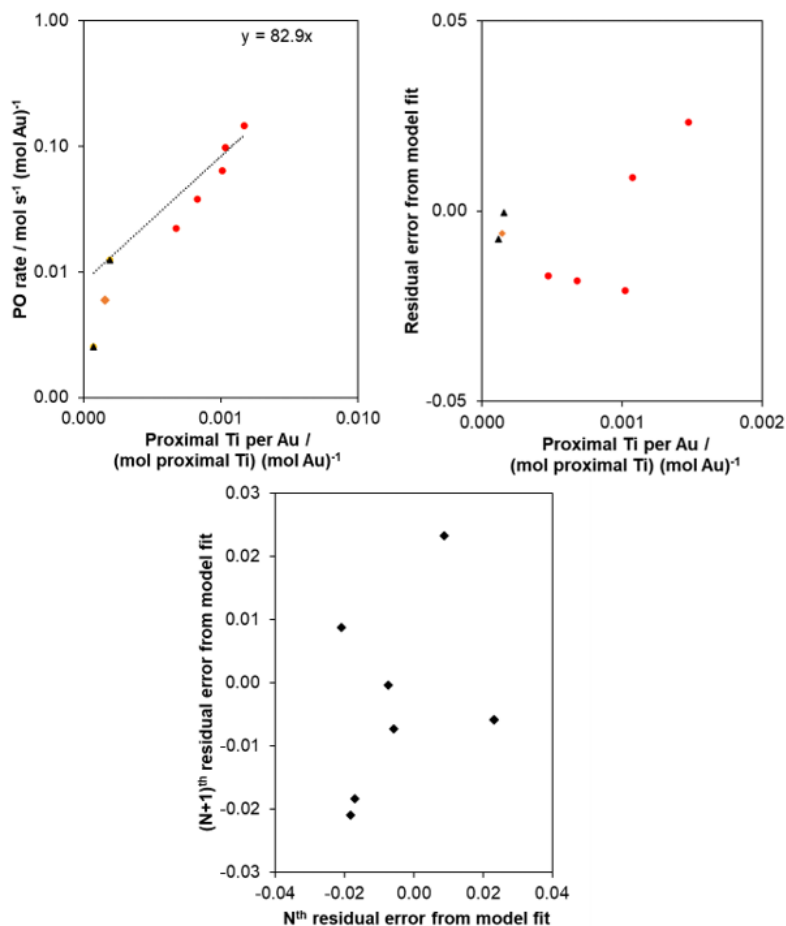


Figure 4.30. (Top left) Plot of PO rate normalized to gold mass vs. the molar proximal Ti per Au ratio. The average turnover frequency required for this model is shown in the top right corner of the plot. (Top right) Residual error plot for the top left plot. (Bottom) Lag plot for the residual error plot. These plots contain data for the Au-PVP/TS-1 catalysts from this work (0.083Au-PVP/TS-1(126) (black triangles) and 0.11Au-PVP/TS-1(73) (orange diamond)) as well as Au-DP/TS-1(100) (red circles) catalysts from [39].

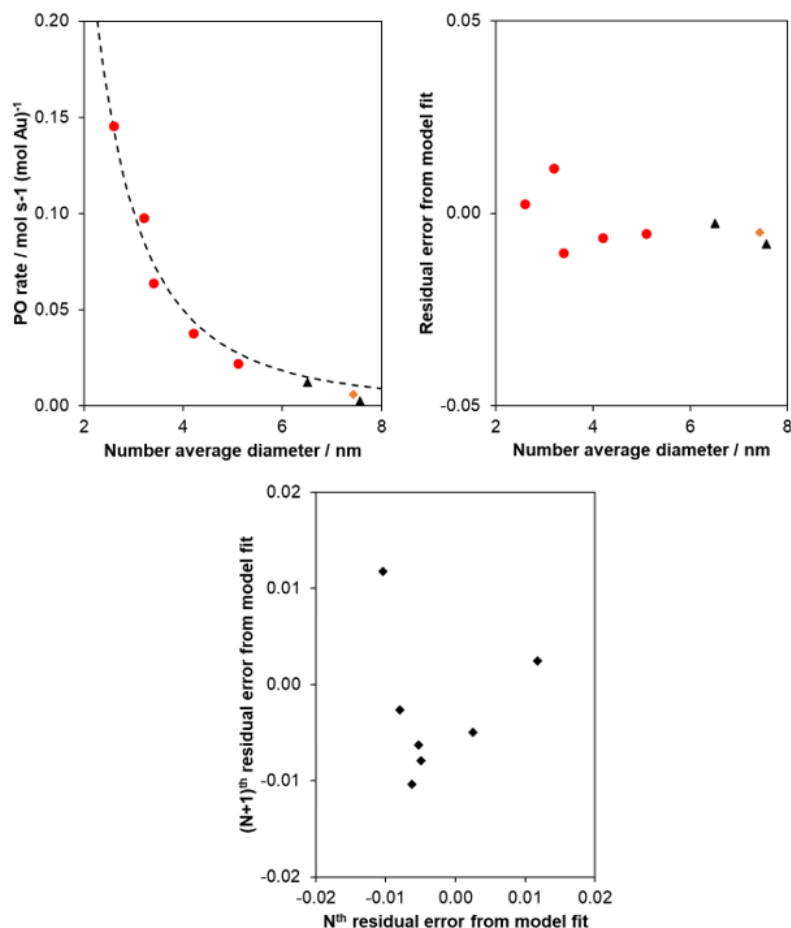


Figure 4.31. (Top left) Model fit for the proximal Ti model to propylene epoxidation rate data as a function of average gold nanoparticle diameter. (Top right) Residual error plot for the model fit. (Bottom) Lag plot for the residual error plot. These plots contain data for the Au-PVP/TS-1 catalysts from this work (0.083Au-PVP/TS-1(126) (black triangles) and 0.11Au-PVP/TS-1(73) (orange diamond)) as well as Au-DP/TS-1(100) (red circles) catalysts from [39].

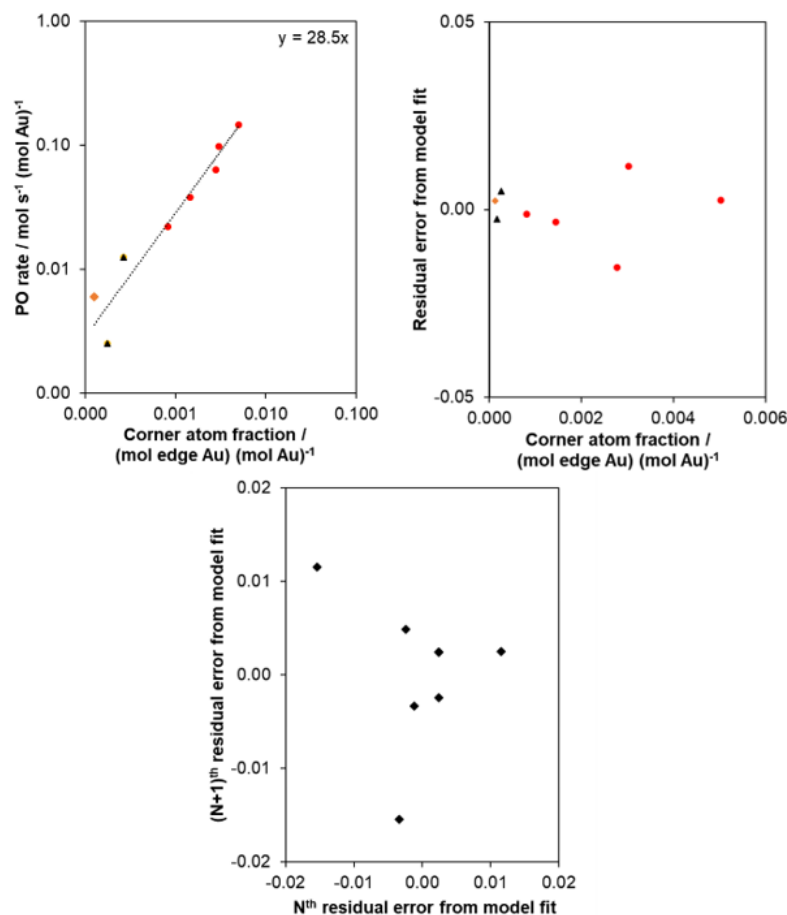


Figure 4.32. (Top left) Plot of PO rate normalized to gold mass vs. corner atom fraction. The average turnover frequency required for this model is shown in the top right corner of the plot. (Top right) Residual error plot for the top left plot. (Bottom) Lag plot for the residual error plot. These plots contain data for the Au-PVP/TS-1 catalysts from this work (0.083Au-PVP/TS-1(126) (black triangles) and 0.11Au-PVP/TS-1(73) (orange diamond)) as well as Au-DP/TS-1(100) (red circles) catalysts from [39].

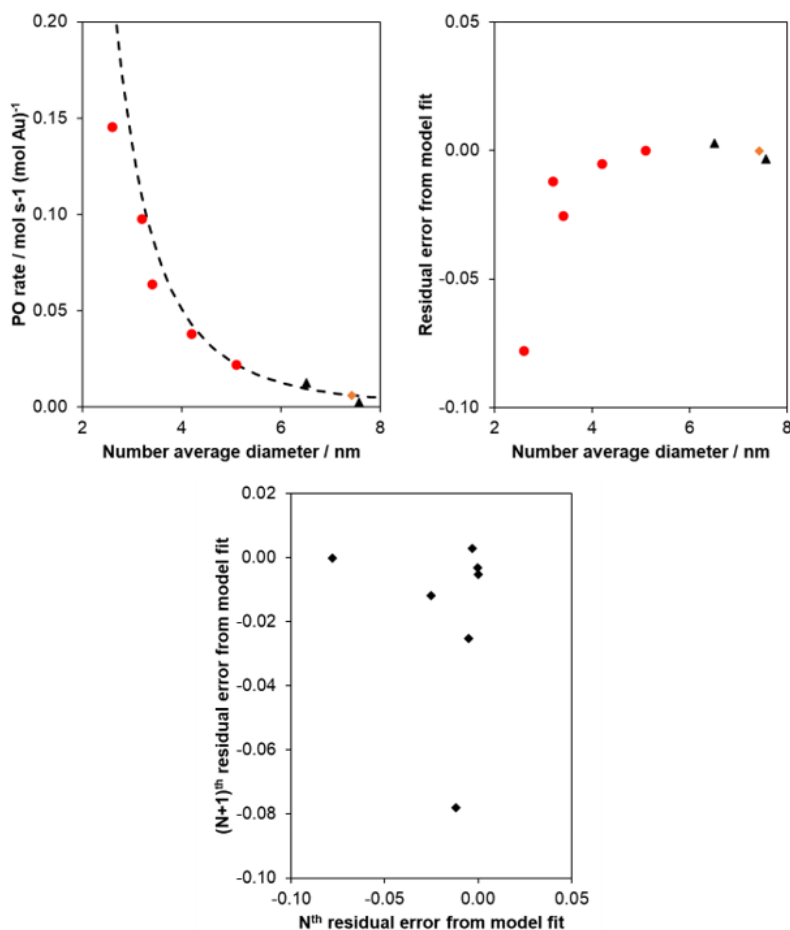


Figure 4.33. (Top left) Model fit for the corner model to propylene epoxidation rate data as a function of average gold nanoparticle diameter. (Top right) Residual error plot for the model fit. (Bottom) Lag plot for the residual error plot. These plots contain data for the Au-PVP/TS-1 catalysts from this work (0.083Au-PVP/TS-1(126) (black triangles) and 0.11Au-PVP/TS-1(73) (orange diamond)) as well as Au-DP/TS-1(100) (red circles) catalysts from [39].

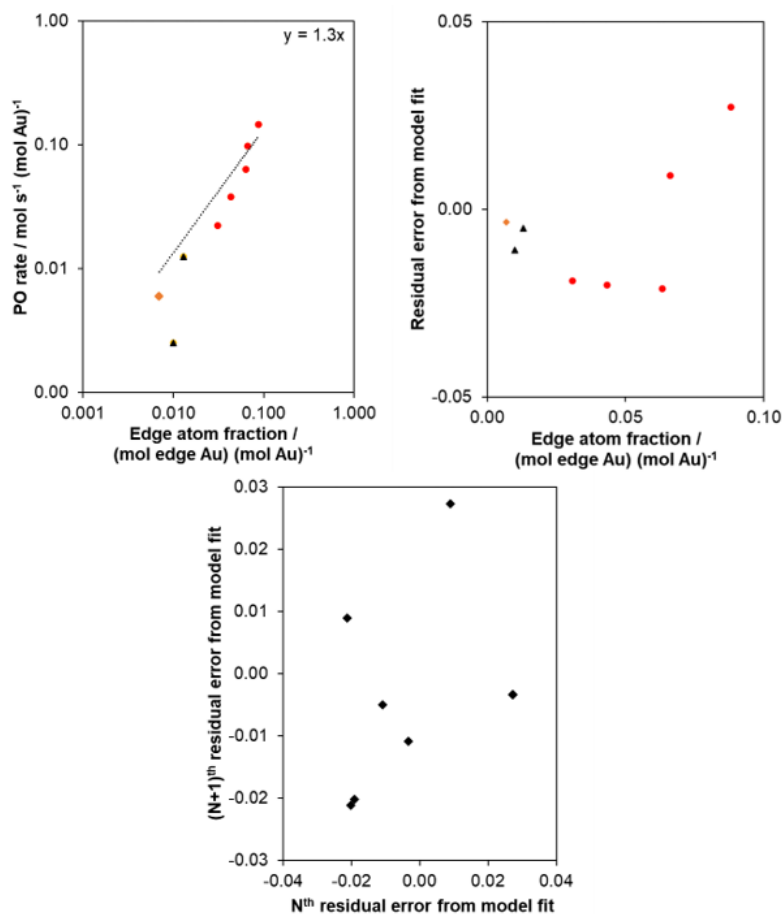


Figure 4.34. (Top left) Plot of PO rate normalized to gold mass vs. edge atom fraction. The average turnover frequency required for this model is shown in the top right corner of the plot. (Top right) Residual error plot for the top left plot. (Bottom) Lag plot for the residual error plot. These plots contain data for the Au-PVP/TS-1 catalysts from this work (0.083Au-PVP/TS-1(126) (black triangles) and 0.11Au-PVP/TS-1(73) (orange diamond)) as well as Au-DP/TS-1(100) (red circles) catalysts from [39].

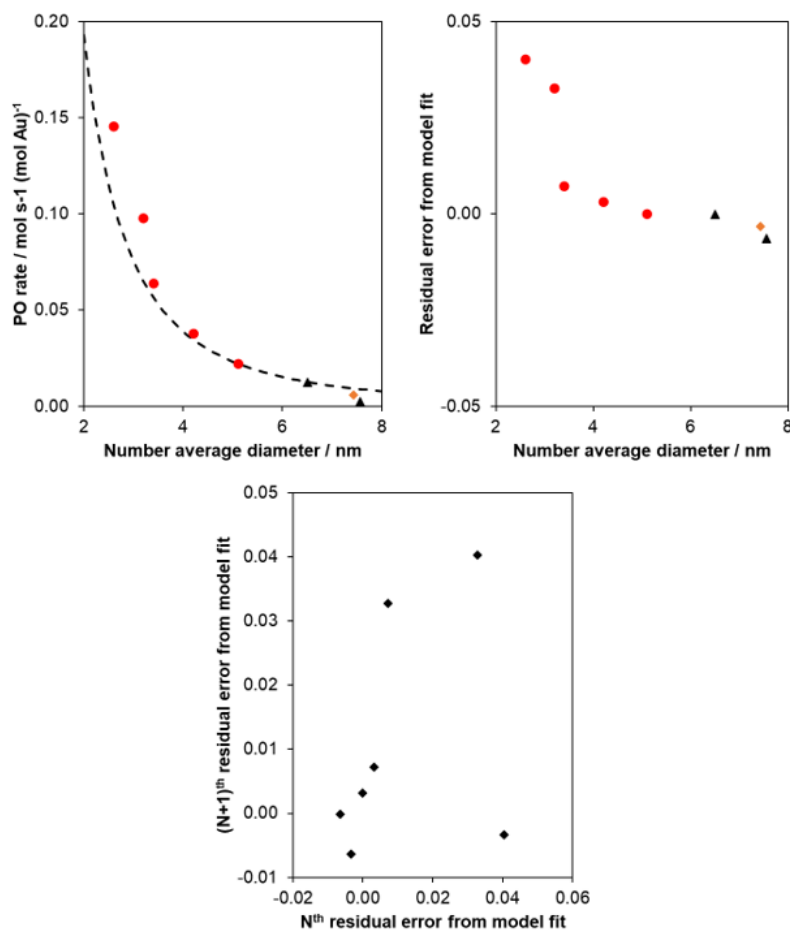


Figure 4.35. (Top left) Model fit for the edge model to propylene epoxidation rate data as a function of average gold nanoparticle diameter. (Top right) Residual error plot for the model fit. (Bottom) Lag plot for the residual error plot. These plots contain data for the Au-PVP/TS-1 catalysts from this work (0.083Au-PVP/TS-1(126) (black triangles) and 0.11Au-PVP/TS-1(73) (orange diamond)) as well as Au-DP/TS-1(100) (red circles) catalysts from [39].

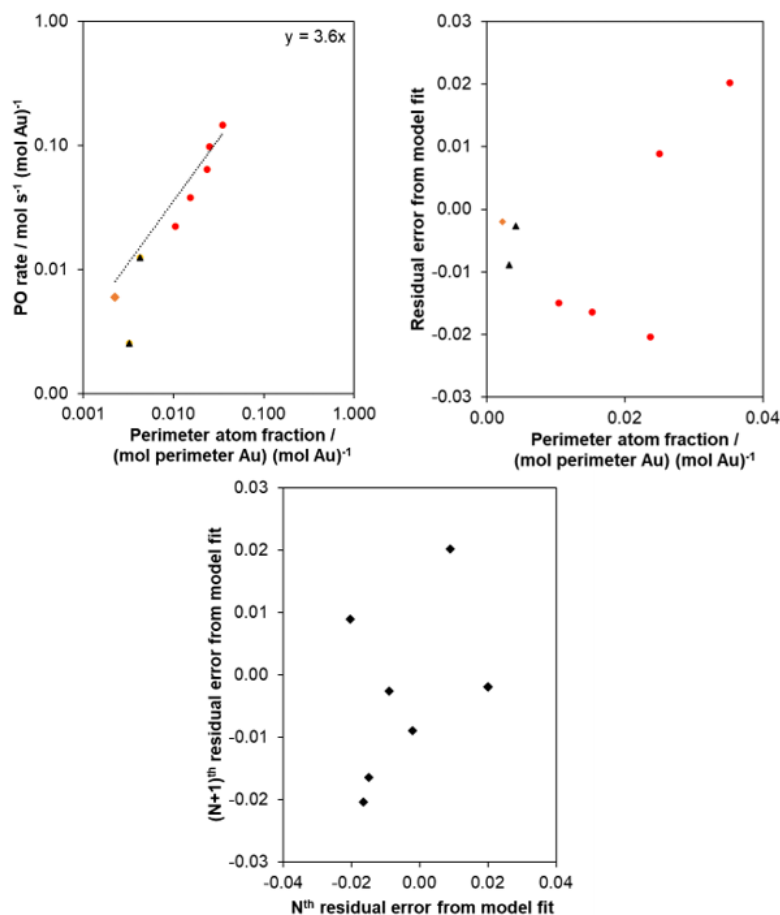


Figure 4.36. (Top left) Plot of PO rate normalized to gold mass vs. perimeter atom fraction. The average turnover frequency required for this model is shown in the top right corner of the plot. (Top right) Residual error plot for the top left plot. (Bottom) Lag plot for the residual error plot. These plots contain data for the Au-PVP/TS-1 catalysts from this work (0.083Au-PVP/TS-1(126) (black triangles) and 0.11Au-PVP/TS-1(73) (orange diamond)) as well as Au-DP/TS-1(100) (red circles) catalysts from [39].

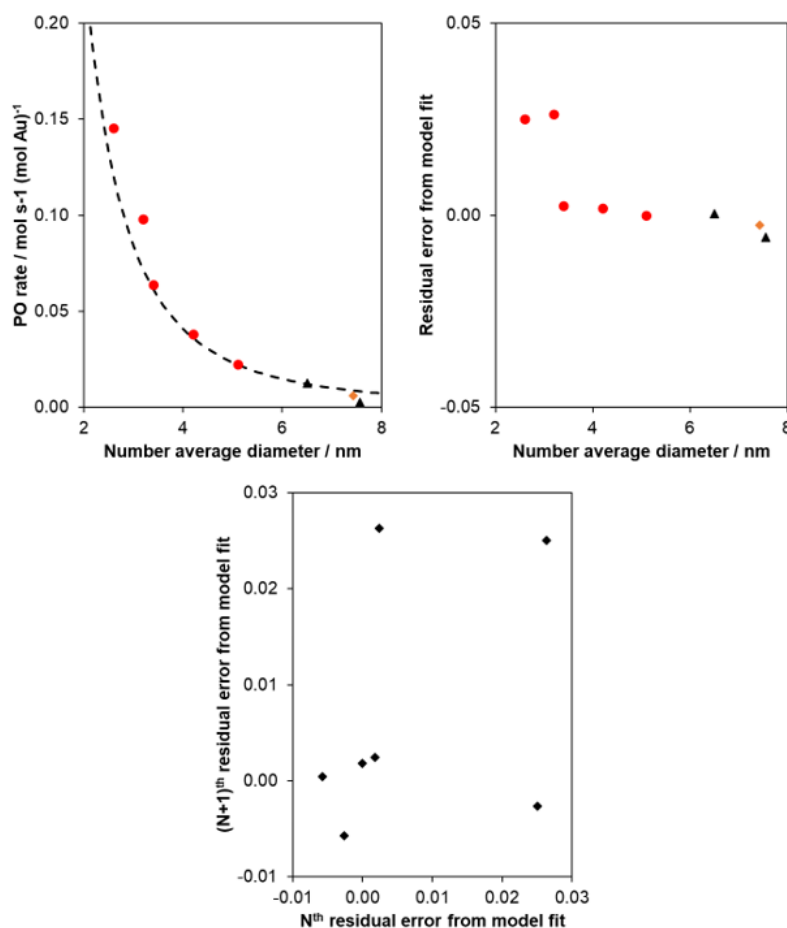


Figure 4.37. (Top left) Model fit for the perimeter model to propylene epoxidation rate data as a function of average gold nanoparticle diameter. (Top right) Residual error plot for the model fit. (Bottom) Lag plot for the residual error plot. These plots contain data for the Au-PVP/TS-1 catalysts from this work (0.083Au-PVP/TS-1(126) (black triangles) and 0.11Au-PVP/TS-1(73) (orange diamond)) as well as Au-DP/TS-1(100) (red circles) catalysts from [39].

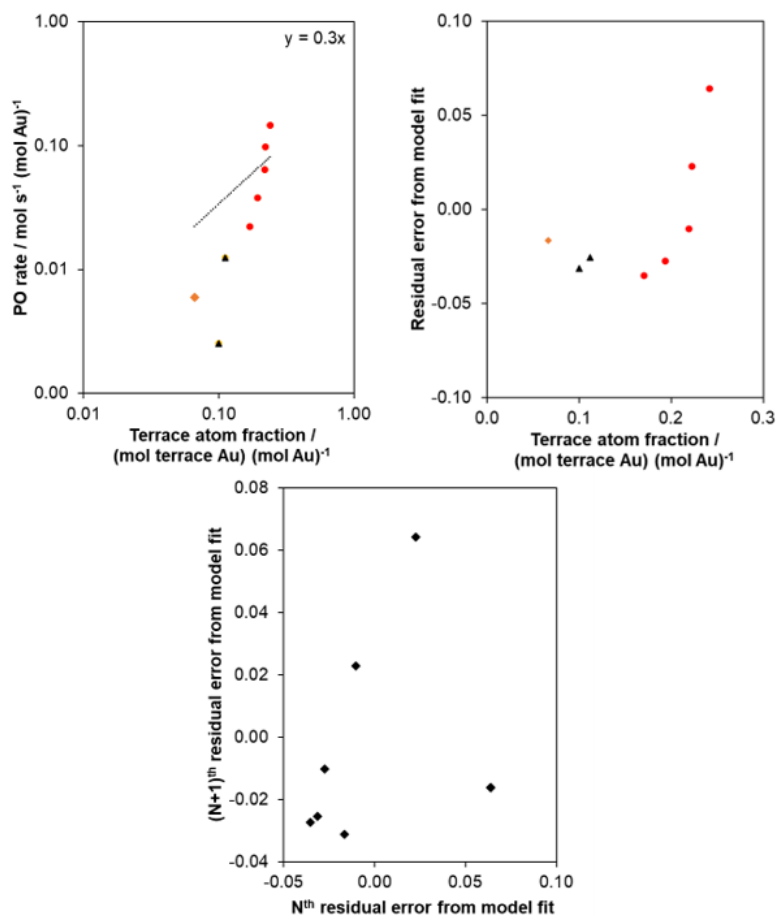


Figure 4.38. (Top left) Plot of PO rate normalized to gold mass vs. terrace atom fraction. The average turnover frequency required for this model is shown in the top right corner of the plot. (Top right) Residual error plot for the top left plot. (Bottom) Lag plot for the residual error plot. These plots contain data for the Au-PVP/TS-1 catalysts from this work (0.083Au-PVP/TS-1(126) (black triangles) and 0.11Au-PVP/TS-1(73) (orange diamond)) as well as Au-DP/TS-1(100) (red circles) catalysts from [39].

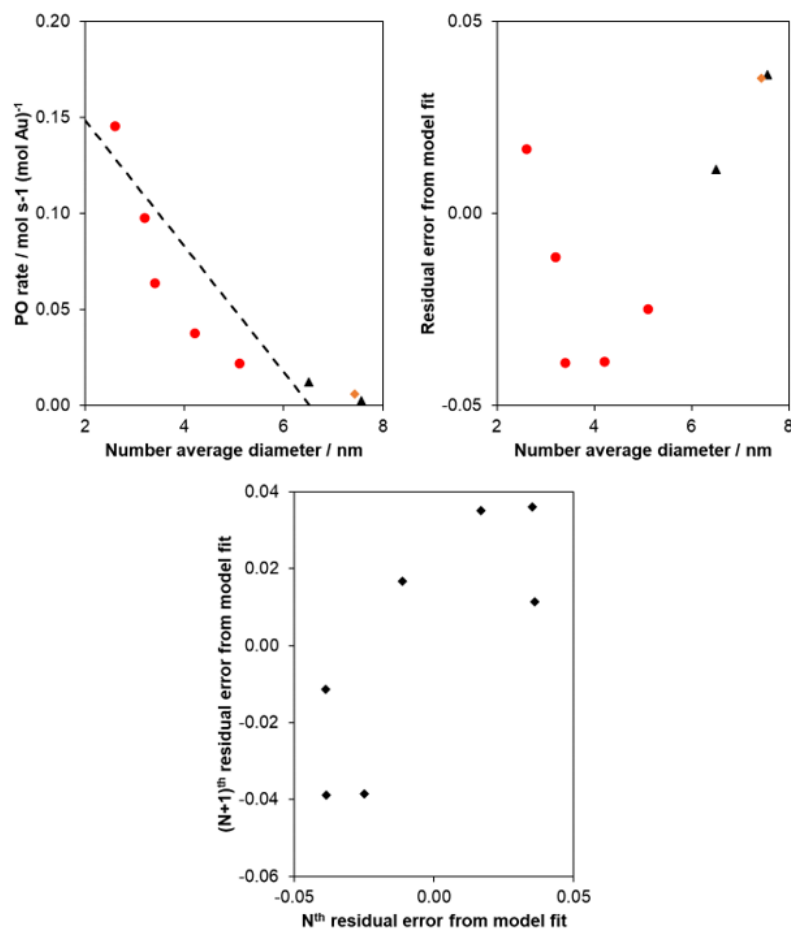


Figure 4.39. (Top left) Model fit for the terrace model to propylene epoxidation rate data as a function of average gold nanoparticle diameter. (Top right) Residual error plot for the model fit. (Bottom) Lag plot for the residual error plot. These plots contain data for the Au-PVP/TS-1 catalysts from this work (0.083Au-PVP/TS-1(126) (black triangles) and 0.11Au-PVP/TS-1(73) (orange diamond)) as well as Au-DP/TS-1(100) (red circles) catalysts from [39].

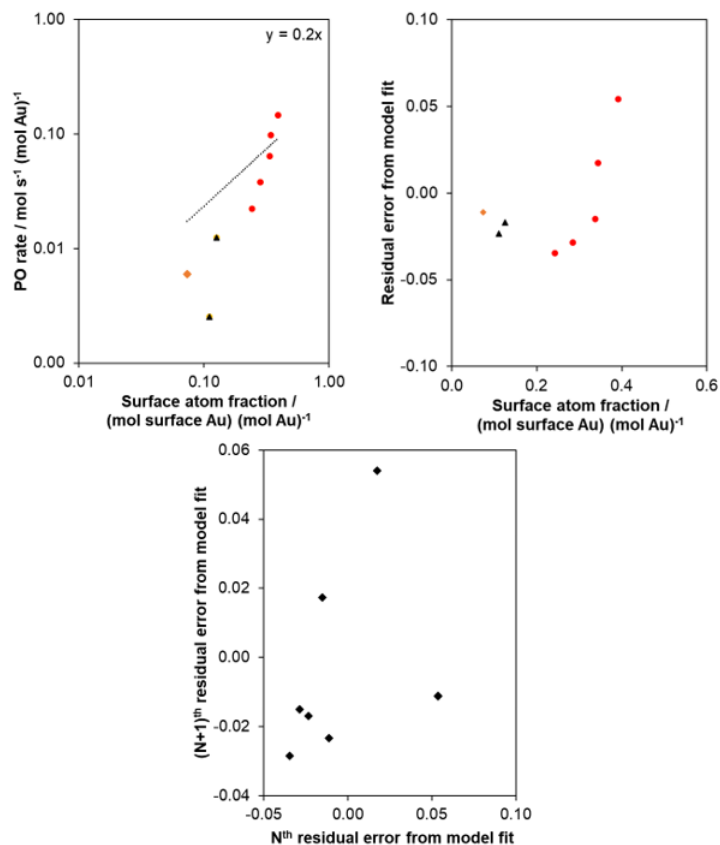


Figure 4.40. (Top left) Plot of PO rate normalized to gold mass vs. surface atom fraction. The average turnover frequency required for this model is shown in the top right corner of the plot. (Top right) Residual error plot for the top left plot. (Bottom) Lag plot for the residual error plot. These plots contain data for the Au-PVP/TS-1 catalysts from this work (0.083Au-PVP/TS-1(126) (black triangles) and 0.11Au-PVP/TS-1(73) (orange diamond)) as well as Au-DP/TS-1(100) (red circles) catalysts from [39].

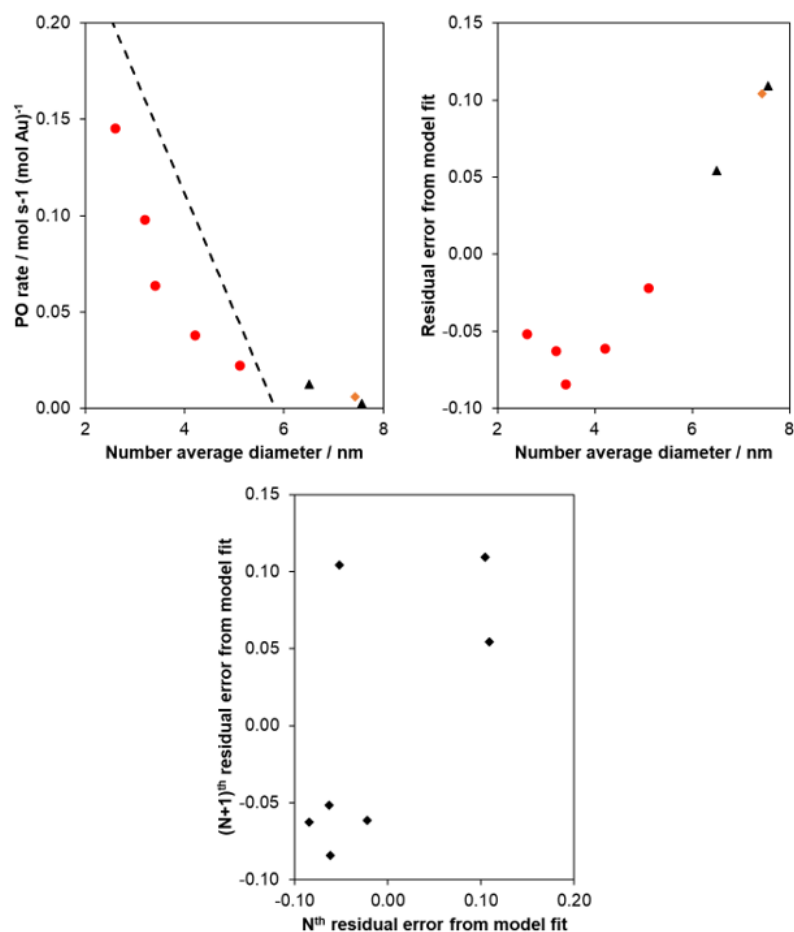


Figure 4.41. (Top left) Model fit for the surface model to propylene epoxidation rate data as a function of average gold nanoparticle diameter. (Top right) Residual error plot for the model fit. (Bottom) Lag plot for the residual error plot. These plots contain data for the Au-PVP/TS-1 catalysts from this work (0.083Au-PVP/TS-1(126) (black triangles) and 0.11Au-PVP/TS-1(73) (orange diamond)) as well as Au-DP/TS-1(100) (red circles) catalysts from [39].

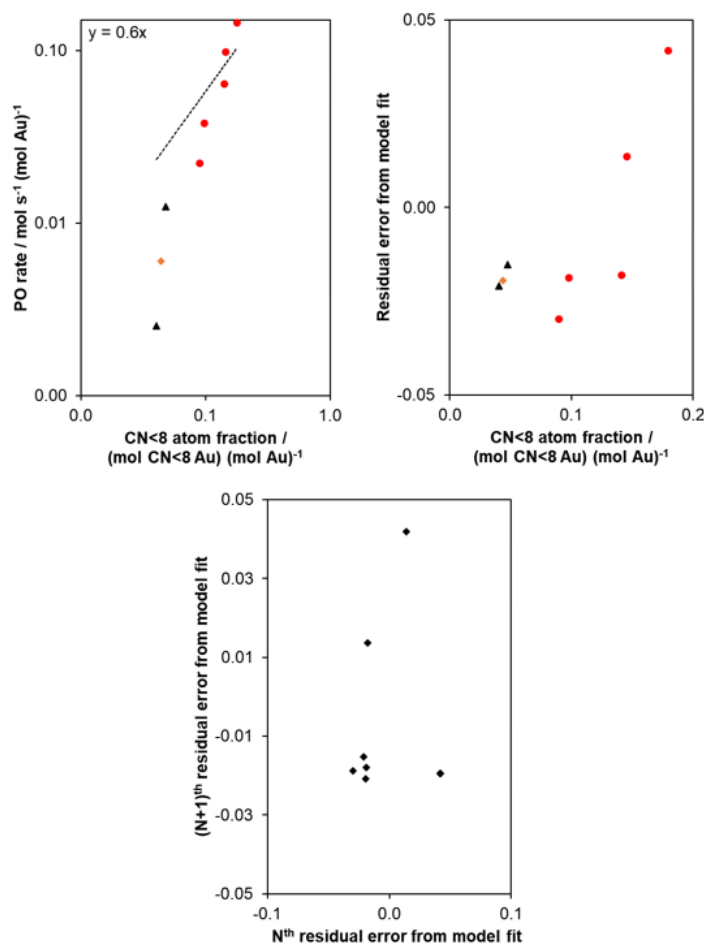


Figure 4.42. (Top left) Plot of PO rate normalized to gold mass vs. CN<8 atom fraction for a spherical nanoparticle model [41]. The average turnover frequency required for this model is shown in the top right corner of the plot. (Top right) Residual error plot for the top left plot. (Bottom) Lag plot for the residual error plot. These plots contain data for the Au-PVP/TS-1 catalysts from this work (0.083Au-PVP/TS-1(126) (black triangles) and 0.11Au-PVP/TS-1(73) (orange diamond)) as well as Au-DP/TS-1(100) (red circles) catalysts from [39].

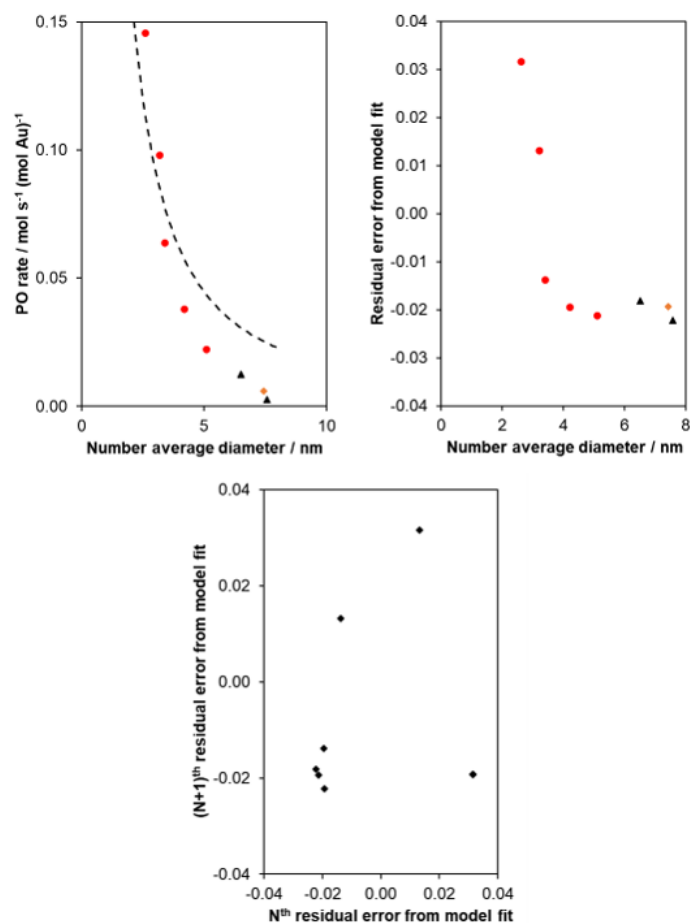


Figure 4.43. (Top left) Model fit for CN<8 atoms from a spherical nanoparticle model [41] to propylene epoxidation rate data as a function of average gold nanoparticle diameter. (Top right) Residual error plot for the model fit. (Bottom) Lag plot for the residual error plot. These plots contain data for the Au-PVP/TS-1 catalysts from this work (0.083Au-PVP/TS-1(126) (black triangles) and 0.11Au-PVP/TS-1(73) (orange diamond)) as well as Au-DP/TS-1(100) (red circles) catalysts from [39].

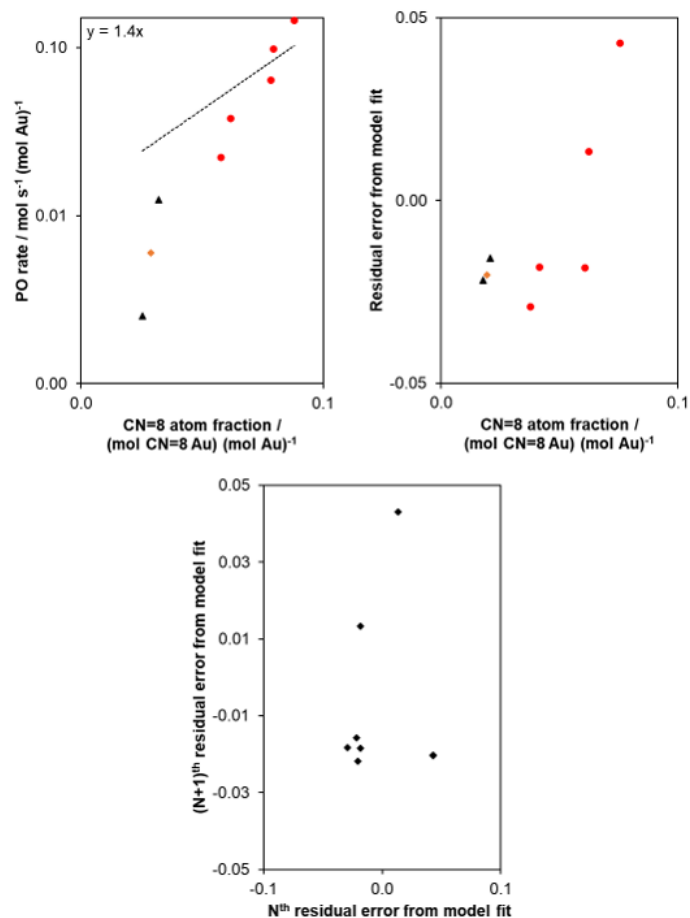


Figure 4.44. (Top left) Plot of PO rate normalized to gold mass vs. CN=8 atom fraction for a spherical nanoparticle model [41]. The average turnover frequency required for this model is shown in the top right corner of the plot. (Top right) Residual error plot for the top left plot. (Bottom) Lag plot for the residual error plot. These plots contain data for the Au-PVP/TS-1 catalysts from this work (0.083Au-PVP/TS-1(126) (black triangles) and 0.11Au-PVP/TS-1(73) (orange diamond)) as well as Au-DP/TS-1(100) (red circles) catalysts from [39].

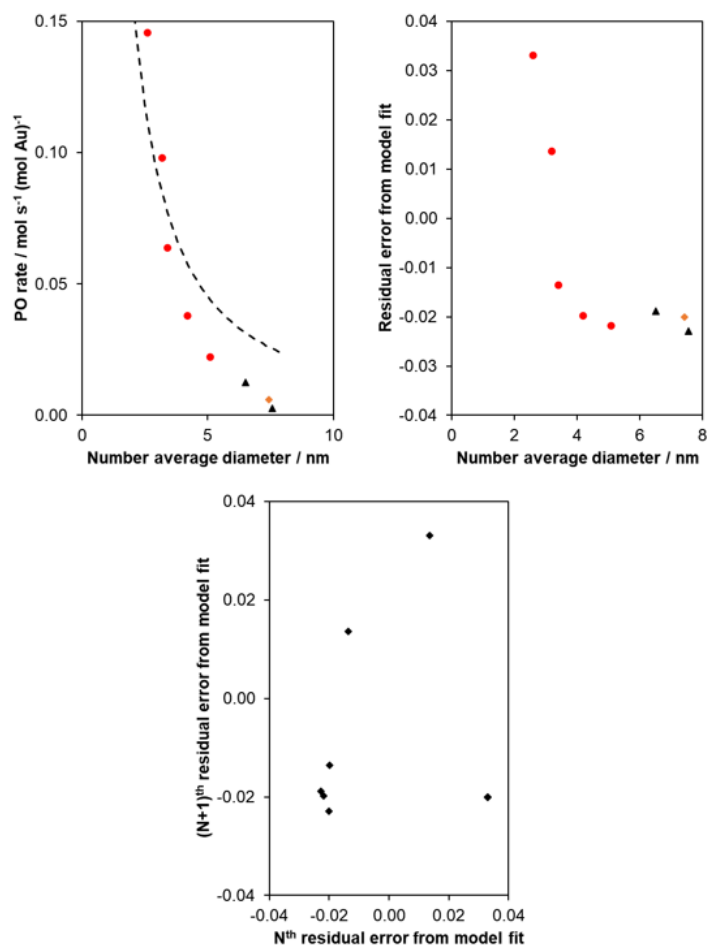


Figure 4.45. (Top left) Model fit for CN=8 atoms from a spherical nanoparticle model [41] to propylene epoxidation rate data as a function of average gold nanoparticle diameter. (Top right) Residual error plot for the model fit. (Bottom) Lag plot for the residual error plot. These plots contain data for the Au-PVP/TS-1 catalysts from this work (0.083Au-PVP/TS-1(126) (black triangles) and 0.11Au-PVP/TS-1(73) (orange diamond)) as well as Au-DP/TS-1(100) (red circles) catalysts from [39].

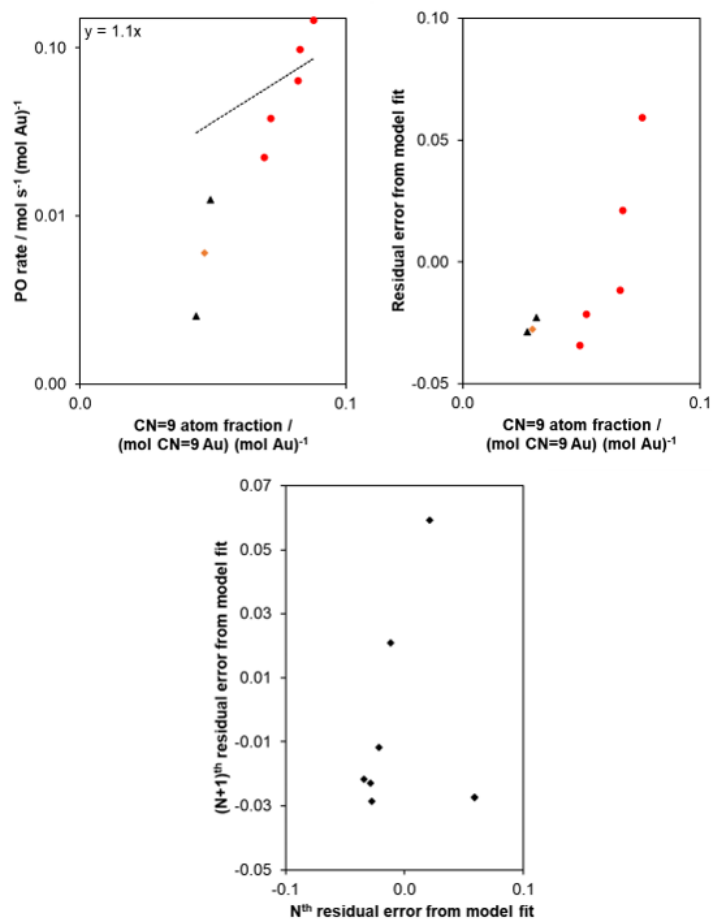


Figure 4.46. (Top left) Plot of PO rate normalized to gold mass vs. CN=9 atom fraction for a spherical nanoparticle model [41]. The average turnover frequency required for this model is shown in the top right corner of the plot. (Top right) Residual error plot for the top left plot. (Bottom) Lag plot for the residual error plot. These plots contain data for the Au-PVP/TS-1 catalysts from this work (0.083Au-PVP/TS-1(126) (black triangles) and 0.11Au-PVP/TS-1(73) (orange diamond)) as well as Au-DP/TS-1(100) (red circles) catalysts from [39].

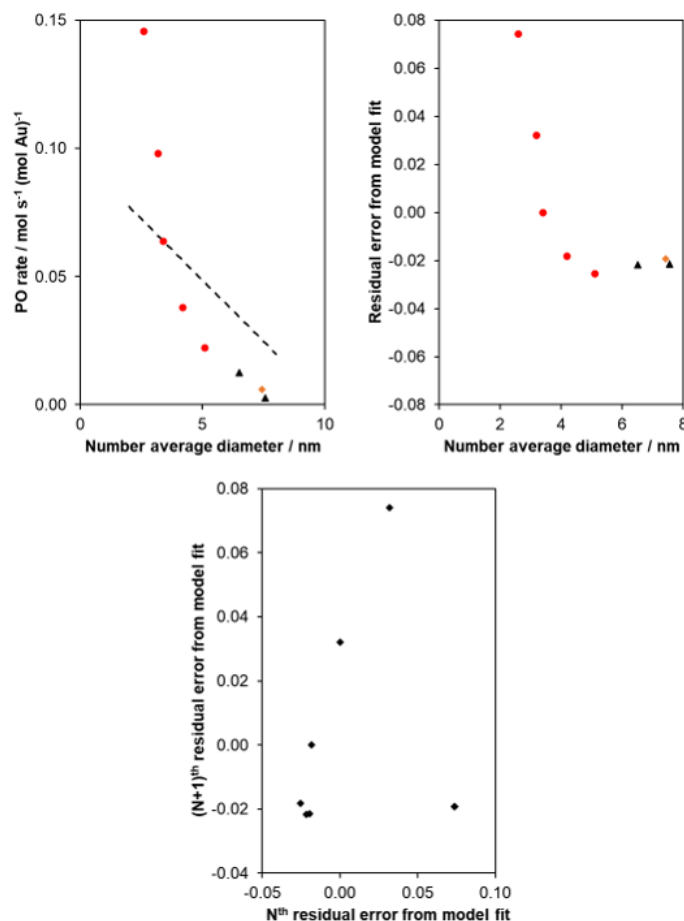


Figure 4.47. (Top left) Model fit for CN=9 atoms from a spherical nanoparticle model [41] to propylene epoxidation rate data as a function of average gold nanoparticle diameter. (Top right) Residual error plot for the model fit. (Bottom) Lag plot for the residual error plot. These plots contain data for the Au-PVP/TS-1 catalysts from this work (0.083Au-PVP/TS-1(126) (black triangles) and 0.11Au-PVP/TS-1(73) (orange diamond)) as well as Au-DP/TS-1(100) (red circles) catalysts from [39].

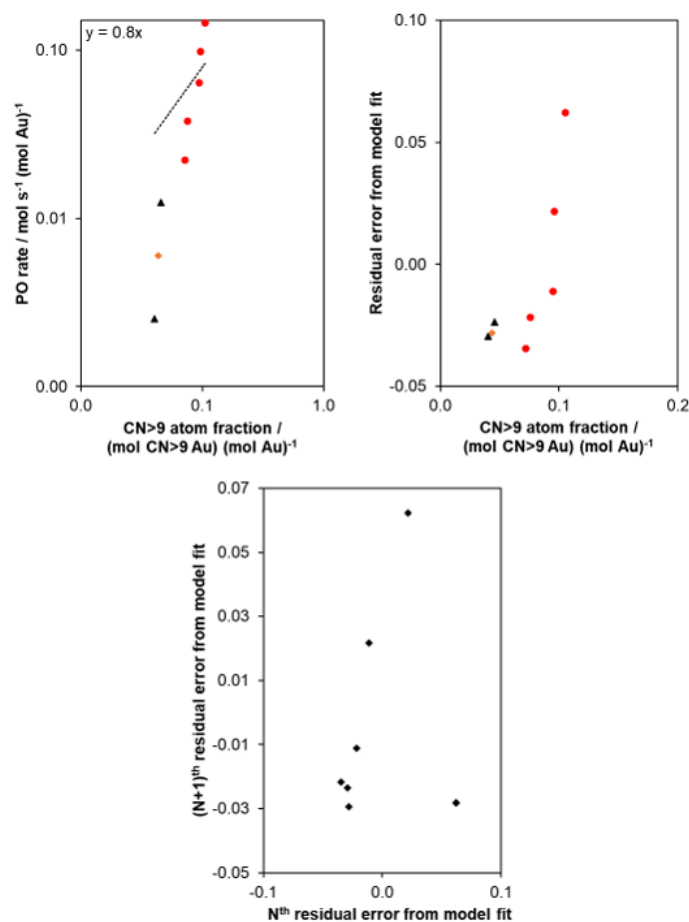


Figure 4.48. (Top left) Plot of PO rate normalized to gold mass vs. CN>9 atom fraction for a spherical nanoparticle model [41]. The average turnover frequency required for this model is shown in the top right corner of the plot. (Top right) Residual error plot for the top left plot. (Bottom) Lag plot for the residual error plot. These plots contain data for the Au-PVP/TS-1 catalysts from this work (0.083Au-PVP/TS-1(126) (black triangles) and 0.11Au-PVP/TS-1(73) (orange diamond)) as well as Au-DP/TS-1(100) (red circles) catalysts from [39].

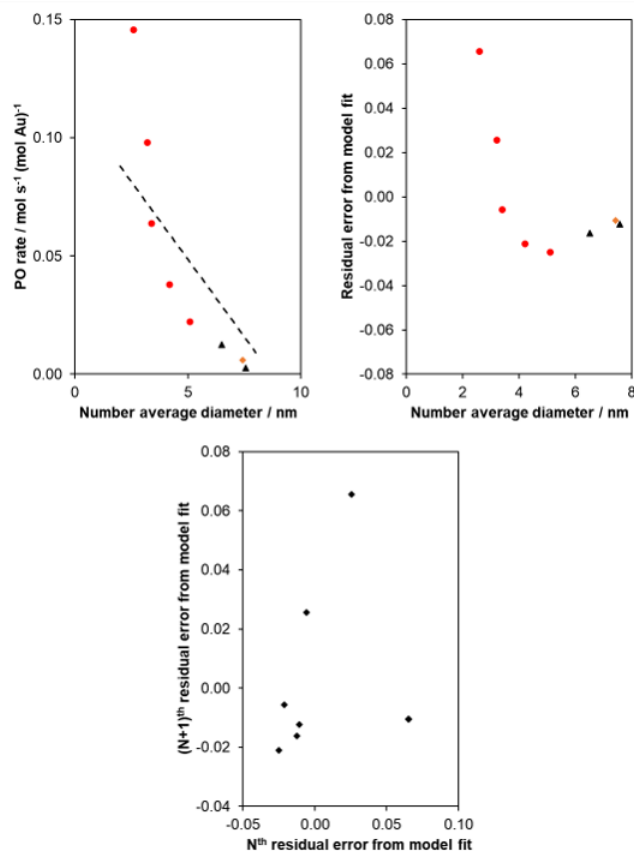


Figure 4.49. (Top left) Model fit for CN>9 atoms from a spherical nanoparticle model [41] to propylene epoxidation rate data as a function of average gold nanoparticle diameter. (Top right) Residual error plot for the model fit. (Bottom) Lag plot for the residual error plot. These plots contain data for the Au-PVP/TS-1 catalysts from this work (0.083Au-PVP/TS-1(126) (black triangles) and 0.11Au-PVP/TS-1(73) (orange diamond)) as well as Au-DP/TS-1(100) (red circles) catalysts from [39].

4.5.13 Model fits of hydrogen oxidation rate data

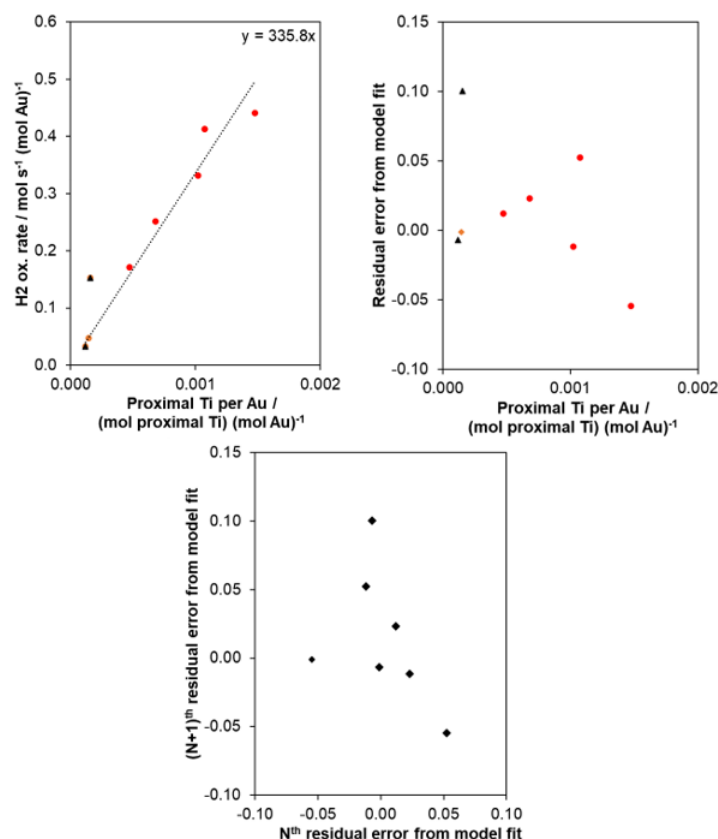


Figure 4.50. (Top left) Plot of hydrogen oxidation rate normalized to gold mass vs. molar proximal Ti to Au ratio. The average turnover frequency required for this model is shown in the top right corner of the plot. (Top right) Residual error plot for the top left plot. (Bottom) Lag plot for the residual error plot. These plots contain data for the Au-PVP/TS-1 catalysts from this work (0.083Au-PVP/TS-1(126) (black triangles) and 0.11Au-PVP/TS-1(73) (orange diamond)) as well as Au-DP/TS-1(100) (red circles) catalysts from [39].

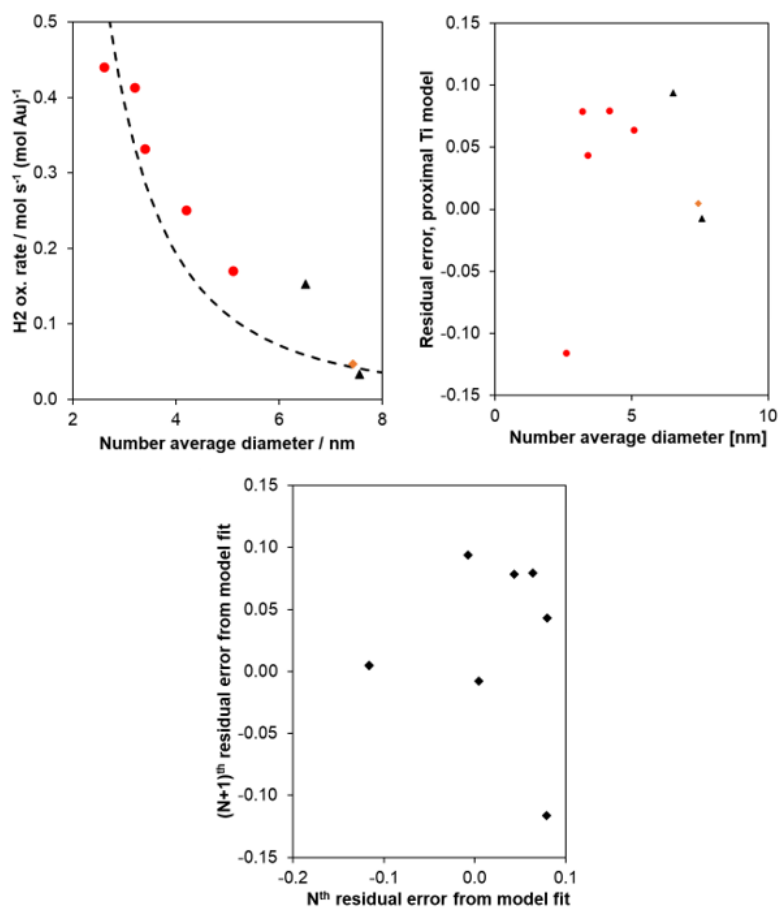


Figure 4.51. (Top left) Model fit for the proximal Ti model to hydrogen oxidation rate data as a function of average gold nanoparticle diameter. (Top right) Residual error plot for the model fit. (Bottom) Lag plot for the residual error plot. These plots contain data for the Au-PVP/TS-1 catalysts from this work (0.083Au-PVP/TS-1(126) (black triangles) and 0.11Au-PVP/TS-1(73) (orange diamond)) as well as Au-DP/TS-1(100) (red circles) catalysts from [39].

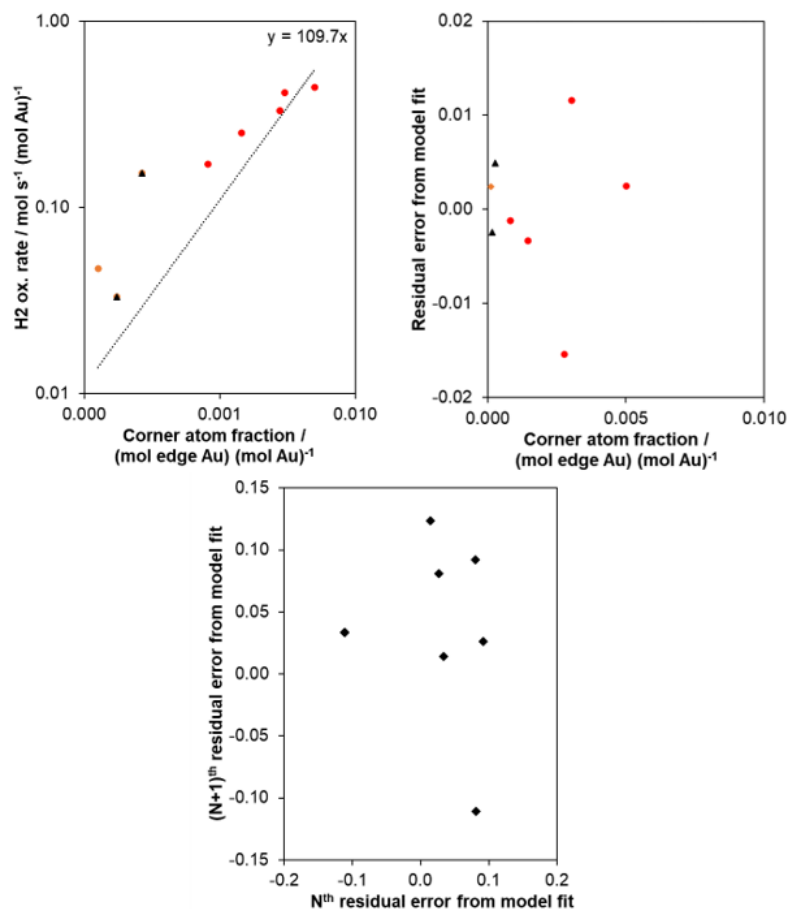


Figure 4.52. (Top left) Plot of hydrogen oxidation rate normalized to gold mass vs. corner atom fraction. The average turnover frequency required for this model is shown in the top right corner of the plot. (Top right) Residual error plot for the top left plot. (Bottom) Lag plot for the residual error plot. These plots contain data for the Au-PVP/TS-1 catalysts from this work (0.083Au-PVP/TS-1(126) (black triangles) and 0.11Au-PVP/TS-1(73) (orange diamond)) as well as Au-DP/TS-1(100) (red circles) catalysts from [39].

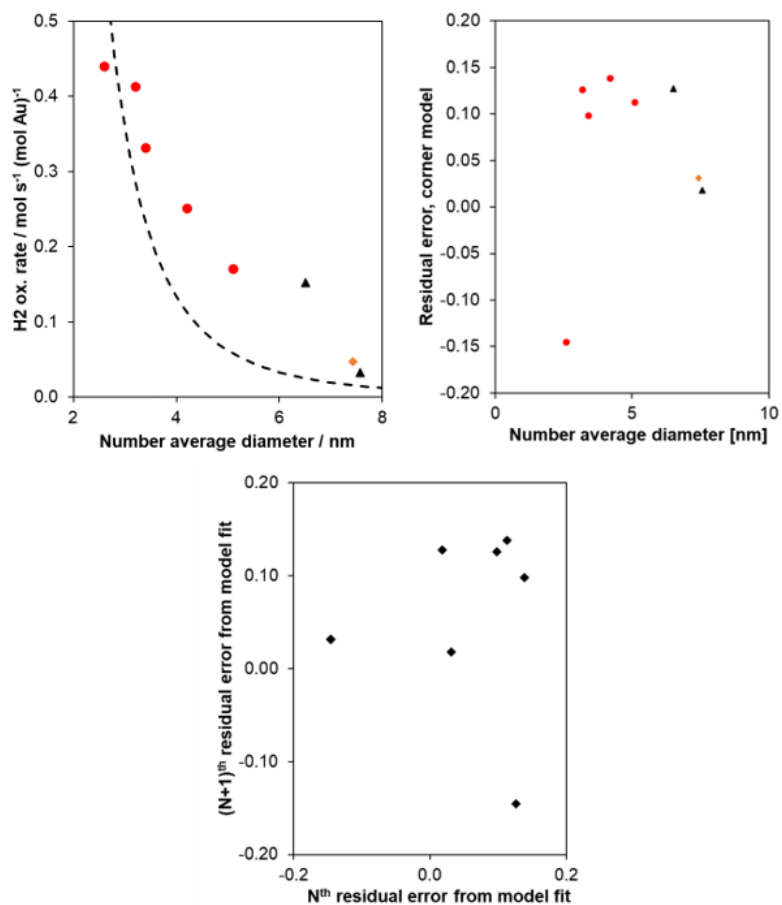


Figure 4.53. (Top left) Model fit for the corner model to hydrogen oxidation rate data as a function of average gold nanoparticle diameter. (Top right) Residual error plot for the model fit. (Bottom) Lag plot for the residual error plot. These plots contain data for the Au-PVP/TS-1 catalysts from this work (0.083Au-PVP/TS-1(126) (black triangles) and 0.11Au-PVP/TS-1(73) (orange diamond)) as well as Au-DP/TS-1(100) (red circles) catalysts from [39].

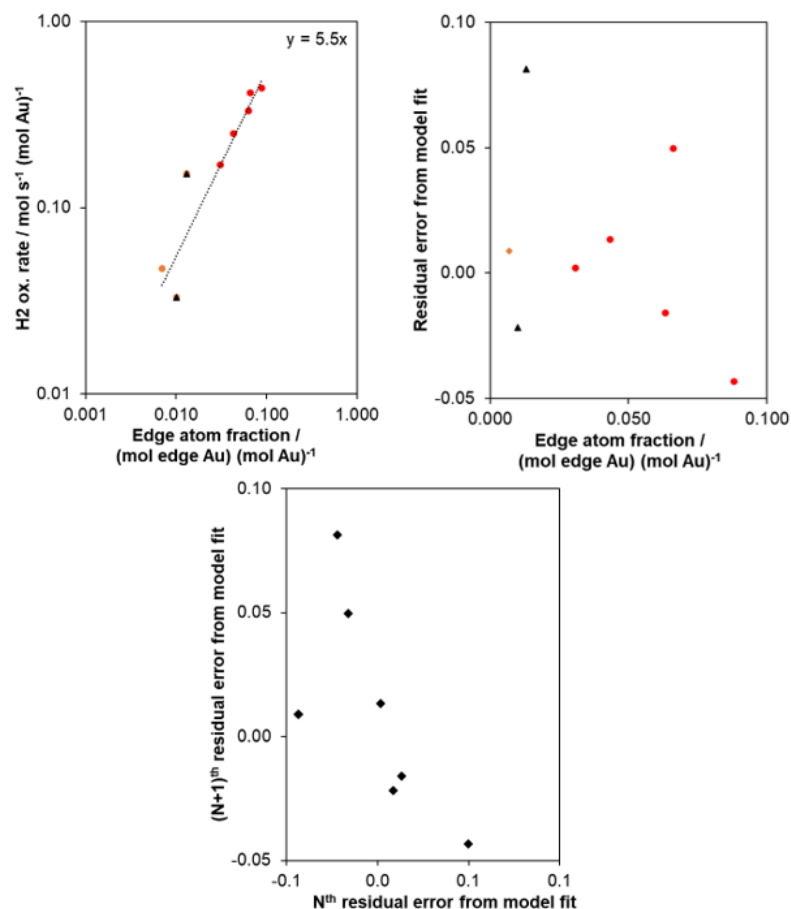


Figure 4.54. (Top left) Plot of hydrogen oxidation rate normalized to gold mass vs. edge atom fraction. The average turnover frequency required for this model is shown in the top right corner of the plot. (Top right) Residual error plot for the top left plot. (Bottom) Lag plot for the residual error plot. These plots contain data for the Au-PVP/TS-1 catalysts from this work (0.083Au-PVP/TS-1(126) (black triangles) and 0.11Au-PVP/TS-1(73) (orange diamond)) as well as Au-DP/TS-1(100) (red circles) catalysts from [39].

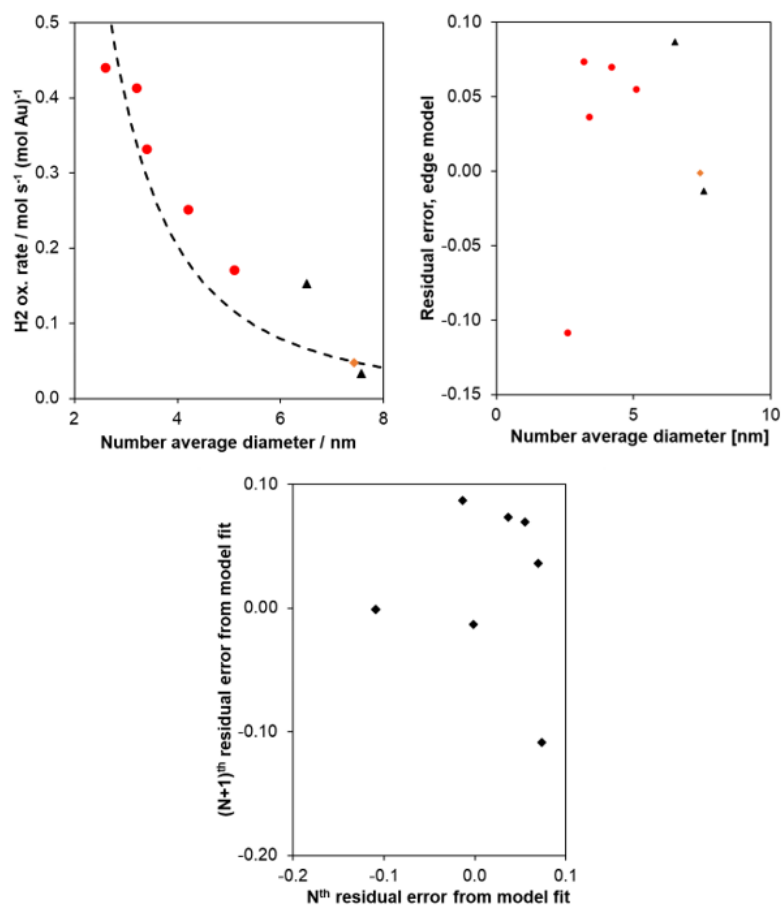


Figure 4.55. (Top left) Model fit for the edge model to hydrogen oxidation rate data as a function of average gold nanoparticle diameter. (Top right) Residual error plot for the model fit. (Bottom) Lag plot for the residual error plot. These plots contain data for the Au-PVP/TS-1 catalysts from this work (0.083Au-PVP/TS-1(126) (black triangles) and 0.11Au-PVP/TS-1(73) (orange diamond)) as well as Au-DP/TS-1(100) (red circles) catalysts from [39].

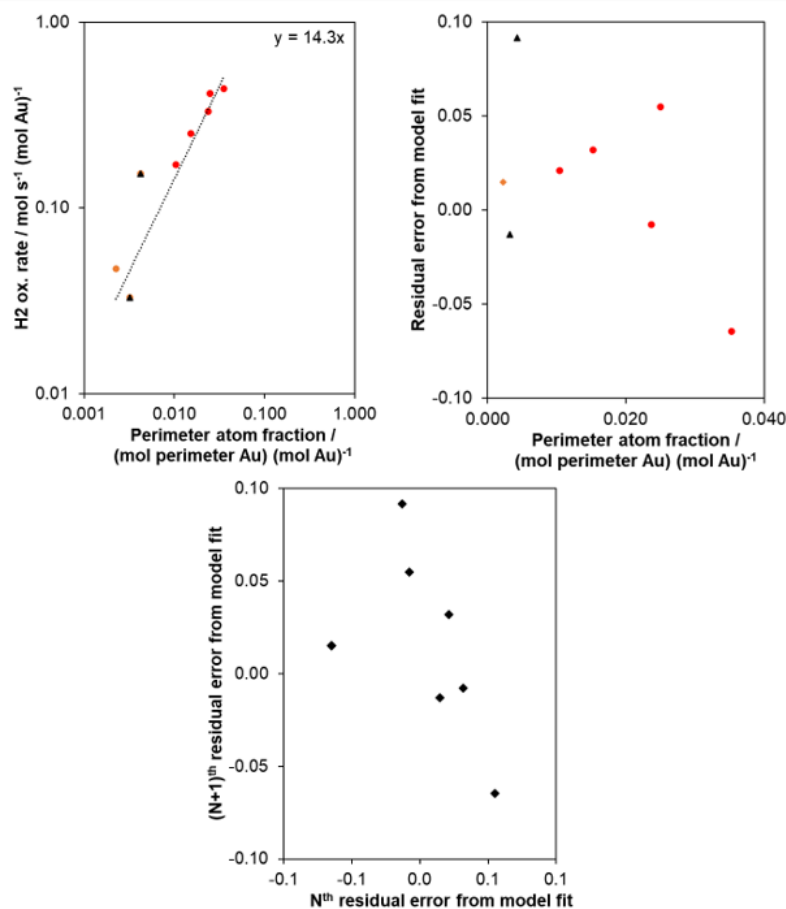


Figure 4.56. (Top left) Plot of hydrogen oxidation rate normalized to gold mass vs. perimeter atom fraction. The average turnover frequency required for this model is shown in the top right corner of the plot. (Top right) Residual error plot for the top left plot. (Bottom) Lag plot for the residual error plot. These plots contain data for the Au-PVP/TS-1 catalysts from this work (0.083Au-PVP/TS-1(126) (black triangles) and 0.11Au-PVP/TS-1(73) (orange diamond)) as well as Au-DP/TS-1(100) (red circles) catalysts from [39].

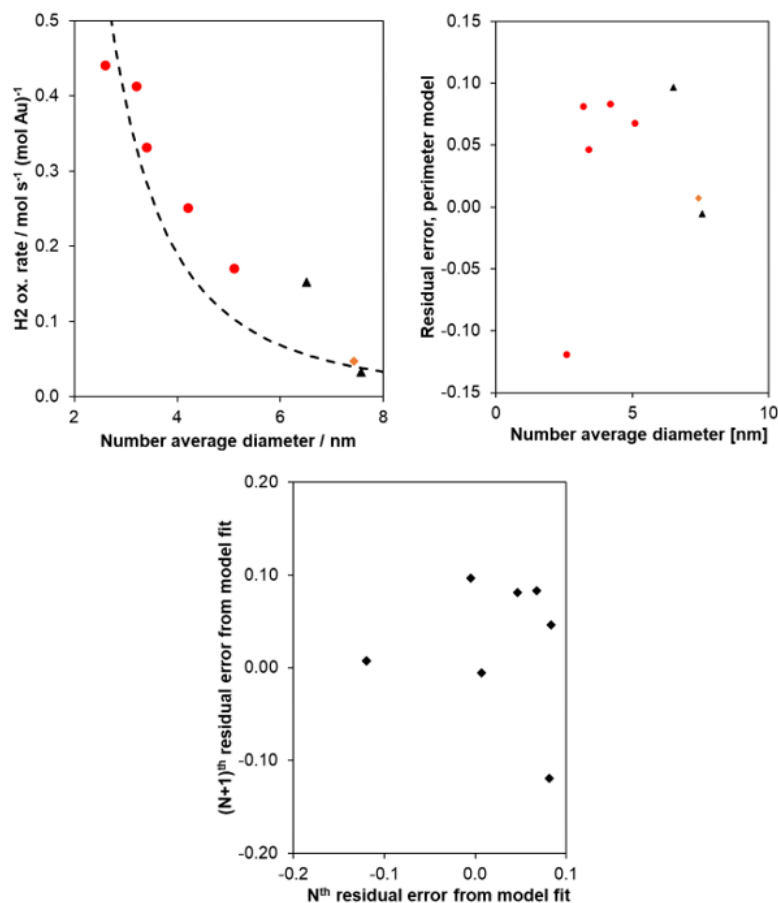


Figure 4.57. (Top left) Model fit for the perimeter model to hydrogen oxidation rate data as a function of average gold nanoparticle diameter. (Top right) Residual error plot for the model fit. (Bottom) Lag plot for the residual error plot. These plots contain data for the Au-PVP/TS-1 catalysts from this work (0.083Au-PVP/TS-1(126) (black triangles) and 0.11Au-PVP/TS-1(73) (orange diamond)) as well as Au-DP/TS-1(100) (red circles) catalysts from [39].

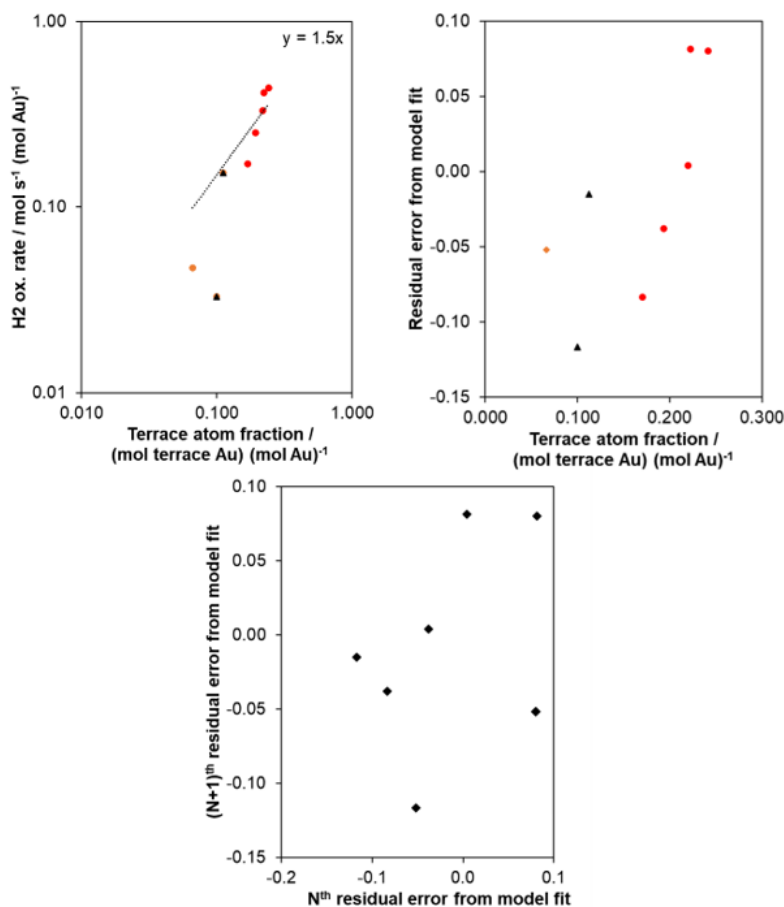


Figure 4.58. (Top left) Plot of hydrogen oxidation rate normalized to gold mass vs. terrace atom fraction. The average turnover frequency required for this model is shown in the top right corner of the plot. (Top right) Residual error plot for the top left plot. (Bottom) Lag plot for the residual error plot. These plots contain data for the Au-PVP/TS-1 catalysts from this work (0.083Au-PVP/TS-1(126) (black triangles) and 0.11Au-PVP/TS-1(73) (orange diamond)) as well as Au-DP/TS-1(100) (red circles) catalysts from [39].

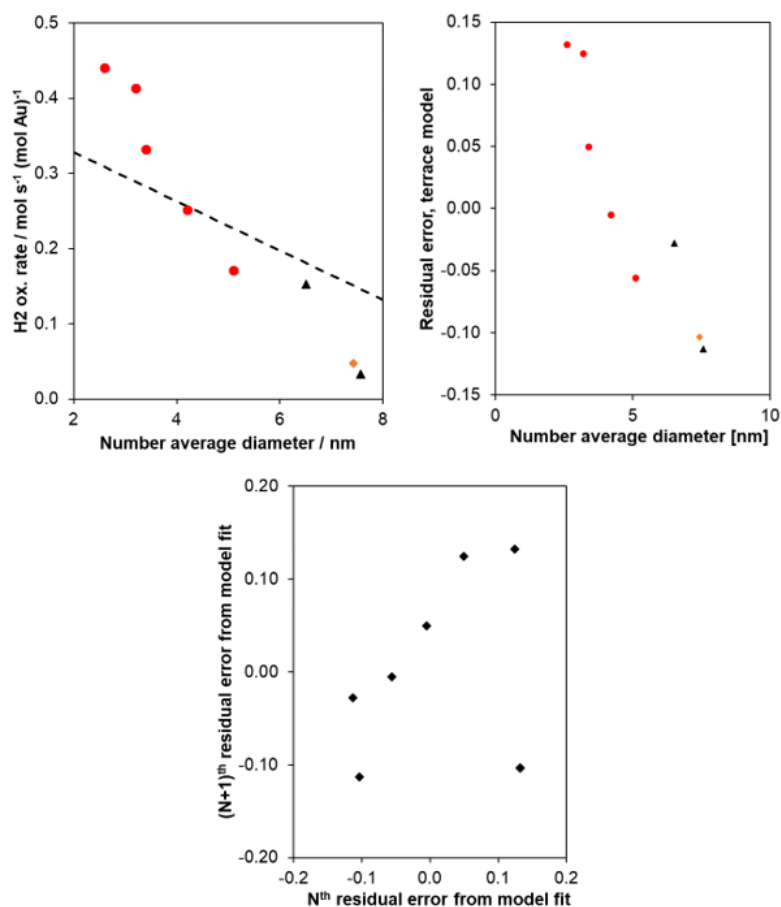


Figure 4.59. (Top left) Model fit for the terrace model to hydrogen oxidation rate data as a function of average gold nanoparticle diameter. (Top right) Residual error plot for the model fit. (Bottom) Lag plot for the residual error plot. These plots contain data for the Au-PVP/TS-1 catalysts from this work (0.083Au-PVP/TS-1(126) (black triangles) and 0.11Au-PVP/TS-1(73) (orange diamond)) as well as Au-DP/TS-1(100) (red circles) catalysts from [39].

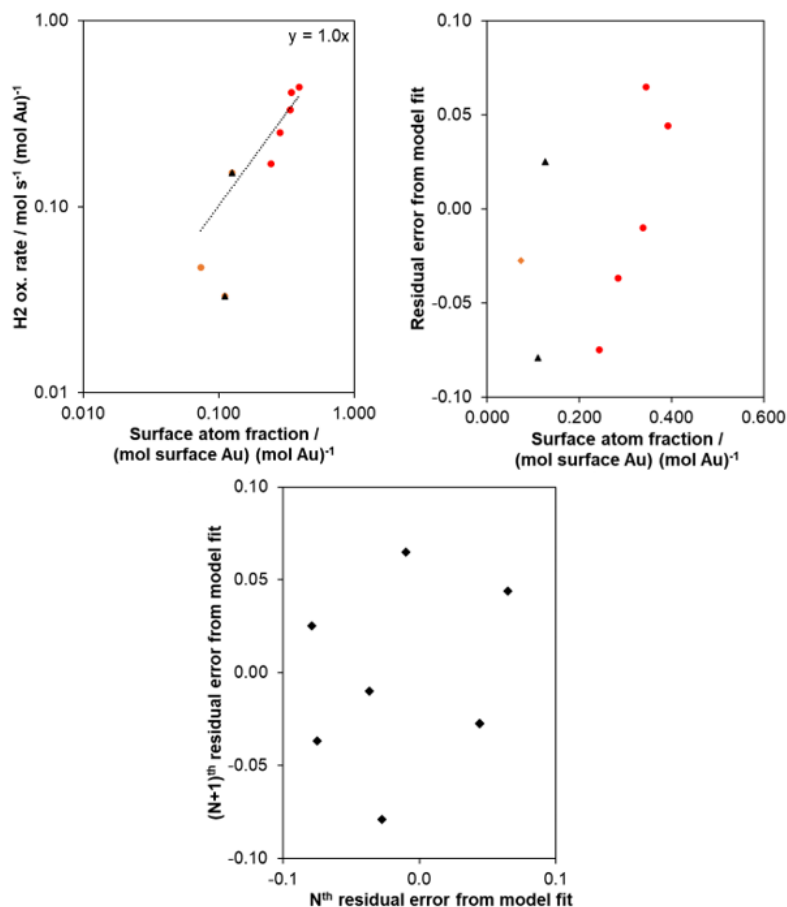


Figure 4.60. (Top left) Plot of hydrogen oxidation rate normalized to gold mass vs. surface atom fraction. The average turnover frequency required for this model is shown in the top right corner of the plot. (Top right) Residual error plot for the top left plot. (Bottom) Lag plot for the residual error plot. These plots contain data for the Au-PVP/TS-1 catalysts from this work (0.083Au-PVP/TS-1(126) (black triangles) and 0.11Au-PVP/TS-1(73) (orange diamond)) as well as Au-DP/TS-1(100) (red circles) catalysts from [39].

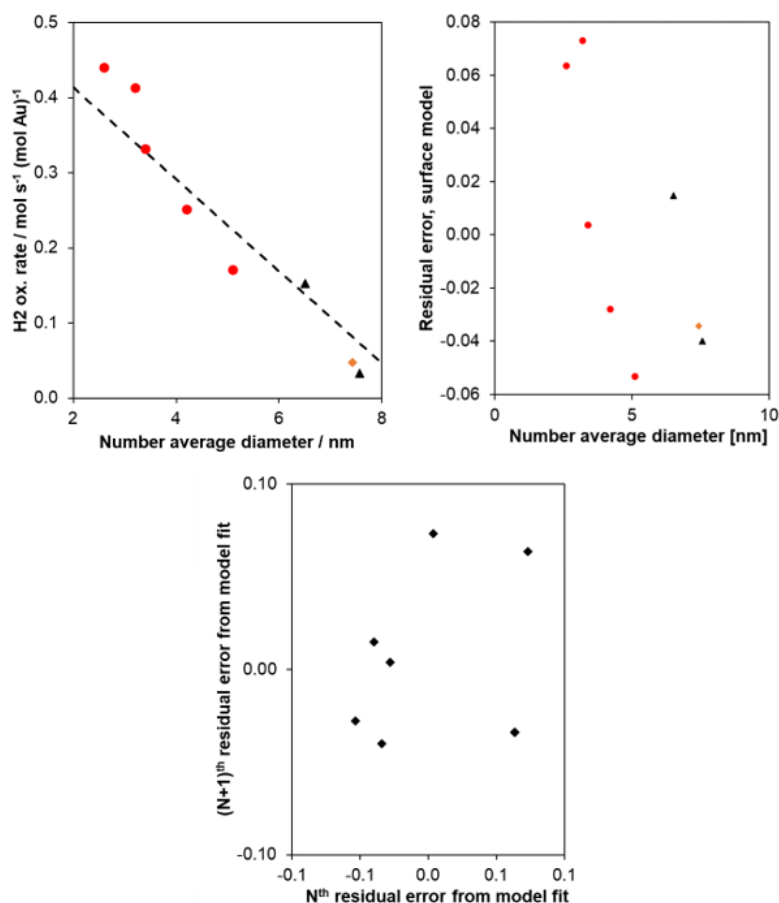


Figure 4.61. (Top left) Model fit for the surface model to hydrogen oxidation rate data as a function of average gold nanoparticle diameter. (Top right) Residual error plot for the model fit. (Bottom) Lag plot for the residual error plot. These plots contain data for the Au-PVP/TS-1 catalysts from this work (0.083Au-PVP/TS-1(126) (black triangles) and 0.11Au-PVP/TS-1(73) (orange diamond)) as well as Au-DP/TS-1(100) (red circles) catalysts from [39].

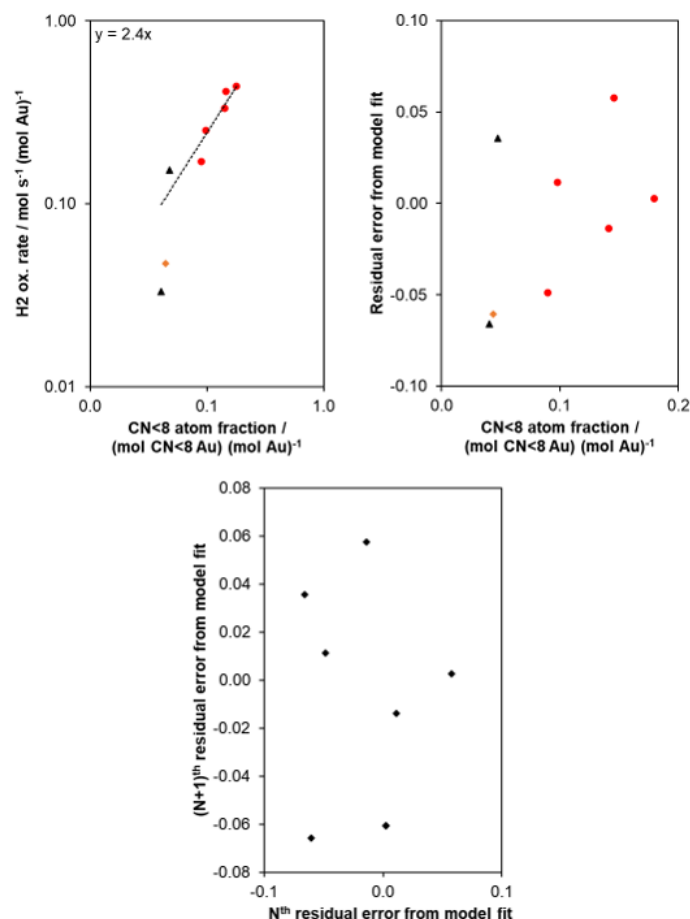


Figure 4.62. (Top left) Plot of hydrogen oxidation rate normalized to gold mass vs. CN<8 atom fraction for a spherical nanoparticle model [41]. The average turnover frequency required for this model is shown in the top right corner of the plot. (Top right) Residual error plot for the top left plot. (Bottom) Lag plot for the residual error plot. These plots contain data for the Au-PVP/TS-1 catalysts from this work (0.083Au-PVP/TS-1(126) (black triangles) and 0.11Au-PVP/TS-1(73) (orange diamonds)) as well as Au-DP/TS-1(100) (red circles) catalysts from [39].

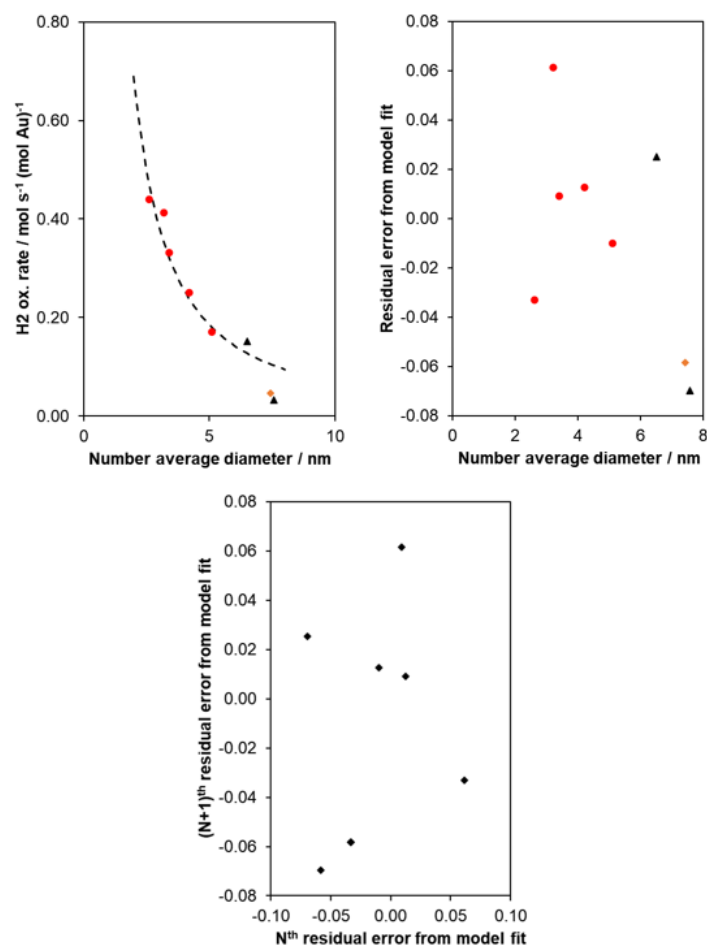


Figure 4.63. (Top left) Model fit for CN<8 atoms from a spherical nanoparticle model [41] to hydrogen oxidation rate data as a function of average gold nanoparticle diameter. (Top right) Residual error plot for the model fit. (Bottom) Lag plot for the residual error plot. These plots contain data for the Au-PVP/TS-1 catalysts from this work (0.083Au-PVP/TS-1(126) (black triangles) and 0.11Au-PVP/TS-1(73) (orange diamond)) as well as Au-DP/TS-1(100) (red circles) catalysts from [39].

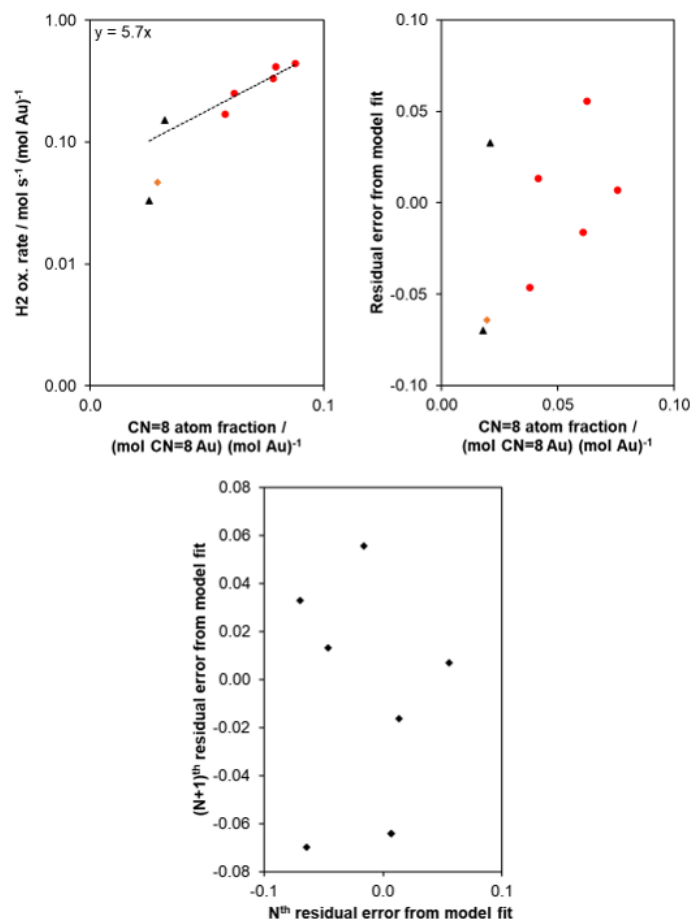


Figure 4.64. (Top left) Plot of hydrogen oxidation rate normalized to gold mass vs. CN=8 atom fraction for a spherical nanoparticle model [41]. The average turnover frequency required for this model is shown in the top right corner of the plot. (Top right) Residual error plot for the top left plot. (Bottom) Lag plot for the residual error plot. These plots contain data for the Au-PVP/TS-1 catalysts from this work (0.083Au-PVP/TS-1(126) (black triangles) and 0.11Au-PVP/TS-1(73) (orange diamonds)) as well as Au-DP/TS-1(100) (red circles) catalysts from [39].

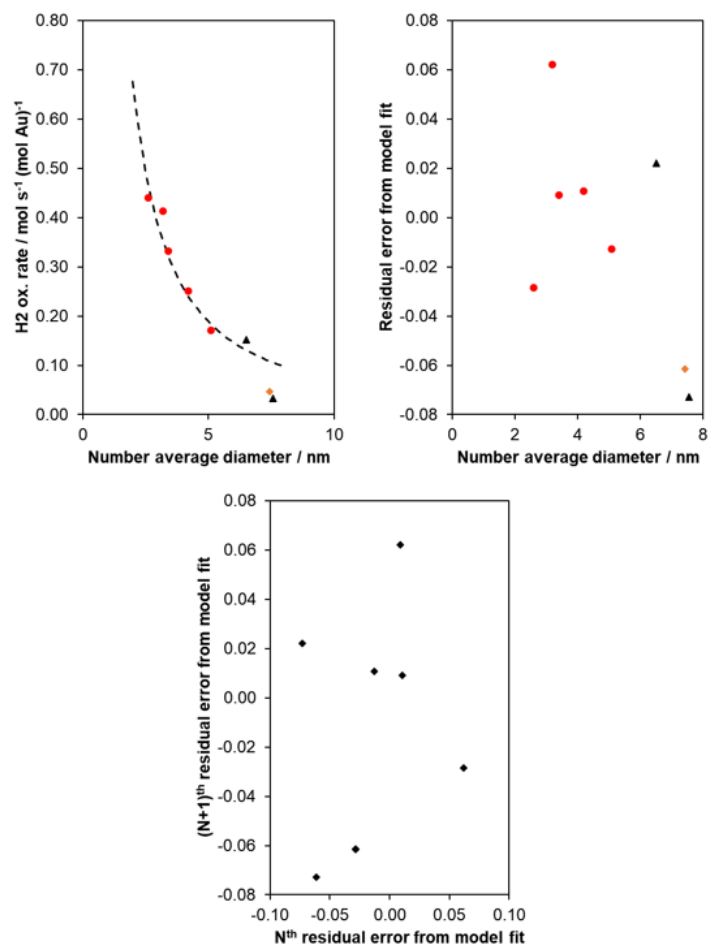


Figure 4.65. (Top left) Model fit for CN=8 atoms from a spherical nanoparticle model [41] to hydrogen oxidation rate data as a function of average gold nanoparticle diameter. (Top right) Residual error plot for the model fit. (Bottom) Lag plot for the residual error plot. These plots contain data for the Au-PVP/TS-1 catalysts from this work (0.083Au-PVP/TS-1(126) (black triangles) and 0.11Au-PVP/TS-1(73) (orange diamond)) as well as Au-DP/TS-1(100) (red circles) catalysts from [39].

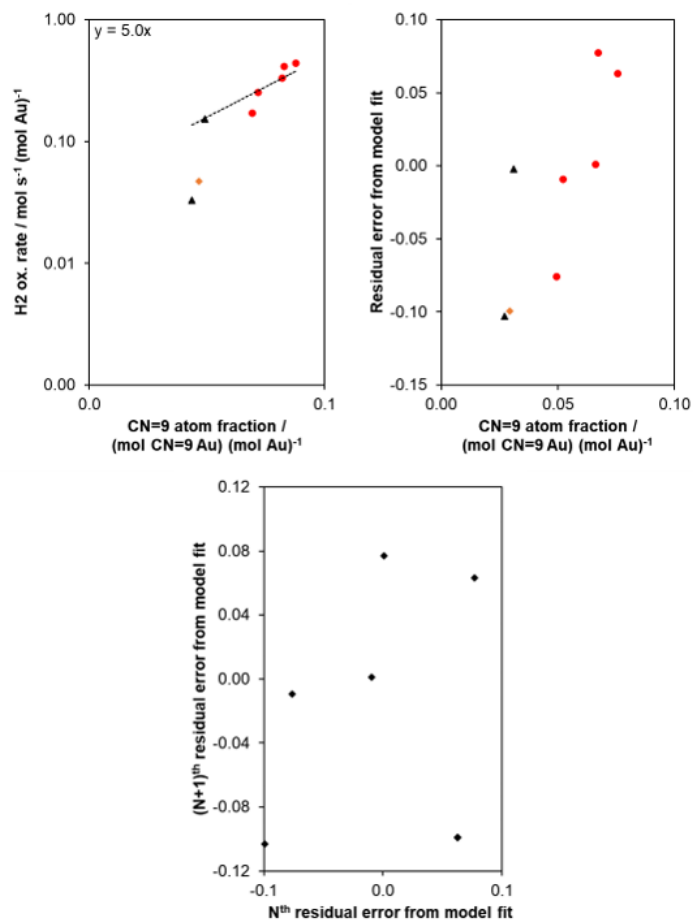


Figure 4.66. (Top left) Plot of hydrogen oxidation rate normalized to gold mass vs. CN=9 atom fraction for a spherical nanoparticle model [41]. The average turnover frequency required for this model is shown in the top right corner of the plot. (Top right) Residual error plot for the top left plot. (Bottom) Lag plot for the residual error plot. These plots contain data for the Au-PVP/TS-1 catalysts from this work (0.083Au-PVP/TS-1(126) (black triangles) and 0.11Au-PVP/TS-1(73) (orange diamond)) as well as Au-DP/TS-1(100) (red circles) catalysts from [39].

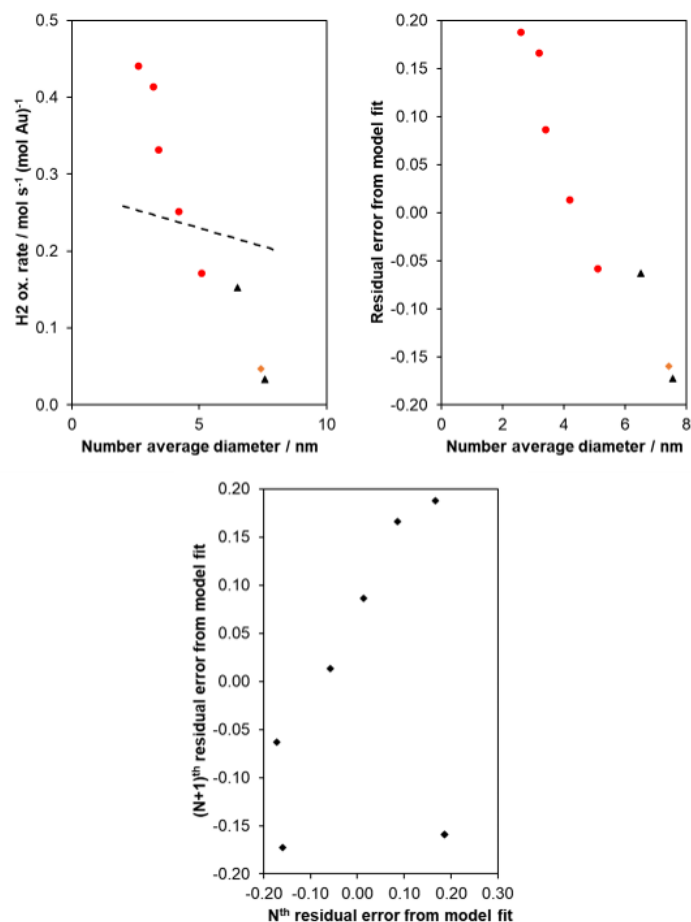


Figure 4.67. (Top left) Model fit for CN=9 atoms from a spherical nanoparticle model [41] to hydrogen oxidation rate data as a function of average gold nanoparticle diameter. (Top right) Residual error plot for the model fit. (Bottom) Lag plot for the residual error plot. These plots contain data for the Au-PVP/TS-1 catalysts from this work (0.083Au-PVP/TS-1(126) (black triangles) and 0.11Au-PVP/TS-1(73) (orange diamonds)) as well as Au-DP/TS-1(100) (red circles) catalysts from [39].

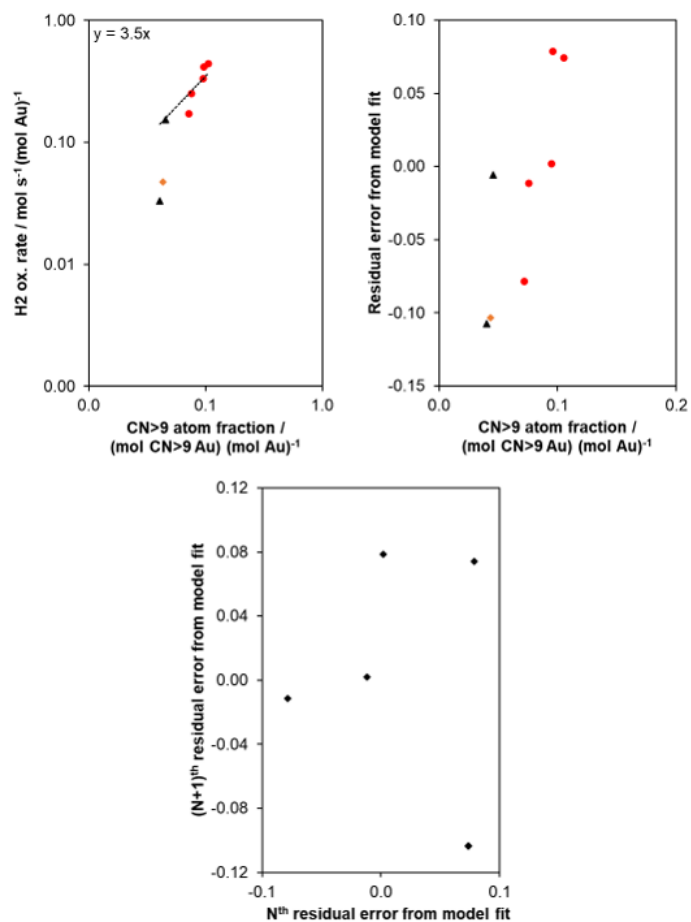


Figure 4.68. (Top left) Plot of hydrogen oxidation rate normalized to gold mass vs. CN>9 atom fraction for a spherical nanoparticle model [41]. The average turnover frequency required for this model is shown in the top right corner of the plot. (Top right) Residual error plot for the top left plot. (Bottom) Lag plot for the residual error plot. These plots contain data for the Au-PVP/TS-1 catalysts from this work (0.083Au-PVP/TS-1(126) (black triangles) and 0.11Au-PVP/TS-1(73) (orange diamonds)) as well as Au-DP/TS-1(100) (red circles) catalysts from [39].

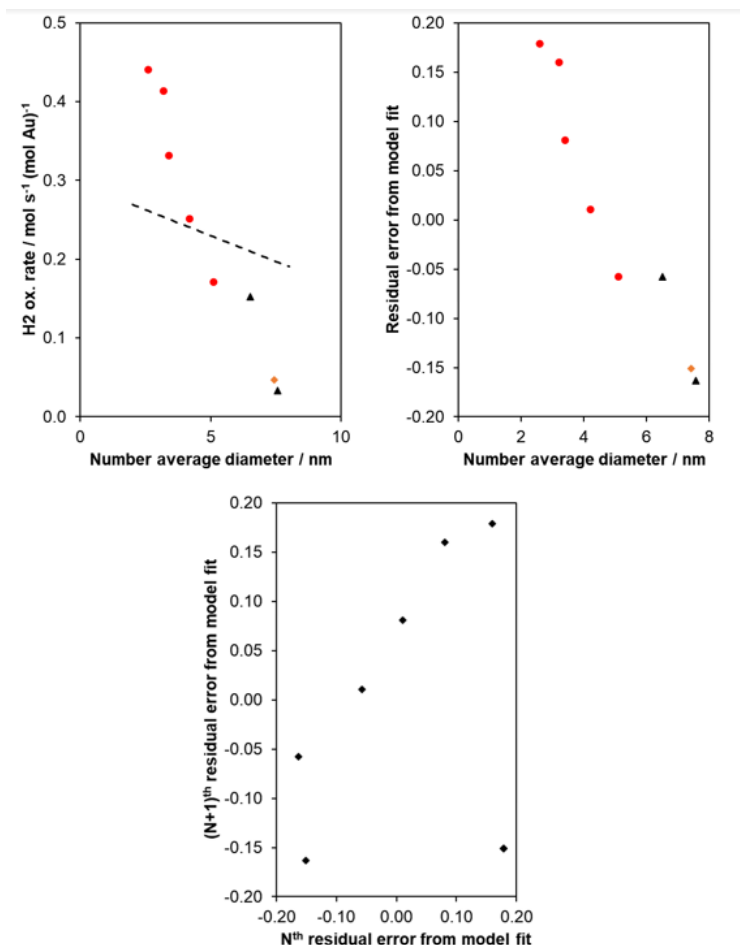


Figure 4.69. (Top left) Model fit for CN>9 atoms from a spherical nanoparticle model [41] to hydrogen oxidation rate data as a function of average gold nanoparticle diameter. (Top right) Residual error plot for the model fit. (Bottom) Lag plot for the residual error plot. These plots contain data for the Au-PVP/TS-1 catalysts from this work (0.083Au-PVP/TS-1(126) (black triangles) and 0.11Au-PVP/TS-1(73) (orange diamond)) as well as Au-DP/TS-1(100) (red circles) catalysts from [39].

References

- [1] H. Baer, M. Bergamo, A. Forlin, L. H. Pottenger, and J. Lindner, "Propylene oxide," in *Ullmann's Encyclopedia of Industrial Chemistry*, John Wiley & Sons, Ltd, 2012, ISBN: 978-3-527-30673-2. DOI: [10.1002/14356007.a22_239.pub3](https://doi.org/10.1002/14356007.a22_239.pub3). [Online]. Available: https://onlinelibrary.wiley.com/doi/abs/10.1002/14356007.a22_239.pub3.
- [2] T. A. Nijhuis, M. Makkee, J. A. Moulijn, and B. M. Weckhuysen, "The production of propene oxide: catalytic processes and recent developments," *Ind. Eng. Chem. Res.*, vol. 45, no. 10, pp. 3447–3459, May 1, 2006, ISSN: 0888-5885. DOI: [10.1021/ie0513090](https://doi.org/10.1021/ie0513090). [Online]. Available: <http://dx.doi.org/10.1021/ie0513090>.
- [3] J. Lu, X. Zhang, J. J. Bravo-Suárez, T. Fujitani, and S. T. Oyama, "Effect of composition and promoters in au/TS-1 catalysts for direct propylene epoxidation using h₂ and o₂," *Catalysis Today*, Special Issue dedicated to Marc Jacques Ledoux on the occasion of his 60th birthday, vol. 147, no. 3, pp. 186–195, Oct. 15, 2009, ISSN: 0920-5861. DOI: [10.1016/j.cattod.2008.09.005](https://doi.org/10.1016/j.cattod.2008.09.005). [Online]. Available: <http://www.sciencedirect.com/science/article/pii/S0920586108004239>.
- [4] M. Haruta, B. S. Uphade, S. Tsubota, and A. Miyamoto, "Selective oxidation of propylene over gold deposited on titanium-based oxides," *Res. Chem. Intermed.*, vol. 24, no. 3, pp. 329–336, Mar. 1, 1998, ISSN: 0922-6168, 1568-5675. DOI: [10.1163/156856798X00276](https://doi.org/10.1163/156856798X00276). [Online]. Available: <https://link.springer.com/article/10.1163/156856798X00276>.
- [5] J. J. Bravo-Suárez, Lu, C. G. Dallos, T. Fujitani, and S. T. Oyama, "Kinetic study of propylene epoxidation with h₂ and o₂ over a gold/mesoporous titanasilicate catalyst," *J. Phys. Chem. C*, vol. 111, no. 46, pp. 17 427–17 436, Nov. 1, 2007, ISSN: 1932-7447. DOI: [10.1021/jp075098j](https://doi.org/10.1021/jp075098j). [Online]. Available: <http://dx.doi.org/10.1021/jp075098j>.
- [6] A. K. Sinha, S. Seelan, M. Okumura, T. Akita, S. Tsubota, and M. Haruta, "Three-dimensional mesoporous titanasilicates prepared by modified sol–gel method: ideal gold catalyst supports for enhanced propene epoxidation," *J. Phys. Chem. B*, vol. 109, no. 9, pp. 3956–3965, Mar. 1, 2005, ISSN: 1520-6106. DOI: [10.1021/jp0465229](https://doi.org/10.1021/jp0465229). [Online]. Available: <http://dx.doi.org/10.1021/jp0465229>.
- [7] B. S. Uphade, T. Akita, T. Nakamura, and M. Haruta, "Vapor-phase epoxidation of propene using h₂ and o₂ over au/ti-MCM-48," *Journal of Catalysis*, vol. 209, no. 2, pp. 331–340, Jul. 25, 2002, ISSN: 0021-9517. DOI: [10.1006/jcat.2002.3642](https://doi.org/10.1006/jcat.2002.3642). [Online]. Available: <http://www.sciencedirect.com/science/article/pii/S0021951702936420>.
- [8] B. S. Uphade, Y. Yamada, T. Akita, T. Nakamura, and M. Haruta, "Synthesis and characterization of ti-MCM-41 and vapor-phase epoxidation of propylene using h₂ and o₂ over au/ti-MCM-41," *Applied Catalysis A: General*, vol. 215, no. 1, pp. 137–148, Jul. 13, 2001, ISSN: 0926-860X. DOI: [10.1016/S0926-860X\(01\)00527-0](https://doi.org/10.1016/S0926-860X(01)00527-0). [Online]. Available: <http://www.sciencedirect.com/science/article/pii/S0926860X01005270>.

- [9] J. Lu, X. Zhang, J. J. Bravo-Suárez, K. K. Bando, T. Fujitani, and S. T. Oyama, “Direct propylene epoxidation over barium-promoted au/ti-TUD catalysts with h₂ and o₂: Effect of au particle size,” *Journal of Catalysis*, vol. 250, no. 2, pp. 350–359, Sep. 10, 2007, ISSN: 0021-9517. DOI: [10.1016/j.jcat.2007.06.006](https://doi.org/10.1016/j.jcat.2007.06.006). [Online]. Available: <http://www.sciencedirect.com/science/article/pii/S0021951707002345>.
- [10] T. Hayashi, K. Tanaka, and M. Haruta, “Selective vapor-phase epoxidation of propylene over au/TiO₂ catalysts in the presence of oxygen and hydrogen,” *Journal of Catalysis*, vol. 178, no. 2, pp. 566–575, Sep. 10, 1998, ISSN: 0021-9517. DOI: [10.1006/jcat.1998.2157](https://doi.org/10.1006/jcat.1998.2157). [Online]. Available: <http://www.sciencedirect.com/science/article/pii/S0021951798921571>.
- [11] C. Qi, J. Huang, S. Bao, H. Su, T. Akita, and M. Haruta, “Switching of reactions between hydrogenation and epoxidation of propene over au/ti-based oxides in the presence of h₂ and o₂,” *Journal of Catalysis*, vol. 281, no. 1, pp. 12–20, Jul. 1, 2011, ISSN: 0021-9517. DOI: [10.1016/j.jcat.2011.03.028](https://doi.org/10.1016/j.jcat.2011.03.028). [Online]. Available: <http://www.sciencedirect.com/science/article/pii/S0021951711001114>.
- [12] J. Huang, T. Takei, T. Akita, H. Ohashi, and M. Haruta, “Gold clusters supported on alkaline treated TS-1 for highly efficient propene epoxidation with o₂ and h₂,” *Applied Catalysis B: Environmental*, vol. 95, no. 3, pp. 430–438, Apr. 6, 2010, ISSN: 0926-3373. DOI: [10.1016/j.apcatb.2010.01.023](https://doi.org/10.1016/j.apcatb.2010.01.023). [Online]. Available: <http://www.sciencedirect.com/science/article/pii/S0926337310000378>.
- [13] W.-S. Lee, M. Cem Akatay, E. A. Stach, F. H. Ribeiro, and W. Nicholas Delgass, “Enhanced reaction rate for gas-phase epoxidation of propylene using h₂ and o₂ by cs promotion of au/TS-1,” *Journal of Catalysis*, 50th Anniversary Special Issue, vol. 308, pp. 98–113, Dec. 2013, ISSN: 0021-9517. DOI: [10.1016/j.jcat.2013.05.023](https://doi.org/10.1016/j.jcat.2013.05.023). [Online]. Available: <http://www.sciencedirect.com/science/article/pii/S0021951713001966>.
- [14] L. Barrio, P. Liu, J. A. Rodriguez, J. M. Campos-Martin, and J. L. G. Fierro, “Effects of hydrogen on the reactivity of o₂ toward gold nanoparticles and surfaces,” *J. Phys. Chem. C*, vol. 111, no. 51, pp. 19 001–19 008, Dec. 1, 2007, ISSN: 1932-7447. DOI: [10.1021/jp073552d](https://doi.org/10.1021/jp073552d). [Online]. Available: <https://doi.org/10.1021/jp073552d>.
- [15] S. M. Lang, T. M. Bernhardt, R. N. Barnett, B. Yoon, and U. Landman, “Hydrogen-promoted oxygen activation by free gold cluster cations,” *J. Am. Chem. Soc.*, vol. 131, no. 25, pp. 8939–8951, Jul. 1, 2009, ISSN: 0002-7863. DOI: [10.1021/ja9022368](https://doi.org/10.1021/ja9022368). [Online]. Available: <https://doi.org/10.1021/ja9022368>.
- [16] D. G. Barton and S. G. Podkolzin, “Kinetic study of a direct water synthesis over silica-supported gold nanoparticles,” *J. Phys. Chem. B*, vol. 109, no. 6, pp. 2262–2274, Feb. 1, 2005, ISSN: 1520-6106. DOI: [10.1021/jp048837u](https://doi.org/10.1021/jp048837u). [Online]. Available: <http://dx.doi.org/10.1021/jp048837u>.
- [17] W.-S. Lee, M. Cem Akatay, E. A. Stach, F. H. Ribeiro, and W. Nicholas Delgass, “Reproducible preparation of au/TS-1 with high reaction rate for gas phase epoxidation of propylene,” *Journal of Catalysis*, vol. 287, pp. 178–189, Mar. 2012, ISSN: 0021-9517. DOI: [10.1016/j.jcat.2011.12.019](https://doi.org/10.1016/j.jcat.2011.12.019). [Online]. Available: <http://www.sciencedirect.com/science/article/pii/S0021951711004222>.

- [18] W.-S. Lee, L.-C. Lai, M. Cem Akatay, E. A. Stach, F. H. Ribeiro, and W. N. Delgass, "Probing the gold active sites in au/TS-1 for gas-phase epoxidation of propylene in the presence of hydrogen and oxygen," *Journal of Catalysis*, vol. 296, pp. 31–42, Dec. 2012, ISSN: 0021-9517. DOI: [10.1016/j.jcat.2012.08.021](https://doi.org/10.1016/j.jcat.2012.08.021). [Online]. Available: <http://www.sciencedirect.com/science/article/pii/S0021951712002783>.
- [19] B. Taylor, J. Lauterbach, G. E. Blau, and W. N. Delgass, "Reaction kinetic analysis of the gas-phase epoxidation of propylene over au/TS-1," *Journal of Catalysis*, vol. 242, no. 1, pp. 142–152, Aug. 15, 2006, ISSN: 0021-9517. DOI: [10.1016/j.jcat.2006.06.007](https://doi.org/10.1016/j.jcat.2006.06.007). [Online]. Available: <http://www.sciencedirect.com/science/article/pii/S002195170600203X>.
- [20] J. W. Harris, J. Arvay, G. Mitchell, W. N. Delgass, and F. H. Ribeiro, "Propylene oxide inhibits propylene epoxidation over au/TS-1," *Journal of Catalysis*, vol. 365, pp. 105–114, Sep. 1, 2018, ISSN: 0021-9517. DOI: [10.1016/j.jcat.2018.06.015](https://doi.org/10.1016/j.jcat.2018.06.015). [Online]. Available: <http://www.sciencedirect.com/science/article/pii/S0021951718302379>.
- [21] R. B. Khomane, B. D. Kulkarni, A. Paraskar, and S. R. Sainkar, "Synthesis, characterization and catalytic performance of titanium silicalite-1 prepared in micellar media," *Materials Chemistry and Physics*, vol. 76, no. 1, pp. 99–103, Jul. 28, 2002, ISSN: 0254-0584. DOI: [10.1016/S0254-0584\(01\)00507-7](https://doi.org/10.1016/S0254-0584(01)00507-7). [Online]. Available: <http://www.sciencedirect.com/science/article/pii/S0254058401005077>.
- [22] H. Tsunoyama, H. Sakurai, Y. Negishi, and T. Tsukuda, "Size-specific catalytic activity of polymer-stabilized gold nanoclusters for aerobic alcohol oxidation in water," *J. Am. Chem. Soc.*, vol. 127, no. 26, pp. 9374–9375, Jul. 1, 2005, ISSN: 0002-7863. DOI: [10.1021/ja052161e](https://doi.org/10.1021/ja052161e). [Online]. Available: <https://doi.org/10.1021/ja052161e>.
- [23] H. Tsunoyama, H. Sakurai, N. Ichikuni, Y. Negishi, and T. Tsukuda, "Colloidal gold nanoparticles as catalyst for carbon–carbon bond formation: application to aerobic homo-coupling of phenylboronic acid in water," *Langmuir*, vol. 20, no. 26, pp. 11 293–11 296, Dec. 1, 2004, ISSN: 0743-7463. DOI: [10.1021/la0478189](https://doi.org/10.1021/la0478189). [Online]. Available: <https://doi.org/10.1021/la0478189>.
- [24] J. Tauc, "Optical properties and electronic structure of amorphous ge and si," *Materials Research Bulletin*, vol. 3, no. 1, pp. 37–46, Jan. 1, 1968, ISSN: 0025-5408. DOI: [10.1016/0025-5408\(68\)90023-8](https://doi.org/10.1016/0025-5408(68)90023-8). [Online]. Available: <http://www.sciencedirect.com/science/article/pii/0025540868900238>.
- [25] J. Tauc, R. Grigorovici, and A. Vancu, "Optical properties and electronic structure of amorphous germanium," *physica status solidi (b)*, vol. 15, no. 2, pp. 627–637, 1966, ISSN: 1521-3951. DOI: [10.1002/pssb.19660150224](https://doi.org/10.1002/pssb.19660150224). [Online]. Available: <https://onlinelibrary.wiley.com/doi/abs/10.1002/pssb.19660150224>.
- [26] E. A. Davis and N. F. Mott, "Conduction in non-crystalline systems v. conductivity, optical absorption and photoconductivity in amorphous semiconductors," *The Philosophical Magazine: A Journal of Theoretical Experimental and Applied Physics*, vol. 22, no. 179, pp. 0903–0922, Nov. 1, 1970, ISSN: 0031-8086. DOI: [10.1080/14786437008221061](https://doi.org/10.1080/14786437008221061). [Online]. Available: <https://doi.org/10.1080/14786437008221061>.

- [27] Y. Jiao, A.-L. Adedigba, N. F. Dummer, J. Liu, Y. Zhou, Y. Guan, H. Shen, M. Perdjon, and G. J. Hutchings, “The effect of t-atom ratio and TPAOH concentration on the pore structure and titanium position in MFI-type titanosilicate during dissolution-recrystallization process,” *Microporous and Mesoporous Materials*, vol. 305, p. 110 397, Oct. 1, 2020, ISSN: 1387-1811. DOI: [10.1016/j.micromeso.2020.110397](https://doi.org/10.1016/j.micromeso.2020.110397). [Online]. Available: <https://www.sciencedirect.com/science/article/pii/S1387181120304005>.
- [28] X. Feng, Z. Song, Y. Liu, X. Chen, X. Jin, W. Yan, C. Yang, J. Luo, X. Zhou, and D. Chen, “Manipulating gold spatial location on titanium silicalite-1 to enhance the catalytic performance for direct propene epoxidation with h₂ and o₂,” *ACS Catal.*, vol. 8, no. 11, pp. 10 649–10 657, Nov. 2, 2018. DOI: [10.1021/acscatal.8b02836](https://doi.org/10.1021/acscatal.8b02836). [Online]. Available: <https://doi.org/10.1021/acscatal.8b02836>.
- [29] R. Gounder and M. E. Davis, “Titanium-beta zeolites catalyze the stereospecific isomerization of d-glucose to l-sorbose via intramolecular c5–c1 hydride shift,” *ACS Catal.*, vol. 3, no. 7, pp. 1469–1476, Jul. 5, 2013. DOI: [10.1021/cs400273c](https://doi.org/10.1021/cs400273c). [Online]. Available: <https://doi.org/10.1021/cs400273c>.
- [30] X. Xue, W. Ji, Z. Mao, H. Mao, Y. Wang, X. Wang, W. Ruan, B. Zhao, and J. R. Lombardi, “Raman investigation of nanosized TiO₂: Effect of crystallite size and quantum confinement,” *J. Phys. Chem. C*, vol. 116, no. 15, pp. 8792–8797, Apr. 19, 2012, ISSN: 1932-7447. DOI: [10.1021/jp2122196](https://doi.org/10.1021/jp2122196). [Online]. Available: <https://doi.org/10.1021/jp2122196>.
- [31] M. Behrens and R. Schlögl, “X-ray diffraction and small angle x-ray scattering,” in *Characterization of Solid Materials and Heterogeneous Catalysts*, John Wiley & Sons, Ltd, 2012, pp. 609–653, ISBN: 978-3-527-64532-9. DOI: [10.1002/9783527645329.ch15](https://doi.org/10.1002/9783527645329.ch15). [Online]. Available: <https://onlinelibrary.wiley.com/doi/abs/10.1002/9783527645329.ch15>.
- [32] H. Zhang and J. F. Banfield, “Understanding polymorphic phase transformation behavior during growth of nanocrystalline aggregates: insights from TiO₂,” *J. Phys. Chem. B*, vol. 104, no. 15, pp. 3481–3487, Apr. 1, 2000, ISSN: 1520-6106. DOI: [10.1021/jp000499j](https://doi.org/10.1021/jp000499j). [Online]. Available: <http://dx.doi.org/10.1021/jp000499j>.
- [33] Z. Wang, X. Liu, M. Lv, P. Chai, Y. Liu, and J. Meng, “Preparation of ferrite MFe₂O₄ (m = co, ni) ribbons with nanoporous structure and their magnetic properties,” *J. Phys. Chem. B*, vol. 112, no. 36, pp. 11 292–11 297, Sep. 11, 2008, ISSN: 1520-6106. DOI: [10.1021/jp804178w](https://doi.org/10.1021/jp804178w). [Online]. Available: <https://doi.org/10.1021/jp804178w>.
- [34] J. Lu, X. Zhang, J. J. Bravo-Suárez, S. Tsubota, J. Gaudet, and S. T. Oyama, “Kinetics of propylene epoxidation using h₂ and o₂ over a gold/mesoporous titanosilicate catalyst,” *Catalysis Today*, M. Albert Vannice Festschrift, vol. 123, no. 1, pp. 189–197, May 30, 2007, ISSN: 0920-5861. DOI: [10.1016/j.cattod.2007.02.005](https://doi.org/10.1016/j.cattod.2007.02.005). [Online]. Available: <http://www.sciencedirect.com/science/article/pii/S0920586107001009>.
- [35] P. T. Tsilingiris, “Thermophysical and transport properties of humid air at temperature range between 0 and 100°C,” *Energy Conversion and Management*, vol. 49, no. 5, pp. 1098–1110, May 1, 2008, ISSN: 0196-8904. DOI: [10.1016/j.enconman.2007.09.015](https://doi.org/10.1016/j.enconman.2007.09.015). [Online]. Available: <https://www.sciencedirect.com/science/article/pii/S0196890407003329>.
- [36] N. V. Kul’kova and L. P. Levchenko, *Kinet. Katal.*, vol. 6, p. 765, 1965.

- [37] K.-H. Choi, B.-Y. Coh, and H.-I. Lee, “Properties of adsorbed oxygen on au/SiO₂,” *Catalysis Today*, vol. 44, no. 1, pp. 205–213, Sep. 30, 1998, ISSN: 0920-5861. DOI: [10.1016/S0920-5861\(98\)00192-8](https://doi.org/10.1016/S0920-5861(98)00192-8). [Online]. Available: <https://www.sciencedirect.com/science/article/pii/S0920586198001928>.
- [38] R. Van Hardeveld and F. Hartog, “The statistics of surface atoms and surface sites on metal crystals,” *Surface Science*, vol. 15, no. 2, pp. 189–230, Jun. 1, 1969, ISSN: 0039-6028. DOI: [10.1016/0039-6028\(69\)90148-4](https://doi.org/10.1016/0039-6028(69)90148-4). [Online]. Available: <http://www.sciencedirect.com/science/article/pii/0039602869901484>.
- [39] X. Feng, X. Duan, G. Qian, X. Zhou, D. Chen, and W. Yuan, “Insights into size-dependent activity and active sites of au nanoparticles supported on TS-1 for propene epoxidation with h₂ and o₂,” *Journal of Catalysis*, vol. 317, pp. 99–104, Aug. 2014, ISSN: 0021-9517. DOI: [10.1016/j.jcat.2014.05.006](https://doi.org/10.1016/j.jcat.2014.05.006). [Online]. Available: <http://www.sciencedirect.com/science/article/pii/S0021951714001274>.
- [40] W. D. Williams, M. Shekhar, W.-S. Lee, V. Kispersky, W. N. Delgass, F. H. Ribeiro, S. M. Kim, E. A. Stach, J. T. Miller, and L. F. Allard, “Metallic corner atoms in gold clusters supported on rutile are the dominant active site during water–gas shift catalysis,” *J. Am. Chem. Soc.*, vol. 132, no. 40, pp. 14 018–14 020, Oct. 13, 2010, ISSN: 0002-7863. DOI: [10.1021/ja1064262](https://doi.org/10.1021/ja1064262). [Online]. Available: <http://dx.doi.org/10.1021/ja1064262>.
- [41] R. Reske, H. Mistry, F. Behafarid, B. Roldan Cuenya, and P. Strasser, “Particle size effects in the catalytic electroreduction of CO₂ on cu nanoparticles,” *J. Am. Chem. Soc.*, vol. 136, no. 19, pp. 6978–6986, May 14, 2014, ISSN: 0002-7863. DOI: [10.1021/ja500328k](https://doi.org/10.1021/ja500328k). [Online]. Available: <https://doi.org/10.1021/ja500328k>.
- [42] S. T. Oyama, X. Zhang, J. Lu, Y. Gu, and T. Fujitani, “Epoxidation of propylene with h₂ and o₂ in the explosive regime in a packed-bed catalytic membrane reactor,” *Journal of Catalysis*, vol. 257, no. 1, pp. 1–4, Jul. 1, 2008, ISSN: 0021-9517. DOI: [10.1016/j.jcat.2008.04.023](https://doi.org/10.1016/j.jcat.2008.04.023). [Online]. Available: <http://www.sciencedirect.com/science/article/pii/S0021951708001681>.
- [43] G. Djéga-Mariadassou, *Kinetics of Heterogeneous Catalytic Reactions*.
- [44] Y. Lei, F. Mehmood, S. Lee, J. Greeley, B. Lee, S. Seifert, R. E. Winans, J. W. Elam, R. J. Meyer, P. C. Redfern, D. Teschner, R. Schlögl, M. J. Pellin, L. A. Curtiss, and S. Vajda, “Increased silver activity for direct propylene epoxidation via subnanometer size effects,” *Science*, Apr. 9, 2010. [Online]. Available: <https://www.science.org/doi/abs/10.1126/science.1185200>.
- [45] S. Lee, L. M. Molina, M. J. López, J. A. Alonso, B. Hammer, B. Lee, S. Seifert, R. E. Winans, J. W. Elam, M. J. Pellin, and S. Vajda, “Selective propene epoxidation on immobilized au_{6–10} clusters: The effect of hydrogen and water on activity and selectivity,” *Angewandte Chemie International Edition*, vol. 48, no. 8, pp. 1467–1471, 2009, ISSN: 1521-3773. DOI: <https://doi.org/10.1002/anie.200804154>. [Online]. Available: <https://onlinelibrary.wiley.com/doi/abs/10.1002/anie.200804154>.

- [46] M. Yang, J. Liu, S. Lee, B. Zugic, J. Huang, L. F. Allard, and M. Flytzani-Stephanopoulos, "A common single-site Pt(II)-O(OH)x- species stabilized by sodium on "active" and "inert" supports catalyzes the water-gas shift reaction," *J. Am. Chem. Soc.*, vol. 137, no. 10, pp. 3470–3473, Mar. 18, 2015, ISSN: 0002-7863. DOI: [10.1021/ja513292k](https://doi.org/10.1021/ja513292k). [Online]. Available: <https://doi.org/10.1021/ja513292k>.
- [47] M. Yang, S. Li, Y. Wang, J. A. Herron, Y. Xu, L. F. Allard, S. Lee, J. Huang, M. Mavrikakis, and M. Flytzani-Stephanopoulos, "Catalytically active Au-O(OH)x- species stabilized by alkali ions on zeolites and mesoporous oxides," *Science*, vol. 346, no. 6216, pp. 1498–1501, Dec. 19, 2014, ISSN: 0036-8075, 1095-9203. DOI: [10.1126/science.1260526](https://doi.org/10.1126/science.1260526). [Online]. Available: <http://science.sciencemag.org/content/346/6216/1498>.
- [48] R. B. Bird, W. E. Stewart, and E. N. Lightfoot, *Transport Phenomena*. John Wiley & Sons, Inc.
- [49] J. J. Bravo-Suárez, K. K. Bando, J. Lu, M. Haruta, T. Fujitani, and T. Oyama, "Transient technique for identification of true reaction intermediates: hydroperoxide species in propylene epoxidation on gold/titanosilicate catalysts by x-ray absorption fine structure spectroscopy," *J. Phys. Chem. C*, vol. 112, no. 4, pp. 1115–1123, Jan. 1, 2008, ISSN: 1932-7447. DOI: [10.1021/jp077501s](https://doi.org/10.1021/jp077501s). [Online]. Available: <http://dx.doi.org/10.1021/jp077501s>.
- [50] G. Mul, A. Zwijnenburg, B. van der Linden, M. Makkee, and J. A. Moulijn, "Stability and selectivity of Au/TiO_2 and $\text{Au/TiO}_2/\text{SiO}_2$ catalysts in propene epoxidation: An in situ FT-IR study," *Journal of Catalysis*, vol. 201, no. 1, pp. 128–137, Jul. 1, 2001, ISSN: 0021-9517. DOI: [10.1006/jcat.2001.3239](https://doi.org/10.1006/jcat.2001.3239). [Online]. Available: <http://www.sciencedirect.com/science/article/pii/S0021951701932397>.